Effect of High Dosage Air-Entraining Admixture Usage on Micro Concrete Properties

Ilker Bekir Topcu[1]*, Ozgun Atesin[1], Tayfun Uygunoglu[2]
[1]Eskişehir Osmangazi University, Civil Engineering Department, 26480 Eskisehir, Turkey.
[2]Afyon Kocatepe University, Civil Engineering Department, 03200 Afyonkarahisar, Turkey.
*CorrespondingAuthor email: ilkerbt@ogu.edu.tr

Abstract

In concrete production, because of air entraining admixtures (AEA) are used for a small percentage by weight of cement (in the range from 0.06% to 0.2%), there is a possible risk adding more admixture in concrete than calculated from personnel or equipment's sensitivity errors. In this situation concrete's strength and durability performances are diminishing. In this work, it was investigated the effect of high dosage air entraining admixture usage on mortar properties. It was carried out unit weight, flowability, setting time, air content, compressive strength, flexural strength, ultrasound velocity tests and microstrucural inspections on specimens which were produced with 5 different dosages including control. As a result of experiments, in case of using admixtures with overdose, there would be loss of quality of physical and mechanical properties of concrete, for this reason it is concluded that, there must be some legal regulations using chemical admixtures sensitively.

1. INTRODUCTION

Starting with the production, concrete has to endure various durability problems. One of these durability problems is freezing and thawing action whose catastrophic damage can be prevented (or diminished) with air entraining admixtures (AEA). Air entraining admixture allows a controlled quantity of small, uniformly distributed air bubbles to be incorporated during mixing which remain after hardening [1]. Air entrainers are used to develop a large number of small spherical air bubbles in the concrete (diameter in range from 50 to 300 micron [2,3]) which are homogeneous and stable after the mixing process. Compared to capillary pores and gel pores in concrete, entrained air voids are very much larger in size [4] but smaller than the entrapped voids. While water freezes inside the entrapped voids in concrete, it expands about 9% in volume. This volume change enforces internal pressure inside the concrete that exceeds its tensile strength, causing cracking, spalling and eventual disintegration. Providing space for ice in concrete in freezing conditions, entrained air voids help to diminish internal hydraulic pressure and thus protect the hardened concrete. Thus, the entrained air void in concrete is a desirable and intentionally produced void.

Because of air entraining admixtures are used for a small percentage by weight of cement (about 0.1 to 0.3%), there is a possible risk adding more admixture in concrete than calculated. Several researches [5–7] proved that air-entraining admixture dosage is the most significant parameter that affects concrete properties. Using AEAs with overdose may produce a reduction in strength [8], aggravate freeze-thaw damage [9], increase permeability and delay in setting [10]. The aim of this study is to determine the effect of overdose usage of air entraining admixture on concrete properties. For this purpose, it was produced mortars with the use of five different admixture dosages. All components (sand, water, cement) except admixture were treated equally. To determine the fresh state properties of mortar; unit weight, flowability, setting time and air content tests were

conducted. To determine the properties of hardened state of mortars; compressive strength, flexural strength and ultrasound velocity were observed. Finally, micro structure analyses were conducted.

2. EXPERIMENTAL STUDY

2.1. Materials

Cement: Locally available CEM I 42.5 R Portland cement, which satisfies EN 197-1, was used. The chemical and physical properties of cement are given in Table 1.

Table 1. Chemical and physical properties of cement.

SiO_2	CaO	Al_2O_3	Fe_2O_3	MgO	Na_2O	K_2O	SO_3	LOI
19.42	63.80	4.47	2.70	1.21	0.28	0.59	2.89	4.18

Spec. Gravity	Blaine, cm^2/g	Compressive Strength, MPa		
3.06	3455	25.2 (2-day)	44.9 (7-day)	59.8 (28-day)

Mixing water: As mixing water, Eskisehir tap water was used. The chemical analysis of the drinkable water is given in Table 2.

Table 2. Chemical analysis of mixing water.

pH (20°C)	Cl- mg/l	SO4 mg/l	Mg mg/l	Ca mg/l	Zn mg/l	Cu mg/l	Fe mg/l	NO_3 mg/l	ClO_2 mg/l
7.49	6.53	91.5	41.5	63.8	0.375	0.092	0.074	4.35	< 0.09

Sand: In order to produce mortar, sand that satisfies EN 196-1 was used.

Admixture: In order to investigate the effects of air-entraining admixture, commercially available AEA, supplied from Grace Company, were used and its characteristics are given in Table 3.

Table 3. Properties of AEA.

Properties	AEA
Ingredient	Sodium salt mixture
Color	Brown
State	Liquid
Density g/ml (20°C)	1.009
pH (20°C)	6.6
Total Chloride %	< 0.10
Total Solid (%)	3.6

2.2. Method

In order to observe the differences in concrete by the dosage of admixture, cement and CEN standard sand quantities were set to equal in each mixture. Mixing water was reduced as much as admixture amount. The water-cement ratio is selected as 0.50 for the mortar production. In principle, 5 different norm dosages including control were prepared for each admixture. But in order to reach definitive results for some tests, like compressive strength test, additional dosages in the range of 0% - 2% were applied. The designation and norm dosages of admixtures are given in Table 4.

Prepared mortar was cast into 4 x 4 x 16 cm dimensioned formworks made of steel directly after mixing. The samples were separated into groups, each cured at a constant temperature of 20 °C in the curing pool.

Table 4. The designation and norm dosages of admixture.

Admixture	Optimum Dosage[1]	Dosages and Designations				
AEA	0.06% - 0.2%	0% Control C-0	0.1% AEA-0.1	0.5% AEA-0.5	1.0% AEA-1	2.0% AEA-2

[1]Optimum dosage refers to dosage range that suggested by producer. It refers to a range, because optimum dosage must be assessed after preliminary trials depending upon the actual mix constituents and specifications required.

2.3. Tests

Fresh unit weight was obtained by following EN 12350-6 and using Eq.1.

$$D = \frac{m_2 - m_1}{V} \qquad (1)$$

Where D is unit weight (t/m^3), m1 empty weight (t) of cast, m^2 weight (t) of cast with mixture and V is the volume (m^3) of cast.

To evaluate the flowability of mixtures, the flow table tests were carried out following EN 1015-3 [11]. As a test procedure; after lifting the slump cone, two diameters perpendicular to each other are measured and their mean is noted as relative slump.

To measure initial and final setting times, EN 480-2 code was followed. Using Vicat apparatus with the needle of (1.13 ± 0.05) mm diameter, setting times were observed.

Air content in fresh mortar specimens were measured with an apparatus that work with principle of pressure method which is based on Boyle's law [12]. Prepared mixture was poured into impermeable cast, then cast was pressurized to the certain pressure and then impermeability was removed in controlled manner. At this time air content was observed with the aid of manometer.

Ultrasound wave transmission measurements were implemented using commercially available instrument that satisfies ASTM 597-02. Principally, a pulse is generated at one end of the specimen and the onset of the pulse is picked at the other side. The signal transition duration via specimen is observed. Distance that ultrasound applied to time ratio gives the ultrasound velocity value.

Flexural and compressive strength were measured by means of a hydraulic press. Flexural strength tests were implemented on three 4x4x16 cm dimensioned specimens per mortar, satisfying the EN 1015-11 code. Specimens were placed to 3-point flexural strength apparatus (one-point loading) with the span of 10 mm. The loading rate in flexural tests was 0.05 MPa/sec. The six samples collected from the flexural rupture were used for the compressive analysis. The loading rate in compressive tests was 0.3 MPa/sec. Compressive strength values were collected at ages 7, 28, 56 and 90 days.

After completing mechanical tests on 90 days old specimens, mortar samples were taken, in order to perform microscopic observations. The qualitative phase analysis of hydrated cementitious systems by XRD proved to be a good way of interpreting hydration kinetics [13–15]. In this work, quantitative XRD analysis was carried

out to obtain information about the phase compositions of the mortars. For microstructural analysis, diffractograms were recorded with a Panalytical Empyrean diffractometer, operated at 45 kV and 40 mA, from 10 to 80° 2θ at 0.08° increments, using CuKα radiation. All samples were ground to powder, placed to sample holder of diffractogram and measured about 5 minutes. Evaluation of the observed data was performed with the HighScore Plus™ software.

In this work, SEM analyses were carried out using Zeiss Supra 40VP. First, specimens were cut to small dimensions (1 cm x 1 cm) in order to fit into the sample holder. Samples were fixed to sample holder with carbon tape, then samples were covered with platinum using Quorum Q150R ES. Samples were placed to sample room of Supra 40VP and vacuumed environment was provided using inert nitrogen gas. Ensuring the observation conditions, specimens were analyzed and various photos were recorded.

Bruner Emmet Teller (BET) method is a widely used method to obtain porosity of samples, pore size distribution and specific surface area. As a BET analyzer, The Micromeritics Asap 2020 was used for NAD analysis. In the range of 1 to 2.5 g of sample is picked up for NAD analyses. Samples were degassed by pre heating for a designated temperature with a dry, inert nitrogen gas in order to remove moisture in the specimen prior to measurements.

3. RESULTS AND DISCUSSION

3.1. Fresh mortar properties

3.1.1. Fresh unit weight

Because of its nature, air entraining admixtures have an effect of diminishing unit weight of concrete. In this work, it was observed continuous reduction of unit weight with the increasing admixture ratio as seen in Fig. 1. The most important result of this test is that using AEA within the range of optimum dosage, namely 0.1%, has an effect of considerable drop of unit weight which corresponds to 16%, compared to control mixture. Another key point of the graph is that; speed of unit weight drop is diminishing after 0.5% of dosage.
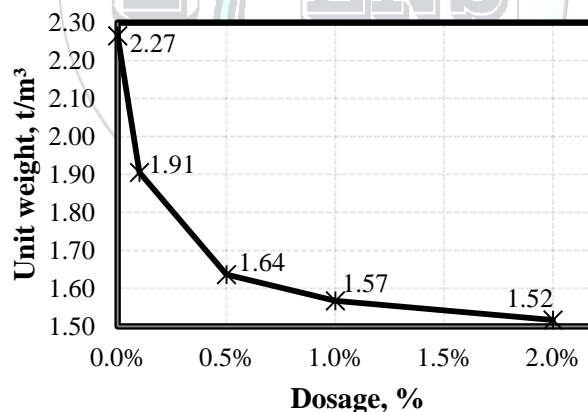

Fig. 1. Fresh unit weight variation depending on admixture dosage.

3.1.2. Flowability (Flow table)

As mentioned in literature, AEAs have an effect of imparting plasticity to the fresh concrete [4,16,17]. As can be seen in Fig. 2, using AEA with the dosage of 0.1%, increased flowability 34% compared to control mixture. But after optimum dosage there is no considerable flowability augmentation, even it can be said that there is no change after the dosage of 1%.
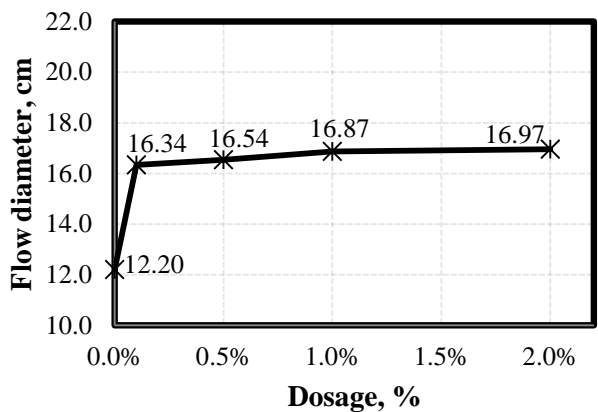
Fig. 2. Flow diameter values obtained from flow table.

3.1.3. Setting times

Fig. 3 illustrates initial and final setting time results. Initial setting times are varying from 179 to 433 minutes, while final setting times vary from 239 to 588 minutes. After certain point for initial setting, namely 0.5%, there is no considerable change for initial setting time while dosage of the admixture is increasing. But, delay of the initial setting time of 2% AEA dosage corresponds to 254 minutes when compared to control mixture. Similar trends were observed for the final setting times. With the increment of dosage, final setting times were extended.
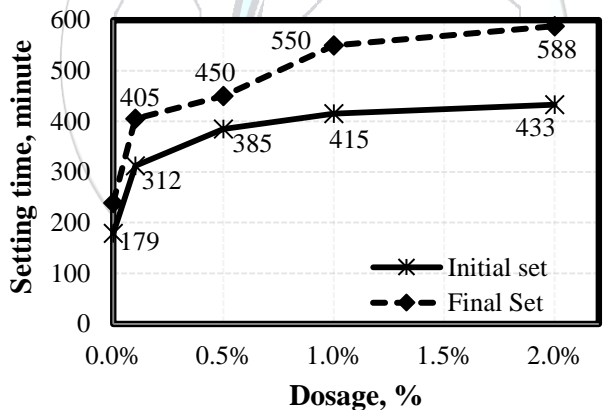

Fig. 3. Initial and final setting time variation depending on admixture dosage.

3.1.4. Air content

Probably the most important parameter for air entrained concrete is air content. As expected, with the increment of dosage, air content in mortar was augmented. As can be seen in Fig. 4, using AEA within the optimum dosage, namely 0.1%, has augmented air content more than twice compared to control mixture. Moreover, slightly exceeding the optimum dosage range, namely 0.5%, air content of mortar specimen escalated to 11.4%, nearly four times of control mixture. But, another significant point of this test is that there is no considerable air content augmentation beyond the dosage of 0.5%. Based on the test results, using AEA more than 0.5% dosage has no avail practically on the base of air content.
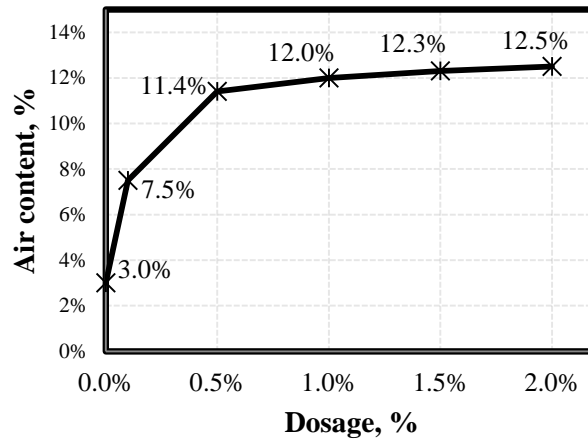
Fig. 4. Air content variation depending on admixture dosage

3.2. Hardened mortar properties

3.2.1. Ultrasound velocity

Ultrasound velocity test results at the age of 28-days are plotted in Fig. 5. Ultrasound velocity values are varying from 2.37 km/sec to 4.09 km/sec for AEA used mortars. AEA used mixtures' ultrasound velocity values were reduced 14.8%, 30.2%, 36.9, %39.6% and %42.7 compared to control mixture at 0.1%, 0.5%, 1%, 1.5% and 2% dosages respectively.
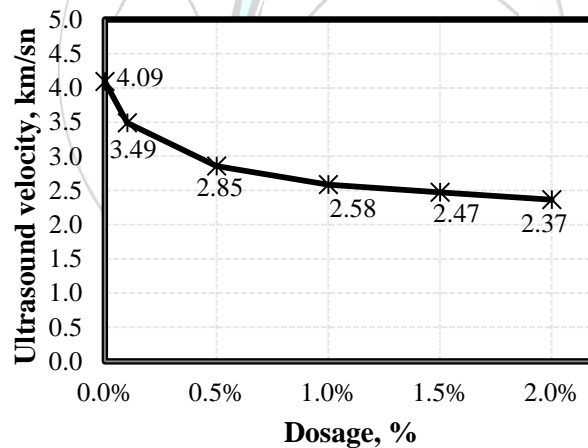

Fig. 5. Ultrasound velocity variation depending on admixture dosage

3.2.2. Flexural strength

AEA used mixtures' flexural strength values at the age of 28-days are presented in Fig. 6. With the augmentation of air content, flexural strength values were diminished because of reverse ratio of air content to strength. AEA used mixtures' flexural strength values were decreased 49.3%, 78.3%, 82.9%, 85.2% and 86.3% compared to control mixture at 0.1%, 0.5%, 1%, 1.5% and 2% dosages respectively. The key point of the graph is that there is a rapid drop of strength up dosage of 0.5%, but beyond this dosage there is no considerable strength drop.
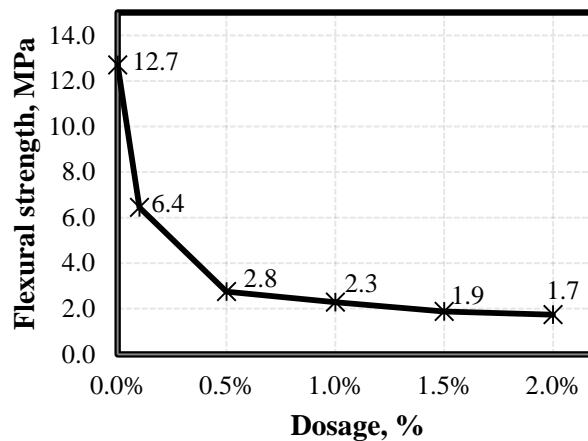
Fig. 6. 28-day aged mortar flexural strength variation depending on admixture dosage.

3.2.3. Compressive strength

Compressive strength tests were conducted at the ages of 7, 28, 56 and 90 days old specimens. Instead of representing each day separately, in order to see strength gain, all values are combined one graph. Fig. 7 illustrates the compressive strength variations depending on time and admixture dosage, for AEA used mixtures. Considering Fig. 7, there is a continuous compressive strength loss with the augmentation of dosage. But on the other hand, speed of compressive strength drop is diminishing after 0.5% of dosage. Although, there is a compressive strength reduction at the dosage of 0.1% compared to control mixture, strength gain depending on time is continuous and stable. But exceeding 0.1%, there is no strength gain depending on time; in other words, specimens reach their ultimate strength nearly at the age of 7 days.
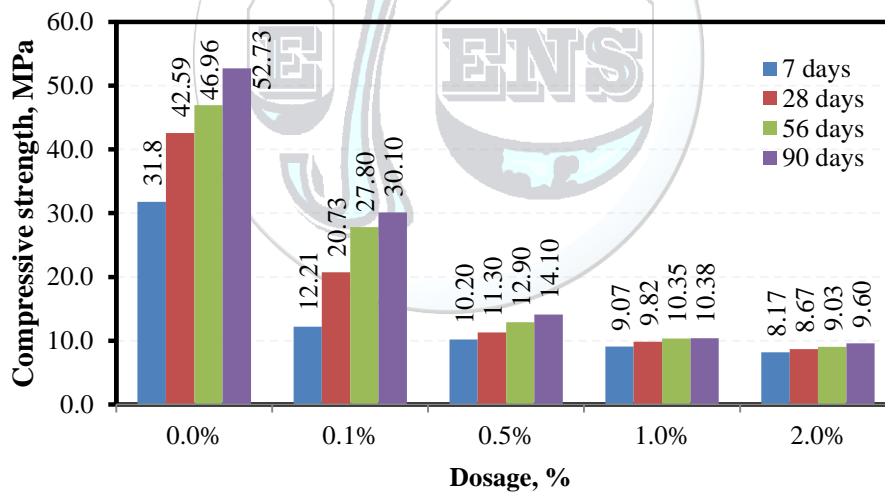

Fig. 7. Mortars compressive strength variation depending on admixture dosage

3.3. Microstructural analysis

3.3.1. X-ray diffraction (XRD) analysis

Because of sand is the main ingredient of concrete proportionally, quarts is the main phase of XRD analysis. XRD analysis of AEA used mixtures for 6 different dosages including control are plotted in Fig. 8. There is no significant phase difference between XRD analysis, because of there is no mineral admixture addition. It can be said that, AEA doesn't change internal structure and/or chemical composition. Physical differences (flowability, strength etc) observed on specimens are due to air content.
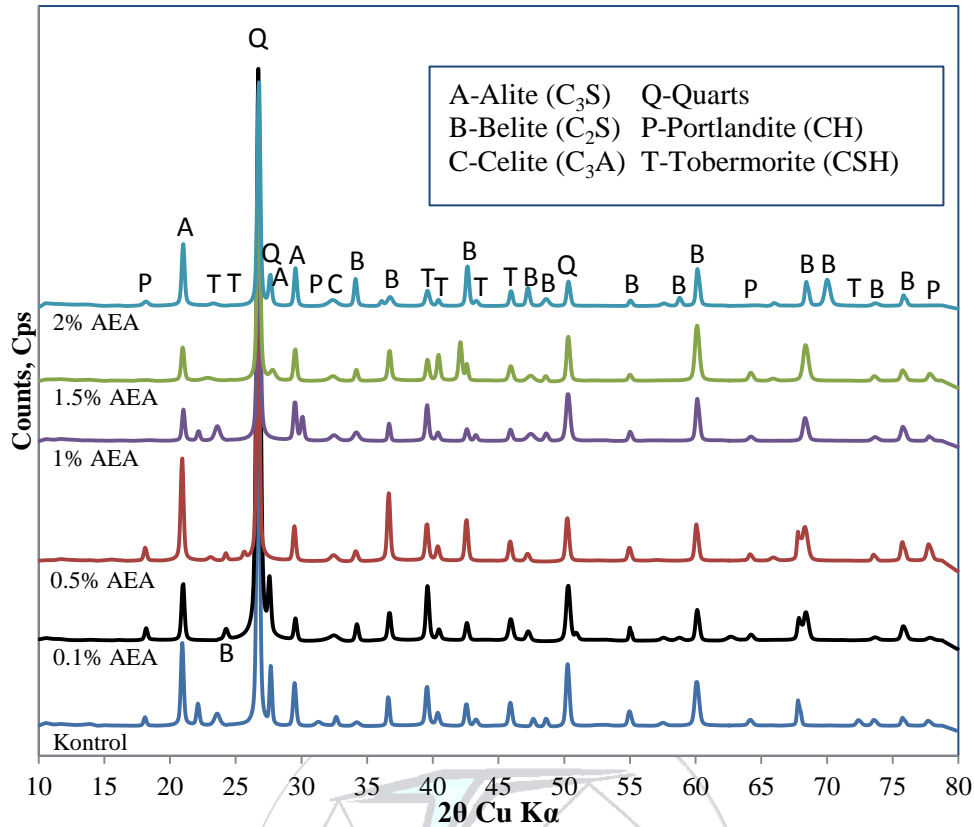
Fig. 8. AEA used mortars XRD analysis.

3.3.2. Scanning electron microscope (SEM) analysis

Fig. 9 shows the result of SEM analysis of the 100 times magnified surface of the AEA included specimens at 90 days-age. Because there is no ingredient in mortar aside from main materials (such as sand, cement and water) that can be seen by SEM analysis, and the basis of the work is the entrained-air, air voids were investigated. Samples used for SEM analysis were taken from specimens with rupture technique, instead of cutting. Since the plane of examination does not usually cut through the center of the spheres [18], in order to observe true air void diameters, rupture technique was applied, because of specimens are tent to rupture the weakest section which is the center of the void. Considering Fig. 9, samples have air voids in the range from 50μm to 500 µm in diameter. It can be easily seen that with the increment of dosage, air void content is augmenting.

(a)   (b)
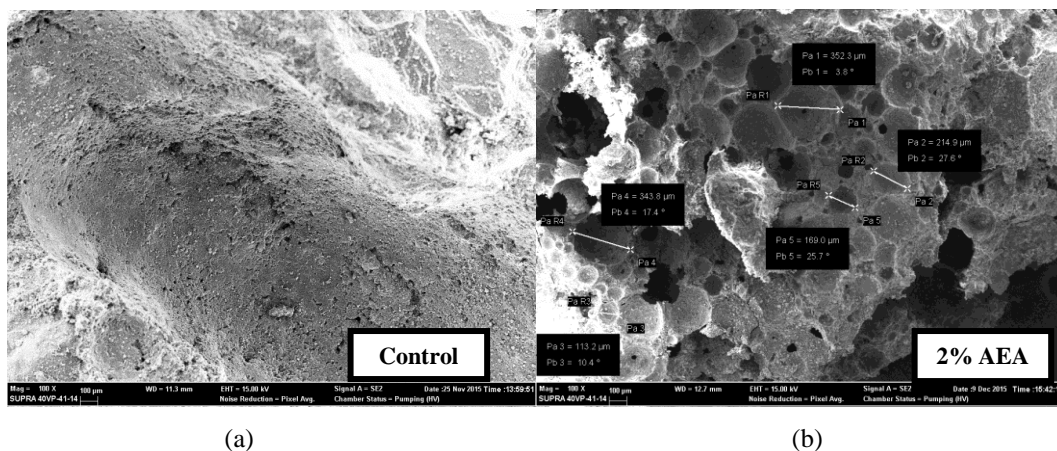
Fig. 9. SEM image of specimens (magnification x100). (a) Without AEA, (b) 2% AEA

3.3.3. Nitrogen absorption/desorption (NAD) analysis

The micropore volume obtained from t-Plot, mesopore volume obtained from Barett, Jonyer and Halenda (BJH) method and total pore, sum of two, are summarized in Table 5.

Table 5. Total pore volume of 90-day aged mixtures.

Type	t-Plot micropore (cm³/g x 10-2)	BJH Desorption mesopore (cm³/g x 10-2)	Total Pore Volume (cm³/g x 10-2)
C-0	0.0436	1.8375	1.8811
AEA-0.1	0.0114	1.4417	1.4531
AEA-2	0.0846	2.0830	2.1676

According to IUPAC (International Union of Pure and Applied Chemistry), sizes of pores are categorized in three groups; macropores (greater than 50 nm), mesopores (between 2 to 50 nm) and micropores (less than 2 nm) [19,20]. With BET analysis, pores less than 500 nm can be analyzed. But, as mentioned before, entrained air voids are in the range of 50 to 300 micron, which equals to 50000 to 300000 nanometer. For this reason, entrained air voids are ignored in BET analysis, because of BET analysis is in nano scale, not in macro scale.

Using AEA within the range of optimum dosage, the total pore amount was less by 22.8% than the total pore amount of the control mixture at the age of 90 days. But, using AEA with overdose, the total pore amount was larger by 15.2% than the total pore amount of the control mixture. According to analysis, using AEA with the dosage of 0.1%, pore volume has decreased. This phenomenon can be explained by workability property. It is known that, air entraining admixtures have an effect of enhancing workability [21], and for this reason pore volume was diminished.

Pore size distribution of three different mixtures is given in Fig. 10. It can be seen that there are two peaks, first one is around 30 Å pore width (left part was unable to measure) and the second one is around 240 pore width. AEA-0.1 mixture has more pores compared to control at first peak, while AEA-2 has the most pores than control and AEA-0.1 at 30 Å pore size. On the other hand, AEA-0.1 mixture has less pores, compared to control at second peak, while AEA-2 again has more pores than control and AEA-0.1 at second peak.
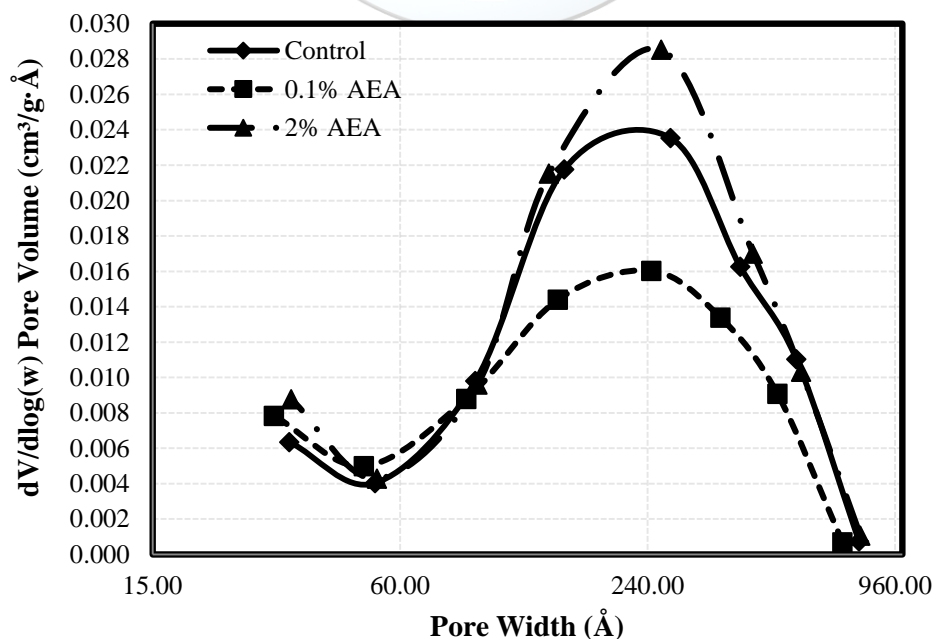
Fig. 10. BJH desorption pore volume curves for three mixes at 90 days.

4. CONCLUSIONS

In this study it was investigated to determine the effect of overdose usage of air entraining admixture on concrete properties. To evaluate the possible effects, fresh state and hardened state tests were conducted. Also as microstructural analyses, XRD, SEM and BET analyses were performed. Based on the experimental results, the following conclusions are drawn:

1.   As expected, with the increment of dosage, AEA used mixtures' fresh unit weight values were decreased considerably. This drop corresponds to 33% at the dosage of 2% compared to control mixture.

2.   It is known that spherical shape of AEA has an effect of enhancing workability. For this reason, with the increment of dosage, specimens' flowability has augmented. But this augmentation trend tent to slow down after the dosage of 0.1%

3.   It can be easily said that AEA usage extends setting times.

4.   As expected, the more AEA usage, the more air content in concrete.

5.   According to test results, it is obvious that AEA usage decreases the strength of concrete, both flexural and compressive. This result derives from the air void presence. For this reason, AEA must be used carefully on high strength concrete applications.

6.   According to micro structural analysis, both XRD and SEM, AEA has no effect on chemical composition and CSH formation of concrete. Differences of the physical properties of concrete with the dosage variation are due to air void presence in concrete.

7.   With the aid of BET analysis, it was observed that AEA has a positive effect on diminishing nanoscale pores (less than 500 nm) within the range of optimum dosage. This phenomenon can be explained with workability property. With increasing workability, nanoscale pores are diminishing.

With the sum of all tests and analyses, AEA must be used carefully and within the range of optimum dosages, otherwise there would be loss of physical and mechanical properties of concrete. For this reason, chemical admixtures in general, must be used in process of concrete production in plants and uncontrolled usage in the field must be prohibited.

ACKNOWLEDGMENT

REFERENCES

[1]   TS EN 934-2+A1 Admixtures for concrete, mortar and grout - Part 2: Concrete admixtures - Definitions, requirements, conformity, marking and labelling, Turkish Standards Institution, 2013.

[2]   J. Jasiczak, K. Zielinski, Effect of protein additive on properties of mortar, Cement and Concrete Composites. 28 (2006) 451–457. doi:10.1016/j.cemconcomp.2005.12.007.

[3]   B. Łaźniewska-Piekarczyk, The frost resistance versus air voids parameters of high performance self compacting concrete modified by non-air-entrained admixtures, Construction and Building Materials. 48 (2013) 1209–1220. doi:10.1016/j.conbuildmat.2013.07.080.

[4]   L. Du, K.J. Folliard, Mechanisms of air entrainment in concrete, Cement and Concrete Research. 35 (2005) 1463–1471. doi:10.1016/j.cemconres.2004.07.026.

[5]   M. Pigeon, J. Marchand, R. Pleau, Frost resistant concrete, Construction and Building Materials. 10 (1996) 339–348. doi:10.1016/0950-0618(95)00067-4.

[6]   A.H. Akca, N.Ö. Zihnioğlu, High performance concrete under elevated temperatures, Construction and Building Materials. 44 (2013) 317–328. doi:10.1016/j.conbuildmat.2013.03.005.

[7]   D.S. Zhang, Air entrainment in fresh concrete with PFA, Cement and Concrete Composites. 18 (1996) 409–416. doi:10.1016/S0958-9465(96)00033-9.

[8]   M. Grantham, Advanced Concrete Technology, Elsevier, 2003. doi:10.1016/B978-075065686-3/50269-X.

[9]   F. Rendell, R. Jauberthie, M. Grantham, Deteriorated Concrete: Inspection and Physicochemical Analysis, Thomas Telford Ltd, 2002.

[10] B. Łaźniewska-Piekarczyk, The methodology for assessing the impact of new generation superplasticizers on air content in self-compacting concrete, Construction and Building Materials. 53 (2014) 488–502. doi:10.1016/j.conbuildmat.2013.11.092.

[11] R. Yu, P. Spiesz, H.J.H. Brouwers, Development of an eco-friendly Ultra-High Performance Concrete (UHPC) with efficient cement and mineral admixtures uses, Cement and Concrete Composites. 55 (2015) 383–394. doi:10.1016/j.cemconcomp.2014.09.024.

[12] V.S. Ramachandran, Concrete Admixtures Handbook, Elsevier, 1996. doi:10.1016/B978-081551373-5.50001-5.

[13] S.T. Bergold, F. Goetz-Neunhoeffer, J. Neubauer, Quantitative analysis of C–S–H in hydrating alite pastes by in-situ XRD, Cement and Concrete Research. 53 (2013) 119–126. doi:10.1016/j.cemconres.2013.06.001.

[14] C. Karakurt, Microstructure properties of waste tire rubber composites: an overview, Journal of Material Cycles and Waste Management. (2014) 422–433. doi:10.1007/s10163-014-0263-9.

[15] I.B. Topçu, M.U. Toprak, T. Uygunoğlu, Durability and microstructure characteristics of alkali activated coal bottom ash geopolymer cement, Journal of Cleaner Production. 81 (2014) 211–217. doi:10.1016/j.jclepro.2014.06.037.

[16] M. Griffith, H.O. Sugo, A.W. Page, S.J. Lawrence, The Influence of Air Entraining Agent on Bond Strength and Mortar Microstructure., (2001) 357–366.

[17] B. Łaźniewska-Piekarczyk, Examining the possibility to estimate the influence of admixtures on pore structure of self-compacting concrete using the air void analyzer, Construction and Building Materials. 41 (2013) 374–387. doi:10.1016/j.conbuildmat.2012.11.100.

[18] S. Diamond, The microstructure of cement paste and concrete - A visual primer, Cement and Concrete Composites. 26 (2004) 919–933. doi:10.1016/j.cemconcomp.2004.02.028.

[19] D. Snoeck, L.F. Velasco, A. Mignon, S. Van Vlierberghe, P. Dubruel, P. Lodewyckx, et al., The effects of superabsorbent polymers on the microstructure of cementitious materials studied by means of sorption experiments, Cement and Concrete Research. 77 (2015) 26–35. doi:10.1016/j.cemconres.2015.06.013.

[20] T. Hemalatha, M. Gunavadhi, B. Bhuvaneshwari, S. Sasmal, N.R. Iyer, Characterization of micro- and nano- modified cementitious system using micro analytical techniques, Cement and Concrete Composites. 58 (2015) 114–128. doi:10.1016/j.cemconcomp.2015.01.004.

[21] H. Ziari, P. Hayati, J. Sobhani, Airfield self-consolidating concrete pavements (ASCCP): Mechanical and durability properties, Construction and Building Materials. 72 (2014) 174–181. doi:10.1016/j.conbuildmat.2014.08.047.

Enhancing Heat Transfer from a Porous Plate with Transpiration Cooling

Mustafa Kilic[1], Tolga Taner[2]

[1]Adana Science and Technology University, Department of Mechanical Engineering, 01180 Seyhan /Adana, Turkey
Corresponding author: mkilic@adanabtu.edu.tr
[2]Aksaray University, Department of Motor Vehicles and Transportation Technology, 68100, City Centre/Aksaray, Turkey.

Abstract

The present study is focused on developing structural solid surface geometry to improve heat transfer by cooling of air with transpiration cooling. Effects of flow rate of water ($\dot{m}_{water}$= 0.000083, 0.000116, 0.000166, 0.000249 kg/s) and particle diameter of porous plate (Dp= 40, 50, 100, 200 μm) on local wall temperature and cooling efficiency of porous plate and the system inside a rectangular channel with air as a hot gas stream and water as a coolant were investigated experimentally. High performance polyethylene as a porous media was used not only to form a thermal barrier but also an active cooling plate by evaporating water from the surface of porous media to cool air. Temperatures were measured by T-type thermocouples. Two electric heaters were used to support enough power to the system. It was observed that increasing water flow rate did not cause a prominent decrease on surface temperature and cooling efficiency of porous plate. The higher injection rates result in further increase of the cooling effectiveness. Cooling efficiency of porous plate changed from 38 to 90 %. Increasing water flow rate as a coolant causes a prominent increase on cooling efficiency of the system. Increasing water flow rate three times causes an increase of 26.4 % on cooling efficiency of the system. Decreasing particle diameter causes a significant decrease on surface temperature. Difference of cooling efficiency of porous plate from Dp=40 to Dp=200 μm decreases from 12% to 2 % from inlet region to end of porous plate.

1. INTRODUCTION

Transpiration cooling is considered as an attractive cooling technique. This method has been used to protect solid surface exposed to high-heat-flux, high-temperature environments such as hypersonic vehicle combustors, liquid rocket thrusters, gas turbine blades, water oxidation technology, the first wall and blanket region in fusion reactors, the nose of aerospace vehicles during the atmospheric re-entry phase of their flight. Transpiration cooling processes involve simultaneously two different heat transfer mechanisms: conduction through a solid plus convection. In transpiration cooling process: fluid coolant is injected into porous matrix in the direction opposite to heat flux, at the same time absorbs the heat conducted into the solid matrix and transports heat flux through the convection passing pores, finally the coolant forms a thin film on the hot side surface to reduce the heat flux coming into the porous matrix and to cool the hot gas stream. The porous matrix in transpiration cooling can be some different types of porous media. Sintered stainless steel walls, metal fibers ceramics and porous plastics can be used as a porous media. The structure generally has a large number of pores with diameter ranging between 5 and 200 μm and can be made of different shaped particles as spherical, porous plate thicknesses can be change between 1 and 10 mm or more.

Interest and research in this topic may even have accelerated in recent years because of its high potential of heat transfer. Many investigators have performed experimental and numerical studies to determine the heat transfer characteristics for transpiration cooling. Jiang et al. [1] investigated turbulent flow and heat transfer in a rectangular channel without and with transpiration cooling experimentally and numerically. They used two-

layer k-ε model to calculate the turbulent velocity and thermal characteristics of the main flow. They used sintered bronze particles as porous wall and air as coolant. The nominal particle diameter of the sintered porous wall was 0.1 mm and the porosity was 0.45. Their results showed that the transpiration cooling greatly increases the boundary layer thickness and reduces the wall skin friction and increasing coolant blowing ratio sharply reduced both the wall temperature and the convection heat transfer coefficient. Liu et al. [2] investigated the transpiration cooling mechanisms for thermal protection of a nose cone experimentally and numerically for various cooling gasses. In their study: the effects of injection rates, model geometry, inlet temperature and Reynolds number of the main stream were studied for air, nitrogen, argon, carbon dioxide and helium. Two-dimensional numerical simulation using the RNG k-ε turbulence model for the main stream flow and the Darcy-Brinkman- Forchheimer momentum equation and thermal equilibrium model were used to compare the general features in the experiments. Their results showed that the injection rate strongly influenced the cooling effectiveness. The increase of the main stream inlet Reynolds number dramatically reduced the cooling effectiveness. And the coolant thermos physical properties, especially specific heat, most strongly influenced the cooling effectiveness. Liu et al.[3] investigated the flow and heat transfer characteristic of transpiration cooling through sintered porous flat plates with particle diameters dp= 40 and 90 μm experimentally and numerically with dry air as the coolant stream. In their study their parameters were solid matrix thermal conductivity, injection rate and particle diameter. They showed that the cooling effectiveness increased with increasing injection rate, the temperature distribution on the porous bronze plate was more uniform than that on the sintered stainless steel plates and the cooling performance for the porous wall with the smaller particle diameters was better. Arai and Suidzu [4] investigated experimentally effects of the porous ceramic coating material such as permeability of cooling gas, thermal conductivity and adhesion strength. The mixture of 8 wt.% yttria-stabilized zirconium and polyester powders was employed as the coating material, in order to deposit the porous ceramic coating onto Ni-based super alloy substrate in their study. They showed that porous ceramic coating has superior permeability for cooling gas and transpiration cooling system for gas turbine could be achieved by using porous ceramic coating. He et al. [5] investigated new conversation equation for mass, momentum and energy to describe the performances of fluid flow, heat absorption and phase change in porous matrix. Their model's main differences from previous models are firstly, considering the compressibility of vapor in the momentum and energy equations, secondly, adding a term of the momentum transfer caused by liquid phase change into the momentum equation of vapor and liquid phases in two-phase region, finally in the energy equation of two-phase region, taking the variations of temperature and pressure into account. Their results showed that with an increase in heat flux and decrease in coolant mass flow rate the temperature difference over the two-phase region falls and a higher external heat flux or lower coolant mass flow rate will accelerate the phase change process and increase he area of two-phase region and vapor region. Wang et al [6] investigated the effect of different mainstream temperature, Reynolds numbers, and coolant injection ratio on transpiration cooling of the wedge shape nose cone with an equal thickness porous wall using liquid water as coolant. They obtained that the average temperature over the transpiration area falls with an increase in the coolant injection ratio, whereas the average cooling effectiveness rise and There is an optimal injection rate, at which the coolant passing through pores with liquid state when the driving force for the coolant injection is the minimum and the cooling effectiveness is high. Tsai et al. [7] investigated the transient cooling process in a sudden-expansion channel with the injection of cold air from the porous bottom wall experimentally. They identified distinct flow features under various rates of coolant injection. They categorized flow features to four cooling patterns; the recirculation pattern, the elevated recirculation pattern, the transpiration pattern and film pattern. Langener et al. [8] investigated transpiration cooling applied to flat C/C material under subsonic main-flow conditions. In their study; main-stream Mach number ranged from Mg= 0.3-0.7 and totals temperature was 523 K. Air, argon and helium were used as coolants. They showed that thickness of sample and main stream total temperature did not affect the cooling efficiency. The coolant used and its specific capacity was the most influential parameter for the cooling efficiency. And with higher Mach number the cooling efficiency decreased. Tsai and Lee [9, 10] investigated the correlation between superheat levels and heat fluxes when used sintered powder structures as wicks. Their parameters were 45 μm, 75 μm, 150 μm of powder sizes and powder shapes of spherical, dendritic. Their results showed that smaller powders structures achieved higher effective thermal conductivities for both powder shapes. Spherical powder structures achieved twice the effective thermal conductivity of dendritic powder ones for each powder size. And at the same superheat level structures of smaller powder size and dendritic powder shape achieved higher heat fluxes. He et al [11] investigated performance of evaporative cooling with cellulose and Polyvinyl Chloride (PVC) corrugated media experimentally. The heat and mass transfer and pressure drop across the two media with three thicknesses (100, 200, 300 mm) were studied. Their results showed that the pressure drop range of the cellulose media is 1.5-101.7 Pa while the pressure drops of the PVC media are much lower with the range of 0.9-49.2 Pa, depending on the medium thickness, air velocity and water flow rate. The cooling efficiency of the cellulose media vary from 43% to 90% while the cooling efficiency of the PVC media are 8% to 65% depending on the medium thickness and air velocity. Most of these previous investigations can be divided into two categories. The first group focused on analyses of the characteristics of the boundary layer,

turbulent or laminar flow in transpiration conditions. The second group focused on transpiration cooling effectiveness at high pressure and temperature to simulate practical operational conditions. However, there are few studies of developing structural solid surface geometry and controlling the temperature of hot gas stream and surface to enhance heat transfer by using transpiration cooling. The objective of this study is to investigate the local wall temperature and cooling effectiveness distribution along the surface of a porous flat plate with air as a hot gas stream and water as a coolant to figure out the influence of mass flow rate of water, and particle diameters of porous plate.

2. MATERIALS AND METHODS

In This study; an experimental investigation of effects of mass flow rate of water, and particle diameters of porous plate on local wall temperature and cooling efficiency along the surface of a porous flat plate inside a rectangular channel with air as a hot gas stream and water as a coolant was done. For this purpose a porous plate was used not only to form a thermal barrier but also an active cooling system by evaporating water from the surface of porous media.

2.1 Experimental Apparatus

A schematic of the experimental facility, which consists of an air blower, flow meter for air and water, a computerized data acquisition system, a test section, a power unit, an absolute and differential manometer and a calibrator thermometer, is shown in Fig. 1. The power unit includes variac and parallel connected air heaters. The test section is composed of a polycarbonate rectangular channel and a porous plate. Details of the test section are shown in Fig.2. The channel is made of polycarbonate sheet and its geometry is shown in Fig. 2. Dimensions of test section were arranged as 220x880x10 mm (width, length, high). Hydraulic diameter of the channel is 19.1 mm. Then porous plates (high performance polyethylene) were arranged and located over water channel in test section precisely. Temperatures at the centers of porous plate were measured using calibrated T-type thermocouples inserted through 2 mm holes inside the thickness of the porous plate. Calibrated thermocouples were located in the middle of porous plates in this arrangements (6,16,28,38,50,60,72,82 cm).
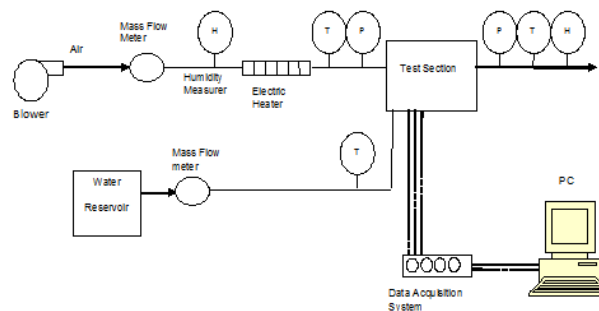

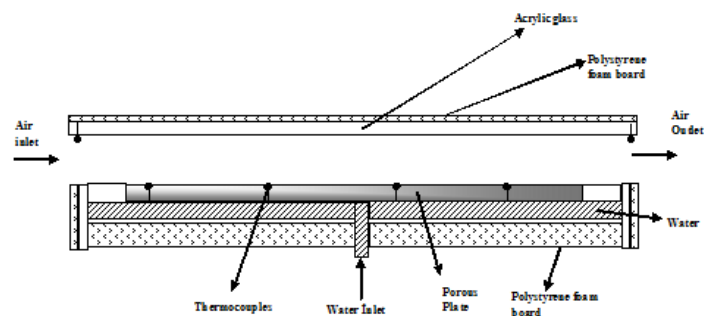Figure. 1. Schematic of experimental apparatus

Figure. 2. Details of the test section

Conventional temperature measurements of the porous plate surface were used to evaluate cooling efficiency of the system. Two electric heaters were used to support enough power to the system to increase air temperature to the needed level. This electric heater was connected parallel and they supplied 280-620 W power to the system according to needed power. A variac was used to arrange voltage to support needed power for the system. The total power supplied was monitored using digital multimeters for the control of voltage and current. Then flow meter of air and water were added to the system. For each particle diameter (40, 50, 100, and 200 micrometer) porous plates were prepared again and tested for different parameter. Air temperatures

ranged between 47°C and 77°C. Polystyrene foam board was used to insulate the top side of the channel with a thickness of 50 mm (k = 0.032 W/(m.K)). The ambient temperatures in the experiments varied between 20°C to 24°C. The system was assumed to be steady state when variations of the surface temperatures and the inlet and outlet fluid temperatures of water and air were all within ±0.1 ºC.

2.2 Data Reduction

The focus of the present investigation is to develop structural solid surface geometry to improve heat transfer by cooling of air with transpiration cooling. Inlet and outlet temperature of hot stream gas (air) were chosen according to the inlet and outlet temperature of cooling systems. In this application there is a porous plate in a rectangular channel, this porous plate is wetted by water of which reservoir temperature is Twater= 22 ºC. Air enters into the channel with some different temperatures and velocities. For this application dry air (relative humidity of air, x=0) was used as a hot gas stream.

In this application; all Reynolds numbers were bigger that 3000 so it can be assume that it is a turbulent flow. Mean average film temperature in the channel is calculated as;

$$T_{avg} = \frac{T_{airin} + T_{surface}}{2}$$

(1)

where Tairin is the inlet temperature of air, Tsurface is the average surface temperature of porous plate. So It can be calculated, as explained by Mills [12], some physical properties of air by using thermodynamics tables as; ρ is the density of air, cp specific heat of air, γ is the kinematic viscosity, Pr is the Prandtl number and Sc Schmidt number. So Stanton number with zero porosity can be calculated as;

$$St^* = 0.0296 (\mathrm{Re})^{-0.2} (\mathrm{Pr})^{-2/3}$$

(2)

And convective heat transfer coefficient with zero-mas-transfer will be;

$$hc^* = \rho.V_{air}.Cp.St^*$$

(3)

where ρ is the density of air, Vair is air velocity, cp specific heat of air and St* is stanton number.

So mass transfer driving force is;

$$B_m = \frac{m_{ev} - m_s}{m_s - 1}$$

(4)

where mev is mass fraction of water vapor at channel flow and ms is mass fraction of water vapor at surface.

And mass transfer St number can be calculated as;

$$St^*{}_{mass} = 0.0296 (\mathrm{Re})^{-0.2} (Sc)^{-2/3}$$

(5)

So the zero mass transfer limit conductance will be;

$$g^*{}_{mass} = \rho.V_{air}.St^*{}_{mass}$$

(6)

where ρ is the density of air, Vair is air velocity and St*mass is the mass transfer stanton number. And the mass transfer conductance is;

$$g_{mass} = g^*{}_{mass}.\frac{\ln(1 + B_m)}{B_m}$$

(7)

where $g^*{}_{mass}$ is the the zero mass transfer limit conductance, Bm is the mass transfer driving force. So mass flow rate of evaporated water is;

$$m_{ev} = g_{mass}.B_m$$

(8)

Then heat transfer blowing parameter is;

$$B_h = \frac{\dot{m}_{ev}.Cp}{hc^*} \tag{9}$$

where $\dot{m}_{ev}$ is the mass flow rate of evaporated water, cp specific heat of air and hc* is convective heat transfer coefficient with zero-mas-transfer. And convective heat transfer coefficient for surface of porous plate is;

$$h_c = h_c^* . \frac{B_h}{\exp(B_h)-1} \tag{10}$$

So energy balance equation on the surface of porous plate is;

$$\dot{m}_{air}.(h_{airout} - h_{airin}) = \dot{m}_{water}.(h_{waterin} - h_{fg} - h_{waterout}) \tag{11}$$

where $\dot{m}_{air}$ is the mass flow rate of air, h_{airout} is the outlet enthalpy of air, h_{airin} is the inlet enthalpy of air, $\dot{m}_{water}$ is the mass flow rate of water, $h_{waterin}$ is the inlet enthalpy of water, $h_{waterout}$ is the outlet enthalpy of water, and h_{fg} is the latent heat of water.

And convection heat transfer can be calculated as;

$$\dot{q}_{conv} = \dot{m}_{water}.(h_{fg} + h_{waterout} - h_{waterin}) = h_c.A.(T_{air} - T_{surafce}) \tag{12}$$

where $\dot{m}_{water}$ is the mass flow rate of water, $h_{waterin}$ is the inlet enthalpy of water, $h_{waterout}$ is the outlet enthalpy of water, h_{fg} is the latent heat of water, hc is the convective heat transfer coefficient for surface of porous plate, A is surface area of porous plate, Tair is the temperature of air and Tsurface is the avarage surface temperature of porous plate.

Conductıon heat transfer from porous plate to water will be;

$$\dot{q}_{cond} = \dot{m}_{water}.(h_{surfece} - h_{waterin}) \tag{13}$$

where $\dot{m}_{water}$ is the mass flow rate of water, $h_{surface}$ is the enthalpy of water at surface temperature, $h_{waterin}$ is the enthalpy of water at inlet temperature.

So cooling efficiency of the porous plate, shows protecting degree of main surface by decreasing surface temperature with using porous plate, is;

$$\eta = \frac{T_{surface} - T_{airin}}{T_{water} - T_{airin}} \tag{14}$$

And cooling efficiency of the system, shows cooling degree of air with using this system, will be;

$$\eta_{sys} = \frac{T_{airin} - T_{airout}}{T_{airin} - T_{surface}} \tag{15}$$

Moffat [13, 14] presented a general description of sources of errors in engineering measurements and discussion of the use of uncertainty in the planning of experiments. In addition to that, the uncertainty associated with the experimental data is estimated using Root-Sum-Square (RSS) method, to combine the individual uncertainty terms of the independent variables in the calculation of the heat transfer, by Caggese et

al. [15] and Fechter et al. [16]. Table 3 shows uncertainty levels of measured parameters and their errors in the calculation of efficiency of porous plate, efficiency of the system and the Reynolds number. In the present experiments, the temperature measurements were accurate within ± 0.1 °C, and the velocity measurements were accurate within ± 2%. The uncertainty of Re, efficiency of porous plate, and efficiency of the system for the ranges of parameters studied under steady-state conditions is within ± 0.7% , ± 3.4% and ± 6.4%, respectively.

Table 3. Experimental uncertainties

Parameter	Units	Value	Errors	%
Vair	m/s	3.35	± 0.2	± 5.9
Tsurface	° C	Tsurface= 33 °C	± 0.1	± 0.3
Re	-	Re =3580	26.57	0.7
η	-	η = 79.1	2,68	3.4
η_{sys}	-	η_{sys} = 48.74	3.13	6.4

3 RESULTS AND DISCUSSION

In this section, experimental results were presented for different water flow rate as a coolant, and particle diameters of porous plate.

3.1 Effect of water flow rate

Experiments were conducted for different water flow rate for Re=3300 and T_{inlet}= 77 ºC. Water flow rates ,applied in experimental, are between 0,000083 and 0.000249 kg/s. Surface temperature was measured for different water flow rates. Measured temperature was shown in Fig.3.
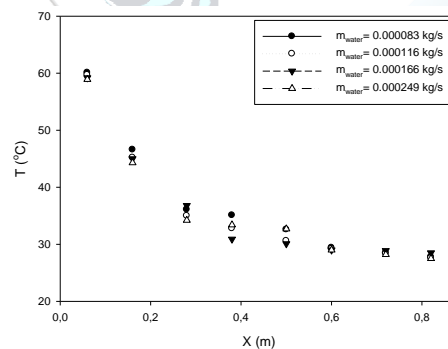

Figure. 3. Surface temperatures for different water flow rate

It was observed that increasing water flow rate did not cause a prominent decrease on surface temperature and cooling efficiency for the water flow rate of experiments. Because flow rate of water is slightly changed to determine the optimum value of water flow rate. The higher injection rates result in further increase of the cooling effectiveness. The difference of cooling efficiency decreased up to the end of the porous plate because air temperature also decreases at that region. Cooling efficiency of porous plate for different water flow rate was shown in Fig.4. It is observed that surface temperature changed from 27 to 56 ºC and cooling efficiency changed from 90 to 38%. If we continue to increase flow rate of water, droplets would occurred on the surface of porous plate and covered the surface. Then amount of evaporated water from the surface decreased. So effect of porous plate on heat transfer, extending surface area, also decreased. Cooling efficiency of the system for different water flow rate was shown in Fig.5.
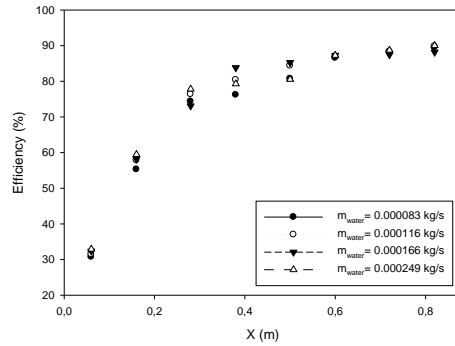
Figure. 4. Cooling efficiency of porous plate for different water flow rate
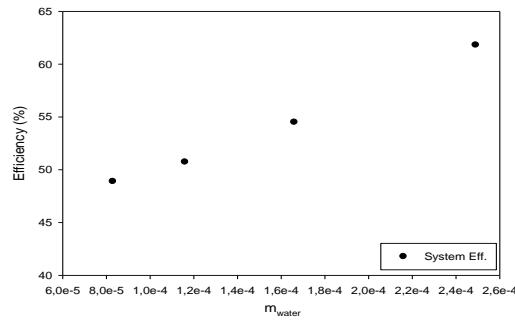

Figure. 5. Cooling efficiency of the system for different water flow rate

Increasing water flow rate as a coolant causes a prominent increase on cooling efficiency of the system. Increasing water flow rate three times causes an increase of 26.4 % on cooling efficiency of the system. Because increasing flow rate of water not only causes an increase on the quantity of evaporated water and amount of heat taken from the air but also decrease of temperature of air and surface.

3.2 Effect of Particle Diameter

In this study effect of particle diameters on heat transfer from the surface is investigated. It is known that heat transfer occurs from the cavities of particles of surface. It is thought that if particle diameter of porous plate is decreased an increase on heat transfer can be obtained. But there should be a limit for decreasing particle diameter of surface. So experiments were conducted for different particle diameter D_p=40, 50, 100 and 200 μm for Re=3300, T_{inlet}= 77 ºC and water flow rate $\dot{m}_{water}$= 0,000083 kg/s. Surface temperature was measured for different particle diameter. Measured temperature values were shown in Fig.6.
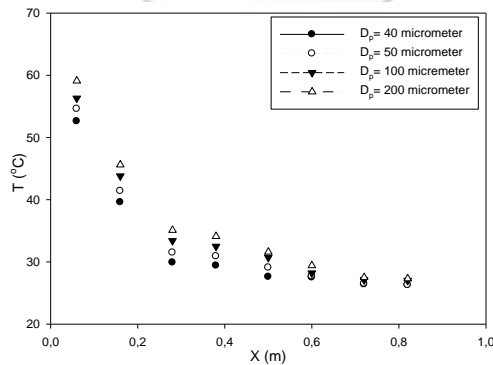

Fig. 6. Surface temperatures for different particle diameter

It can be seen that decreasing particle diameter causes a significant decrease on surface temperature. The reason of this, decreasing particle diameter causes an increase on surface area for evaporation and heat transfer. Effect of particle diameter on surface temperature can be detected easily at the inlet region of porous plate but this difference decrease slightly to the end of porous plate. Cooling efficiency of porous plate for different particle diameter was shown in Fig.7.
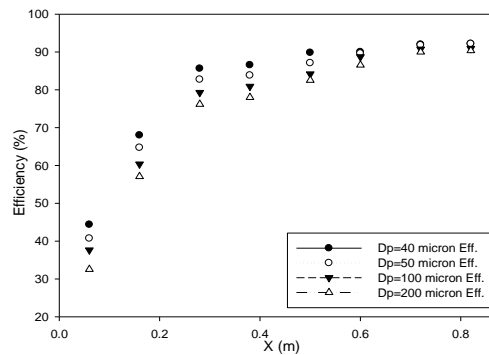
Fig. 7. Cooling efficiency of porous plate for different particle diameter

Beyond the point of x=0,6 m there is not a significant change among different particle diameter. Difference of cooling efficiency from D_p=40 to D_p=200 μm decreases from 12% to 2 % from inlet region to end of porous plate.

4 CONCLUSIONS

The present study is focused on developing structural solid surface geometry to improve heat transfer by cooling of air with transpiration cooling. Effects of particle diameters and mass flow rate of water on local wall temperature and cooling effectiveness along the surface of a porous flat plate inside a rectangular channel with air as a hot gas stream and water as a coolant were investigated experimentally. Surface temperature of porous plate were measured and cooling efficiency of system were calculated for different flow rate of water ($\dot{m}_{water}$= 0.000083, 0.000116, 0.000166, 0.000249 kg/s) and particle diameter of porous plate (D_p= 40, 50, 100, 200 μm).

The following conclusions can be drawn from the experimental results;

Increasing water flow rate did not cause a prominent decrease on surface temperature and cooling efficiency of porous plate for the water flow rate of experiments. Because flow rate of water is slightly changed to determine the optimum value of water flow rate. The higher injection rates result in further increase of the cooling effectiveness. Surface temperature changed from 27 to 56 ºC and cooling efficiency changed from 90to 38 %. Increasing water flow rate as a coolant causes a prominent increase on cooling efficiency of the system. Increasing water flow rate three times causes an increase of 26.4 % on cooling efficiency of the system.

Decreasing particle diameter causes a significant decrease on surface temperature. The reason of this, decreasing particle diameter causes an extension on surface area for evaporation and heat transfer. Difference of cooling efficiency of porous plate from D_p=40 to D_p=200 μm decreases from 12% to 2 % from inlet region to end of porous plate.

Acknowledgment

References

[1]. [1] P.X.,Jiang, L.Yu, J.G.Sun, J.Wang, "Experimental and numerical investigation of convection heat transfer in transpiration cooling", Applied Thermal Engineering, vol.24, pp.1271-1289, 2004.

[2]. [2] Y.Q.Liu, P.X. Jiang,.S.S. Jin, J.G. Sun, "Transpiration cooling of a nose cone by various foreign gases", Int. Journal of Heat and Mass Transfer, vol.53 , pp.5364-5372, 2010.

[3]. [3] Y.Q. Liu, P.X. Jiang, Y.B. Xiong, Y.P. Wang, "Experimental and numerical investigation of transpiration for sintered porous flat plates", Applied Thermal Engineering, vol.50, pp.997-1007, 2013.

[4]. [4] M. Arai, T. Suidzu, "Porous ceramic coating for transpiration cooling of gas turbine blade", J.Thermal Spray Technology, vol.22, pp.690-698, 2012.

[5]. [5] F. He, J. Wang, L. Xu, X. Wang, "Modeling and simulation of transpiration cooling with phase change", Applied Thermal Engineering, vol.58, pp.173-180, 2013.

[6]. [6] J. Wang, L. Zhao, X. Wang, J. Ma, J. Lin, "An experimental investigation on transpiration cooling of wedge shaped nose cone with liquid coolant", Int.J.Heat and Mass Transfer, vol.75, pp.442-449, 2014.

[7]. [7] G. Tsai, Y.C. Lin, H.W. Wang, Y.F. Lin, Y.C Su., T.J. Yang, "Cooling transient in a sudden-expansion channel with varied rates of wall transpiration", Int.J.Heat and Mass Transfer, vol.52, pp.5990-5999, 2009.

[8]. [8] T. Langener, J. Wolserdorf, M. Selzer, H. Hald, "Experimental investigations cooling applied to C/C material", Int.J. Thermal Science, vol.54, pp. 70-81, 2012.

[9]. [9] Y.Y Tsai, C.H. Lee, "Experimental study of evaporative heat transfer in sintered powder structure at low superheat levels", Experimental Thermal and Fluid Science, vol.52,pp.230-238, 2014.

[10]. [10] Y.Y Tsai, C.H. Lee, "Effect of sintered structural parameters on reducing the superheat level in heat pipe evaporators", Int.J.Thermal Science, vol.76, 225-234, 2014.

[11]. [11] S. He, Z. Guan, H Gurgenci., K. Hooman, Y. Lu, A.M. Alkhedhair, "Experimental study of film media used for evaporative pre-cooling air", Energy Conversion and Management, vol.87, pp.874-884, 2014.

[12]. [12] A.F. Mills, Mass Transfer, University of Los Angeles California, USA, 2001.

[13]. [13] R.J.Moffat, "Describing the uncertainties in experimental results", Experimental Fluid Science, vol. 1, pp.3-17, 1998.

[14]. [14] R.J.Moffat, "Using uncertainty analysis in the planning of an experiment", ASME Journal of Fluid Engineering, vol.107, pp.173-178, 1985.

[15]. [15] O.Caggese, G.Gnaegi, G.Hannema, A.Terzis, P.Ott, "Experimental and numerical investigation of a fully confined impingement round jet", International Journal of Heat and Mass Transfer, vol. 21, pp.156-163, 2000.

[16]. [16] S.Fechter, A.Terzis, P.Otto, B.Weigand, J.V.Wolfersdorf, M.Cochet, "Experimental and numerical investigation of narrow impingement cooling channels", International Journal of Heat and Mass Transfer, vol. 67, pp.1208-1219, 2013.

Comparison of Performance of Conventional Membrane Bioreactor with Dynamic Membrane Bioreactor

Mehmet Akif Veral[1], Abdullah Kizilet[2], Ozer Cinar[1]*

[1]*Yildiz Technical University, Department of Bioengineering, 34210, Esenler/İstanbul, Turkey.*

[2]*Department of Bioengineering and Sciences, Kahramanmaras Sutcu Imam University, 46100, Kahramanmaras, Turkey.*

[3]*Yildiz Technical University, Department of Environmental Engineering, 34220, Esenler/İstanbul, Turkey..*

*CorrespondingAuthor email: ocinar@yildiz.edu.tr

Abstract

The purpose of this study is about comparison of non-woven and 0.45 µm pore size real membrane placed in one aerobic tank and under same conditions. Comparison has been made between dynamic membrane bioreactors (DMBR) and membrane bioreactor (MBR), which have been employed in a widespread manner, to develop a convenient solution of high membrane cost handicap. Both membrane types operated under same aerobic conditions such as; volume, LMH and SADm. In addition, they have been fed with synthetic municipal wastewater and operated periodically to hinder membrane fouling. At the end of approximate one-month adaptation time course, bioreactors, which have reached stable conditions, have been operated to gather the data throughout 60 days. COD removal rates and turbidity results have been compared and non-woven dynamic membrane results have shown similar results to real membrane in terms of efficiency. Furthermore, dynamic membrane has exposed air back wash and pressure changes examined. While average COD removal is determined 93% for non-woven dynamic membrane and 95% for 0.45 µm pore size real membrane, turbidity values haveobtained1,5 NTU and 0,7 NTU for non-woven and 0.45 µm real membrane, respectively.

1. INTRODUCTION

There has been growing relevance for biological wastewater treatment methods using membranes. Solid-liquid separation processes are being done in the way of biological wastewater treatment and in particular, membrane bioreactors (MBRs) are playing essential role in treatment processes [1]. With the benefits and usage of micro/ultrafiltration, MBR ensures significant benefits and progression if it is compared with conventional active sludge processes (CASP), while pore size of the membrane doesn't allow to pass all substances or colloidal particles through the pores whose range is between 0.05-0.4 µm [2].MBRs are combination of permeable membranes and they include the physical separation of refined water and biomass. In conventional active sludge process, biochemical oxidation and water/biomass separation occurs in two different tank but MBRs make it convenient to proceed in one tank [1, 3]. Therefore, membrane bioreactors hinder the production of sludge whose amount normally increases throughout the process and employ high concentration of constituents of mixed liquor that comprises colloidal particles or solid substances suspended in the reactor. It also provides high dispelling yield of biological oxygen demand (BOD) and chemical oxygen demand (COD) [3]. While process has been done by using aerobic and anaerobic bacteria cultures, different types of membranes are being tested for better performance. Combination of the reactors and more convenient module designs ensures visually induced footprint. Throughout the separation process,

usage of the membrane that filtrates the mixed liquor enhances the quality of excreted effluent. Therefore, MBR systems permit engagement of the bacteria in each other and forming flocs through the surface of the membrane and it also blocks the transition of colloidal particles from the pores and sustains sterilization [4, 5]. However, there are wide spread applications of aerobic MBR studies in the literature, there are also anaerobic processes in the applications of MBR system [6, 7]. Although, effluent quality and low system footprint are mentioned as benefits of MBRs, it has some primary limitations like; low flux, energy demand, membrane cost and clogging control. All those problems can be solved by using dynamic membrane technology (DMBR) [1, 8, 9]. Generally, membrane pores are plunged because of organic materials orcolloidal particles. DM layer hinders the blockage of support material by biomass filtration layer that underlies on DM itself [10, 11, 12]. Throughout the process, transition/movement of the suspended solid particles creates a cake layer on the membrane. Generation of the cake layer can decide the refusal characteristics of the process because cake layer itself plays the secondary membrane role hence after [13, 14, 15]. Water backwash, air backwash or scrubbing methods can be efficient to clean the dynamic membranes without using chemical substances [16]. Nevertheless, cleaning without using chemical substances may employ transient deprivation of effluent. One of the most critical properties for the dynamic membranes is the preclusion of the solid substances through the surface of the secondary membrane which can be comprised or regenerated by itself called self-forming dynamic membrane (SFDM). However, formation and/or reformation of the dynamic membrane layer may diminish the transmissivity of the membrane which is similar hitch that has been seen in conventional MBRs [17]. Micro/ultrafiltration membranes are overpriced than other low cost materials like mesh, non-woven fabric and woven wire cloth which can be used as support material for the generation of dynamic layer [9, 18, 19, 20]. In addition, employing low cost materials, which are mentioned above, instead of using traditional materials ensures high rate flow of liquid at lower transmembrane pressure (TMP) in cost saving field [3, 15, 21, 22].

In this study, two different types of membranes, non-woven and 0.45 μm pore size real membrane, have been employed and compared in each other in terms of Turbidity, TMP, SMP, EPS and CST analyses.

2. MATERIAL AND METHOD

Two different membrane modules were performed and one lab scale aerobic membrane bioreactor (AeMBR) tank was designed. It was made of plexiglas at dimensions of 8x14x38 cm operated in total volume of around 3000 ml and active volume of 2500 ml. Suspended solids concentration was stabilized at 5000 mg AKM/L. Reactor was equipped with water level sensor and aeration device, which procures mixing and continuous physical membrane cleaning, at the bottom. Inside of the tank, two different membrane types, non-woven flat-sheet polyethersulfone (PES) microfiltration and0.45 μm pore size real membrane, were employed for the operation and double-sided support layer was utilized for the membrane stableness. Each membrane module, made of 12x12 cm plexiglas, had volume of 217 ml and active surface area was adjusted to 7.5x7.5 cm2(Fig.1).
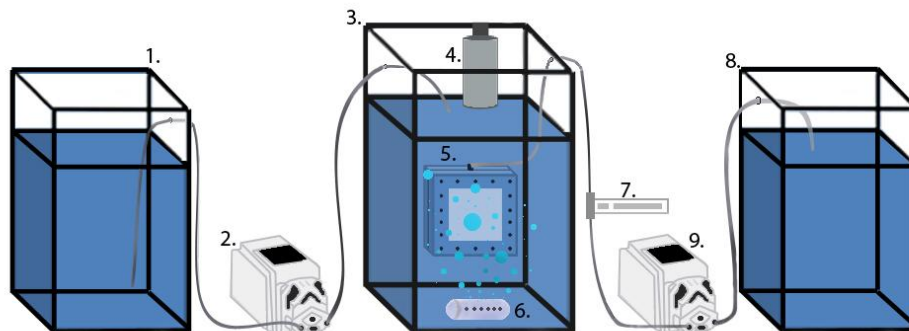

Fig.1. Schematic representation of MBR system: 1. Feed Tank, 2. Feed Pump, 3. Reactor, 4. Level Sensor, 5. Membrane Modules, 6. Air Diffuser, 7. Air Flow Regulator, 8. Permeate Tank, 9. Suction Pump

MBR system was operated at 11.11 LMH flux and 10 LMH net flux. SADm value and membrane suction pumps' flow rate was 1 Nm^3 (air)/m^2.hour and 2.08 ml/minute, respectively. Membranes were operated 4.5 min. and kept 0.5 min rest. When the membrane pressure reached 250 mbar pressure, dynamic membrane module was subjected to physical cleaning process. Every day, air backwash operation implemented to the membranes to reduce plugging at 22.5 L (air)/hr. flux through 1 minute. It was noticed that physical cleaning and air backwash pressure values were at desired level, in terms of transmembrane pressure (TMP).

Synthetic Wastewater Characteristics and Operation Procedures

The feed water of the MBR system was synthetic wastewater and feed chamber was filled regularly as 7000 ml every day. Chemicals of synthetic wastewater were represented at Table 1 and sucked permeate accumulated into two different tanks. Established AeMBR was operated interminably, because throughout its operation no kind of sludge elimination process was employed. However, pumps were adjusted 4.5 minutes of suction pressure so as to apply 30 seconds rest. This is one of the methodologies widely used to prevent plugging. To prevent clogging, non-woven dynamic membrane was administered for backwash operation each day, one minute and 0.45 μm pore size membrane was not employed for the same operation.

Table 1. Synthetic Wastewater Content

Chemicals	Concentration (mg/L)
$C_6H_{12}O_6.H_2O$	500
$NaHCO_3$	2754
NH_4Cl	230
K_2HPO_4	37
KH_2PO_4	67
$MnSO_4.H_2O$	0.4289
$ZnSO_4.7H_2O$	0.1053
$NaSO_3$	0.2811
$CuSO_4.5H_2O$	0.0556
$FeSO_4.7H_2O$	5.92
$NiSO_4.6H_2O$	0.1
$CoCl.6H_2O$	1

Net Flux Calculations

Amount of water passing along the unit surface area of membrane per unit of time is simply called flux, J. In this context, flux can be formulated as [3];

$$Flux = \frac{Flow}{Area} \qquad\qquad J = \frac{Q}{A} = \frac{Volume}{Time \; x \; Area} \qquad\qquad (1)$$

MBR system was operated in 5 minutes periods, as 4.5 min. working and 0.5 min. rest. Net flux is represented with the following formula [3];

$$Net \; flux = flux \times \frac{running \; \; time}{waiting \; \; time \; + running \; \; time} = 11{,}11 \times \frac{4{,}5 \; min.}{(0{,}5+4{,}5) \; min.} \cong 10 \; LMH \qquad (2)$$

2.1. Surface area, Flow and SADm Calculations

Dimensions of the membrane were 7.5cmx7.5cm. Active surface area calculation is presented with an equation below;

$$Active \; surface \; area = 7{,}5 \; cm \times 7{,}5 \; cm \times 2(membrane \; modules), = 0{,}01125 m^2$$

Flow, can be calculated by multiplying the flux and membrane surface area. Active surface area and flux are calculated as 0.01125 m^2 and 11.11 LMH (L/m^2.saat), respectively. Flow is calculated by the following equation [3];

$$Flow = 11{,}11 \frac{L}{m^2.hour} \times 0{,}01125 \; m^2 = 0{,}125 \; L/hour \qquad (3)$$

Volume of permeate which should be evacuated from the operation and volume of flow that should be sucked by the pumps were computed via following balance, respectively;

$$Permeate = 0{,}125 * 24 = 3000 \; L$$

$$Flow = \frac{Volume}{Time} = \frac{3000 \; L}{1440 \; min.} = 2{,}083 \cong 2{,}08 \; ml/minute$$

System was operated under 1 Nm³xhr/m² SADm value and required oxygen amount is calculated as;

$$SADm = \frac{Q(air)}{Area} \qquad SADm = \frac{Nm^3/hr}{m^2} \quad 1 = \frac{Nm^3(air)}{0.1125 \times 1hr} \qquad\qquad (4)$$

Amount of air for a membrane module calculated as 11.25 L/hour. In our system, two membrane modules were operated, so total amount of air for the reactor was calculated as 22.5 L/hour.

2.2. Analytic Methods

2.2.1. Chemical Oxygen Demand

While samples taken from feed tank were two times diluted for analysis, samples taken from permeate tank were not diluted and directly utilized in the NTU experiment. There were four experimental tubes reserved for the COD process. 2 individual, 2.5 ml, samples were taken from real and dynamic membranes permeate and 2.5 ml distilled water was taken as witness sample. On the other hand, 1.25 ml sample from the feed tank was mixed with 1.25 ml distilled water for two times dilution. These four different types of samples were stored individually to the tubes and 1.5 ml potassium dichromate and 3.5 ml silver sulfuric acid (AgSO4) were added inside of the tubes. After then, tubes were stored inside of the thermoreactor, for 120 minutes at 1500C. WTW CR 3200 brand thermoreactor was used and after two hours, tubes were

taken from thermoreactor and allowed to cool down. Titration process was ensured by using magnet inside beaker placed on mixer. While beaker was stirring the mixture, two drops of ferroin indicator were added and titrated with the FAS solution. At the end, consumptions were noted.

2.2.2. Determination of Turbidity, Transmembrane Pressure, CST

Suspended solids inside of the water and soluble inorganic constituents can cause and also increase the turbidity parameters. Unit of the turbidity is NTU in nefolometric turbidimeters. In experimental phase, WTW TURB 550IR type turbidimeter instrument was employed. Therefore, determination of the turbidity was done by two individual 35 ml samples taken to the 50 ml falcon tubes from the permeate of 0.45 pore size real membrane and non-woven dynamic membrane. Before turbidimeter was run, 1000 NTU, 10 NTU and 0.02 NTU standard solutions glass tubes were cleaned up painstakingly with glass-cloth and put to dedicated wells of the instrument respectively for calibration process. Turbidimeter glass tube was washed with the soap and rinsed. Then, washed with distilled water, wiped with glass-cloth, shaken two times with few drops of sample of interest for the measurement and 25 ml sample was put inside of the tube which was shaken at that moment. Tube was placed inside of the instrument and measurement results were noted for both sample types. Transmembrane Pressure (TMP) Measurement: Throughout the experiment, pressure measurements were done daily with TMP instrument. As a result of dynamic membrane pressure reach of 250 mbar it was sentenced to backwash. Increase in pressure indicates that membrane blockage occurred. All pressure measurements were carried out programmable digital manometer (KELLER-Leon record, Swiss), and Installerlogger5 the software. Air Backwash: Backwashing the membrane with water and the negative or positive pressure to be lifted to rest on was one method for preventing the blockage problem. Membranes operated at high flux can run in a shorter time period and blockage can be prevented by more frequent backwashing or rest periods applying (D.C. Stuckey, 2012). In this experiment, backwash was employed only for non-woven dynamic membrane, daily. Backwashing was done for 1 minute, while flux was kept constant. Capillary Suction Time (CST), SMP, EPS Analyses: Capillary suction time (CST) is a widely utilized methodology to measure the filterability and related with the movement of water from the sludge through 1 cm path in a particular time period, in a porous capillary membrane. In experiment, the determination of sludge filtration properties and to determine the relationship of capillary absorption time with obstruction, CST instrument (Triton 304M, England) was used to determine CST. SMP was determined after centrifugation of the samples at 4000 rpm for 10 min. from the reactor effluent obtained at experimental stages of filtering supernatant samples and amount of protein and carbohydrates obtained from filtrate. Samples taken from reactor were centrifuged for the EPS analyze and EPS in biomass was extracted. EPS extraction process was carried out just as specified in the book of Judd (2006) with the heating. EPS value was stated as protein and carbohydrate concentration. Analyses were made by Bradford (1976) and Dubois (1956) methods, respectively.

3. RESULTS AND DISCUSSION

3.1. COD Experimental Results

Through the operation of MBR system, COD experiment results are represented at Fig. 2 by the samples taken from influent synthetic feed wastewater, non-woven dynamic membrane and 0.45 μm pore size real membrane permeate. COD tests were made every three days for 60 days. During the experiment, it was noticed that COD concentrations of non-woven dynamic membrane was lower than 0.45 μm pore size real membrane. COD concentration of dynamic membrane was time to time higher than the real membrane because it takes time to ensure the stability of the dynamic membrane and backwashing operations from time to time when membrane stableness was disrupted.
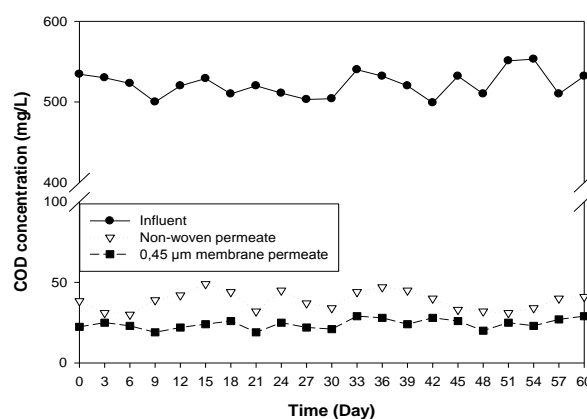

Fig. 2: COD concentrations of influent, real and dynamic membrane Throughout MBR operation.

Until reactor reaches decisive condition, COD concentrations are high. In this context, COD data taken from the samples were imprinted when the reactor come up with stable standards. There has been reduction of COD concentrations of non-woven dynamic membrane after day 42. It was thought that this reduction occurred due to inefficient removal yield of cake layer that formed on the surface of membrane by plugging.

COD concentrations of non-woven dynamic membrane were quite close to the real membrane when the cake layer on membrane surface became stable. Throughout the operation duration, total COD concentration of influent wastewater was maximum 551 mg/L and COD concentrations from permeate were 19 mg/L and 30 mg/L for real and dynamic membrane, respectively. COD values from influent wastewater may change due to the environmental circumstances which can be affected. Through 60 days, COD removal performance results of 0.45 μm pore size real membrane and non-woven dynamic membrane were given at Fig.3. Along the operation, it was noticed that COD removal yield of non-woven dynamic membrane was lower than 0.45 μm pore size real membrane. It was because of non-woven dynamic membrane permeate contains high COD causing bacteria concentration. COD analyses were not exposed any kind of filtration operations and directly performed with titrimetric method in terms of representing real values.
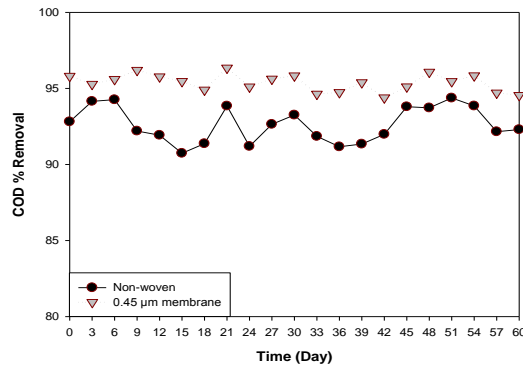

Fig. 3: COD removal yields of real and dynamic membrane through the MBR operation.

Close COD concentration percentages between non-woven and dynamic membrane from permeate was already noticed in research made by Lee et al. [23]. However, some studies employment of non-woven fabric filter and micro-filter membranes showed convenient performance for mixed liquor separation [24].

3.2. Turbidity Results

Turbidity results of the samples taken from non-woven dynamic membrane and 0.45 μm pore size real membrane are represented at Fig. 4. Samples were taken every three days and determination of turbidity was made through two mounts for every three days.
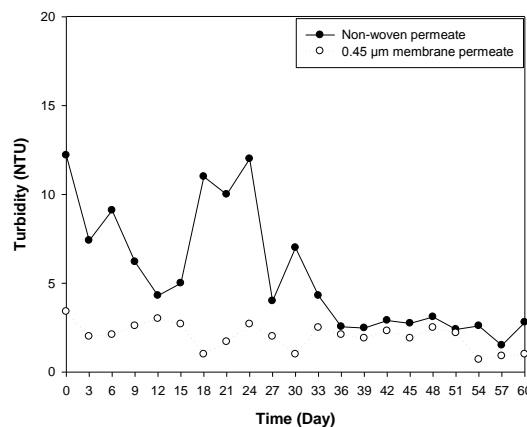

Fig.4: Turbidity results of dynamic and real membrane through MBR operation.

In the filtration of the standard turbidity solution, turbidity removal of the dynamic membrane showed [3, 25]. There have been changes at the removal performance of the membranes in MBR. The reason of high turbidity results of dynamic membrane is because of the membrane stability which was ensured at first 24 days. 0.45 μm pore size real membrane came up with much better turbidity results. Last 30 days of the experiment, turbidity values of dynamic membrane were quite close to the real membrane due to the plugging and increase at the removal yield.

3.3. TMP Measurements

In the experiment, distilled water transition was ensured over the membrane surface for both membrane types and pressure measurements were recorded. Even though the pressure values were obtained when distilled water released for 24-hour measurements, operation was repeated for better performance and comparison. Pressure measurements of real membrane were made and noted every three days. Fig. 5 represents the pressure measurement of the real membrane. After then, the system has been started to run and synthetic wastewater feeding.

In MBR system, synthetic wastewater from 0.45 μm pore size real membrane was filtered. It was observed for the real membrane that the pressure was below 100 mbar when the system at stable condition and pressure value rose to levels of 250 mbar. Beside of interrupted suction operation, any physical or chemical washing was not applied.
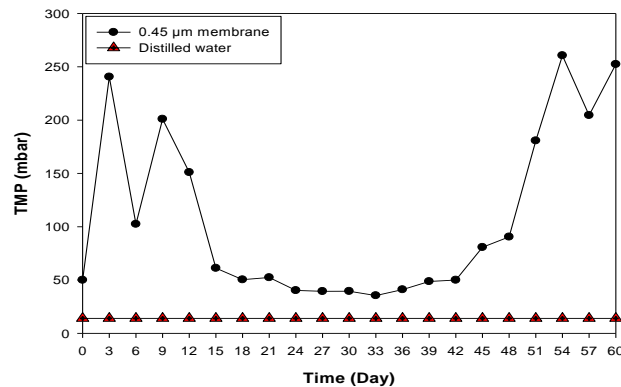

Fig.5: Pressure measurement of the real membrane through MBR operation.

Dynamic membrane was also exposed to interrupted suction operation, 4.5 minutes working and half a minute rest, and 1-minute back washing. In MBR system, synthetic wastewater prepared from non-woven dynamic membrane was filtered and while the system was operating, pressure measurements of dynamic membrane and released distilled water were recorded and represented at Fig. 6. When the measured pressure reached 250 mbar, non-woven dynamic membrane exposed to physical washing. Pressure increment is the result of membrane plugging. During the experiment, physical cleaning was applied three times. Physical cleaning was applied as removal of membrane module and skinning the cake layer from the surface of the membrane. After physical cleaning, significant pressure reduction has been observed. After physical cleaning, increment in pressure is because of the permanent plugging of the pores of the membrane and there are a lot of experiments indicated for this situation.
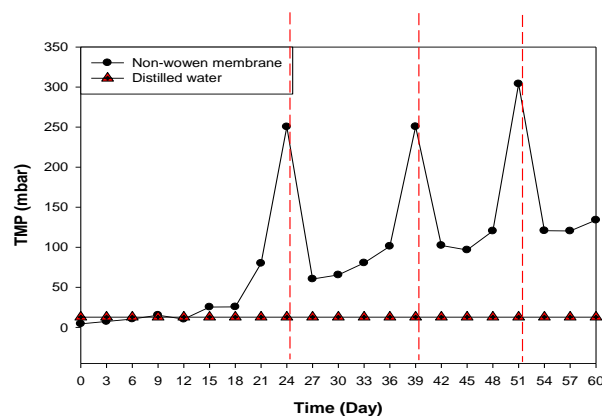
Fig. 6: Pressure measurements through MBR operation.

3.4. The Effect of Air Backwash

It was only wanted to examine the effect of air backwash for non-woven dynamic membrane, before backwashing and after air backwashing, 12-hour pressure measurement additionally made. Fig. 7 represents the pressure reduction after air backwash. The effect of air backwash has been made for once throughout the MBR operation. TMP values for 30th day were saved with 12-hour period and 2-minute intervals. After 1-minute air backwash operation, TMP values again observed with 12-hour period and effects of air backwash were recorded. Findings showed that air backwash reduced the present TMP value averagely 20%.

Fig. 7: Pressure values before and after air backwash.

3.5. SMP EPS Results
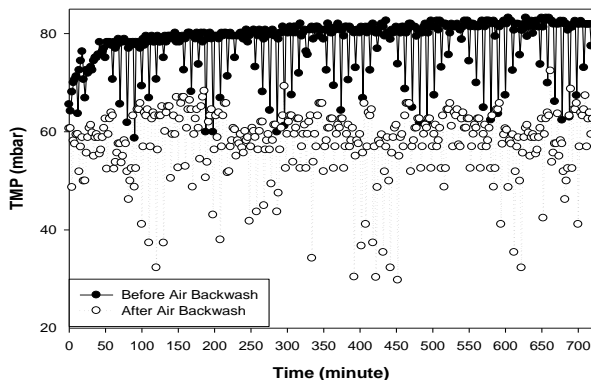
Throughout the experiment, SMP and EPS analyses were made firstly at day-15 and secondly at day-30. Protein and carbohydrate dependent SMP and EPS concentrations are represented at Table 2. It was noticed that, day-15 SMP and EPS concentrations were higher than the day-30. These results shows gradually heal of COD removal inside of the reactor.

Table 2. SMP and EPS results regarding permeate of dynamic membrane, real membrane and mixed liquor.

	Non-woven		0.45 membrane		Supernatant			
	SMP		SMP		SMP		EPS	
Time	Protein (mg/L)	Carbohydrate (mg/L)	Protein (mg/L)	Carbohydrate (mg/L)	Protein (mg/L)	Carbohydrate (mg/L)	Protein (mg/L)	Carbohydrate (mg/L)
Day 15	0,05989	24,601	0,07567	85,261	0,999	147,943	0,1465	171,533
Day 30	0,18964	59,649	0,27584	195,46	0,431	99,752	0,1379	66,389

At day-15, analyze results of permeate of dynamic and real membrane were lower than the results of day-30. When this situation is examined with the turbidity values of both modules, it can be noticed that COD removal yield is lower than for the first time in days.

Figures and tables must be numbered. Figures and tables captions must be centered in 8 pt italic with small caps. Captions with figure numbers must be placed after their associated figures, as shown in Figure 1. Captions with table numbers must be placed before their associated tables, as shown in Table I.

3.6. CST Results

CST is used to identify the sludge characteristics and it measures the time of water drop from the sludge moved 1 cm path in a porous membrane. CST results of fully mixed liquor samples are represented at Fig. 8.
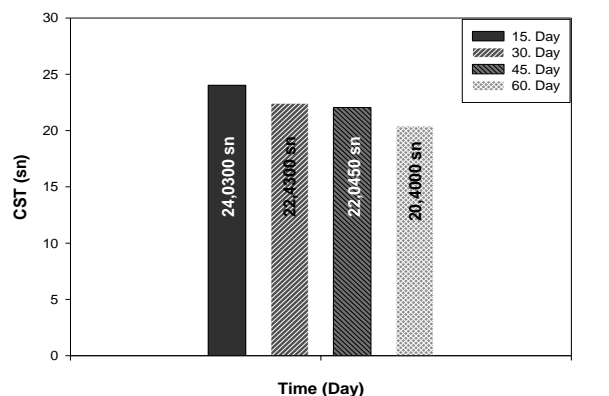

Fig. 8: CST analyzes results of the MBR mixed liquor.

CST analyses from day 15, 30, 45 and 60 were found as 24.03 sec., 22.43 sec., 22.045 sec. and 20.40 sec., respectively. Findings showed that CST values are gradually reducing. This shows the increment in viscosity of the sludge in the reactor, and thus demonstrates that the membrane filtration rate gets better.

4. CONCLUSION

In this study the comparison of DMBR and MBR was studied. Both membrane types operated under same aerobic conditions such as; volume, LMH and SADm. At the end of approximate one-month adaptation time course, bioreactors, which have reached stable conditions, have been operated to gather the data throughout 60 days. COD removal rates and turbidity results have been compared and non-woven dynamic membrane results have shown similar results to real membrane in terms of efficiency. Furthermore, dynamic membrane has exposed air back wash and pressure changes examined.

REFERENCES

[1]. S. Judd, The MBR book. Oxford, Elsevier, 2006.

[2]. G.T.Seo, B.H. Moon,T.S. Lee,T.J. Lim, I.S. Kim, Non-woven fabric filter separation activated sludge reactor for domestic wastewater reclamation. Wat. Sci. Tech., 47(1), 133–138, 2002.

[3]. H. D. Park, I. S. Chang, K. J. Lee, Principles of Membrane Bioreactors for Wastewater Treatment, CRC Press, Taylor&Francis Group, 2015.

[4]. W.Fuchs, C.Resch, M.Kernstock, M. Mayer, P.Scoeberl, R. Braun,Influence of operational conditions on the performance of a mesh filter activated sludge process. Water Res. 39 (4), 803–810, 2005.

[5]. Y. Kiso, Y.J. Jung, K.S. Min, W. Wang, M. Simase, T. Yamada. Coupling of sequencing batch reactor and mesh filtration: operational parameters and wastewater treatment performance. Water Res. 39, 4887–4898, 2005.

[6]. M.H.Al-Malack and G.K. Anderson, Formation of dynamic membranes with crossflow microfiltration. J. Membr. Sci. 112, 287–296, 1996.

[7]. M. Ye, H. Zhang, Q. Wei, H. Lei, F. Yang, X. Zhang, Study on the suitable thickness of a pac−pre-coated dynamic membrane coupled with a bioreactor for municipal wastewater treatment. Desalination 194, 108–120, 2006

[8]. C. Wisniewskand A. Grasmick,Coll Surf A: PhysicochemEng Aspects 138:403, 1998.

[9]. P.Côté, D. Thompson, Water SciTechnol 41:209, 2000.

[10]. Y. Wu, X. Huang, X. Wen, F. Chen, Function of dynamic membrane in selfforming dynamic membrane coupled bioreactor. Water Sci. Technol. 51 (6–7), 107–114, 2005.

[11]. L. Chu andS. Li, Filtration capability and operational characteristics of dynamic membrane bioreactor for municipal wastewater treatment. Sep. Purif. Technol. 51, 173–179, 2006.

[12]. F. Li, J. Chen, C. Deng, The kinetics of crossflow dynamic membrane bioreactor. Water SA 32 (2), 199–203, 2006.

[13]. H.Q. Chu, D. Cao, W. Jin, B.Z. Dong, Characteristics of bio-diatomite dynamic membrane process for municipal wastewater treatment. J. Membr. Sci. 325, 271–276, 2008.

[14]. D.W. Cao, H.Q. Chu, W. Jin, B.Z Dong, Characteristics of the biodiatomite dynamic membrane (cake layer) for municipal wastewater treatment. Desalination 250, 544–547, 2010.

[15]. D. Jeison, I. Diaz, J.B. van Lier, Anaerobic membrane bioreactors: are membranes really necessary? Electron. J. Biotech. 11 (4), 1–7, 2008.

[16]. A.E. Marcinkowsky, K.A. Kraus, H.O. Phillips, J.S. Johnson, A.J.Shor, Hyperfiltration studies IV. Salt rejection by dynamically formed hydrous oxide membranes. J. Am. Chem. Soc. 88 (24), 5744–5750, 1966.

[17]. D. Freilich, G.B. Tanny, The formation mechanism of dynamic hydrous Zr(IV) oxide membrane on microporous supports. J. Colloid Int. Sci. 64, 362–370, 1978.

[18]. T. Ohtani, M. Nakajima, Y.Nawa, A. Watanabe, Formation of dynamic UF membrane with fine Zr particles. J. Membr. Sci. 64, 273–281, 1991.

[19]. M. Rumyantsev, A.Shauly, S.Yiantsios, D.Hasson, A.Karabelas, R.Semiat, Parameters affecting the properties of dynamic membranes formed by Zr hydroxide colloids. Desalination 131, 189–200, 2000.

[20]. M. Altman, R. Semiat, D. Hasson, Removal of organicfoulantsfromfeedwatersbydynamicmembranes. Desalination 125, 65–75, 1999.

[21]. R.Y.Horng, C. Huang, M.C. Chang, H. Shao, B.L.Shiau, Y.J. Hu, Application of TiO2 photocatalytic oxidation and non-woven membrane filtration hybrid system for degradation of 4-chlorophenol. Desalination 245, 619-182, 2009.

[22]. Y. Zhao, Y. Tan, F.S. Wong, A.G. Fane, N. Xu, Formation of Mg(OH)2 dynamic membranes for oily water separation: effects of operating conditions. Desalination 191, 344–350, 2006.

[23]. J. Y. Lee, S. K. Maeng, B. K. Choi, K. H. Ahn, K. G. So, Characteristics of flux and gel layer on microfilter and non-woven fabric filter surface based on anoxic–aerobic MBRs, Bioprocess Biosyst Eng, 35:1389–1398, 2012.

[24]. L. Chu and S. Li, Filtration capability and operational characteristics of dynamic membrane bioreactor for municipal wastewater treatment, Separation and Purification Technology, 51, 173–179, 2006.

[25]. X. H. Zhou, H. C. Shi, Q. Cai, M. He, Y. X. Wu, Function of selfforming dynamic membrane and biokinetic parameters determination by microelectrode, Water Res 42:2369–2376, 2008.

Diagnosis of Coronary Artery Disease Using Deep Belief Networks

Gokhan Altan[1],*, Novruz Allahverdi[2], Yakup Kutlu[3]

[1]Mustafa Kemal University, Department of Informatics, 31000, Hatay, Turkey.
[2]KTO Karatay University, Department ofComputerEngineering, 42020, Karatay/Konya, Turkey.
[3]Iskenderun Technical University, Department of ComputerEngineering, 31200, Iskenderun/Hatay, Turkey.
*CorrespondingAuthor email: gokhan_altan@hotmail.com

Abstract

In this study, a decision-support system is presented to aid cardiologists during the diagnosis and to create a base for a new diagnosis system which separates two classes (CAD and no-CAD patients) using an electrocardiogram (ECG).

24 hour filtered ECG signals from PhysioNet were used. 15 second short-term ECG segments were extracted from 24 hour ECG signals to increase the number of samples and to provide a convenient transformation in a short period of time. The Hilbert-Huang Transform, which is effective on non-linear and non-stationary signals, was used to extract the features from short-term ECG signals. Instinct Mode Function (IMF) was extracted by applying Empirical Mode Decomposition to short-term ECG signals. The Hilbert Transform (HT) was applied to each IMF to obtain instantaneous frequency characteristics of the signal. Dataset was created by extracting statistical features from HT applied to IMF. Deep Belief Networks (DBN) which have a common use in Deep Learning algorithms were used as the classifier. DBN classification accuracy in the diagnosis of the CAD is discussed. The extracted dataset was tested using the 10-fold cross validation method. The test characteristics (sensitivity, accuracy and specificity) that are the basic parameters of independent testing in the medical diagnostic systems were calculated using this validation method. Short-term ECG signals of CAD patients and no-CAD groups were classified by the DBN with the rates of 98.05%, 98.88% and 96.02%, for accuracy, specificity and sensitivity, respectively.

The DBN model achieved higher accuracy rates than the Neural Network

1. INTRODUCTION

An electrocardiogram (ECG) is a uniform signal that records electrical changes at certain intervals of the heartbeat. It is also known as a map which shows the electrical activity of the heart. The ECG signals (ECGs), which are recorded with the aid of electrodes placed at different parts of the body, can have different electrical charges at any time. Electrical charges specify leads in the ECG. Bipolar and unipolar leads occur as a result of the position of the electrodes [1]. The ECG is a type of biomedical signal that is widely used for a variety of diagnosis and monitoring of cardiac diseases [2]. The electrical charges that are obtained directly as the result of discomfort of the heart and segments and intervals between waves on the ECG are of a paramount importance for the identification of the cardiac abnormalities in a subject [3].

Cardiac diseases have a high mortality rate worldwide. One of the most common cardiac diseases is Coronary Artery Disease (CAD). It is usually known as atherosclerosis in which there is a cardiac abnormality because of the narrowing of the arteries that feed the heart in time. In this cardiac disease, plaque caused by cholesterol collects in the coronary arteries and over time congestion results due to dilation of plaque. As a result of biological conditions, the arteries fail to feed the heart and it disrupts the rhythmic systole activity of the heart [4], [5]. CAD in adults results in heart attacks or a congestive heart. In the diagnosis of CAD, there are many clinical trials like physical examinations from which ST-deviation is measured, lab tests, Electrocardiogram (ECG), echocardiogram, stress tests and electron beam computed tomography, coronary angiography and cardiac catheterization [4]. In the literature, a diagnosis of the CAD has worked with various

signal-processing methods using the clinical dataset (age, sex, history, physical exam, cardiac risk factors, exercise stress test data, heart rate, etc.) on the rule-based fuzzy classification [6], Other methods include using the clinical attributes on data mining techniques [7]–[14]; the chronic conditions, risk factors, and laboratory results of data mining techniques [15]; the clinical attributes on data discretization, data partitioning and reduced error pruning [16]; the history and physical examination data and the diastolic heart sounds [17]; both the heart rate variability (HRV) features and the non-linear features (Poincare Plot, entropy, etc.) [18]–[22]; the P wave features on the ECG [7]; the Wavelet Packet Transformation (10 levels) [23]; the cardiac analysis of ST measures [24], [25]; the Empirical Mode Decomposition (EMD) and Teager Energy operator [26]; the Discrete Wavelet Transformation (DWT) [27], [28] and using the Principal Component Analysis (PCA) [28], [29]. In this study, the Hilbert-Huang Transform (HHT) is applied to filtered short-term ECGs from the PhysioNet database to extract features.

HHT is an adaptive method to analyze the nonlinear and non-stationary signals [30]. It has a common use in the biomedical signal analysis transformations due to these characteristics. The HHT is applied to the ECG for the diagnosis of Atrial Fibrillation [31] and Congestive Heart Failure [32]. In this study, the HHT would be applied to the filtered short-term ECGs for designing an effective statistical feature extraction model and classification of HHT-based statistical features using Deep Learning (DL) algorithms.

The DL is a comparatively new algorithm that is utilized to estimate the classification performances in many distributions such as speech recognition [33], [34], computer vision [35], [36], natural language processing [37]–[39], physiological data [40]–[42], biomedical datasets [43], [44] and non-linear signals [45], [46]. The DL aims to discover the multiple and deeper levels of distributions for a better classification performance. The basic concept of the DL is based on enhancing the classification performance using an artificial neural network model with multilayer hidden units. The most important difference of the DL is this: while both the multilayer neural network model and the DL has the same structure, it has at least two hidden layers and an unsupervised pre-training phase [47]. The depth of the DL is defined by the number of hidden layers on the model. The DL can also show a higher performance than neural networks with a small number of neurons. A fewer number of neurons on models can make it more convenient to calculate weights using supervised learning [48].

The aim of this study is to design a deep CAD diagnosis system that can be an alternative short-term ECG-based statistical feature based classification method to studies in the literature. 100 instances of 15 second ECG forms would be extracted from long-time ECGs in preprocessing. In this way, using short-term ECG forms would solve analysis problems and would enhance the number of samples up to 100x. The HHT would be applied to separated short-term ECGs and Instinct Mode Functions (IMFs) would be extracted. The system would extract statistical features from IMFs that are obtained applying the HHT. Each Instinct Mode Function (IMF) group obtained would be classified using the Deep Belief Networks (DBN) algorithm. Classification performances of the diagnosed subjects with or without the CAD would be examined.

2. MATERIALS AND METHODS

ECGs were used in the proposed diagnosis system. We preferred the moving window analysis technique and segmented long-time ECGs recorded into 15 second windows which were used in the preprocessing part. 15 second short-term ECGs were utilized in this study. IMFs were extracted applying HHT and statistical features were calculated for the obtained IMFs in feature extraction. Statistical features were classified using the DBN. A detailed description of the structure of the system is presented in the following sections.

2.1. Database

In the literature, different databases including different diagnosis systems were used for the diagnosis of the CAD. Clinical characteristics in particular [7]–[14] were used to separate subjects with or without CAD. Outside of the literature, the Long-Term ST Database [49] was used in the diagnosis of the CAD. The Long-Term ST Database contains 85 long-term ECGs from 80 subjects, chosen to exhibit a variety of events of ST segment changes. There are 25 subjects labeled as undiagnosed CAD patients and 60 subjects labeled as diagnosed CAD in this database. The individual recordings of the Long-Term ST Database are between 21 and 24 hours in duration.

2.2. Preprocessing

The information in a biomedical signal is unevenly distributed. We would like to call attention to the fact that all data records were from the PhysioNet databases as filtered long-term ECGs. Long-term ECGs may have too much noise while being recorded because of physical and recording conditions. The short-term ECGs usually have an ability to represent the Long-term ECG characteristics. The short-term ECG is a less affected form of represented Long-term ECG. That is why short-term ECGs were randomly segmented into 15 second short-term ECGs using the moving window analysis technique 100 times. In this way, the number of instances from each subject in the dataset could be increased by 100x.

2.3. Hilbert-Huang Transform

HHT is an effective analysis technique for non-linear signals. It has a common use in biomedical signals (ECG, EMG, EEG, etc.). It has a flexible mathematical formulation and is easily adaptable for various types of processes [32]. HHT is a two-stage transform. The first stage is EMD and the second stage is the Hilbert Spectrum Analysis (HSA). EMD extracts frequency-modulated signals that are named IMFs. After IMFs are extracted, HSA is applied to each IMF to calculate the instantaneous frequency and amplitude [50]. Considering all these characteristics, our work focuses on HHT analysis in short-term ECGs.

EMD is an algorithm that breaks down natural form non-linear signals without leaving the time domain. EMD assumes a random signal which consists of its own self-oscillation at different frequencies. Oscillations are symmetrical to the mean of the local minimum and the local maximum at a t time. EMD extracts Instinct Mode functions which are a complete and nearly orthogonal basis at different frequencies [31]. IMFs are all in the time-domain and of the same length as the original signal. EMD has a detailed formula in the literature [30]. In the formula, X represents the original signal, c represents extracted IMF and r_n represents the residual signal [30], [31].

$$X(t) = \sum_{j=1}^{n} c_{j+r_n} \tag{1}$$

After sifting through IMFs by obtaining a monotonic residual signal, the Hilbert Transform (HT) can be applied to each IMF to compute the instantaneous frequencies spectral analysis. The instantaneous frequencies give most important information about the signal characteristics. After performing the HT to each IMF component, the amplitude and frequency of each component as functions of time is [30]:

$$x(t) = \mathbb{R}\{\sum_{i=1}^{n} a_i(t)e^{j\omega(t)dt}\} \tag{2}$$

The frequency-time distribution of the amplitude is designated as the HSA, $H(\omega, t)$ and the marginal spectrum is $h(\omega)$ as follows [30] :

$$h(\omega) = \int_0^t H(\omega, t)dt \tag{3}$$

2.4. Deep Belief Networks

The DBN is a machine learning algorithm become more popular because of its semi-supervised learning methods. The DBN has a two stage learning process: unsupervised learning followed by supervised learning. In the first stage, it evaluates weights and biases between visible and hidden layers using an unsupervised pre-training of stacked Restricted Boltzmann Machines (RBM). RBMs are stacked between two adjacent layers which are visible-hidden layers or hidden-hidden layers. RBMs are energy-based functions and have only connections between adjacent nodes. Weights and biases between hidden and visible layers are evaluated with the aid of the probability of greedy layer-wise method. At the second stage, pre-training is followed by supervised fine-tuning with weighted neurons and biases to improve parameters.

The DBN can be defined as a specialized model with many hidden layers of DL. The upper layers of the DBN may hold more detailed and descriptive features to identify the solution of diagnosing systems, whereas lower layers may not. The DBN has more important advantages than the classical neural networks such as achieving high performance with a small number of training sets, and having the ability of utilizing the connections between the features in deeper processes. In the supervised learning phase, weights and biases are updated using fine-tuning in which the gradient descent or ascent algorithms are used for improving the accuracies and sensitivities of models [51], [52]. The DBN is a probabilistic joint distribution of input vector x and the ℓ hidden layers as follows:

$$P(x, h^1, ..., h^\ell) = \left(\prod_{k=0}^{\ell-2} P(h^k | h^{k+1})\right) P(h^{\ell-1}, h^\ell) \tag{4}$$

$P(h^{\ell-1}, h^\ell)$ is the probability of conditional distribution between the adjacent layers and h^0 is the input vector.

The energy function of the state (h^{k-1}, h^k) is defined as:

$$E(h^{k-1}, h^k; \theta) = -\sum_{s=1}^{D_{k-1}} \sum_{t=1}^{D_k} w_{st}^k h_s^{k-1} h_t^k - \sum_{s=1}^{D_{k-1}} b_s h_s^{k-1} - \sum_{t-1}^{D_k} c_t h_t \tag{5}$$

where $\theta = (w_{st}, b, c)$ which are the parameters of the DBN; w_{st}^k is the weight between s^{th} neuron in the layer h^{k-1} and t^{th} neuron in the layer h^k; b_s is the sth bias of layer h^{k-1} and c_t is the tth bias of layer h^k. D_k is the number of neurons in the kth layer. The probabilistic distribution of the energy function is:

$$P(h^{k-1}; \theta) = \frac{\sum_{h^k} \exp(-E(h^{k-1}, h^k; \theta))}{\sum_{h^{k-1}} \sum_{h^k} \exp(-E(h^{k-1}, h^k; \theta))} \tag{6}$$

After layer-wise unsupervised learning, calculated weights are refined using supervised learning based on gradient descent. This fine-tuning process updates w parameters for a better discriminative ability and for obtaining higher classification performances [53].

Accuracy (ACC), Specificity (SPE) and Sensitivity (SEN) are used to evaluate the performance of medical diagnosis systems. Calculation of these performance measurements are described in [22], [54].

3. RESULTS

Various biomedical signals and clinical characteristics are analyzed with lots of digital signal processing methods and data mining algorithms in medical diagnosis systems. Computer-based diagnosis systems may have support decision systems for improving clinicians' performance and classification performance. Computer-based diagnosis systems can also be enhanced using biomedical signal processing methods and can be utilized as an alternative or additional method to the

clinical characteristics of the subjects. In this study, the ECG is used to diagnose the subjects with or without CAD. The DBN structure of the proposed diagnosis system is seen in Fig.1.
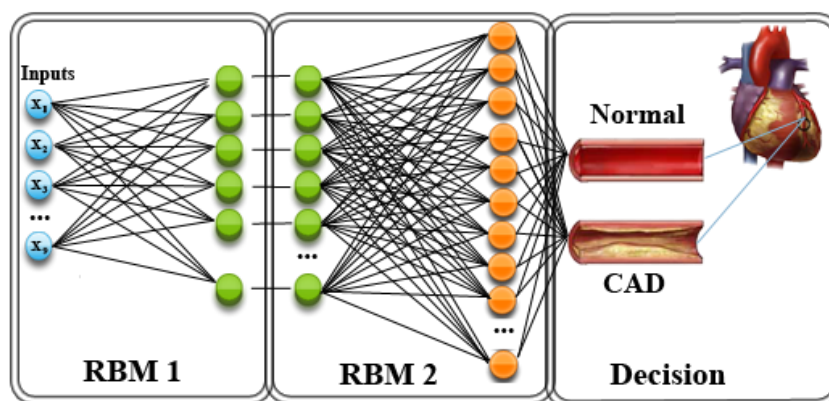

Figure 1. Structure of the DBN Classifier to diagnose CAD

Long-term ECGs may have much more noise than the short-term ECGs. Physical conditions such as coughing, changing the standing possession, instantaneous movements and recording conditions such as dislocation of the probe, etc. can handle noise in the long-term ECGs. The short-term ECG is less affected by these kinds of conditions. The short-term ECGs usually have an ability to represent the long-term ECG characteristics in most cardiac diseases. 15 second short-term ECGs were segmented from 85 long-term ECGs using the moving window analysis technique 100 times. The number of instances was increased to 8500 ECGs.

EMD was applied to each short-term ECG and the IMFs ranging in number from 10 to 14 were extracted for 8500 ECGs. Obtained IMFs can be seen in Fig.2. HT was applied to each IMF and the instantaneous frequencies spectral features were computed. HT allows deriving the analytic representation of a signal and includes phase features.
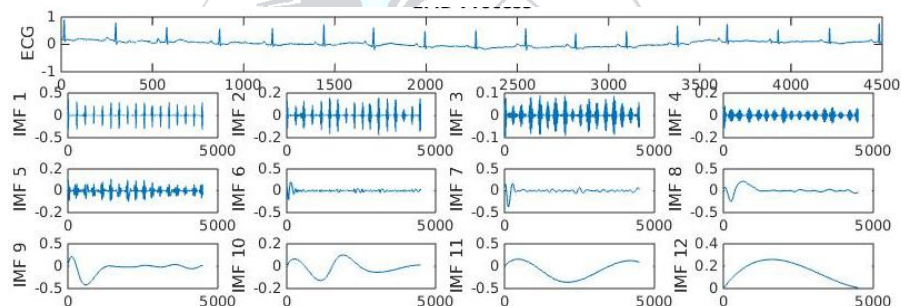

Figure 2. A randomly selected Short-term ECG and Extracted IMFs by applying EMD

HHT is used for feature extraction using the Hilbert Spectral Analysis in most of the studies. In this study, the IMFs that were extracted after the HHT process were used as the base of the features, but not directly used as the features. Statistical features (minimum (Min), maximum (Max), skewness (Skw), median, mean, Standard Deviation (SD), correlation (Corr), mode and energy) were calculated from each IMF for creating the diagnosis dataset. Each short-term ECG had a number of 9 statistical features multiplied by the number of the extracted IMF. The MATLAB statistical toolbox is used for calculation of statistical features. As it is seen in Table I, the highest five responsible features in the diagnosis of the CAD are Max and Min of the 3rd IMF, Max and Corr of the 4th IMF and Min of the 5th IMF. The lowest responsible features are mode values of IMFs.

Table I. Performance of each statistical feature for reduced the short-term ECG in diagnosis of the CAD

	Max	Min	Corr	Energy	Mean	SD	Skw	Median	Mode	All
SEN	85.05	80.98	78.72	60.67	52.70	57.10	43.50	39.77	21.05	96.02
SPE	92.56	81.40	62.52	78.52	73.20	30.24	22.52	5.36	28.00	98.88
ACC	87.26	81.11	73.95	65.92	58.73	49.20	37.33	29.65	23.09	98.05

The system was tested using a 10-fold cross validation. The dataset was randomly divided into 10 folds with the same number of subjects with and without the CAD. 9-folds of dataset were used for the training of the DBN classifier and one fold was used for testing the DBN. We subdivided the 9-folds of the dataset into 100 batches to speed-up and update weights step by step on the learning phase. The DBN that was utilized in the proposed diagnosis model has one input layer, 2 hidden layers and one output layer (Fig.1). The input layer has 9 input units for statistical features.

Greedy layer-wise pre-training is used in this model at the unsupervised learning stage of the DBN with 5 epochs. The DBN has 2 hidden layers with 100 hidden units for each. All feature sets were normalized to 0-1. The output layer has two outputs (subjects with and without CAD). To unfold the DBN to a neural network for the supervised learning stage of DBN, model parameters were selected by iterations. The learning rate is 2 and the activation function of the hidden layers on the supervised learning phase is the hyperbolic tangent function to avoid bias in the gradients and to have a stronger gradient. And a sigmoid output function was utilized. After training the DBN, test results were performed and the reliability and statistical performances of the model were calculated.

Table II. Comparison of the models on diagnosis of the CAD

Authors	ACC	SPE	SEN	Method	Classification	Data
Lee at. al[21]	85.00-90.00	-	-	HRV measurements	SVM	HRV
Dua et. al. [20]	89.50	-	-	HRV measurements	ANN	HRV
Kim et. al. [22]	75.00	-	-	HRV measurements	MDA	HRV
Giri et. al. [28]	96.80	93.70	100.00	DWT, LDA, PCA	GMM	HRV
Patidar et. al. [29]	99.70	99.80	99.60	Co-entropy, PCA	SVM	HRV
Arafat et. al. [24]	86.00	-	-	ST measures	Fuzzy Clustering	ECG
Alizadensani et. al. [25]	94.08	-	-	Q waveand ST measures	SVM	ECG
Thisstudy	98.05	98.88	96.02	HHT, Statistical Features	DBN	ECG

*MDA: Multiple Discriminant Analysis, SVM: Support Vector Machines, ANN: Artificial Neural Network, LDA: Linear Discriminant Analysis, GMM: Gaussian Mixture Model, HRV: Heart Rate Variability

As it is seen in Table II, when we compared the classification performances in literature, high accuracy rates were achieved using various classification methods on both ECG and HRV data. The highest classification performance on ECG data is achieved using the DBN on ECG based features. The achieved performance measurements that are achieved using the proposed method have a remarkable point in both HRV and ECG studies. Subjects with and without CAD were separated with a classification accuracy rate of 98.05%, a specificity of 98.88% and a sensitivity of 96.02% using statistical features from IMFs.

4. CONCLUSIONS

Linear and non-linear HRV features, various analysis techniques on ECG, heart sounds and clinical characteristics were used to evaluate diagnosis of the CAD. Different classification methods were utilized on these features to achieve high classification performances. In this study, the HHT that has a widespread utilization on non-linear signals was used to extract features from filtered ECGs. The proposed system diagnoses the subjects with or without the CAD. In this integrated system, DBN was used to classify the statistical features of IMFs. Accuracy, specificity and sensitivity achievements were used to evaluate system performance.

HRV are the Poincare plots, cross Corr, SD, arithmetic mean, Skw, kurtosis, and approximate entropy measurements between R waves which are extracted from 5 min short-term ECGs. Using HRV does not take into consideration the durations and intervals of the other waves except R waves on the ECGs. In this study, the ECG was used considering that all waves (whole ECG) may carry significant characteristics in diagnosis of the CAD. As seen in Table 1, an accuracy rate of 98.05%, a specificity rate of 98.88% and a sensitivity rate of 96.02% were achieved in the diagnosis of the CAD. It is difficult to compare the classification accuracies with the literature, because of different databases. Achieved performances show that the proposed method has an ability to separate the subjects with and without the CAD. Thus, the highest accuracy is achieved in the studies using ECG signals and most of the studies using HRV. The biggest advantage of the proposed method compared to HRV is using 15 second short-term ECG segments.

REFERENCES

[1]. M. Gabriel Khan, *Rapid ECG Interpretation(Contemporary Cardiology)*, 3rd edition. Humana Press, 2007.

[2]. U. F. Chan, W. W. Chan, S. H. Pun, M. I. Vai, and P. U. Mak, "Flexible implementation of front-end bioelectric signal amplifier using fpaa for telemedicine system," in *Annual International Conference of the IEEE Engineering in Medicine and Biology - Proceedings*, 2007, pp. 3721–3724.

[3]. Y. Özbay and G. Tezel, "A new method for classification of ECG arrhythmias using neural network with adaptive

activation function," *Digit. Signal Process.*, vol. 20, no. 4, pp. 1040–1049, 2010.

[4]. "CAD Information." [Online]. Available: http://www.nhlbi.nih.gov/health/health-. [Accessed: 01-Jan-2016].

[5]. G. K. Hansson, "Inflammation, atherosclerosis, and coronary artery disease," *N. Engl. J. Med.*, vol. 352, no. 16, pp. 1685–1695, 2005.

[6]. K. Polat and S. Güneş, "A hybrid approach to medical decision support systems: Combining feature selection, fuzzy weighted pre-processing and AIRS," *Comput. Methods Programs Biomed.*, vol. 88, no. 2, pp. 164–174, 2007.

[7]. R. Yilmaz and R. Demirbag, "P-wave dispersion in patients with stable coronary artery disease and its relationship with severity of the disease," *J. Electrocardiol.*, vol. 38, no. 3, pp. 279–284, 2005.

[8]. İ. Babaoglu, O. Findik, and E. Ülker, "A comparison of feature selection models utilizing binary particle swarm optimization and genetic algorithm in determining coronary artery disease using support vector machine," *Expert Syst. Appl.*, vol. 37, no. 4, pp. 3177–3183, 2010.

[9]. Y. N. Devi and S.Anto, "An Evolutionary-Fuzzy Expert System for the Diagnosis of Coronary Artery Disease," , *An Evol. Fuzzy Expert Syst. Diagnosis Coron. Artery Dis.*, vol. 3, no. 4, pp. 1478–1484, 2014.

[10]. M. G. Tsipouras, T. P. Exarchos, D. I. Fotiadis, A. P. Kotsia, K. V. Vakalis, K. K. Naka, and L. K. Michalis, "Automated Diagnosis of Coronary Artery Disease Based on Data Mining and Fuzzy Modeling," *IEEE Trans. Inf. Technol. Biomed.*, vol. 12, no. 4, pp. 447–458, 2008.

[11]. Noor Akhmad Setiawan, P. A. Venkatachalam, and Ahmad Fadzil M.Hani, "Diagnosis of coronary artery disease using artificial intelligence based decision support system," *Proc. Int. Conf. Man-Machine Syst.*, 2009.

[12]. N. Ghadiri Hedeshi and M. Saniee Abadeh, "Coronary artery disease detection using a fuzzy-boosting PSO approach," *Comput. Intell. Neurosci.*, vol. 2014, 2014.

[13]. M. C. Colak, C. Colak, H. Kocatürk, S. Sağiroğlu, and I. Barutçu, "Predicting coronary artery disease using different artificial neural network models.," *Anadolu Kardiyol. Derg.*, vol. 8, no. 4, pp. 249–254, 2008.

[14]. A. Rajkumar and M. G. S. Reena, "Diagnosis Of Heart Disease Using Datamining Algorithm," *Glob. J. Comput. Sci. Technol.*, vol. 10, no. 10, pp. 38–43, 2010.

[15]. N. Lavesson, A. Halling, and M. Freitag, "Classifying the Severity of an Acute Coronary Syndrome by Mining Patient Data," *26th Annu. Work. Swedish Artif. Intell. Soc.*, vol. 35, pp. 55–63, 2009.

[16]. M. Shouman, T. Turner, and R. Stocker, "Using data mining techniques in heart disease diagnosis and treatment," *Japan-Egypt Conf. Electron. Commun. Comput.*, pp. 173–177, 2012.

[17]. M. Akay, W. Welkowitz, J. L. Semmlow, and J. Kostis, "Application of the ARMA method to acoustic detection of coronary artery disease," *Med. Biol. Eng. Comput.*, vol. 29, no. 4, pp. 365–372, 1991.

[18]. U. R. Acharya, O. Faust, V. Sree, G. Swapna, R. J. Martis, N. A. Kadri, and J. S. Suri, "Linear and nonlinear analysis of normal and CAD-affected heart rate signals," *Comput. Methods Programs Biomed.*, vol. 113, no. 1, pp. 55–68, 2014.

[19]. H. G. Lee, K. Y. Noh, and K. H. Ryu, "Mining biosignal data: Coronary artery disease diagnosis using linear and nonlinear features of HRV," in *Lecture Notes in Computer Science (including subseries Lecture Notes in Artificial Intelligence and Lecture Notes in Bioinformatics)*, 2007, vol. 4819 LNAI, pp. 218–228.

[20]. S. Dua, X. Du, S. Vinitha Sree, and V. I. Thajudin Ahamed, "Novel classification of coronary artery disease using heart rate variability analysis," *J. Mech. Med. Biol.*, vol. 12, no. 4, p. 1240017, 2012.

[21]. H. G. L. H. G. Lee, K. Y. N. K. Y. Noh, and K. H. R. K. H. Ryu, "A Data Mining Approach for Coronary Heart Disease Prediction using HRV Features and Carotid Arterial Wall Thickness," *2008 Int. Conf. Biomed. Eng. Informatics*, vol. 1, 2008.

[22]. H. C. W. Kim, S. Jin, Y. Park, "A study on development of multi-parametric measure of heart rate variability diagnosing cardiovascular disease," *IFMBE Proc. 14*, pp. 3480–3483, 2007.

[23]. M. Karimi, R. Amirfattahi, S. Sadri, and S. A. Marvasti, "Noninvasive detection and classification of coronary artery occlusions using wavelet analysis of heart sounds with neural networks," in *Medical Applications of Signal Processing, 2005. The 3rd IEE International Seminar on (Ref. No. 2005-1119)*, 2005, pp. 117–120.

[24]. S. Arafat, M. Dohrmann, and M. Skubic, "Classification of Coronary Artery Disease Stress ECGs using Uncertainty Modeling," in *2005 ICSC Congress on Computational Intelligence Methods and Applications*, 2005, pp. 1–4.

[25]. R. Alizadehsani, J. Habibi, M. J. Hosseini, H. Mashayekhi, R. Boghrati, A. Ghandeharioun, B. Bahadorian, and Z. A. Sani, "A data mining approach for diagnosis of coronary artery disease," *Comput. Methods Programs Biomed.*, vol. 111, no. 1, pp. 52–61, 2013.

[26]. Z. Zhao and C. Ma, "An Intelligent System for Noninvasive Diagnosis of Coronary Artery Disease with EMD-TEO and BP Neural Network," in *2008 International Workshop on Education Technology and Training & 2008 International Workshop on Geoscience and Remote Sensing*, 2008, pp. 631–635.

[27]. U. R. Acharya, S. V. Sree, M. Muthu Rama Krishnan, N. Krishnananda, S. Ranjan, P. Umesh, and J. S. Suri, "Automated classification of patients with coronary artery disease using grayscale features from left ventricle echocardiographic images," *Comput. Methods Programs Biomed.*, vol. 112, no. 3, pp. 624–632, 2013.

[28]. D. Giri, U. Rajendra Acharya, R. J. Martis, S. Vinitha Sree, T. C. Lim, T. Ahamed, and J. S. Suri, "Automated diagnosis of Coronary Artery Disease affected patients using LDA, PCA, ICA and Discrete Wavelet Transform," *Knowledge-Based Syst.*, vol. 37, pp. 274–282, 2013.

[29]. S. Patidar, R. B. Pachori, and U. Rajendra Acharya, "Automated diagnosis of coronary artery disease using tunable-Q wavelet transform applied on heart rate signals," *Knowledge-Based Syst.*, vol. 82, pp. 1–10, 2015.

[30]. N. E. Huang, Z. Shen, S. R. Long, M. C. Wu, H. H. Shih, Q. Zheng, N.-C. Yen, C. C. Tung, and H. H. Liu, "The empirical mode decomposition and the Hilbert spectrum for nonlinear and non-stationary time series analysis," *Proc. R. Soc. A Math. Phys. Eng. Sci.*, vol. 454, no. 1971, pp. 903–995, 1998.

[31]. U. Maji, M. Mitra, and S. Pal, "Automatic Detection of Atrial Fibrillation Using Empirical Mode Decomposition and Statistical Approach," *Procedia Technol.*, vol. 10, pp. 45–52, 2013.

[32]. G. Altan, A. Yayik, Y. Kutlu, S. Yildirim, and E. Yildirim, "Analyse of Congestive Heart Failure Using Hilbert-Huang Transform," *Dokuz Eylul Univ. Eng. Sci.*, vol. 16, pp. 94–103, 2014.

[33]. G. Hinton, L. Deng, D. Yu, G. Dahl, A. Mohamed, N. Jaitly, V. Vanhoucke, P. Nguyen, T. Sainath, and B. Kingsbury, "Deep Neural Networks for Acoustic Modeling in Speech Recognition," *IEEE Signal Process. Mag.*, vol. 29, no. 6, pp. 82–97, 2012.

[34]. S. M. Siniscalchi, D. Yu, L. Deng, and C. H. Lee, "Exploiting deep neural networks for detection-based speech recognition," *Neurocomputing*, vol. 106, pp. 148–157, 2013.

[35]. C. Farabet, C. Couprie, L. Najman, and Y. Lecun, "Learning hierarchical features for scene labeling," *IEEE Trans. Pattern Anal. Mach. Intell.*, vol. 35, no. 8, pp. 1915–1929, 2013.

[36]. P. Sermanet, K. Kavukcuoglu, S. Chintala, and Y. Lecun, "Pedestrian detection with unsupervised multi-stage feature learning," in *Proceedings of the IEEE Computer Society Conference on Computer Vision and Pattern Recognition*, 2013, pp. 3626–3633.

[37]. Q. Le and T. Mikolov, "Distributed Representations of Sentences and Documents," *Int. Conf. Mach. Learn. - ICML 2014*, vol. 32, pp. 1188–1196, 2014.

[38]. I. Sutskever, O. Vinyals, and Q. Le, "Sequence to sequence learning with neural networks," *Adv. Neural Inf. …*, p. 9, 2014.

[39]. H. Lee, R. Grosse, R. Ranganath, and A. Y. Ng, "Convolutional deep belief networks for scalable unsupervised learning of hierarchical representations," *Proc. 26th Annu. Int. Conf. Mach. Learn. ICML 09*, vol. 2008, pp. 1–8, 2009.

[40]. P. W. Mirowski, Y. LeCun, D. Madhavan, and R. Kuzniecky, "Comparing SVM and convolutional networks for epileptic seizure prediction from intracranial EEG," in *Proceedings of the 2008 IEEE Workshop on Machine Learning for Signal Processing, MLSP 2008*, 2008, pp. 244–249.

[41]. P. W. Mirowski, D. Madhavan, and Y. Lecun, "Time-delay neural networks and independent component analysis for eeg-based prediction of epileptic seizures propagation," in *Advancement of Artificial Intelligence Conference*, 2007, pp. 1892–1893.

[42]. D. Wang and Y. Shang, "Modeling Physiological Data with Deep Belief Networks.," *Int. J. Inf. Educ. Technol.*, vol. 3, no. 5, pp. 505–511, 2013.

[43]. P. Drotár, J. Gazda, and Z. Smékal, "An experimental comparison of feature selection methods on two-class biomedical datasets," *Comput. Biol. Med.*, vol. 66, pp. 1–10, 2015.

[44]. P. Tamilselvan and P. Wang, "Failure diagnosis using deep belief learning based health state classification," *Reliab. Eng. Syst. Saf.*, vol. 115, pp. 124–135, 2013.

[45]. E. de la Rosa and W. Yu, "Randomized algorithms for nonlinear system identification with deep learning modification," *Inf. Sci. (Ny).*, p. -, 2015.

[46]. M. Längkvist, L. Karlsson, and A. Loutfi, "A review of unsupervised feature learning and deep learning for time-series modeling," *Pattern Recognit. Lett.*, vol. 42, no. 1, pp. 11–24, 2014.

[47]. Y. Bengio and O. Delalleau, "Justifying and generalizing contrastive divergence," *Neural Comput.*, vol. 21, no. 6, pp. 1601–1621, 2009.

[48]. G. Hinton, G. Hinton, T. Sejnowski, and T. Sejnowski, *Learning and relearning in Boltzmann machines*, vol. 1. 1986.

[49]. A. L. Goldberger, L. A. N. Amaral, L. Glass, J. M. Hausdorff, P. C. Ivanov, R. G. Mark, J. E. Mietus, G. B. Moody, C.-K. Peng, and H. . Stanley, "PhysioBank, PhysioToolkit, and PhysioNet: Components of a New Research Resource for Complex Physiologic Signals," *Circulation*, vol. 101, pp. 215–220, 2000.

[50]. N. E. Huang, Z. Shen, S. R. Long, M. C. Wu, H. H. Shih, Q. Zheng, N.-C. Yen, C. C. Tung, and H. H. Liu, "The

empirical mode decomposition and the Hilbert spectrum for nonlinear and non-stationary time series analysis," *Proceedings of the Royal Society A: Mathematical, Physical and Engineering Sciences*, vol. 454, no. 1971. pp. 903–995, 1998.

[51]. G. E. Hinton, S. Osindero, and Y.-W. Teh, "A fast learning algorithm for deep belief nets.," *Neural Comput.*, vol. 18, no. 7, pp. 1527–54, 2006.

[52]. Y. Bengio, P. Lamblin, D. Popovici, and H. Larochelle, "Greedy Layer-Wise Training of Deep Networks," *Adv. Neural Inf. Process. Syst.*, vol. 19, no. 1, p. 153, 2007.

[53]. Y. Liu, S. Zhou, and Q. Chen, "Discriminative deep belief networks for visual data classification," *Pattern Recognit.*, vol. 44, no. 10–11, pp. 2287–2296, 2011.

[54]. R. O. Duda, P. E. Hart, and D. G. Stork, *Pattern Classification*. 2000.

Revealing Tectonic Structure by Utilizing the Boundary Analysis Methods on Aeromagnetic Data of Bitlis Zagros Suture Zone and Its Surroundings, Turkey

Fikret Dogru[1]*, Oya Pamukcu[1]

[1] *Dokuz Eylul University, Engineering Faculty, Department of Geophysical Engineering, 35160, İzmir, Turkey*

*Corresponding Author email: fikret.dogru@deu.edu.tr

Abstract

Boundary analysis techniques which are analytic signal, total horizontal derivative (THDR), theta map, tilt angle, hyperbolic of tilt angle (HTA), normalized total horizontal gradient (TDX) and normalized horizontal derivative (NTHD), play an important role in interpreting potential field data. In this study, an enhanced total horizontal derivative of the tilt angle (ETHDR) method was utilized for comparison of results with the other edge detection filters. The sufficiency of the ETHDR method is indicated using theoretical models and field study. Compared with the formal methods, the ETHDR filter more detailed outcomes for buried models and is less sensitive to noise. Aeromagnetic anomaly of Bitlis Zagros Suture Zone (BZSZ) and its surroundings was used for field data. The eastern part of Turkey which has major tectonic structures such as East Anatolian Fault (EAF), Malatya Fault (MF) and Bitlis-Zagros Suture Zone (BZSZ), with the effect of Arabian Plate's northward motion, Anatolian block and Northeastern Anatolian Block escape to west and east, respectively. In the first stage field study, the discontinuities were not found recognizable in the results of boundary analysis methods. Then, pole reduction and upward continuation (5 km and 10 km) were applied to the aeromagnetic data for revealing the deeper effects on data. The same boundary analysis methods were applied to aeromagnetic data after pole reduction and upward continuation. The results were compared with each other and the anomalies were associated with the faults and previous studies. It is thought that there are tectonic boundaries that have not yet been identified geologically in the study area.

Key words

Edge detection, pole reduction, upward continuation, tilt angle, Bitlis-Zagros Suture Zone

1. INTRODUCTION

Boundary analysis method applications are crucial on magnetic anomalies to reveal tectonic structures and mine locations ([1], [2]). Accurate determination of source shape location is becoming the main purpose for interpretation and therefore enhanced methods are becoming more important in data interpretation [3]. There are various procedures that have been utilized to obtain edge detection, for example, analytic signal (AS), tilt angle (TA), theta map (TM) and etc. [4]. An enhanced total horizontal derivative of the tilt angle (ETHDR) method, which was proposed by Arisoy and Dikmen [4], was applied for the boundary analysis of aeromagnetic anomalies with the former methods. Before interpreting the field measurements, noise-corrupted theoretical models were utilized in order to determine spatial resolution of ETHDR method.

Then, same processes were applied on aeromagnetic data. When acceptable results could not be obtained from aeromagnetic data, pole reduction and upward continuation (for 5 km and 10 km) were applied on aeromagnetic data and then same analyzes were implemented. The data was used regarding western of BSZS and its surroundings. The area is so complex in terms of geological units and tectonics. The tectonic regime along the fault changes from east to west; collision zone of Bitlis-Zagros produced by northward movement of Arabian Plate with respect to Eurasia ([5]).

Anatolia, located in the Alpine-Himalaya basin, has taken the current form as a result of a very complicated movement in the Earth's crust. Continental rifting in the Eastern Mediterranean began at the end of Triassic and ended with the formation of the Mesozoic Neotethys ocean after the closure of the Paleotethys Ocean ([6]). The convergence of the African and Eurasian continents that began at the end of the Cretaceous ended with the closure of these ocean basins and the unification of continental parts in the vicinity ([6], [7]). The southern part of the Neotethys extending from southeastern Turkey known as the Bitlis ocean to Cyprus is completely closed due to the continental collision along the BZSZ of the Arab plate in the south and the Eurasian plate in the north ([6], [8]). East Turkey, in which BSZS has such a complex structure, has worked on many geodynamic processes in previous studies. For this reason, possible structure depths, effective elastic thickness of isostatic model, curie depth and corresponding heat flow calculations have been made and the change of crust thickness and boundaries of vertical and horizontal structures have been investigated and possible geophysical models have been established ([9], [10], [11], [12]). In the studies carried out, the BSZS and secondary structural elements that developed due to thrust have been investigated region-wide. In this study, BSZS and its fault locations are discussed in detail with the boundary analysis methods. As a result, gravity, magnetic and seismological studies have been evaluated together in the region.

2. METHODS

A number of methods have been proposed to make rough anomalies more apprehensible. The first filter developed for this purpose was the tilt angle [13], which is the ratio of the vertical derivative to the absolute value of the horizontal derivative of the potential field. The tilt angle is given by

$$Tilt = tan^{-1}\left(\frac{\frac{\partial T}{\partial z}}{THDR}\right) \tag{1}$$

Where,

$$THDR = \sqrt{\left(\frac{\partial T}{\partial x}\right)^2 + \left(\frac{\partial T}{\partial y}\right)^2} \tag{2}$$

T is the potential anomaly and THDR is the total horizontal derivative [14]. The tilt angle amplitudes are restricted to values between $-\pi/2$ and $+\pi/2$; thus the method delimitates the amplitude variations into a certain range. Tilt angle therefore functions like an automatic-gain-control filter, and therefore responds equally well to shallow and deep sources. The tilt angle produces a zero value over the source edges [4]. Wijns introduced the theta map (θ), which is the normalization of the THDR by the AS [15], is given by

$$cos\theta = \left(\frac{THDR}{AS}\right) \tag{3}$$

and

$$AS = \sqrt{\left(\frac{\partial T}{\partial x}\right)^2 + \left(\frac{\partial T}{\partial y}\right)^2 + \left(\frac{\partial T}{\partial z}\right)^2} \tag{4}$$

AS is the analytic signal for the 3D case [16]. The theta map delineates model edges well, but the response of deeper bodies is diffused; consequently, it does not produce the expected sharp gradient over the edges. Recently, Cooper and Cowan presented the horizontal tilt angle method (TDX) as an edge detector [17]:

$$TDX = tan^{-1}\left(\frac{THDR}{\left|\frac{\partial T}{\partial z}\right|}\right) \tag{5}$$

TDX responds equally well to shallow and deep bodies, and also delineates the edges of all the bodies well. TDX has a much sharper gradient over the edges of the magnetized bodies. The proposed Etilt filter is the ratio of the vertical derivative to the total horizontal derivative of the AS:

$$Etilt = tan^{-1}\left(k\frac{\frac{\partial T}{\partial z}}{\sqrt{\left(\frac{\partial A}{\partial x}\right)^2 + \left(\frac{\partial A}{\partial y}\right)^2}} \right) \tag{6}$$

where

$$k = \frac{1}{\sqrt{dx^2 + dy^2}} \tag{7}$$

k is the dimensional correction factor. dx and dy are sampling intervals in the x and y directions, respectively. The dimensional correction factor, k, does not have an effect on the Etilt response.

$$ETHDR = \sqrt{\left(\frac{\partial Etilt}{\partial x}\right)^2 + \left(\frac{\partial Etilt}{\partial y}\right)^2} \tag{8}$$

The ETHDR delineates the edges of the all bodies better than the filters discussed above, as it produces a very sharp gradient over the edges of the bodies. Thus, structural interpretation is very easy and powerful using the ETHDR method.

3. UPWARD CONTINUATION

Upward continuation is a method that transforms anomalies measured on one surface into those that would have been measured on some higher surface. The upward-continued anomalies do not provide direct information about the source, but they can be instructive nonetheless. In particular, the process of upward continuation tends to attenuate anomalies caused by local, near-surface sources relative to anomalies caused by deeper, more profound sources. The potential data at two observation heights are related by the upward continuation operation [18],

$$T_h(x,y,\Delta h) = \frac{1}{2\pi}\int_{-\infty}^{\infty}\int_{-\infty}^{\infty}\frac{T_0(x',y')\Delta h}{[(x'-x)^2 + (y'-y)^2 + \Delta h^2]^{3/2}}\,dx'dy' \tag{9}$$

where $T_0(x,y)$ and $T_h(x, y, h)$ are respectively the potential data at two observation heights separated by a vertical distance Δh. Applying a two-dimensional Fourier transform to equation (1) yields a simpler form in which the Fourier transforms of the two quantities are related to each other by a simple upward continuation operator,

$$\tilde{T}_h(\omega_x, \omega_y, \Delta h) = e^{-\Delta h \omega_r}\tilde{T}_0(\omega_x, \omega_y) \tag{10}$$

where $\tilde{T}_0(\omega_x, \omega_y)$ denotes the Fourier transform of $T_0(x,y)$, (ω_x, ω_y) are wavenumbers in x- and y- direction, and $\omega_r = \sqrt{\omega_x^2 + \omega_y^2}$ is the radial wavenumber. The upward continuation operator attenuates with height the high-frequency content of a potential anomaly.

4. POLE REDUCTION

Pole reduction is an operator, which takes magnetic anomalies and changes their asymmetric form to the symmetric form which would have observed the causative magnetic bodies lain at the magnetic poles. The frequency domain operator is [19],

$$A'(u,v) = \frac{A(u,v)}{(\sin\theta + icos\theta \sin(\emptyset + \alpha))^2} \tag{11}$$

where A(u,v) is the amplitude at frequencies (u,v), θ and φ are the geomagnetic inclination and declination, respectively, and α is $\tan^{-1}$(v/u).

5. THEORETICAL STUDY

In this stage, synthetic magnetic anomaly of three prisms whose depths are 1, 3, 5 km were utilized for theoretical study (Figure 1). Inclination, declination and susceptibility values were taken as 90°, 0° and 0.1 SI respectively. Initially, the noise, %0.5, %5 and %10 of the maximum magnetic data amplitude, was added to magnetic anomaly for interpreting noise-corrupted conditions. The boundary analysis applications which are THDR, AS, Tilt angle, Theta map, TDX, Etilt and ETHDR methods were applied on noise-corrupted data (Figure 2 and Figure 3). Synthetic magnetic anomaly was obtained by using Potensoft program based on MATLAB [20].
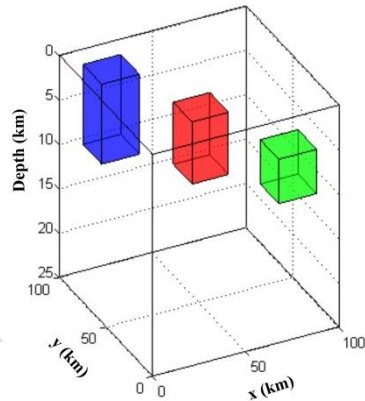
Figure 1. 3D view of theoretical model.
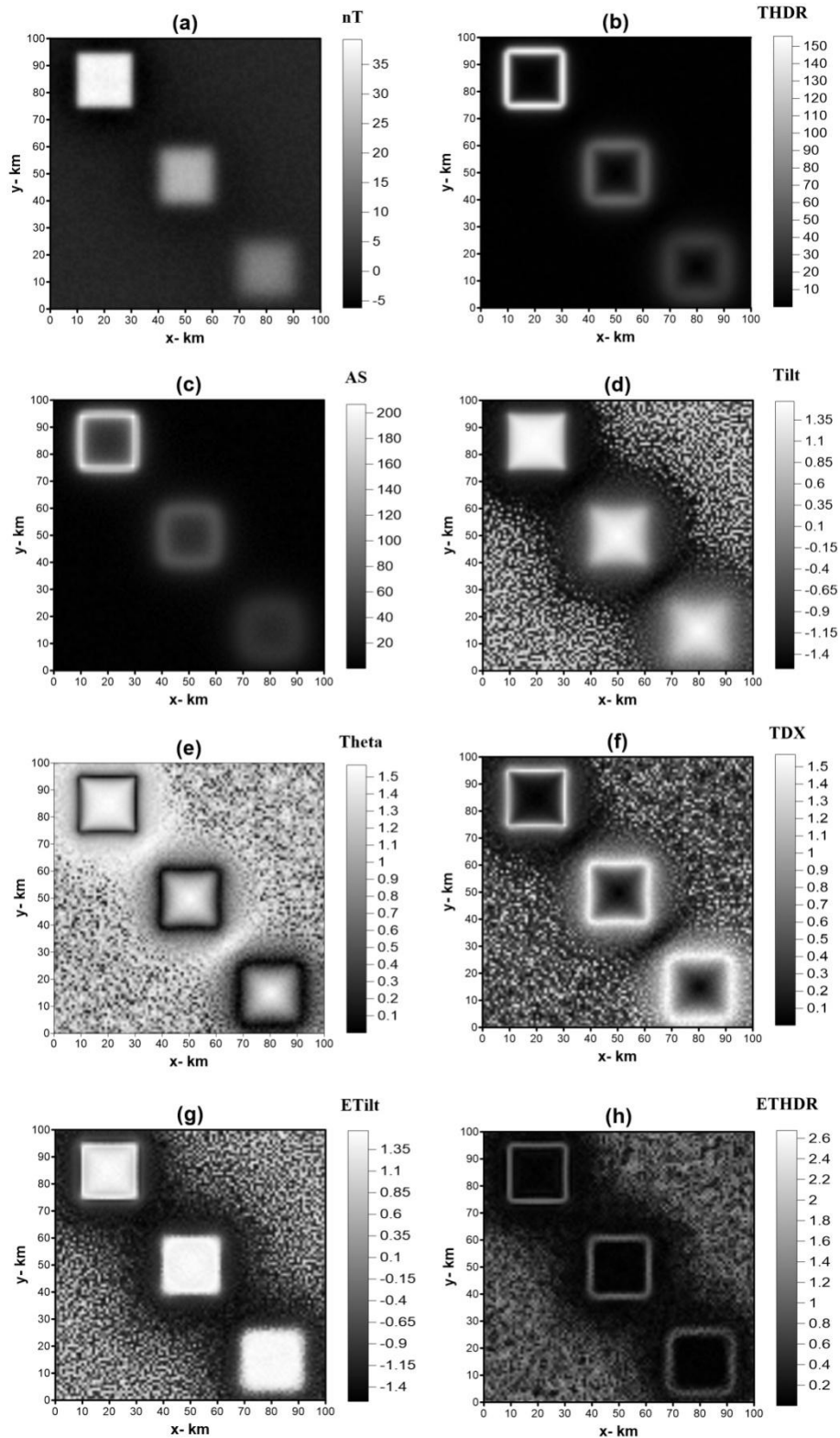
Figure 2. A comparison of boundary analysis filters: a) Theoretical magnetic data resulted from three prismatic bodies with depths of 1, 3 and 5 km. (Image covers 100x100 km area. Uniformly distributed random noise of amplitude equal to % 0.5 of the maximum magnetic data amplitude is added to the magnetic data. b) THDR image map of magnetic data. c) AS image map of magnetic data. d) TA i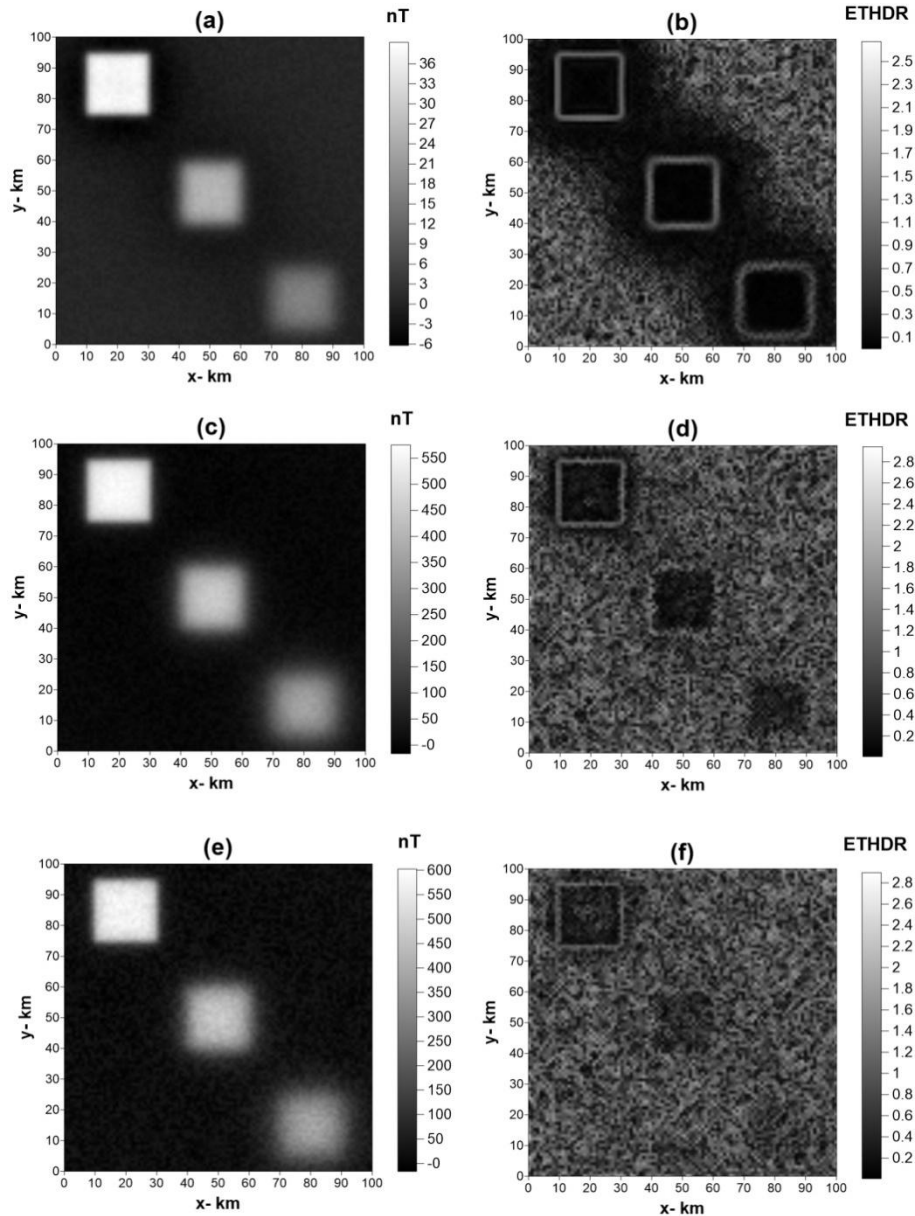mage map of magnetic data. e) TM image map of magnetic data. f) TDX image map of magnetic data. g) Etilt image map of magnetic data. h) ETHDR image map of magnetic data.

Figure 3. A comparison of different amounts of noise effects on the ETHDR responses. a) Magnetic data with uniformly distributed random noise of amplitude equal to % 0.5 of the maximum magnetic data amplitude is added to the magnetic data. b) ETHDR image map of magnetic data in Figure 3a. c) Magnetic data with uniformly distributed random noise of amplitude equal % 5 of the maximum magnetic data amplitude is added to the magnetic data. d) ETHDR image map of magnetic data in Figure 3c. e) Magnetic data with uniformly distributed random noise of amplitude equal % 10 of the maximum magnetic data amplitude is added to the magnetic data. f) ETHDR image map of magnetic data in Figure 3e.

6. FIELD STUDY

The study area is located in the West of Bitlis that includes complex geological units and faults. Application stage of this study was provided by the contributions of the Directorate of Mineral Research and Exploration of Turkey (MTA) ([21]). Figure 4 shows the location of the study area and known faults with topography.

Firstly, the boundary analysis methods were applied on aeromagnetic data without using any filters. Maximum anomaly areas are over the northeast of the study area and minimum anomaly areas are over the southwest of the study area (Figure 5a). The boundaries of the faults could not be seen clearly in the results of THDR and AS because of the effects of deeper structure (Figure 5b and 5c). It seems that the noise cause to repress effects of deeper structure because of the complex geological units in the area (Figure 5d, 5e and 5f). It requires pole reduction and other filters when examining the results of Etilt and ETHDR method (Figure 5g and 5h). The result of ETHDR could not be interpreted well because the anomaly

contains the effects of all residual and regional underground structures, also complexity of area in terms of faults and variable topography.
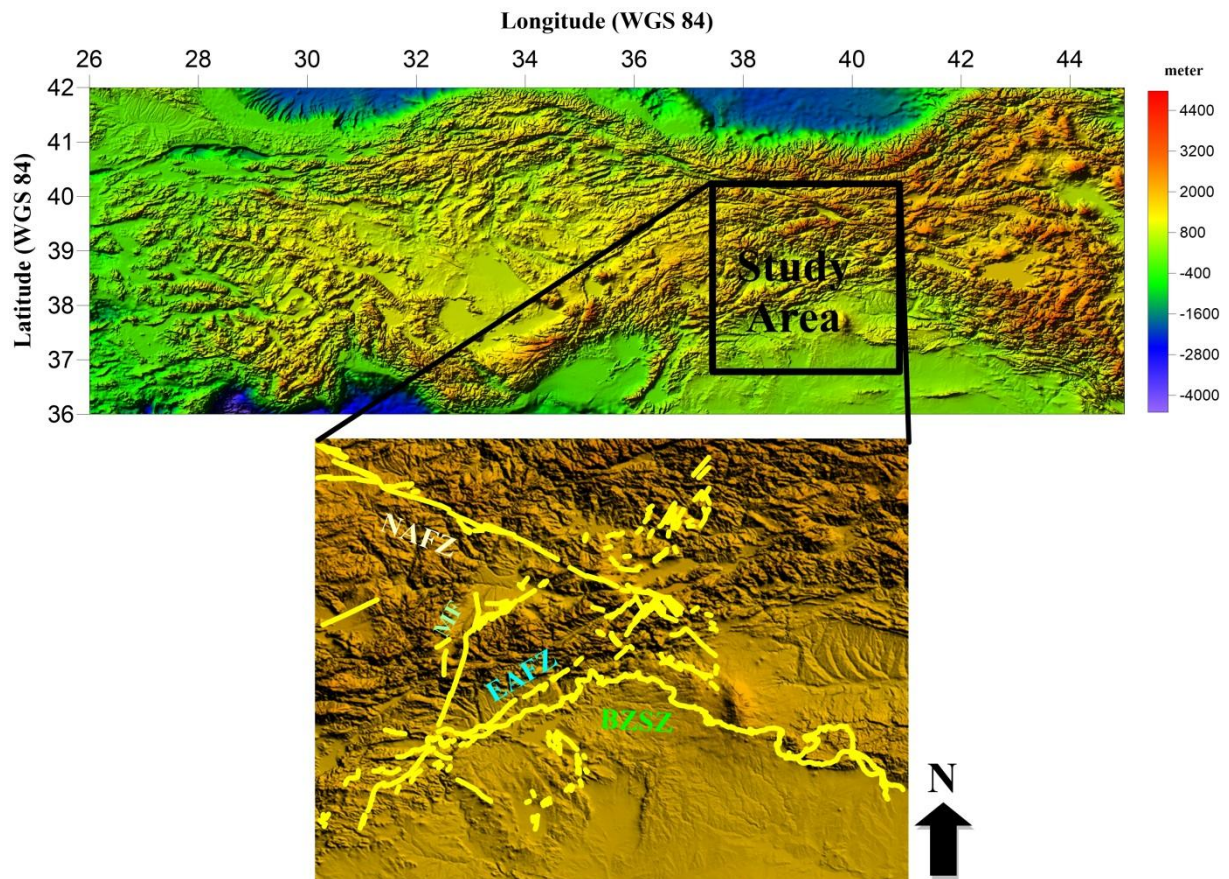

Figure 4. Location of the study area (Topography data are taken from http://topex.ucsd.edu/cgi-bin/get_srtm30.cgi)(NAFZ: North Anatolian Fault Zone, MF: Malatya Fault, EAFZ: East Anatolian Fault Zone and BZSZ: Bitlis-Zagros Suture Zone).
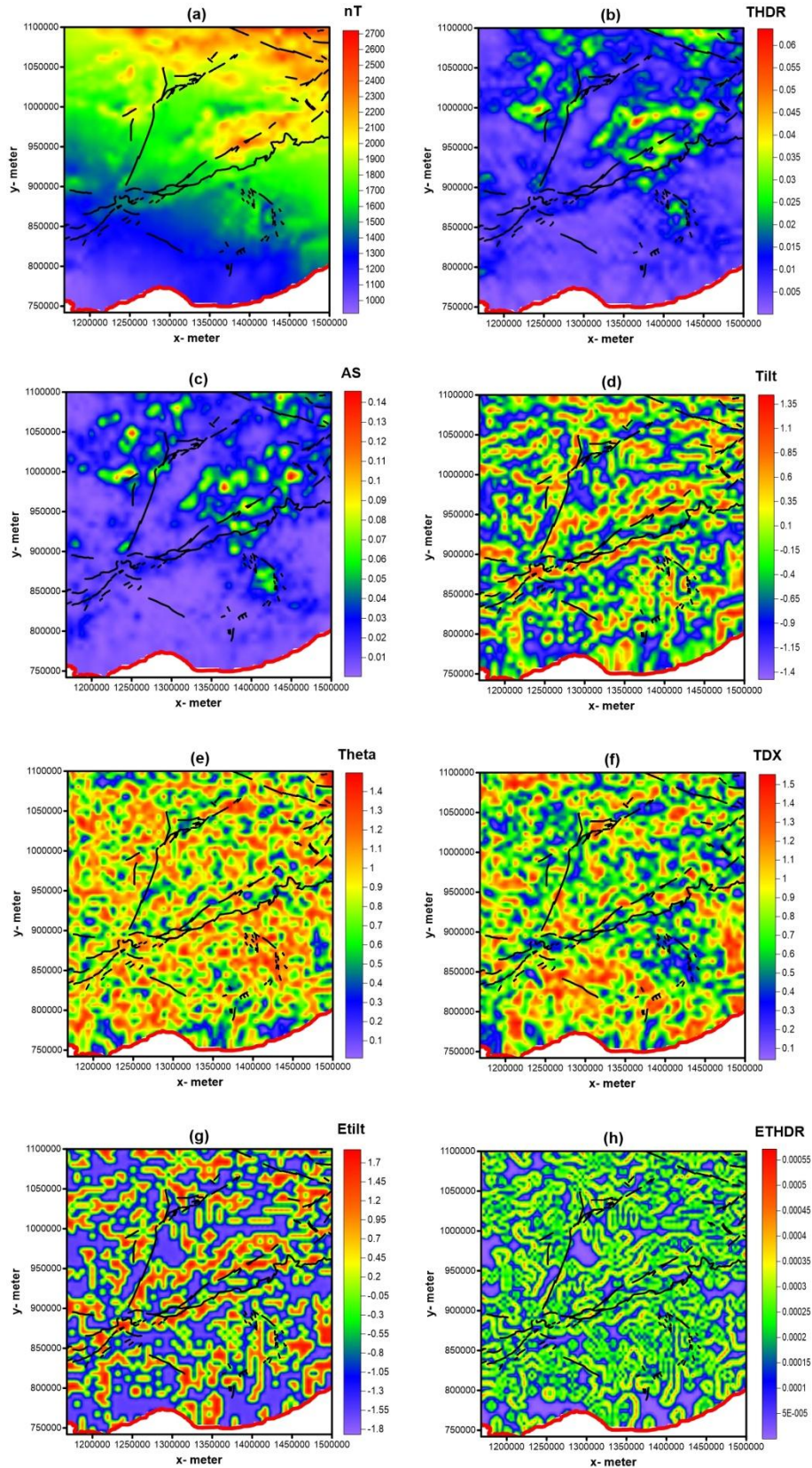
Figure 5. Magnetic anomaly and the results of boundary analysis: a) Magnetic anomaly of the west of Bitlis and its surroundings, b) The result of THDR, c) The result of AS, d) The result of tilt angle, e) The result of theta map, f) The result of TDX, g) The result of Etilt, h) The result of ETHDR method.

Afterwards, pole reduction and upward continuation (5 km and 10km) were applied to the aeromagnetic data and then same boundary analysis methods were implemented to the data. When applying to pole reduction and upward continuation, the

maximum and minimum anomaly areas changed. The effects of deeper bodies were revealed after upward continuation (Figure 6a, Figure 7a). The results of THDR and AS did not change more than the results of unfiltered data but anomalies are smoother (Figure 6b, 6c, 7b, 7c). The results of Etilt, TDX, tilt and theta map give information about the tectonic structures of area (Figure 6d, 6e, 6f, 6g; Figure 7d, 7e, 7f, 7g). The result of ETHDR gives apparent anomaly in the BSZS especially related to low amplitude anomaly areas (Figure 6h and Figure 7h). The increase of the analytical extension level has clarified the location of the tectonic elements.
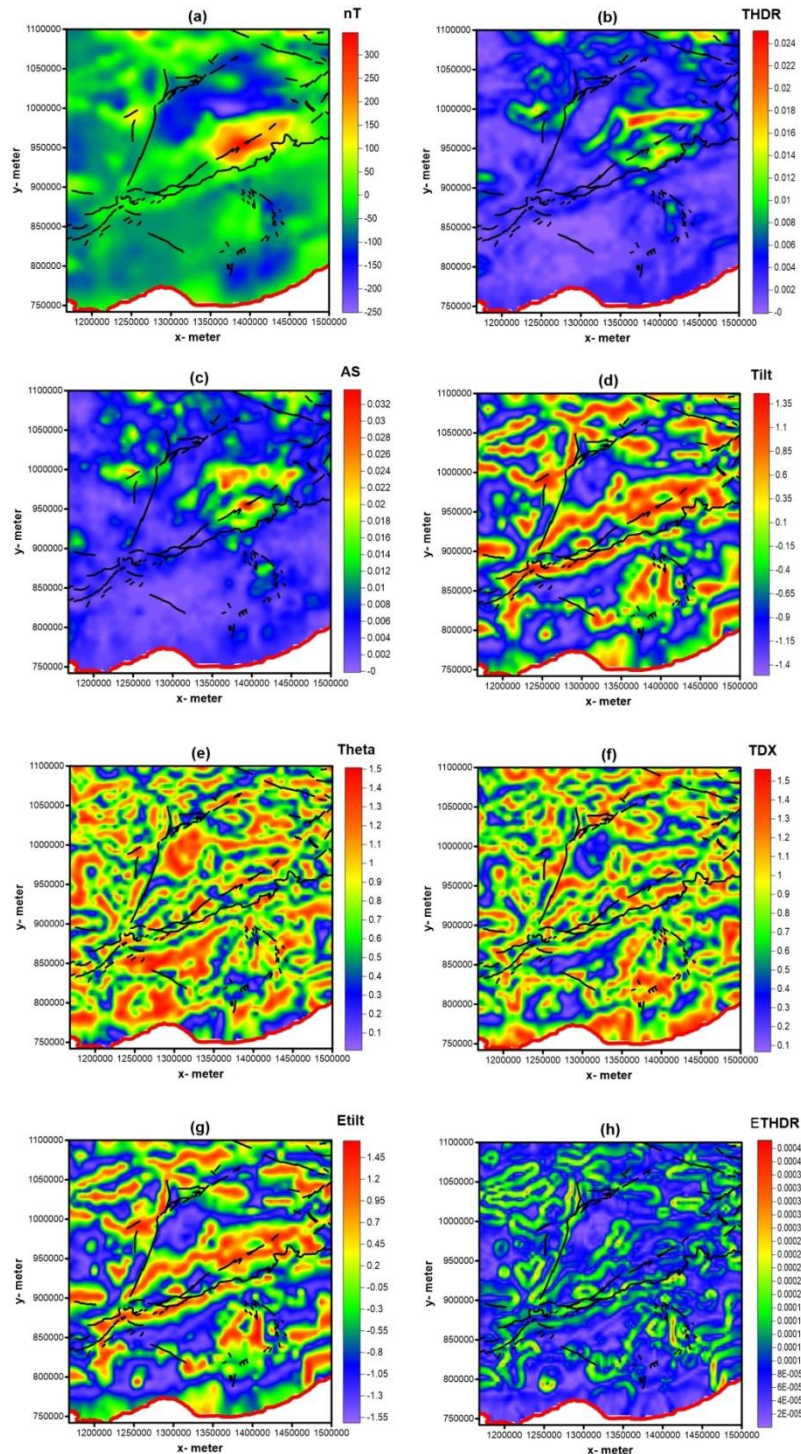
Figure 6. Upward continuation of magnetic anomaly (5km) and the results of boundary analysis: a) Upward continuation of magnetic anomaly of the west of Bitlis and its surroundings, b) The result of THDR, c) The result of AS, d) The result of tilt angle, e) The result of theta map, f) The result of TDX, g) The result of Etilt and h) The result of ETHDR method.
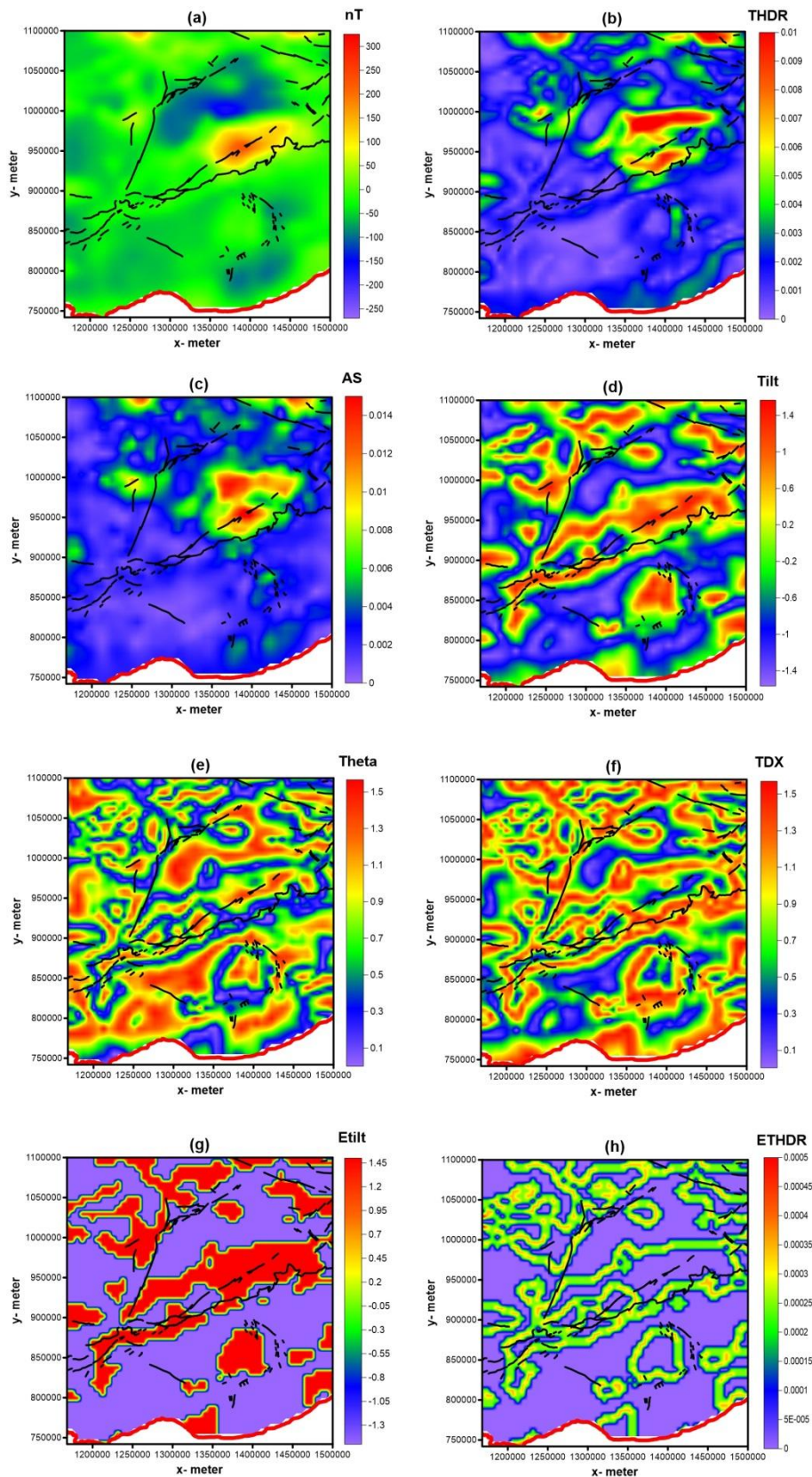
Figure 7. Upward continuation of magnetic anomaly (10km) and the results of boundary analysis: a) Upward continuation of magnetic anomaly of the west of Bitlis and its surroundings, b) The result of THDR, c) The result of AS, d) The result of tilt angle, e) The result of theta map, f) The result of TDX, g) The result of Etilt and h) The result of ETHDR method.

CONCLUSIONS

According to theoretical studies, the results of THDR and AS methods gave similar anomalies, maximum values were found over the prisms in both results but boundary of deeper body was not clear (Figure 2b and 2c). It seems that the ratio of the noise increased in the results of tilt angle, theta map, TDX, Etilt and ETHDR methods but ETHDR was outperformed for determining the boundaries of buried structures from former methods and also ETHDR method is less sensitive the noise (Figure 2d, 2e, 2f and 2g). For comparison, uniformly distributed random noise of amplitude equal %0.5, %5 and %10 of the maximum magnetic data amplitude was added to synthetic magnetic anomaly (Figure 3a, 3c and 3e). The results are acceptable until the results of %10 noise-corrupted data, because the deeper bodies are not recognizable after %5 noise (Figure 3b, 3d and 3f).

As field study, THDR, AS, Tilt, Theta map, TDX, Etilt, ETHDR boundary analysis methods were implemented successfully to the pole reduced and analytical extended (5 km and 10 km) aeromagnetic data which was collected by MTA in the eastern part of Turkey. The results of theta map and TDX could not explain the relationship between any tectonic or differences of geological units. The areas that offer close to zero amplitude are related to extension of BZSZ in the results of AS and THDR. The results of AS and THDR are related to geological unit differences and the result of ETHDR is related to tectonic elements. Also as a result of field application, it was found that the success of methods was increased due to applying filtering to anomaly before the application of boundary analysis methods. The relationship between the maximum-minimum amplitude transitions in the results of Figure 6d, 6g and 7 d, 7e, 7f, 7g, 7h and BZSZ and fault locations in the field applications has been successfully determined. Starting from this point of view, there are boundaries that cannot be identified as tectonic elements because they have not been identified yet, so detailed geological field observations should be made.

Pamukçu et al. (2014) observed a relative increase in heat flow values in the north of Bitlis Thrust in the study of the heat flow change in the region obtained from the curie depths calculated using magnetic data throughout Eastern Anatolia [11]. Within the scope of this study, the high amplitude regions in the applications of Figure 6 and Figure 7b and Figure 7c are in agreement with the high heat flow amplitude region that was detected [11]. When the vertical derivative values applied to Bouguer gravity anomaly values in the region are examined, an increase in vertical derivative values is observed [12]. These findings are indicative of the structural element or elements that are continuous in both gravity and magnetic properties in the high-amplitude regions of the applications of Figure 6 and Figure 7b and 7c.

As a conclusion, as the level of applied upward continuation to the aeromagnetic field increases the success of the applied boundary analysis methods to the analytical extended data is determined by observations made with locations of the structural elements. Successful monitoring of structural elements with increasing level of analytical extension to the aeromagnetic data in the study area suggests that the source location of the anomaly is deep in and around BZSZ. This finding is coherent with the results of the study on depth distribution of the earthquakes in the Eastern Anatolian region, the seismogenic layer of BZSZ and its surroundings is thicker than the northern part [23].

ACKNOWLEDGEMENTS

REFERENCES

[1]. M. Pilkington and P. Keating, *Geologic applications of magnetic data and using enhancements for contact mapping, EGM international workshop Adding new value to electromagnetic, gravity and Magnetic methods for exploration*, Capri, Italy, pp 11-14, 2010.

[2]. F. Dogru, O. Pamukcu, and C. Pamukcu, Determination of Mine Location by Using Edge Detection Methods: A Case Study of Sivas-Divrigi. Science PG Earth Science, 5(4), 56-61, 2016.

[3]. N. Bournas and H.A. Baker, Interpretation of magnetic anomalies using the horizontal gradient analytic signal, Annali di Geofisica, 44 (3), pp 506-526, 2001.

[4]. M.O. Arisoy and U. Dikmen, Edge Detection of Magnetic Sources Using Enhanced Total Horizontal Derivative of the Tilt Angle, Bulletin of the Earth Sciences Application and Research Centre of Hacettepe University, 34 (1), pp 73-82, 2013.

[5]. C.O. Faccenna, J. Bellier, , C.P. Martinod and V. Regard, Slab Detachment Beneath Eastern Anatolia: A Possible Cause for the Formation of the North Anatolian Fault, Earth and Planetary Science Letters, Vol. 242, pp. 85-97, 2006.

[6]. A.M.C. Şengör, Y. Yılmaz, Tethyan evolution of Turkey: a plate tectonic approach, Tectonophysics, 75, pp. 181-241, 1981.

[7]. A.M.C. Şengör, Natal'in B.A, Turkic-type orogeny and its role in the making of the continental crust , Ann. Rev. Earth Sci. 24 , pp. 263-337, 1996.

[8]. J. F. Dewey, M.R. Hempton, W.S.F. Kidd, F.A.M.C. Saroglu, and A.M.C. Şengör, Shortening of continental lithosphere: the neotectonics of Eastern Anatolia—a young collision zone. Geological Society, London, Special Publications,19(1), 1-36, 1986.

[9]. O.A. Pamukçu, Z. Akçığ, Ş. Demirbaş, and E. Zor, Investigation of crustal thickness in Eastern Anatolia using gravity, magnetic and topographic data, Pure and Applied Geophysics, 164(11), pp.2345-2358, 2007.

[10]. O.A. Pamukçu and Z. Akçığ, Isostasy of the Eastern Anatolia (Turkey) and discontinuities of its crust, Pure and Applied Geophysics, 168(5), pp.901-917, 2011.

[11]. O. Pamukçu, Z. Akçığ, M. Hisarlı and S. Tosun, Curie Point Depths and Heat Flow of Eastern Anatolia (Turkey), Energy Sources, Part A: Recovery, Utilization, and Environmental Effects, 36(24), pp.2699-2706, 2014.

[12]. O., Pamukçu, T. Gönenç, A.Y. Çirmik, Ş. Demirbaş and S. Tosun, Vertical And Horizantal Analysis Of Crustal Structure In Eastern Anatolia Region, Bulletin of the Mineral Research and Exploration, (151), 2015.

[13]. H.G. Miller and V. Singh, Potential field tilt: a new concept for location of potential filed sources, Journal of Applied Geophysics, 32, pp 213-217, 1994.

[14]. L. Cordell and V.J.S. Grauch, Mapping basement magnetization zones from aeromagnetic data in The San Juan Basin, New Mexico. In: W.J., Hinze, Ed., The utility of regional gravity and magnetic anomaly maps: Society Exploration Geophysics, Tulsa, Oklahoma, 181-197, 1985.

[15]. C. Wijns, C. Perez and P. Kowalczyk, Theta map: edge detection in magnetic data, Geophysics, 70(4), pp 39-43, 2005.

[16]. W.R. Roest, J. Verhoef and M. Pilkington, Magnetic interpretation using the 3-D analytic signal, Geophysics, 57(1), pp. 116-125, 1992.

[17]. G.R.J. Cooper and D.R. Cowan, Enhancing potential field data using filters based on the local phase, Computer and Geosciences, 32, pp 1585-1591, 2006.

[18]. R.J. Blakely, Potential theory in gravity and magnetic applications, Cambridge University Press, 1995.

[19]. V. Baranov, A new method for interpretation of aeromagnetic maps: Pseudo-gravimetric anomalies, Geophysics, 22, 359-383, 1957.

[20]. M.O. Arisoy and U. Dikmen, Potensoft: MATLAB-based software for potential field data processing, modeling and mapping. Computer and Geosciences, 37, 935-942, 2011.

[21]. MTA (Directorate of Mineral Research and Exploration, Turkey) 1979. Aeromagnetic Map of Eastern Turkey [unpublished].

[22]. URL: http://topex.ucsd.edu/cgi-bin/get_srtm30.cgi

[23]. N. Turkelli, E. Sandvol, E. Zor, R. Gok, T. Bekler, A. Al-Lazki, ... & S. Bayraktutan, Seismogenic zones in eastern Turkey. Geophysical Research Letters, 30(24), 2003.

Indoor Particle Size Distribution and Ionic Content of Particles in the Laboratory of ISTAC Composting Facility

Arslan Saral[1]*, S. Levent Kuzu[1], Şenol Yıldız[2]

[1]Yildiz Technical University, Department of Environmental Engineering, 34220, Esenler/İstanbul, Turkey.

[2]ISTAÇ AŞ, Paşa Mah., Piyalepaşa Bulvarı, No:74, Şişli/İstanbul, Turkey.

*Corresponding Author email: saral@yildiz.edu.tr

Publication Info

Abstract

Particulate matter can be generated through several processes. Formation processes determines the size distribution of the particles. The size distribution gives us important data about the fate of the particles. Composition of the particulate matter includes forensic about their actual sources. The aim of this study is to determine the impact of composting process to laboratory indoor air quality in close proximity to composting process. For this purpose, sampling was conducted at two different points; one of them wass inside the laboratory, whereas the other one was in the composting facility. A low volume cascade impactor was used to collect particulate matter according to their sizes. The impactor was operated for one week at each sampling point. Particles of 10 μm was dominant in the composting facility. The dominant particle size was 5.8 μm inside the laboratory. Particles were ultrasonically extracted in deionized water in order to determine ion concentrations. Ions were quantified in Dionex ICS-3000 ion chromatograph. Ca^{+2}, NH_4^+ and SO_4^{-2} were investigated. NH_4^+ and SO_4^{-2} had highest share in the finest size fraction at both laboratory and plant. Particles of 3.3 μm were enriched with Ca^{+2}. Biological decomposition products were effective in the ionic composition of the fine particles, whereas mechanically generated dusts formed the coarse particle fraction.

Key words

1. INTRODUCTION

Particles in ambient air is among the major pollutants. They referred in three maim groups, which are nuclei mode, accumulation mode, and coarse mode [1]. Nuclei mode are occurred from primary formed gasses, latter they are accumulated to form accumulation mode particles. Accumulation mode particles are usually regarded to be at the proximity of 1 μm aerodymamic size. The size with the highest size is referred as coarse mode. Particle sizes bigger than 2.5 μm are considered as coarse mode. The coarse mode particles are generated through mechanical formation. This formation can either be from industrial activities or from abrasion effect of the wind. Combustion and biological activities generate fine particles (particle diameter less than 2.5 μm). The data of particle size distribution is essential to know further insights of the particle sources. In many cases atmospheric particles exhibits bi-modal size distribution [2]. Apart from biological activities, biological sources could yield coarse particles [3].

Particles carry forensic from their actual sources. The chemical compositions of the particles can be used to distinguish their actual sources. There are several studies, in which the researchers investigated both particle distribution and its composition for source estimations [4]-[6]. In those references studies authors have made comments about the possible sources of the origins of the particles. Additionally, chemical composition data of the particles gives an idea of their probable effects.

Composition of the size segregated particles serves critical data about their sources. In this study, it was aimed to determine the sources of indoor particle, related to their sizes.

2. MATERIALS AND METHODS

2.1. Sampling

Sampling was conducted inside the laboratory of ISTAC AS composting facility. An additional sampling point was in the composting plant in order to differentiate the sources. There was one more plant nearby, which is producing brick. Map of the study area is shown in Figure 1.
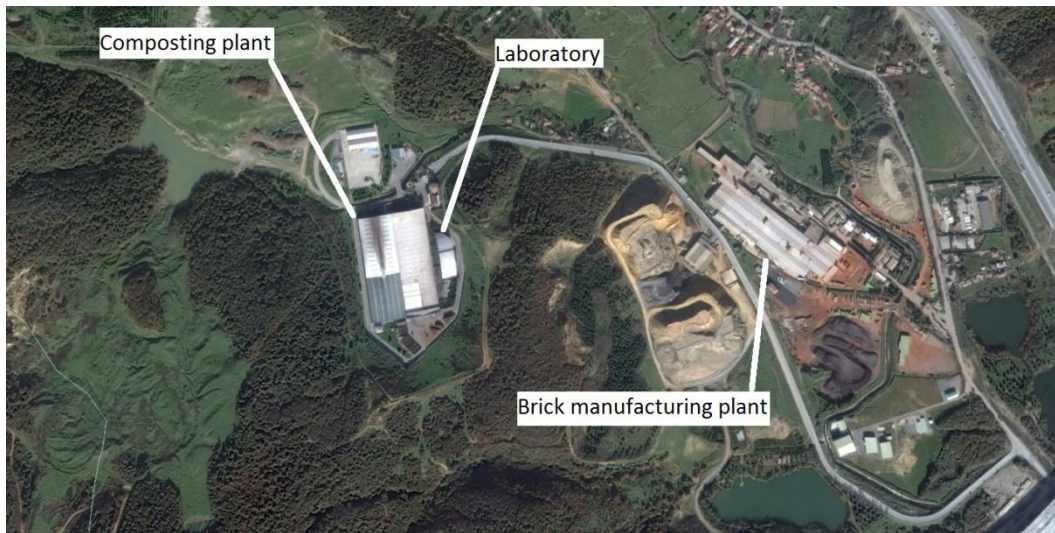
Figure 1. Study area

2.2. Sampling equipment

A low volume cascade impactor (LVCI) was used in the study to make the size segregation of the particles. LVCI was an eight-stage impactor, operated at 28.3 L/min air flow. The sampling at each point took one week in order to collect enough particle for the analyses of ions. This flowrate yielded the cut-off diameters given in Table 1.

Table 1. LVCI cut-off diameters

Stage no	Cut-off diameter (µm)
1	10
2	9
3	5.8
4	4.7
5	3.3
6	2.1
7	1.1
8	0.65

Stages of each diameter were weighed before and after the sampling in order to quantify particle mass at each stage. Further processing was applied for the determination of ions related to particles.

2.3. Sample preparation and quantification

Ionic species on the particles were eluted with deionized water [4]. 50 ml of water was used to collect all of the ions on the particles. The conductivity of the deionized water was 18.2 M.ohm.cm^{-1}. Prepared water samples were taken to vials for quantification in an ion chromatograph. The quantification results gives the concentrations in liquid medium in mg.L^{-1}. This concentration was multiplied with 50 mL to find the mass of ions at each stage.

3. RESULTS AND DISCUSSION

Particle sampling was performed inside the laboratory and plant environments with the LVCI. Particle size distribution data was gathered and source profile was investigated with the achieved particulate matter size data. The modal size distribution inside the laboratory was shown in Figure 2.
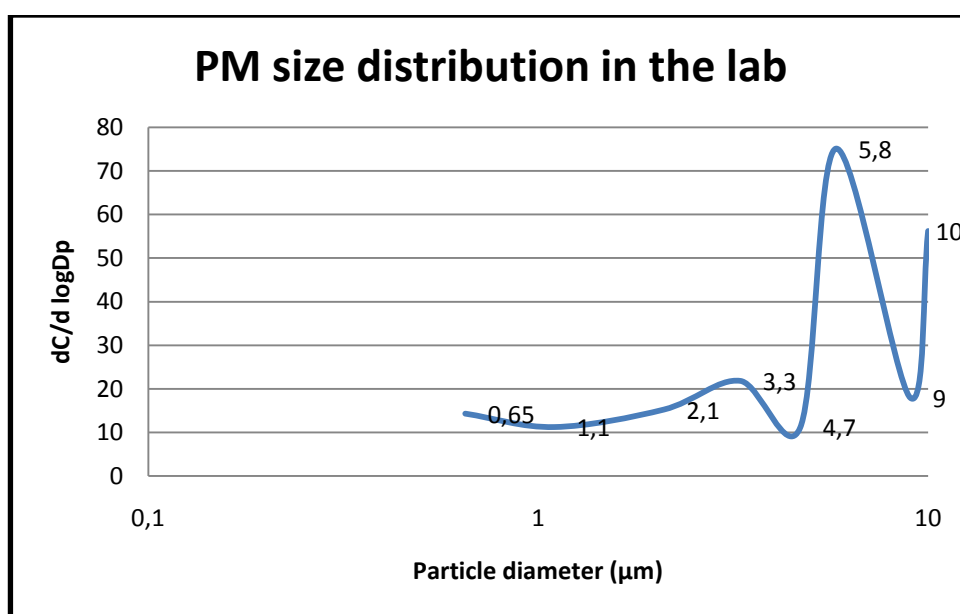

Figure 2. Particle size distribution inside the laboratory

Two peaks were observed. one of them wa at 5.8 μm, whereas the other one was at 3.3 μm. There was not an elevated trend below 1 μm particle size. It was thought that particles having diameter less than 1 μm is released from the plant. However, an additional sampling was required in order to verify this claim inside the plant. The particle size distribution inside the plant was shown in Figure 3.
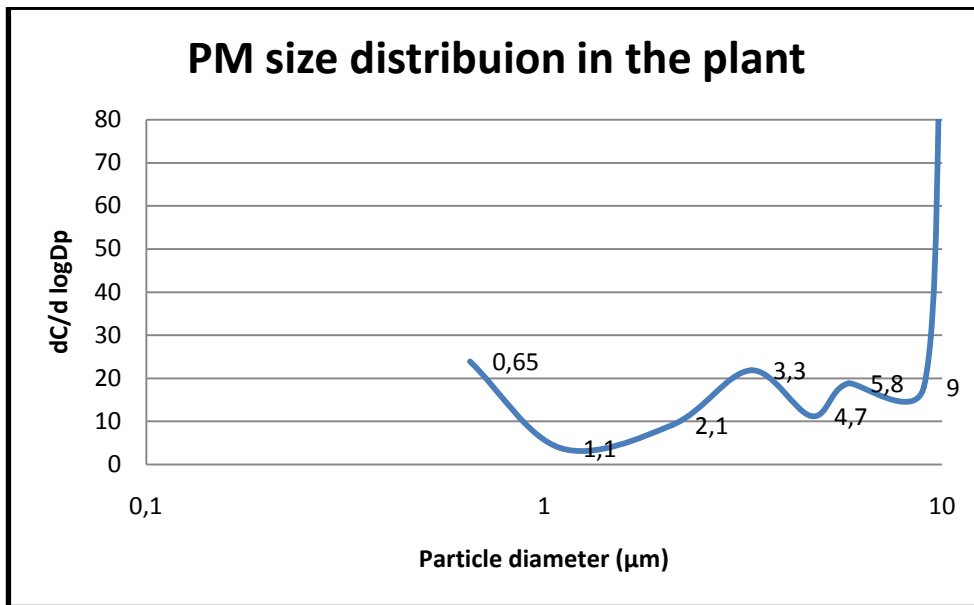
PM size distribuion in the plant

Figure 3. Particle size distribution inside the plant

In this case, there is an important increase below 1 μm particle size. This was the expected case in accordance with the nature of the process in the composting plant. Either of the samplings were shown in Figure 4 in order to make a comparison.
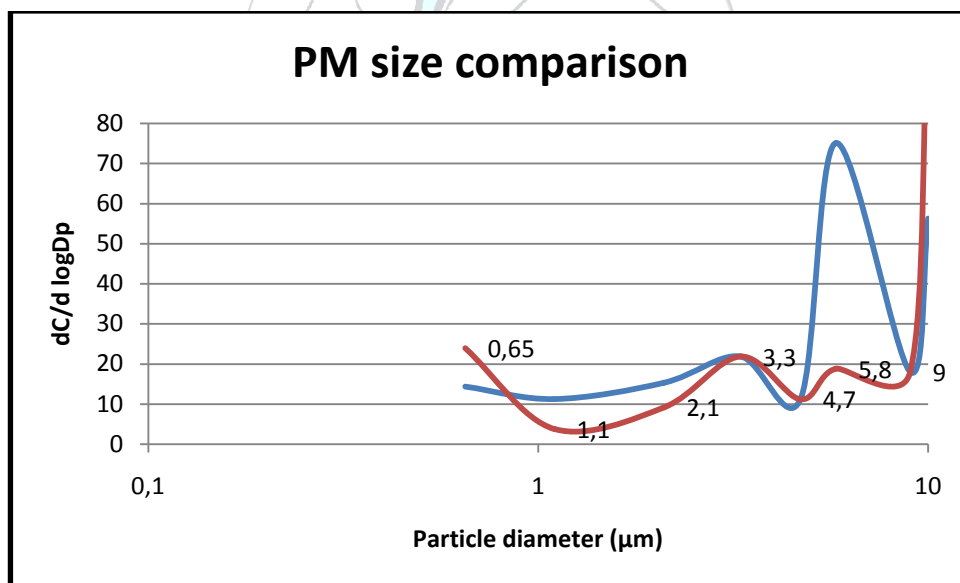
PM size comparison

Figure 4. Comparison of particle size distribution in the plant and the laboratory

The line with blue color shows the distribution inside the laboratory, whereas the line with red color shows the distribution inside the plant. It is observed that major and minor peaks were observed at the same stages in both of the cases. However, their dominancy were different from each other. This fact tells us that same source or sources affect the two sampling points. Further comments can be made according to compositional results.

Air conditioning system is present to supply air to laboratory. The air moving to the system is pre-filtered. However it is seen that particles of 5.8 μm was from the major fractions inside the lab. It can be inferred that this filtration system is not working properly to remove the coarse particles. Coarse particles are usually originated from naturally blown dusts. In order to clarify this point, Ca^{+2} ions were investigated.

The distribution of Ca^{+2} ions at each stage is given in Figure 5.
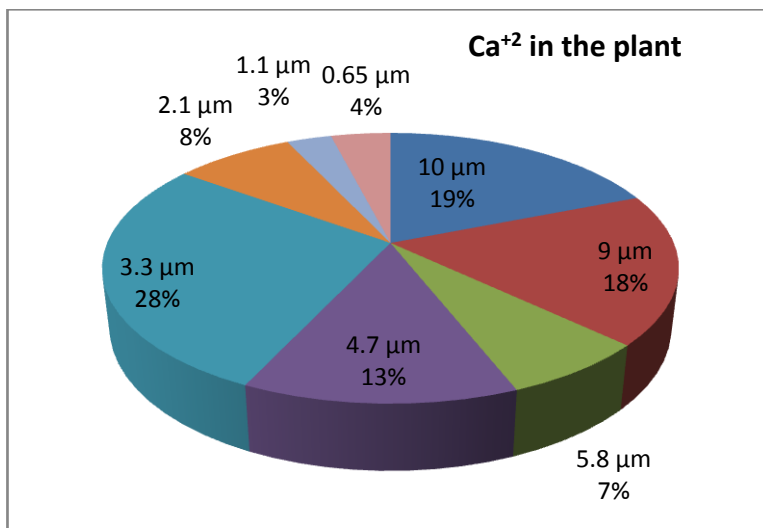
(a)
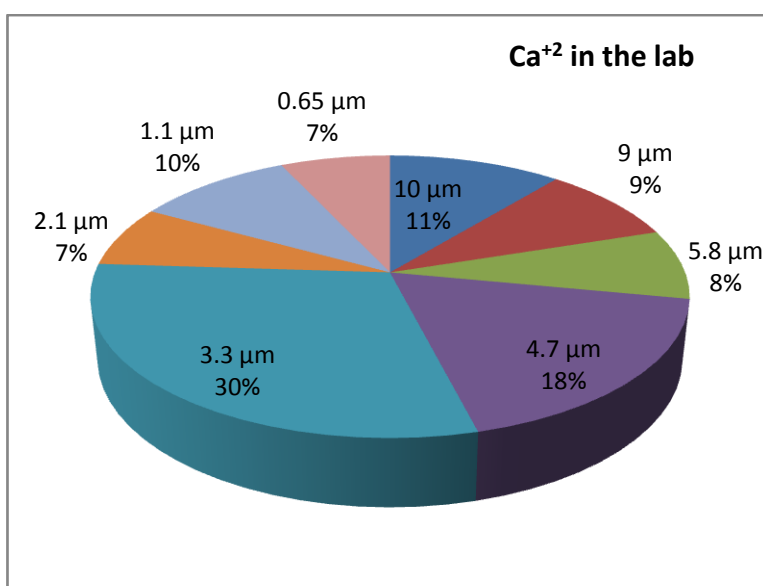
(b)

Figure 5. (a) Ca^{+2} distribution among different stages in plant (b) Ca^{+2} distribution among different stages in lab

Sodium, potassium, and magnesium ions were also quantified along with calcium ions. However there was no difference among the distribution of these species. So that, it was decided not to include them in the paper. Calcium was included as a representer to the major ionic group. Coarse particles were dominated with these ions. The previous comment during the particle size distribution, is verified according to these results.

Organic matter originated compounds such as sulfate and ammonium was enriched in the fine particle mode at both plant and the laboratory. Ammonium was solely in the fine fraction inside the plant, where dense biological activity occurs. Particles less than 0.65 μm had contribution over 80%. Distribution of the ammonium and sulfate ions among the particle sizes are shown in Figure 6.
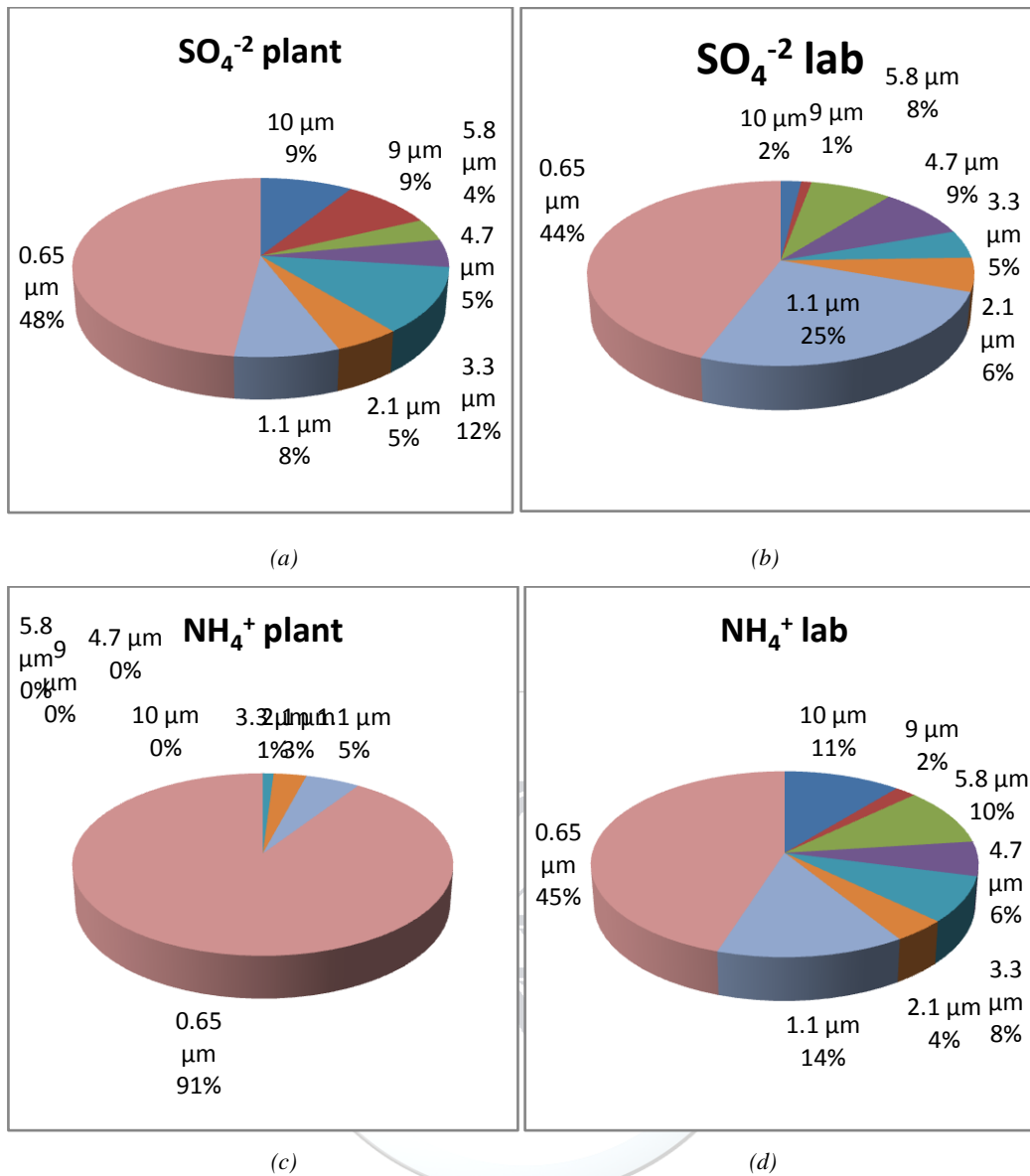
Figure 6. (a) SO_4^{-2} PM distribution in the plant (b) SO_4^{-2} PM distribution in the lab (c) NH_4^+ PM distribution in the plant d) NH_4^+ PM distribution in the plant

Accumulation particles, which are equal to or less than 1 μm, are occurred through the condensation of primary gasses and humidity in the air boost their formation. Sulfate ion can further lead to acidic aerosol forms. This can cause damage on laboratory devices. According to above results, it is inferred that air conditioning is not efficiently supplied.

4. CONCLUSIONS

In this study, air sampling was conducted at two locations; inside the laboratory and composting plant. Sampling was realized by LVCI. Particle size distributions in both of the sites were revealed. Particles of 3.3 μm mass median particle diameter were mostly enriched by calcium ion. This shows the contribution from resuspension of mineral dusts. The nearby brick factory could cause this contribution. Ammonium and sulfate ions were highly enriched in fine particles at both laboratory and composting plant. However, ammonia had much more contribution from the plant itself. Almost entire ammonium ions were below 1 μm. Sulfate content of indoor particles can lead to corrosion of laboratory devices. Some suggestions are listed below in order to improve the quality of indoor air inside the laboratory.

- HEPA filters should be used to improve the filtration capacity at the inlet of the fan system. Additional carbon fitler could reduce the organic content of the air and breakthrough tests should be performed to determine the capacity of carbon filters.

- Air fed to the conditioning system should be taken from the North or East of the laboratory in order to prevent direct contamination from composting process.
- Positive pressure should be present. So that, leaks from the outside air can be prevented.
- Sufficient circulation should be present with higher air fan power.
- Dehummidification of the indoor air is essential.
- Recirculation (close circuit system) should be present in the air conditioning system.

ACKNOWLEDGMENT

REFERENCES

[1]. K. T. Whitby, W. E. Clark, V.A. Marple, G.M. Sverdrup, G. J. Sem, K. Willeke, B. Y. H. Liu, D.Y.H. Pui, " Characterization of California aerosols—I. Size distributions of freeway aerosol", *Atmos Environ.*, vol. 9, pp. 463–482, 1975

[2]. L. Morawska, S. Thomas, M. Jamriska, G. Johnson, "The modality of particle size distributions of environmental aerosols", *Atmos Environ,* vol. 33, pp. 4401–4411, 1999

[3]. J. H. Seinfeld and S. N. Pandis, *Atmospheric Chemistry and Physics: from air pollution to climate change*, 2nd ed., Berlin, USA: Wiley, 2006.

[4]. S. L. Kuzu, A. Saral, S. Demir, G. Summak, G. Demir, "A detailed investigation of ambient aerosol compositions and size distribution in an urban atmosphere", *Environ Sci Pol Res*, vol. 20, pp. 2556-2568, 2013

[5]. Ü. Alver Şahin, K. Scherbakova, B. Onat, "Size distribution and seasonal variation of airborne particulate matter in five areas in Istanbul, Turkey", *Environ Sci Pol Res*, vol. 19, pp. 1198-1209, 2012

[6]. B. Onat, Ü. Alver Şahin, C. Bayat, "Assessment of particulate matter in the urban atmosphere: size distribıtion, metal composition and source characterization using principal component analysis", *J. Environ Mon.*, vol.14, pp. 1400-1409, 2012
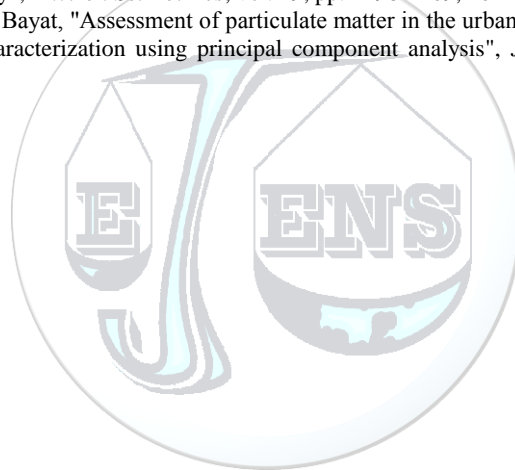
Odorous Volatile Organic Compounds Determined Inside the ISTAC Landfilling Facility and Places at Close Vicinity by Passive Air Sampling Method

Arslan Saral[1]*, S. Levent Kuzu[1], Şenol Yıldız[2]

[1]Yildiz Technical University, Department of Environmental Engineering, 34220, Esenler/İstanbul, Turkey.

[2]ISTAÇ AŞ, Paşa Mah., Piyalepaşa Bulvarı, No:74, Şişli/İstanbul, Turkey.

*Corresponding Author email: saral@yildiz.edu.tr

Abstract

Volatile organic compounds (VOCs) attract the attention of the authorities due to their detrimental effects on environmental and human health. People are exposed to odor problems, which live in close vicinity of the emission sources. This is the most obvious effect of these emissions. In order to manage and control the emissions, released compounds at least should be monitored at source and receptor points. So that, source contributions can be evaluated. Landfilling is the most frequent method used in Turkey to manage and dispose the solid wastes. Although, engineering methods during and after the landfilling process minimizes the undesired effects of the wastes in the environment, odorous compounds released to the atmosphere still remains as a serious problem. Especially, people living in the surrounding residential areas are the most vulnerable ones. Sampling was conducted in the European side of Istanbul. Sampling points were selected to be inside the landfilling facility and residential areas where are reported to be exposed to odor from landfilling activity. Passive sampling method was used in this study. Sample tubes were placed in the area at least for ten days. Then, these tubes were brought to laboratory for further processing and quantification. VOC species were detected and quantified by GC-MS. Total VOC concentrations were ranged between 50 and 850 ppm. The VOC species with the highest concentrations were m&p xylene, 1,2,4-trimethybenzene, 1,4-diethylbenzene, n-decane, n-undecane. Concentrations observed in summer were considerably higher than in winter. The highest concentrations were observed in active landfilling lot, leachate waste water collection tank and composting facility.

1. INTRODUCTION

Investigation of volatile organic compounds (VOCs) are of scientific interest nowadays due to their toxic, carcinogen, and their odor effects [1],[2]. Long time exposure to benzene, toluene, xylene, and chlorinated compounds could yield health problems on landfilling operators [3]. Odor is occurred when insufficient oxygen is present during the decomposition of solid wastes [4]. There are some studis on the composition of landfilling gasses. In Turkey, characterization study was conducted in Izmir Harmandali landfilling area [5]. Diverse types of VOCs were identified in that study. The identified VOCs were monoaromatics, halogenated compounds, aldehydes, esters, ketones, sulfur/nitrogen containing compounds, volatile fatty acids. The main problem of these organic types are their annoying odor in urban areas [6].

The main goal of this study is to determine the VOC levels inside the landfilling facility area and in the residential zones close to the landfilling area, where people living in those areas are usually get annoyed. Finally, spatial distribution of VOCs were determined.

2. MATERIALS AND METHODS

2.1. Study Area

Landfilling facility in the European side of Istanbul is located in Kemerburgaz-Odayeri. This location is to the north of residential area of Istanbul. The prevailing wind direction in Istanbul is north-easterly. For that reason, the sampling points, apart from waste processing facilities, were selected to be the residential sites to the south of the facility. Sampling points are shown in Figure 1.
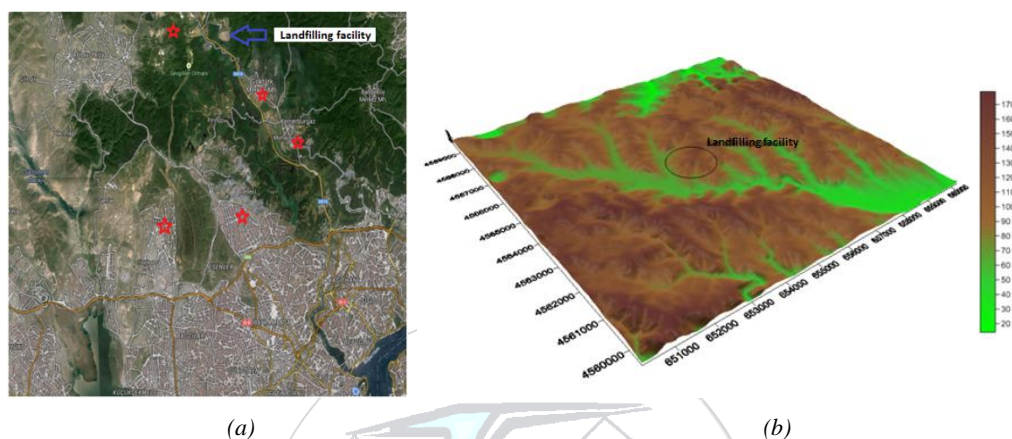

(a)   *(b)*

Figure 1. (a) Map of the study area (b) Geographical properties of the study area (elevation in meters)

The red stars are the residential sites distributed in the sampling train. Geographic properties and meteorological conditions have big importance on the dispersion of the pollutants released from landfilling activities. The map showing the geographical properties of the study area in 10 km x 10km dimensions.

Meteorological data were gathered from Davis Vantage Pro-2 weather station present in Odayeri landfilling facility.

2.2. Sampling Method

The sampling was not in a single point. On the contrary, there were many sampling points distributed within a large area. So that, passive sampling method was selected. It is easy to handle passive sampling and a common method when there is large number of sampling points [7]. Sampling pump is not used so operation is cheaper than active sampling [8].

Passive sampling tubes were filled with 100 mg Carbopack-B adsorbent material and closed with fine mesh at both edges of the tube. Dept of the mesh was 1.5 cm from the edge. These tubes were delivered to the sampling location inside a falcon tubes. They were closed with telfon lids when sampling was finished and returned to the laboratory again in the falcon tubes. Sampling dates are given in Table 1.

Table 1. Sampling dates

Sampling no	Start date	Finish date
1	03.12.2014	17.12.2014
2	15.01.2015	04.02.2015
3	03.03.2015	19.03.2015
4	20.04.2015	05.05.2015
5	02.06.2015	17.06.2015

6	31.07.2015	21.08.2015
7	17.09.2015	15.09.2015
8	26.10.2015	06.11.2015
9	26.11.2015	11.12.2015

Some photos taken from the field studies are shown in Figure 2. Blank samples were taken along with the original samples in order to make quality assurance/quality control tests.
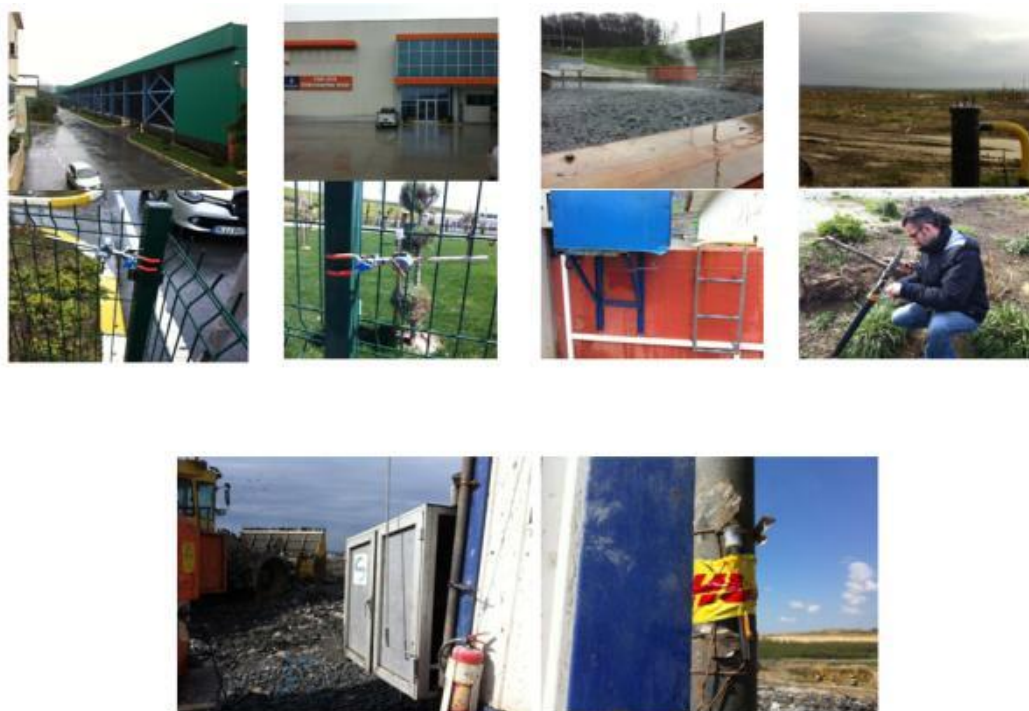

Figure 2.Pictures from field sampling studies

2.3. Sample Preparation

VOCs were adsorbed to adsorbent material at the sampling points. Their desorption was made by solvent extraction. Methanol was selected as the solvent. Chemical desorption process was realized inside the falcon tubes. Meshes of the tubes were removed and adsorbent material were poured in the falcon tubes. 2 ml of methanol was included inside the falcon tube. Then, falcon tubes were placed inside an ultrasonic bath and samples were ultrasonically extracted for 30 minutes. At the outset of each extraction, surrogate standards were included to find the recovery. After that, samples were placed into vials for gas chromatography (GC) analysis.

2.4. Gas Chromatography Analysis

Analyses were performed by Perkin-Elmer GC-MS system. The column was HP-5MS (30 m, 0.25 um, 0.25 id). Sample injection volume was 1 ml. Splitless injection was selected. Carrier gas was ultra pure helium, having pressure of 20 psi. Injector port temperature was kept at 240 ^{o}C. The oven was held 5 min at 35 ^{o}C, then temperature was raised to 110 ^{o}C at a rate of 5 ^{o}C/min. The oven was held at 110 ^{o}C for 2 min. After that, oven temperature was raised to 200 ^{o}C, at a rate of 40 ^{o}C/min. Finally, temperature was increased to 220 ^{o}C and waited there for 2 min. Total run time was 26.25 min.

In order to quantify the compounds 18 masses were investigated at two channels, which were 42, 43, 55, 57, 67 ,69, 71, 78, 83, 84, 85, 91, 92, 93, 98, 104, 105, 119. Forty different VOCs were targeted with these masses. However, 17 VOCs were regularly quantified. These species were: m-xylene, p-xylene, styrene, propylbenzene, n-decane, isopropylbenzene, alpha-

pinene, beta-pinene, propylbenzene, 3,4-ethyltoluene, 1,3,5-trimethylbenzene, 1,2,4-trimethylbenzene, 1,2,3-trimethylbenzene, 2-ethyltoluene, 1,3-diethylbenzene, n-undecane.

2.5. Gas Chromatography Analysis

Blank samples were analyzed as with regular samples. Limit of detection (LOD) was calculated according to blank samples. LOD was calculated as : mean blank sample concentration plus three times of the standard deviation of the blank samples. o-xylene were used as the surrogate standard. Its average recovery efficiency was 53±11%

2.6. Calculation of the Concentrations

Concentration of VOCs were determined in liquid phase. Total air flowrate need to be known in order to find atmospheric concentrations. As the sampling was passive type, it is not accurately possible to find actual flowrate. VOCs accumulated inside the adsorbent by diffusion. Equation 1 and equation 2 are used to calculate ambient air concentrations.

$$Uptake\ rate = \frac{D\left(\frac{cm^2}{sec}\right) x A (cm^2)}{L (cm)} \tag{1}$$

$$Atmospheric\ concentration\ (ppm) = \frac{M_a (mg)}{upta\ ke\ rate\left(\frac{ng}{ppm\ \ x\ min}\right) x\ t\ (min)} \tag{2}$$

where, D is the diffusion coefficient for each VOC type, A is the cross sectional area of the sampling tube, L is the distance between the mesh and the edge of the tube, Ma is the molecular weight of the VOC in concern, and t is the sampling time.

3. RESULTS AND DISCUSSION

The result of each sampling period was shown with the spatial distribution and wind rose acquired for each sampling period. The time spent in the field for sampling no 7 was prolonged and consequently they reached to saturation. The values results for sampling no 7 was not reported for that reason. Spatial distribution of sampling no 1 is given in Figure 3.
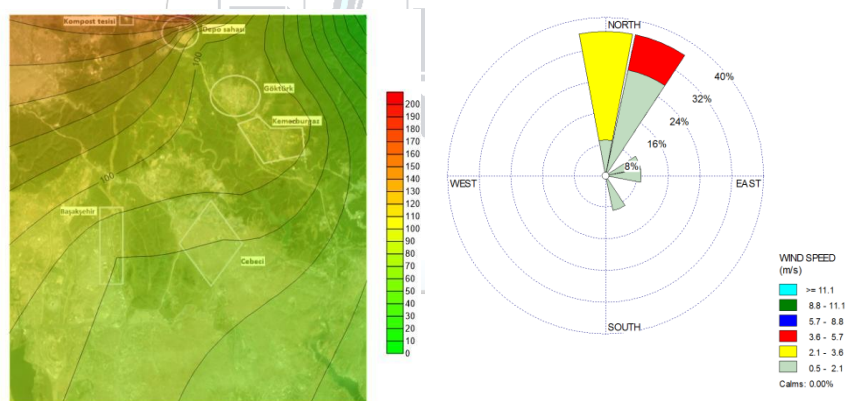

Figure 3.Sampling results of sampling no 1

Prevailing wind direction was N-NE. Wind speed was mostly below 3.6 m/sec. The highest concentration was 200 ppm. The location of the highest concentration was landfilling area. The three highest concentrations in residential areas were 90 ppm, 80 ppm, and 70 ppm for Kemerburgaz, Başakşehir, and Cebeci, respectively.

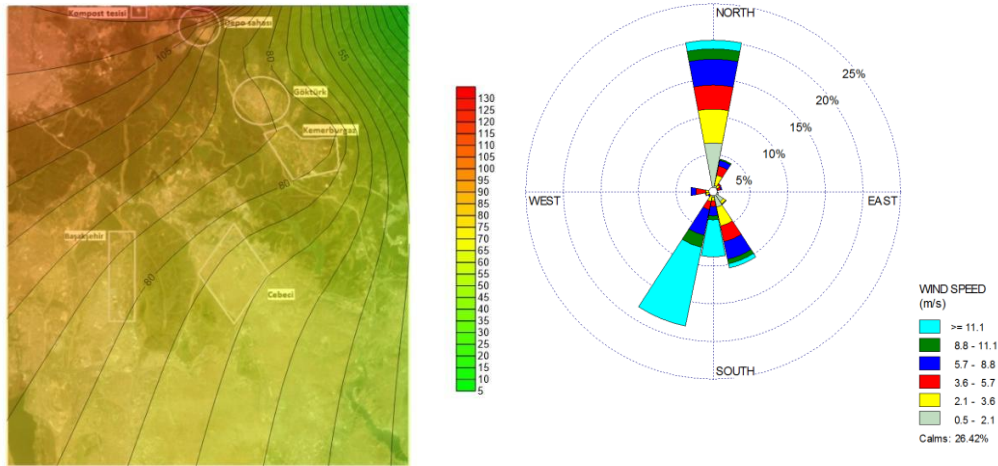Spatial distribution of sampling no 2 is given in Figure 4.

Figure 4. Sampling results of sampling no 2

Prevailing wind direction was N-SW. Wind speed was mostly above 11.1 m/sec. The wind speed was less than 0.5 m/sec during 26% of the whole sampling time. The highest concentration was 130 ppm. The location of the highest concentration was landfilling area. The three highest concentrations in residential areas were 80 ppm, for Kemerburgaz, Başakşehir, and Cebeci. It was 60 ppm in Cebeci.

Spatial distribution of sampling no 3 is given in Figure 5.

Figure 5. Sampling results of sampling no 3

Prevailing wind direction was N. Wind speed was mostly between 5.7-8.8 m/sec. The wind speed was less than 0.5 m/sec during 27% of the whole sampling time. The highest concentration was 50 ppm. The location of the highest concentration was landfilling area. The two highest concentrations in residential areas were 50 ppm for Başakşehir, and Cebeci.

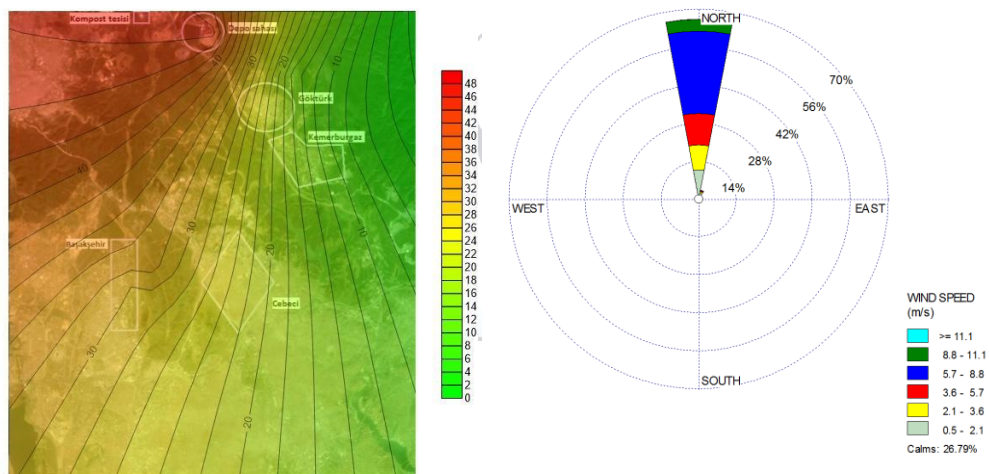Spatial distribution of sampling no 4 is given in Figure 6.

Figure 6. Sampling results of sampling no 4

Prevailing wind direction was S-SSW-NNE. Wind speed was mostly between 5.7-8.8 m/sec. The wind speed was less than 0.5 m/sec during 6% of the whole sampling time. The highest concentration was 56 ppm. The location of the highest concentration was landfilling area. The highest concentrations in residential areas were 5 ppm Göktürk, Kemerburgaz, Başakşehir, and Cebeci.

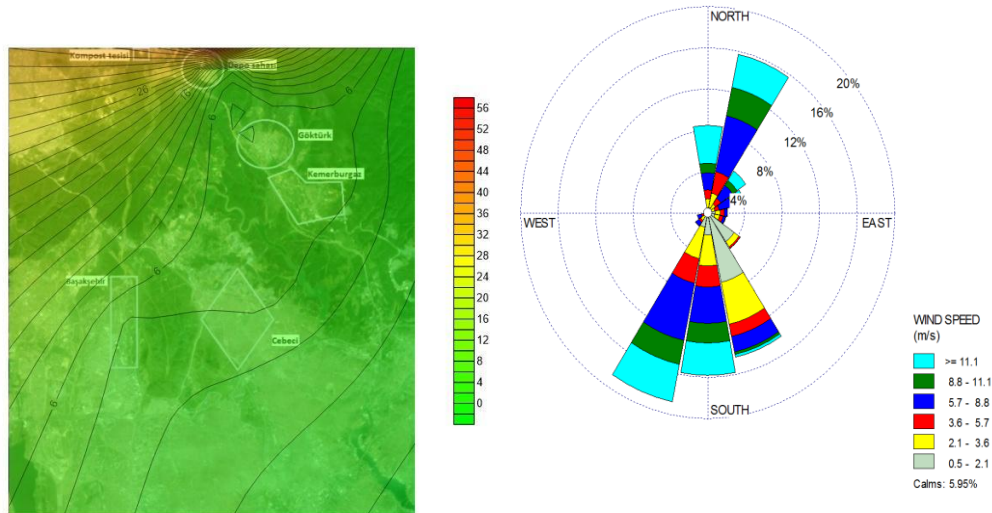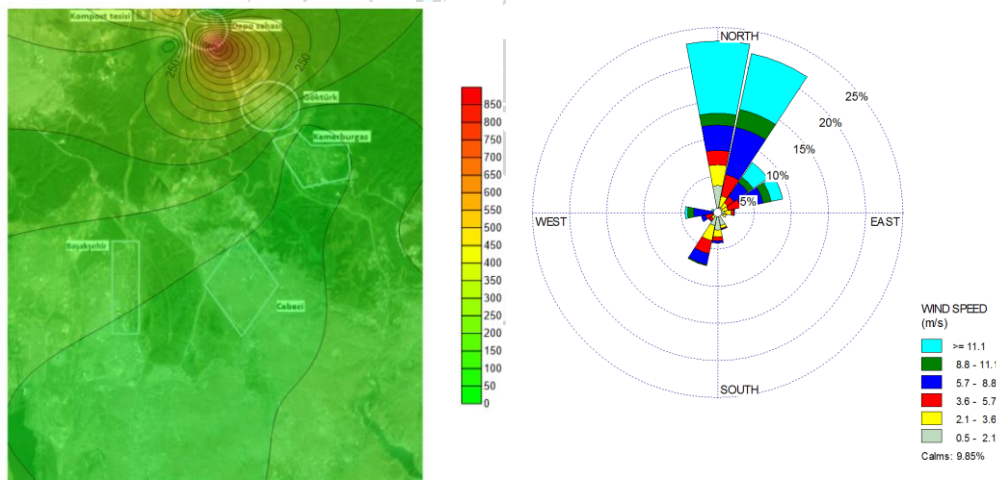Spatial distribution of sampling no 5 is given in Figure 7.

Figure 7. Sampling results of sampling no 5

Prevailing wind direction was N. Wind speed was mostly above 11.1 m/sec. The wind speed was less than 0.5 m/sec during 10% of the whole sampling time. The highest concentration was 850 ppm. The location of the highest concentration was landfilling area. Half of this concentration was observed from the composting facility. The highest concentrations in residential areas were between 50 and 100 ppm at Kemerburgaz, Başakşehir, and Cebeci'.

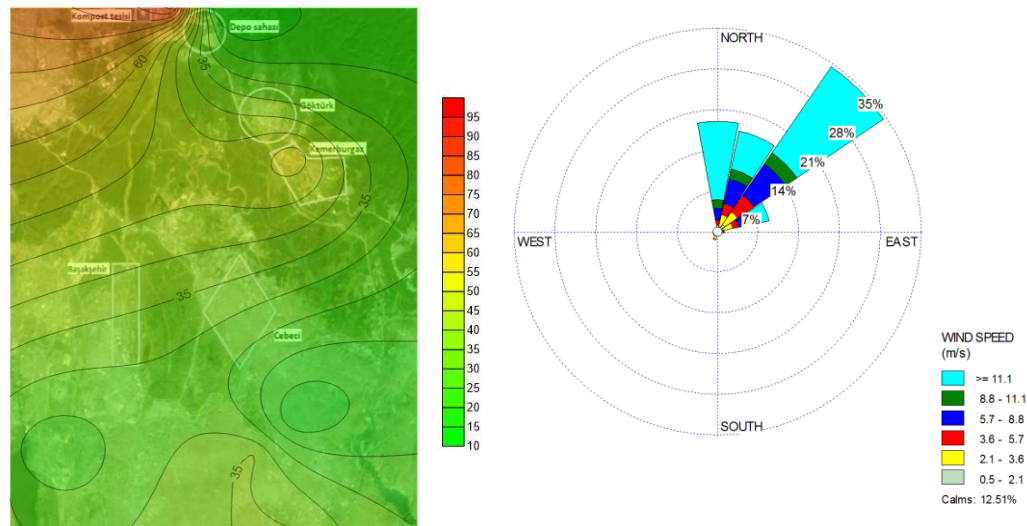Spatial distribution of sampling no 6 is given in Figure 8.

Figure 8. Sampling results of sampling no 6

Prevailing wind direction was N. Wind speed was mostly above 11.1 m/sec. The wind speed was less than 0.5 m/sec during 12% of the whole sampling time. The highest concentration was 100 ppm. The location of the highest concentration was the composting facility. VOC concentration was 60 ppm at the landfilling site. The highest concentration in residential areas was observed in Kemerburgaz as 45 ppm. The concentration was 35 ppm at between 50 and 100 ppm at Göktürk, Başakşehir, and Cebeci.

Spatial distribution of sampling no 8 is given in Figure 9.

Figure 9. Sampling results of sampling no 8

Prevailing wind direction was N. Wind speed was mostly above 11.1 m/sec. The wind speed was less than 0.5 m/sec during 3% of the whole sampling time. The highest concentration was 130 ppm. The location of the highest concentration was the composting facility. VOC concentration was 45 ppm at the landfilling site. The highest concentrations in residential areas were between 35 and 50 ppm in Kemerburgaz.

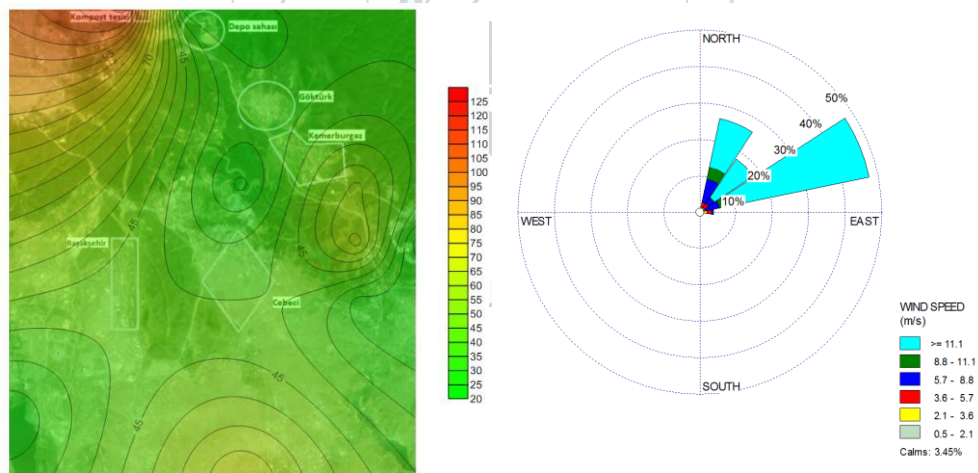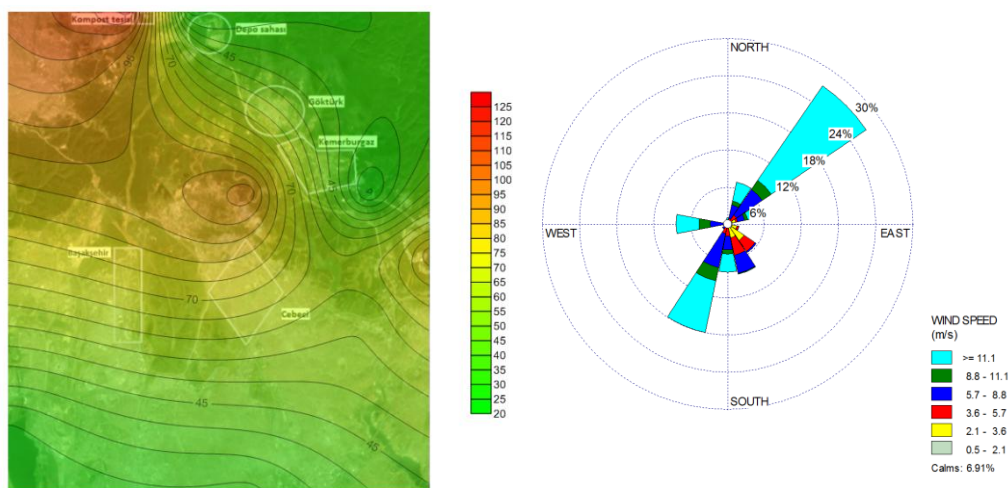Spatial distribution of sampling no 9 is given in Figure 10.

Figure 10. Sampling results of sampling no 9

Prevailing wind direction was N. Wind speed was mostly above 11.1 m/sec. The wind speed was less than 0.5 m/sec during 26% of the whole sampling time. The highest concentration was 300 ppm. The location of the highest concentration was the composting facility. The concentrations were at the same levels for the remaining places.

4. CONCLUSIONS

In this study, VOC concentrations at the waste management facilities were measured and to see their effect on residential sites, sampling was conducted at some specific residential. The highest concentrations were encountered mostly in landfilling area. The highest concentration was 850 ppm However, the variability was very high. Usually half of the VOC concentrations were present in residential areas. The main sources were landfilling, composting, and leachate collection tank. It is suggested to control the emissions from these sources. Daily soil can be laid in order to prevent volatilization of VOCs from landfill and operation can be made within small scale lots. Top of the leachate collection tank could be closed and emissions can be treated in a further step. The emissions of composting facility is treated by a biofilter. However, the treatment process is not working efficiently. It is suggested to revise and modify this system to control the VOCs.

ACKNOWLEDGMENT

REFERENCES

[1]. A. Saral, S. Demir, and Ş. Yıldız, "Assessment of odorous UOBs released from a main MSW landfill site in Istanbul-Turkey via a modelling approach", *J Haz Mat*, vol 168, pp 338-345, 2009.

[2]. M. A. Parra, D. Elustondo, R. Bermejo, and J. M. Santamaria, " Exposure to volatile organic compounds (UOB) in public buses of Pamplona, Northern Spain ", *Sci Tot Environ*, vol 404, pp 18-25, 2008.

[3]. S. C. Zou, S. C. Lee, C. Y. Chan, K. F. Ho, X. M. Wang, L. Y. Chan, and Z. X. Zhang, "Characterization of ambient volatile organic compounds at a landfill site in Guangzhou, South China", *Chemosphere*, vol. 51, pp. 1015-1022, 2003.

[4]. Q. Liu, M. Li, R. Chen, Z. Li, G. Qian, T. An, and J. Fu, "Biofiltration treatment of odors from municipal solid waste treatment plants", *Waste Management*, vol. 29, pp. 2051-2058, 2009.

[5]. F. Dinçer, M. Odabaşı and A. Muezzinoğlu, "Chemical characterization of odorous gases at a landfill site by gas chromatography-mass spectrometry", *J Chrom A*, vol 1122, pp. 222-229, 2006.

[6]. A. Muezzinoglu, "A study of volatile organic sulfur emissions causing urban odors", *Chemosphere*, vol. 51, pp. 245-252, 2003.

[7]. F. Karaca, "Istanbul'un tarihi yarımadasında yüzey yayılım profilinin araştırılması", *Hava Kirliliği Araştırmaları Dergisi*, vol. 1, pp. 53-65, 2012.

[8]. E. Woolfenden, "Sorbent-based sampling methods for volatile and semi-volatile organic compounds in air Part 1: Sorbent-based air monitoring options", *J Chrom A*, vol. 1217, pp. 2674-2684, 2010.

Deep Sea Outfall of Natural Gas Fired Combined Cycle Power Plant Cooling Water Application and Modeling

Tolga Ayeri[1]*, Yüksel Ardali[1]

[1]*Ondokuz Mayis University, Department of Environmental Engineering, 55139, Atakum/Samsun, Turkey.*

*Corresponding Author email: tolga.ayeri@omu.edu.tr

Abstract

Combined Cycle Power Plants are in wide demand throughout the world, because they are characterized by short construction times, low investment costs, high operating efficiencies and low exhaust emissions. This type of power plants can reach fuel to electricity conversion efficiencies of 60%, at the same time it has minimal environmental impacts. The most important reason for this is the use of natural gas, which is a very clean fuel containing little or no sulfur, particulate matter and other unwanted ingredients. This study was investigated the effect of cooling water from natural gas combined power plant to Black Sea region of Turkey. The parameters, which affect the marine ecosystem, were determined and in addition temperature, suspended solid, COD values were measured. Modelling of these measured values was performed throughout discharge line with the CORMIX-2 software developed by EPA (Environmental Protection Agency) as environmentally purpose.

1. INTRODUCTION

Energy is what drives our lives. There is an ongoing global energy challenge caused by increasing energy demand, heavy dependence on oil and other fossil fuels which leads to air, water and land pollution. Large carbon emissions lead to global warming, climate instability and raises health concerns over pollution. Depletion of the fossil resources that are not uniformly distributed globally force the humanity to use the available precious energy resources as efficiently as possible [1].

Electricity power generation industry being the most important energy sector in many countries faces real problems; the continuous increase in fuel prices, exploding growth in energy demand, the recent strict environmental regulations and the severe competition after the liberalization of the energy market. As a result, power generation authorities seek performance improvements of the power plants. Operating more efficiently is important for the power plants to be able to compete in the deregulated energy market [2].
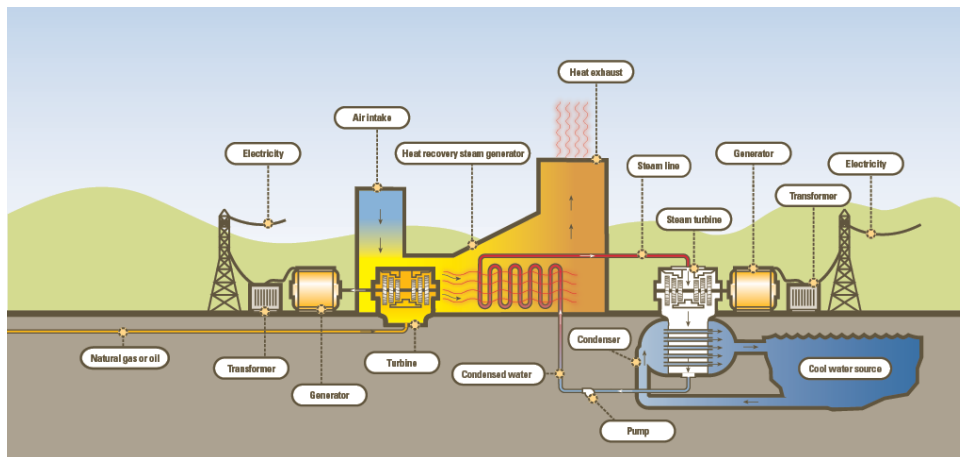
Figure 1. Combined Cycle Power Plants

Gas turbine performance has been enhanced considerably in recent years due to the rapid development of component design and material technologies. Many applied power generation systems based on the gas turbine have been proposed, and several systems have already been applied in real settings. The gas/steam combined cycle plant, for instance, has already emerged as a standard technology for base load power generation [3].

Combined Cycle Power Plants utilize both gas turbines and steam turbines to generate electricity. In a combined cycle power plant, the gas turbine is coupled to a generator to allow it to produce electricity even it runs solo without a steam turbine. As the exhaust stream of the gas turbine has high energy, the gas turbine exhaust is connected to a heat recovery steam generator (HRSG) where steam is produced from the waste heat in the exhaust gas. The generated steam is used to turn the steam turbine that produces more electricity in addition to the simple gas turbine cycle. The steam turbine is connected to a condenser where the excess heat is rejected to the environment. This equipment's are the main components of a combined cycle power plant. These are also the components which determine and dominate the performance of a power plant. Apart from these main components, there are many auxiliary systems such as cooling systems, lubrication systems, pumps etc. in a combined cycle power plant [4].

2. MATERIALS AND METHODS

2.1 Study Area

The Black Sea, with its world's largest anoxic basin, is situated between the folded Alpine belts of the Caucasus and Crimea Mountains to the north and northeast, and the North Anatolian Mountains to the south, with an area of 432,000 km^2 and a volume of 534,000 km^3. The Strait of Bosporus connects the Black Sea to the Sea of Marmara to the south and southwest, which in turn, is connected to the Aegean Sea and the Mediterranean Sea through the Strait of Dardanelles. [5].

Figure 2. Locations of Black Sea

The Black Sea's catchment area which covers entirely or partially 22 countries in Europe and Asia Minor is more than 2 million km^2. Six of these countries are littoral (Bulgaria, Georgia, Romania, the Russian Federation, Turkey and Ukraine), while the other sixteen (Albania, Austria, Belarus, Bosnia-Herzegovovina, Crotia, the Czech Republic, Germany, Hungary, Italy, Macedonia, Moldova, Poland, Slovakia, Slovenia, Switzerland and Yugoslavia) do not have shorelines with the Black Sea.

The length of the Black Sea shoreline is 4,340 km approximately. The Bulgarian coastline is 300 km long; the Georgian coastline 310 km; the Romanian coastline 225 km; the Russian coastline 475 km; the Turkish coastline 1,400 km and the Ukrainian coastline 1,628 km. The Black Sea shoreline is not ragged. There are several big or small peninsulas and bays through the shoreline, but no large islands are present. The largest peninsula is Crimea, located in the north. The largest bays are, Odessa Gulf, Yagorliksky Bay, Tendrovsky Bay, Karkinitsky Bay and Kalamitsky Bay in the north; Novorossiysk Bay in the east; Sinop Bay and Samsun Bay in the south; and bays of Igneada, Burgaz and Varna in the west. The biggest island is Zmeiny (1.5 km^2), located in front of the Danube delta [6].

2.2 Sampling and Analytical Methods

Water samples were taken in the summer and autumn 2016. Temperature (^{0}C), dissolved oxygen (DO), pH and electrical conductivity (EC) were measured on site using a field multi-probe (HQ40d Portable). Chemical oxygen demand (COD) and suspended solid were measured according to Standard Methods for the Examination of Water and Wastewater (APHA 1995). Water quality parameters were assessed accordingly Turkish Water Pollution Regulation (Table 1).

Table 1. Monitoring results of water quality parameters and the limit values (Turkish Water Pollution Control Regulation)

Parameters	Limit Value	Summer	Autumn
pH	6-9	7.92	8.72
Temperature	35 ˚C	19.3	24.8
Suspended Solid (mg/L)	350	2800	646
COD (mg/L)	400	990	79
Dissolved Oxygen (mg/L)	-	9.78	8.93
Electrical Conductivity (µS/cm)	-	26.6	29

2.3 Model Description

CORMIX is a USEPA-approved simulation and decision support system for environmental impact assessment of mixing zones resulting from point source discharges. The methodology contains systems to model submerged single-port (CORMIX1) and multiport diffusers (CORMIX2) as well as surface discharge sources (CORMIX3). Effluents considered may be conservative, non-conservative, heated, or they may contain suspended sediments. The advanced information system tools described herein provide documented water quality modeling, regulatory decision support, mixing zone visualization, and tools for outfall specification and design optimization [7].

3. **RESULTS AND DISCUSSION**

The surface water quality parameters were given in Table 1. The pH of the water samples was within the range of 6.5–9. Also temperature values less than 35 ˚C degrees. The highest values of chemical oxygen demand (COD) were observed in the summer with 990 mg/L (Fig 3). Suspended solid is much higher than limit values both summer and autumn (Fig 4).
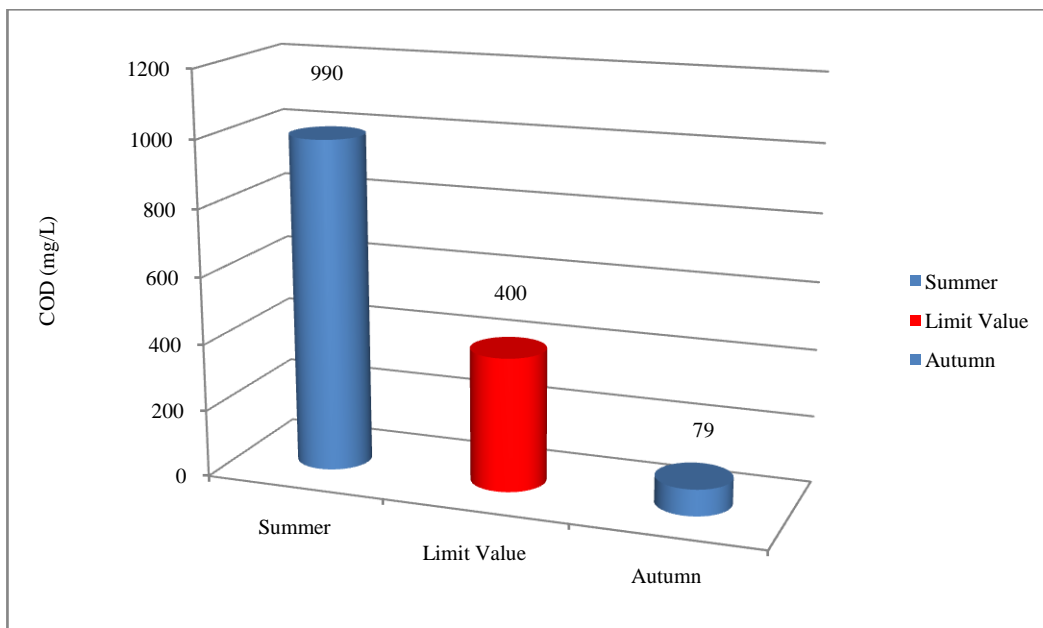
Figure 3. The comparison with the limit values for chemical oxygen demand of monitoring results
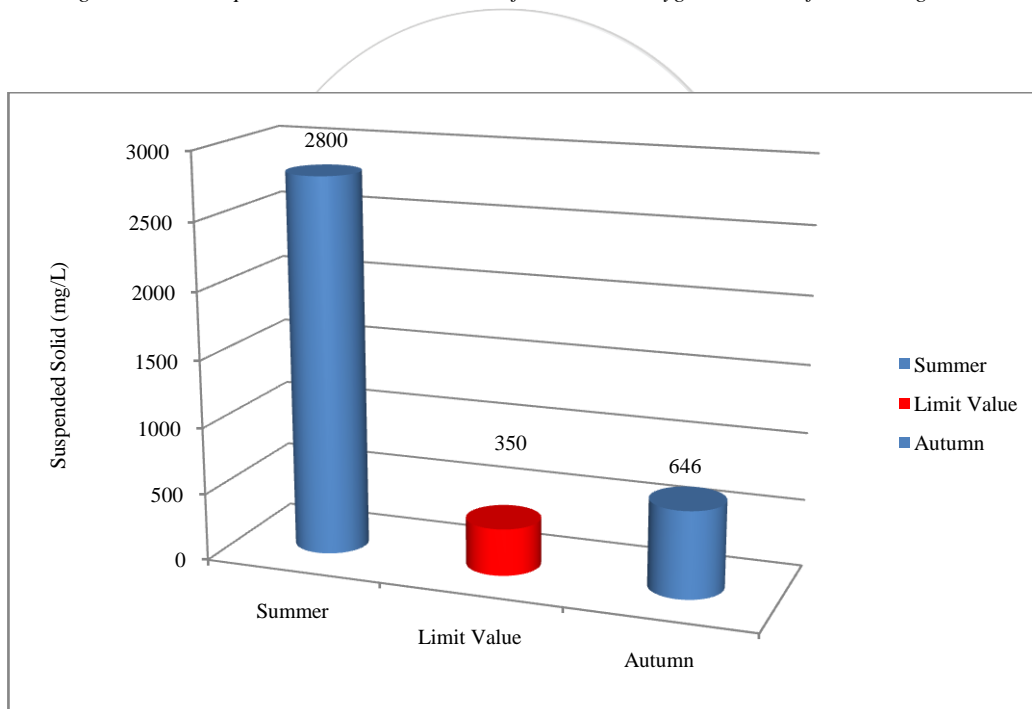
Figure 4. The comparison with the limit values for suspended solids of monitoring results

The electrical conductivity of the water samples was 26.6 and 29 (µS/cm), respectively. There were no boundary values of the electrical conductivity and dissolved oxygen according to Turkish Water Pollution Regulation. In addition, temperature values have to be one centigrade degree between ambient temperature and hot water discharge in accordance with Turkish Water Pollution Regulation. In order to determine the temperature difference was used Cormix2 model. Before mixing with the hot water into the sea, 9 °C degrees temperature difference was observed between ambient temperature and hot water discharge.

The green line in the Figure 5 shows that one degree of difference between ambient temperature and hot water discharge. It indicates that 1 °C temperature difference value is seen that at 10 m. Isometric view of hot water discharge was revealed using Cormix2 (Fig 6). Figure 6 were presented as the change in color code discharged wastewater temperature.
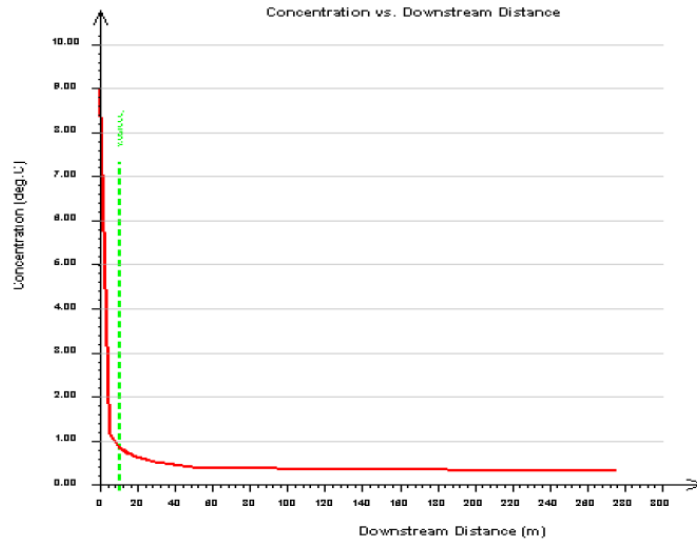
Figure 5. The difference graph between the ambient temperature and hot water discharge
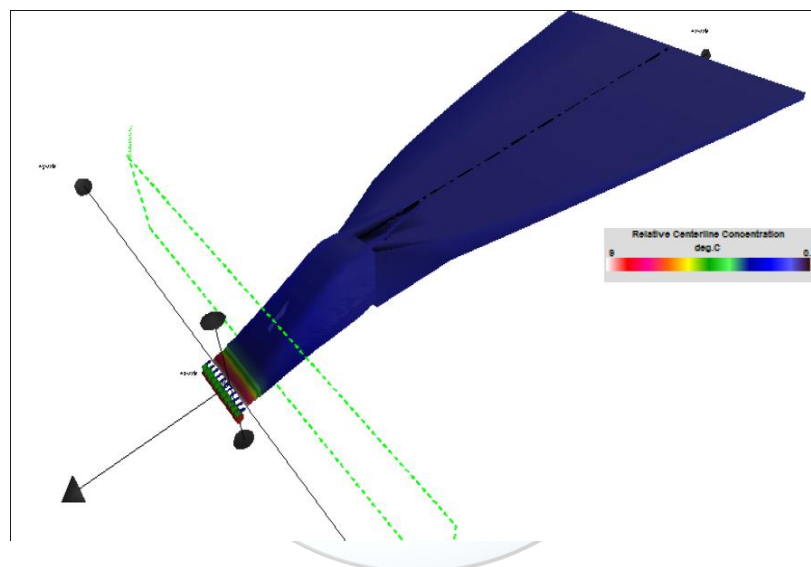
Figure 6. Isometric view of hot water discharge

4. CONCLUSION

In this study concentration of parameters such as pH, temperature, dissolved oxygen, suspended solid, chemical oxygen demand and electrical conductivity were measured in combined cycle power plant using natural gas in the Black Sea coast of Turkey. The CORMIX system is unique among mixing zone prediction methodologies in that it systematically accounts for boundary interaction, predicts density current behavior after boundary interaction, and provides rule-verified mixing zone analysis and advice for outfall design optimization [8]-[9].

A result of increasing erosion due to high precipitation rates are increasing the amount of solid substances carried into the rivers in the Black Sea. Suspended solid of the high value, the amount of solids transported by rivers is considered that due to the increase. The measurement results compared with the model results showed that 0.7 ˚C difference is acceptable. According to the model results, after mixing 10 meters into the sea of waste water has been obtained difference 1˚C. This difference is within acceptable limits as a regard of Turkish Water Pollution Regulation.

ACKNOWLEDGMENT

REFERENCES

[1] Basaran, T., "Global Energy, Environment, Economic System and Hydrogen", Hydrogen Energy Course Project Report, Sabancı University, Istanbul, 2009

[2] Zhao, Y., "An Integrated Framework for Gas Turbine Based Power Plant Operational Modeling and Optimization", Georgia Institute of Technology, PHD Thesis, Atlanta, USA, April 2005

[3] I. S. Ondryas, D. A. Wilson, M. Kawamoto and G. L. Haub *"Options in gas turbine power augmentation using inlet air chilling", Trans ASME Journal of Engineering for Gas Turbines and Power,* vol.113, issue 2, pp. 203-211, April 1991.

[4] Kehlhofer, R., *Combined Cycle Gas & Steam Turbine Power Plants*, 3rd ed.,Penwell Publishing Company, Oklahama, USA, 1997.

[5] Ross, D.A. and Degends, E.T., *Recent sedimentation of Black Sea. In Degends*, E.T. and Ross, D.A. (Eds.), *The Black Sea-Geology-Chemistry-Biology the American Association of Petroleum Geologists*, No. 20, 183-199. 1974

[6] Akturk, "Heavy metals ın sedıments of the black sea," In. Eng. Master of Science, Bogazici Institute of Environmental Science, Istanbul, Turkey, 2005.

[7] Doneker R. L. And Jirka H. G. "CORMIX-GI systems for mixing zone analysis of brine wastewater disposal" *Desalination*, vol. 139, issue 1-3, pp. 263-274, Sep. 2001.

[8] L.R. Davis, *Fundamentals of Environmental Discharge Modeling. CRC Mechanical Engineering Series*, Boca Raton, CRC Press, 1999.

[9] D.J. Baumgartner, W.E. Frick and P.J. Roberts, *Dilution Models for Effluent Discharges*, 3rd ed., USEPA, Newport, OR, 1994.

Preparation and Stability Analysis of Water Based Al2O3, TiO2 and ZnO Nanofluids

Adnan Topuz[1], Tahsin Engin[2], A. Alper Ozalp[3], Beytullah Erdogan[1]*,
Serdar Mert[2], Alper Yeter[4]

[1]Bülent Ecevit University, Engineering Faculty, Department of Mechanical Engineering, Zonguldak, Turkey

[2]Sakarya University, Engineering Faculty, Department of Mechanical Engineering, Sakarya, Turkey

[3]Uludağ University, Engineering Faculty, Department of Mechanical Engineering, Bursa, Turkey

[4]Kale Oto Radyatör Sanayi ve Ticaret A.Ş., Kocaeli, Turkey

*CorrespondingAuthor email: beytullah.erdogan@beun.edu.tr

Abstract

For nanofluids to be able to use practically, they must not cluster and precipitate. Namely, they have to become stable. The target of this study is to determine the parameters that are effective at preparing stable nanofluid and to obtain stable one.To follow nanofluid stability, its sedimentation state is determined by photo capturing and controlling continuously. It is verified by SEM images that the nanofluids, which do not precipitate and are determined as stable, are distributed homogeneously and do not constitute considerable agglomerates. The work fluid is made from Al2O3, TiO2, ZnO nanoparticles and deionized water as base fluid. The solutions are prepared with 0.1%, 0.3%, 0.5%, 0.7% and 1.0% volume concentration. They are mixed 30 minutes by probe type of ultrasonic homogenizer at environment conditions. Sodium Dodecyl Sulfate (SDS) was added to the solutions as surfactant to prevent instability occurred due to agglomeration and sedimentation. At this study, it is investigated that from where the contradictory data for stability experiments in the literature stems. Moreover, the various stable nanofluid preparation parameters that are not available in the literature are given.It is observed that Al2O3, TiO2 and ZnOnanofluids have stability up to 5 days, 7 days and 21 days without considerably sedimentation, respectively. It is ascertained that properties of nanoparticle and nanofluid preparation parameters are important to enable stability.

Key words

Al2O3, TiO2, ZnO, Nanofluid, Stability, Surfactant

1. INTRODUCTION

Heating and cooling demands needed at many sectors like transport, electronic, nuclear, military, space, energy production play a rather important role for appearing new technologies **Error! Reference source not found.**, **Error! Reference source not found.**. To meet these demands at present applications, various methods are used. Some of them are increment at surface areas that heat transfer occurs, higher temperature difference for more heat transfer and material usage having durable to high temperature. However, it is already reached to usage limits of these methods due to the causes like dimensional limits, durable limits of material, production costs. Moreover, due to performance limits of available work fluids i.e. antifreeze, engine oil, fluids that have particles with mili-micrometer sized are used as a solution. Yet, instability occurred because of agglomeration and sedimentation at these particles induces clogging in microchannels and desired developments not be able to be obtained **Error! Reference source not found.**. With time, thanks to production technology developed, particles with nanometer sized and nanofluids have obtained. Nanofluid usage has started as work fluid.

Nanofluid is a suspension obtained by dispersing particles with nanometer sized in a fluid. Nanoparticle sizes used in nanofluids are generally between 1 nm and 100 nm **Error! Reference source not found.**, **Error! Reference source not**

found. - **Error! Reference source not found.**. Nanofluids are prepared by one of the methods called 1-step or 2-step. At 1-step method, nanofluid is prepared by chemical reaction at one-step. As for 2-step method, firstly, particle is produced at nanometer size, and then nanofluid is obtained by mixing them in a base fluid. Nanofluids obtained by 1-step method are more stable than ones obtained by 2-step. However, at 1-step method, particle size cannot be controlled. At 2-step method, nanoparticles needed can be found at desired size and property from many producers **Error! Reference source not found.**, **Error! Reference source not found.**.At 2-step method, nanofluids can be prepared by numerous sub methods: Magnetic stirrer, high shear mixer, ball mill, ultrasonic bath, probe type ultrasonic homogenizer, adding surfactant, changing pH, surface modification of particle **Error! Reference source not found.**, **Error! Reference source not found.**, **Error! Reference source not found.**. In 2-step methods, the most efficient and effective one is determined probe type ultrasonic homogenizer in the literature **Error! Reference source not found.**, **Error! Reference source not found.**, **Error! Reference source not found.**.Nanofluids are desired the properties like high thermal conductivity, high heat transfer performance, long stability time. However, they are not demanded clogging at microchannels due to agglomeration and sedimentation, and increase at pumping losses due to viscosity increment and pressure drop. These unwanted results are generally related to nanofluid stability. Stability of nanofluids can be examined by various methods: Ultra Violet-Visible Spectrophotometer (UV-Vis), Zeta potential, SEM, TEM, DLS, XRay Diffraction, sedimentation method, 3-omega, centrifugation method, photo capturing **Error! Reference source not found.**, **Error! Reference source not found.**, **Error! Reference source not found.**.Nanofluid stability is enabled by the methods like using surfactant, pH changing, modification of nanoparticle **Error! Reference source not found.**, **Error! Reference source not found.**. To enable nanofluid stability, the researchers who do not want a change at thermal properties of nanofluid did not use surfactant **Error! Reference source not found.** - **Error! Reference source not found.**. However, those who use surfactant desired it to prevent stability problem **Error! Reference source not found.**, **Error! Reference source not found.** - **Error! Reference source not found.**, **Error! Reference source not found.** Pg.31, **Error! Reference source not found.** Pg.57, **Error! Reference source not found.**.

Even after only ultrasonic mixing, attraction forces existed between particles cause them to cluster. Nanoparticle groups at micrometer and bigger sized occurred due to that clustering start to behave like particles at macro sized. For they have bigger density than base fluid, they make instability by collapsing the bottom of base fluid. Surfactants are used to prevent that sedimentation. Surfactant covers surface of nanoparticle and make repelling force between them. So, clustering of particles is prevented considerably. Only surfactant usage is not enough to enable stability. Because, when nanoparticles are dispersed in base fluid for the first time, since they are clustered, surfactant cannot affect among them. These agglomerations can be broken by ultrasonication**Error! Reference source not found.**.In the literature, there are different results for same nanofluids whose stability changes from 1 hour to 1 year **Error! Reference source not found.**. There are limited number of studies that include stable nanofluid preparation parameters and indicate them to be standardized **Error! Reference source not found.** Pg.76. This study works to determine the parameters that are effective at preparing stable nanofluid, to standardize these parameters and to obtain stable nanofluid.

This study consists of four sections: Material and Method, Experiment, Results, Conclusions. Material and Method section includes properties of used materials and how to be prepared nanofluids. Experiment section includes two subsections in the way nanofluid stability parameters and nanofluid SEM/TEM images.

2. 2. MATERIAL AND METHOD

2.1. Propertiesof Nanoparticles

Al2O3, TiO2 and ZnO nanoparticles are used to prepare nanofluid. Average sizes of these particles are 20 nm, 10-25 nm and 18 nm, respectively. Nanoparticles are bought from "Nanografi Ltd. Company". All properties of nanoparticles are given in Table 1, their TEM images supplied by the producer are given in Figure 1.Sodium Dodecyl Sulfate (SDS) as surfactant was used to prevent sedimentation of nanoparticles by clustering and to make nanofluid stability keep on. SDS was bought from "Merck Inc." The density of this matter is 1.1 g/cm3 and its pH value is between 6 and 9.
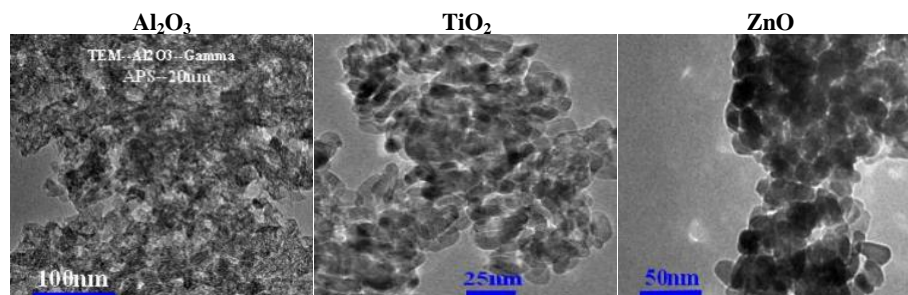
Figure 1. TEM images of nanoparticles

2.2. Preparationof Nanofluids

All nanofluids at this study were prepared by 2-step method. Probe type ultrasonic homogenizer was used to disperse nanoparticles in a deionized water (Ultrasonic Homogenizer Mark/Model: Optic Ivymen System / CY-500, Power: 500W, Frequency: 20kHz, Probe Diameter/Length: Ø5.6/60mm).Firstly, mass amounts of nanoparticle, deionized water and SDS were calculated in accordance with desired nanofluid volumetric concentration, nanofluid volume and SDS weight

concentration from

Figure 2. Preparation of nanofluid with temperature control

Table 2. These quantities were weighed by a precision balance (AND GX-600, Max Mass: 610g, Deviation: 0.001g). Then, nanofluids were prepared in a flask by paying regard to many parameters considered to be effective at nanofluid stability. The nanofluid taken from the bottom location of the flask by a pipet was filled in the glass tubes, which have Ø16x160 mm dimensions with screw thread. Stabilities of nanofluids were examined by photo capturing method according to time.

The most suitable parameters were determined by these images. According to these parameters, the most stable nanofluids were prepared.

The equations used in

Figure 2. Preparation of nanofluid with temperature control

Table 2 for nanofluids to be prepared are the following:

Volume concentration of nanofluid,
$$\phi = \frac{\forall_{np}}{\forall_{nf}} = \frac{\rho_{nf} - \rho_{bf}}{\rho_{np} - \rho_{bf}} \tag{1}$$
Volume of nanofluid,
$$\forall_{nf} = \forall_{np} + \forall_{bf} \tag{2}$$
Mass of nanofluid,
$$m_{nf} = m_{np} + m_{bf} \tag{3}$$
Density for nanofluid, nanoparticle and deionized water,
$$\rho = m/\forall \tag{4}$$
Weight concentration of SDS/Nanoparticle,
$$\phi = m_{SDS}/m_{np} \tag{5}$$

During mixing nanofluids by ultrasonic homogenizer, when it was not taken any precaution, too temperature increment was seen in the sample (nanofluid). Such that, this temperature increment reached 60 degrees in 10 minutes. During mixing, increased temperature affects both chemical-thermal properties of nanofluid and causes ultrasonic homogenizer to work unproductively **Error! Reference source not found.** Pg.32. At the experiments done in this study, it was seen that uncontrolled temperature increment decreased vibrations of ultrasonic homogenizer. This was noticed by change of ultrasonic sound and decrease at surge of the top surface of the sample. Therefore, a heat bath was used to hold nanofluid temperature constant (Mark/Model: Cole Parmer / EW-12108-25, Temperature: -20~200oC, Temperature Stability: ±0.01oC, Bath Capacity: 6L, Heating Capacity: 1kW, Cooling Capacity: 200W, Flow Rate: 11~24L/min). The flask

included nanofluid was put in the heat bath held at constant temperature as Figure 2. So, 100 mL of nanofluids were prepared. In addition, during ultrasonication, high temperatures were seen at the probe of ultrasonic homogenizer. To compensate it, the probe was cooled by a fan.

Table 1. Properties of nanoparticles

Nano Particle	Type	Density (kg/m3)	Purity	Average Size	Specific Surface Area	Shape
Al2O3	Gamma	3890	>%99	20 nm	138 m2/g	Close to spherical
TiO2	Anatase	3900	>%99.5	10-25 nm	200-240 m2/g	Close to spherical
ZnO	—	5606	%99.95	18 nm	40-70 m2/g	Close to spherical

Figure 2. Preparation of nanofluid with temperature control

Table 2.Nanofluids according to volumetric concentration at 20oC

Fluid	Volume Concent. ϕ (%)	Nanofluid Volume $\forall_{nf}$ (mL)	Base Fluid Density ρ_{bf} (kg/m³)	Particle Density ρ_{np} (kg/m³)	Particle Volume $\forall_{np}$ (mL)	Base Fluid Volume $\forall_{bf}$ (mL)	Particle Mass m_{np} (g)	Base Fluid Mass m_{bf} (g)	SDS-Particle Weight Concent. $\phi_{w,SDS}$ (%)	SDS Mass m_{SDS} (g)
Al₂O₃	0,10%	100	998,0	3890	0,10	99,90	0,389	99,700	50,00%	0,195
	0,30%	100	998,0	3890	0,30	99,70	1,167	99,501	25,00%	0,292
	0,50%	100	998,0	3890	0,50	99,50	1,945	99,301	15,00%	0,292
	0,70%	100	998,0	3890	0,70	99,30	2,723	99,101	15,00%	0,408
	1,00%	100	998,0	3890	1,00	99,00	3,890	98,802	15,00%	0,584
TiO₂	0,10%	100	998,0	3900	0,10	99,90	0,390	99,700	50,00%	0,195
	0,30%	100	998,0	3900	0,30	99,70	1,170	99,501	25,00%	0,293
	0,50%	100	998,0	3900	0,50	99,50	1,950	99,301	15,00%	0,293
	0,70%	100	998,0	3900	0,70	99,30	2,730	99,101	15,00%	0,410
	1,00%	100	998,0	3900	1,00	99,00	3,900	98,802	15,00%	0,585
ZnO	0,10%	100	998,0	5606	0,10	99,90	0,561	99,700	50,00%	0,280
	0,30%	100	998,0	5606	0,30	99,70	1,682	99,501	50,00%	0,841
	0,50%	100	998,0	5606	0,50	99,50	2,803	99,301	25,00%	0,701
	0,70%	100	998,0	5606	0,70	99,30	3,924	99,101	15,00%	0,589
	1,00%	100	998,0	5606	1,00	99,00	5,606	98,802	15,00%	0,841

3. 3. EXPERIMENT

3.1. NanofluidStabilityParameters

The parameters that affect stability of nanofluids are classified as follows:adding surfactant, ultrasonic power intensity, ultrasonic mixing time, bath temperature, height of ultrasonic probe, flask diameter, nanoparticle type.

The effect of each parameter on nanofluid stability was investigated as subtitles. The information at the top row of the figures that show effect of these parameters includes (Figure 3-Figure 10): 1. Nanofluid volumetric concentration, 2. Nanofluid type, 3. Investigated parameter, 4. Time passed after preparing nanofluid.Stability was examined by the photos taken daily, according to be transparent from the top surface of the tube and sedimentation at the its bottom.

3.1.1. Adding Surfactant

In this section, it was investigated whether surfactant usage is necessary and if it is necessary, what its concentration value must be. For this purpose, the nanofluids included and not included surfactant were prepared (Figure 3). It was seen that the nanofluids not included surfactant were settled by agglomerating in 20 minutes (Figure 3-a,b,c). After that result was obtained, to enable nanofluid stability, SDS was selected as surfactant widely used in the literature **Error! Reference source not found.**, **Error! Reference source not found.**. At the nanofluids prepared by using SDS, it was seen that agglomeration was prevented and stability was enabled (Figure 3-d,e,f). As a result, it was decided to use SDS for all nanofluids. In order to determine SDS concentration, the nanofluids included SDS between 1% and 100% in the way SDS/Nanoparticle as mass were prepared (Figure 4). At Figure 4, for the nanofluid with 0.5% volumetric concentration, while stability was enabled for SDS with 15% and higher weight concentration, SDS with same 15% weight concentration was insufficient for the nanofluid with 0.2% volumetric concentration. From here, it was concluded that SDS having different weight concentration is necessary for nanofluids with different volumetric concentration. As general trend, it was seen that the more nanofluid volumetric concentration decreases, the more SDS weight concentration needed increases (Figure 4-d,e,f). By this way, the lower limit of SDS weight concentration was determined in a way to change from 15% to 50% for all nanofluids by some experiments (

Figure 2. Preparation of nanofluid with temperature control

Table 2). In the literature, SDS weight concentration is generally given as "Surfactant/Nanoparticle" (**Error! Reference source not found.**, **Error! Reference source not found.**, **Error! Reference source not found.**). Yet, in some studies, this ratio is also given as "SDS/Nanofluid" (**Error! Reference source not found.**, **Error! Reference source not found.**). Therefore, it must be paid attention which reference SDS concentration values are given according to.
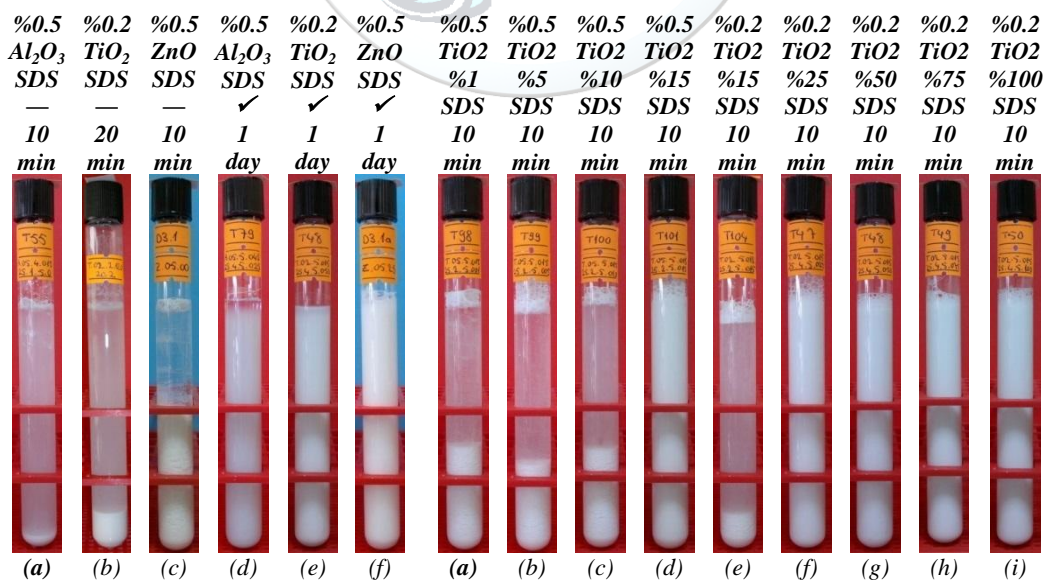

Figure 3. Controlling whether surfactant is necessary or not

Figure 4. Determining SDS weight concentration

It was worked to find a lower limit for using SDS. Because, SDS amount must be used many enough to enable nanofluid stability; it must be used little enough to decrease concretion, not to increase cost and not to affect thermodynamic properties.

3.1.2. Ultrasonic Power Intensity

Ultrasonic vibration power (W/mL) per nanofluid volume was investigated. For this purpose, three different nanofluids were prepared in a way to be their power intensity 3, 4, 5 W/mL (Figure 5). It was seen that the more bigger ultrasonic power intensity is, the more longer stability time is (Figure 5-d,e,f).As a result, it was decided that ultrasonic power must be applied to all nanofluids at full power (500 W) and this power must remain as a constant parameter.

3.1.3. Ultrasonic Mixing Time

It was examined for how much time it is necessary for the nanofluids to expose to ultrasonic vibration. For this, the nanofluids changed from 5 minutes to 240 minutes their mixing time were prepared (Figure 6). It could not be seen that mixing time lasting than 30 minutes had apparent effective on nanofluid stability time (Figure 6-e,f,g). Therefore, it was decided that all nanofluids must be exposed to ultrasonic vibration for 30 minutes. This time is same as numerous studies in the literature (**Error! Reference source not found.**, **Error! Reference source not found.** Pg.32, **Error! Reference source not found.**).

3.1.4. Bath Temperature

It was investigated at what temperature nanofluid must be during mixing it with ultrasonic homogenizer. For that purpose, during mixing, the nanofluids held their temperature constant at 20, 30, 40 and 50 degrees were prepared (Figure 7). It was not seen that temperature had significant effective on stability (Figure 7-e,f,g,h). Consequently, in order to prevent too temperature increase during mixing, it was seen that the heat bath is necessary to be held constant at any temperature. However, since high temperature causes efficiency of ultrasonic homogenizer to decrease and nanofluid volumetric concentration to change (increase) due to evaporating of water, it was made a decision that the heat bath must be held constant at 20-25°C environment temperature.

3.1.5. Ultrasonic Probe Height

Ultrasonic power that ultrasonic homogenizer gives fluid is mainly given from the top surface of the probe. Since conical volume that the tip surface of the probe makes and exposed vibrations changes, it was examined at how many height the probe must be from the bottom of the flask. To control that situation, the nanofluids were prepared by being held the probe at 1, 2, 3, 4 and 5 cm height (Figure 8). It was not seen that the probe height is effective on stability. As a conclusion, the probe can be held at any height from the bottom of the flask. Yet, even if it is little, to benefit from ultrasonic vibrations distributed from the side surfaces of the probe and to decrease noise during working, it was decided that the probe must be held at 1-2 cm height from the bottom of the flask.
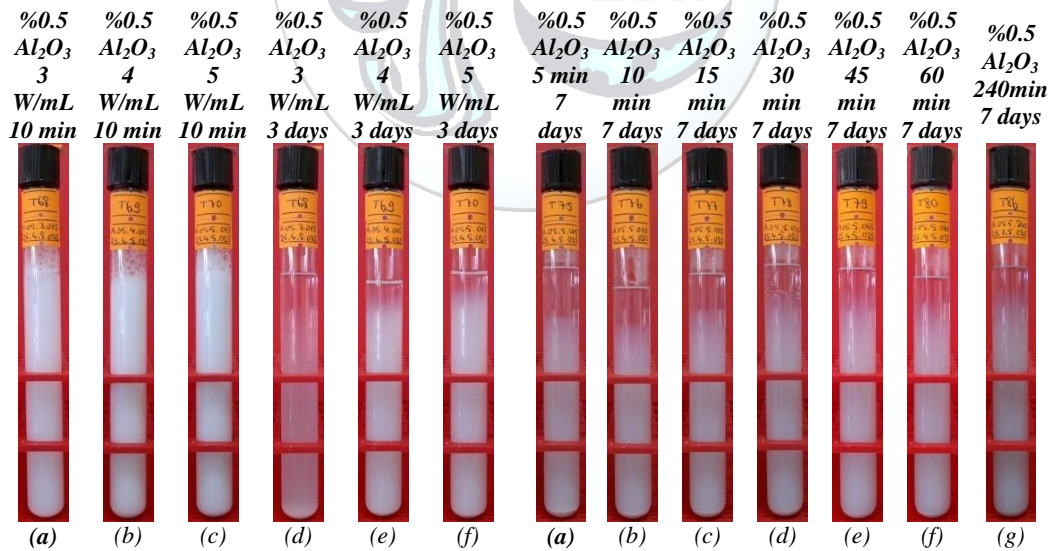

Figure 5. Determining ultrasonic power intensity   *Figure 6. Determining ultrasonic mixing time*
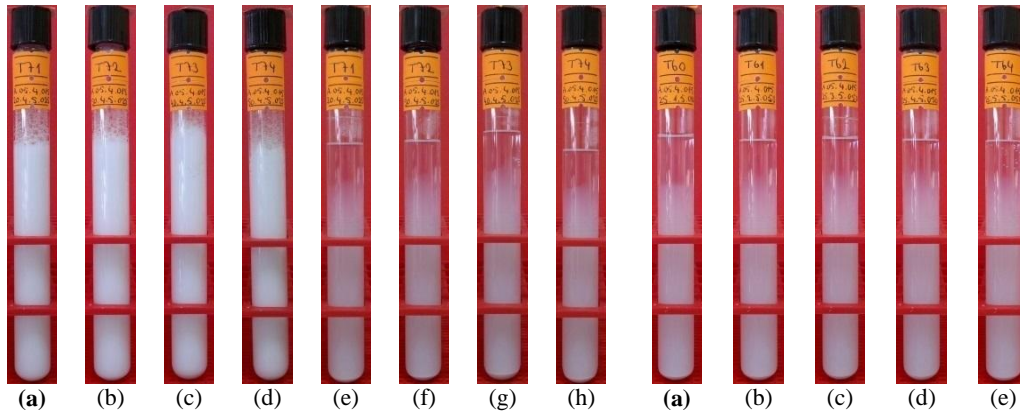
| **(a)** | (b) | (c) | (d) | (e) | (f) | (g) | (h) | **(a)** | (b) | (c) | (d) | (e) |

| *Figure 7. Determining bath temperature (%0.5 Al2O3)* | | | | | | | | *Figure 8. Determining height of ultrasonic probe* | | | | |

3.1.6. Flask Diameter

Due to the reasons described at the probe height section, it was examined what flask diameter must be. For this purpose, the nanofluids were prepared by using 5, 7 and 9 cm diameter of the flask (Figure 9). As determined at the probe height, similarly it was not seen that the flask diameter is effective on stability (Figure 9-d,e,f). As a result, a flask with any diameter can be used.

3.1.7. Nanoparticle Type

For nanofluids included different nanoparticles have different stability time, nanoparticle type was investigated effect on stability. The aim is to determine the nanofluid that had the longest stability time trend between different nanofluids. Al_2O_3, TiO_2 and ZnO nanoparticles were used to test stability time. The stability times of the nanofluids prepared were determined as ZnO, TiO2 and Al2O3 from the longest stability time to the least, respectively (Figure 10)
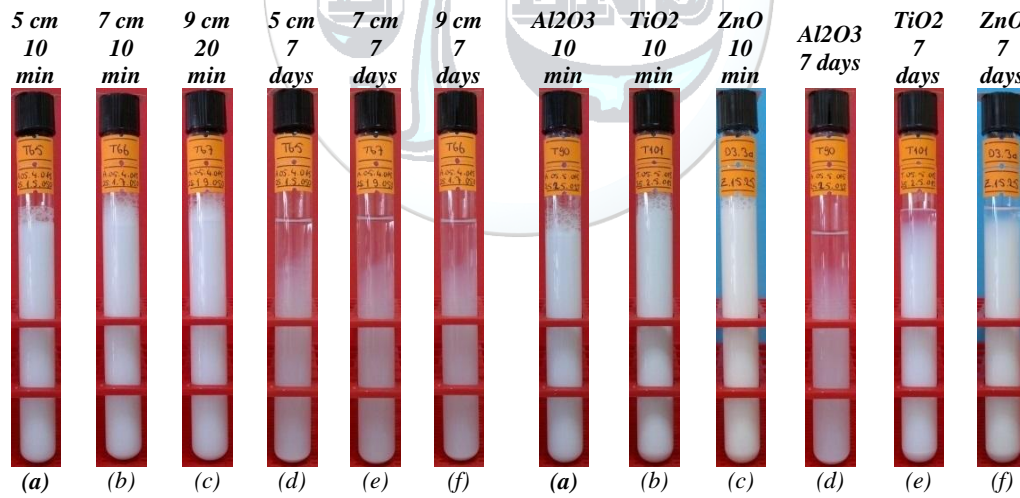
| *5 cm 10 min* | *7 cm 10 min* | *9 cm 20 min* | *5 cm 7 days* | *7 cm 7 days* | *9 cm 7 days* | *Al2O3 10 min* | *TiO2 10 min* | *ZnO 10 min* | *Al2O3 7 days* | *TiO2 7 days* | *ZnO 7 days* |

| *(a)* | *(b)* | *(c)* | *(d)* | *(e)* | *(f)* | *(a)* | *(b)* | *(c)* | *(d)* | *(e)* | *(f)* |

| *Figure 9. Determining flask diameter* | | | | | | *Figure 10. The effect of the nanoparticle type on* | | | | | |
| *(0.5% Al2O3)* | | | | | | *the stability time (Vol. Cont. 0.5 %)* | | | | | |

3.2. StabilityControl of Nanofluid

The nanofluids were prepared by considering the optimum values of the parameters that affect nanofluid stability time. The optimum parameters can be summarized as follows: Surfactant (SDS (

Figure 2. Preparation of nanofluid with temperature control

Table 2)), Ultrasonic power (500 W), Mixing time (30 min), Bath temperature ($25^{o}C$), Probe height (1-2 cm), Nanofluid volume (100 mL (

Figure 2. Preparation of nanofluid with temperature control

Table 2)).The nanofluids were prepared according to the values in

Figure 2. Preparation of nanofluid with temperature control

Table 2 under above conditions. Their images are given in Figure 11 three hours after preparing.Thenanofluids that have the longest stability time at Figure 11 were determined as 0.5%, 0.7% and 1.0% volumetric concentrations for Al_2O_3; 0.3% for TiO_2; all concentrations for ZnO. The stability time without apparently sedimentation for these concentrations was enabled up to 5 days for Al_2O_3, up to 26 days for TiO_2, up to 21 days for ZnO (Figure 12). It changed from some days to 2 weeks for other concentrations. As average, it can be said that the stability time continued up to 5 days for Al_2O_3nanofluid, 7 days for TiO_2nanofluid, 21 days for ZnOnanofluid.

SEM images were taken in order to confirm that the stable nanofluids prepared were distributed homogeneously and did not include big clusters according to the original nanoparticle size. Moreover, TEM images were taken in order to verify that they were at the desired size. SEM and TEM images of the Al_2O_3, TiO_2 and ZnOnanofluids with 0.5% volumetric concentration were given in Figure 14 and Figure 15.For SEM images, SEM device (FEI Quanta FEG 450, STEM Detector, 30 kV) in Bülent Ecevit University, Science and Technology Application and Research Center (ARTMER) was

used (Figure 13). As for TEM images, TEM device (FEI Tecnai G^2 Spirit BioTwin, CTEM, 120 kV) in Middle East Technical University, Central Laboratory, R&D Education and Measurement Center was used.
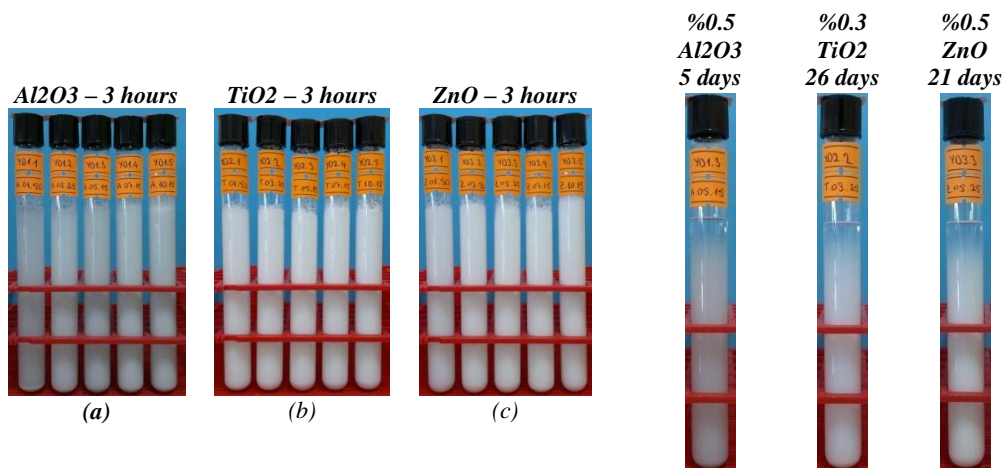

Figure 11. The nanofluids prepared with the optimum parameters

Figure 12. Stability time of the stable nanofluids

Figure 13. STEM device in ARTMER

4. RESULTS

To prevent sedimentation of nanofluids by agglomerating, SDS as surfactant is necessary. For this study, SDS weight concentrations are given in

Figure 2. Preparation of nanofluid with temperature control

Table 2.It is required to run the ultrasonic homogenizer at full power. In this study, the device was run at 500 W powers.The ultrasonic mixing time was determined as 30 minutes.The bath temperature was chosen as 25°C.

The tip of the ultrasonic probe was held at 1-2 cm height from the bottom of the flask.It was seen that Al_2O_3, TiO_2 and ZnOnanofluids prepared with the optimum parameters at 0.1%, 0.3%, 0.5%, 0.7% and 1.0% volumetric concentrations didn't show apparently sedimentation up to 5, 7 and 21 days as average, respectively.It was found that the nanofluids prepared with the optimum parameters remained stable max. 5 days for 0.5% Al_2O_3, 26 days for 0.3% TiO_2 and 21 days for

ZnO.SEM and TEM images were taken for the stable nanofluids. It was found that homogeneous distribution obtained and the nanoparticles were at the specified size from the images.

5. CONCLUSIONS

To minimize some controversial results (i.e. instability, stability time up to one year, anomalous thermal conductivity increase, too heat transfer increase) seen at different studies, nanoparticle properties used have to be same. Some of these properties are producer, nanoparticle size (20nm, 50nm), nanoparticle shape (spherical, cylindrical, porous), nanoparticle purity (99%) and quality (homogeneous size distribution, specified size and shape).

At nanofluid stability researches, zeta potential of nanofluid can be compared with images showed it remained stable. By this way, it can be appeared physically whether 30 mV of zeta potential limit value is enough (**Error! Reference source not found.**, **Error! Reference source not found.**, **Error! Reference source not found.**).

At SEM/TEM images given for nanofluid stability analyses, not only nanoparticle size images, but images at scale showed suspension distributed homogeneously must be also given.
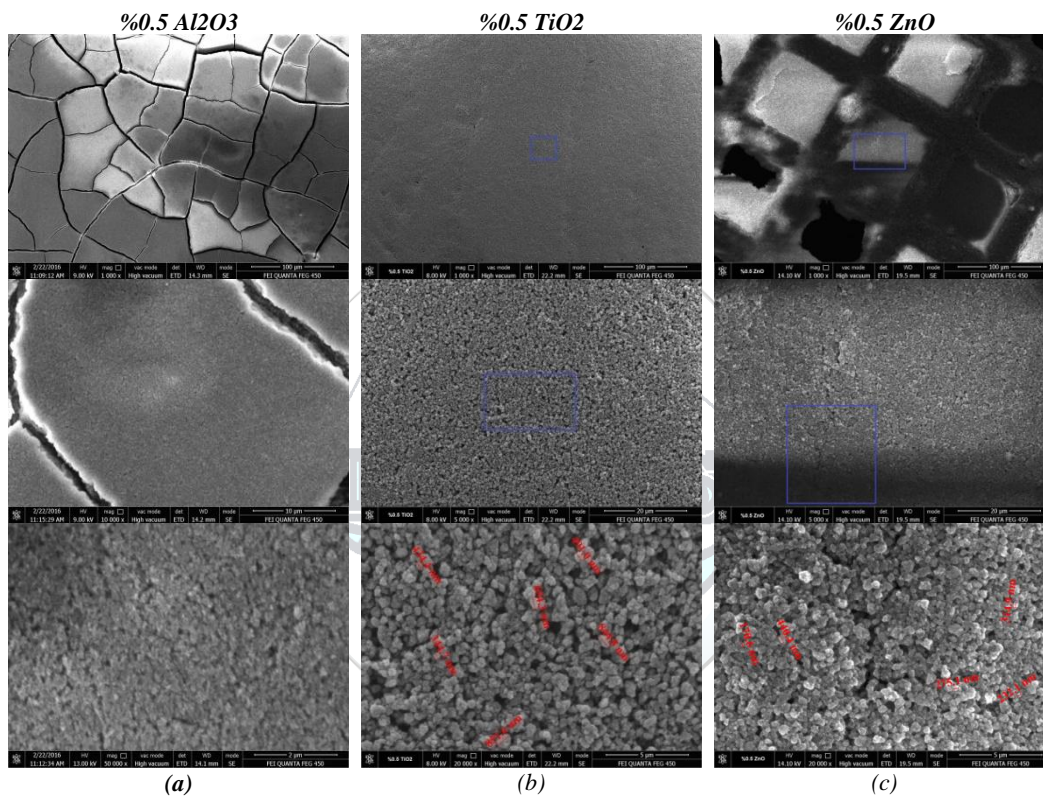
Figure 14. SEM images the nanofluids with 0.5% vol. concentration
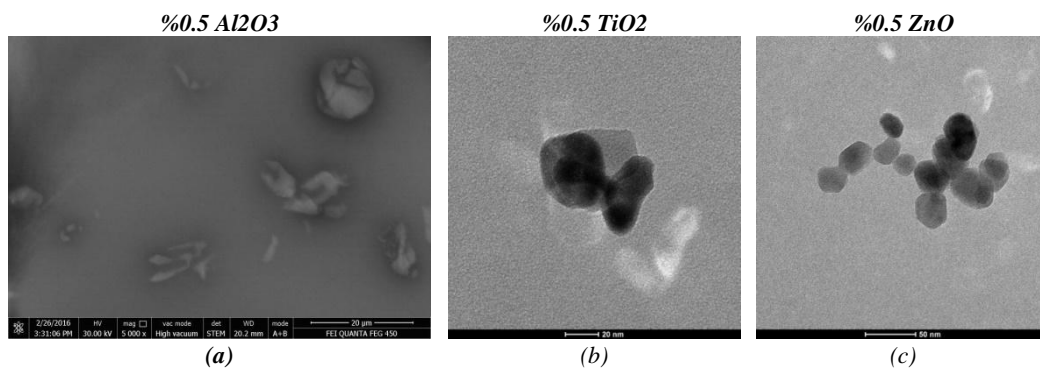
Figure 15. TEM images the nanofluids with 0.5% vol. concentration

ACKNOWLEDGMENT

REFERENCES

[1] *Ghadimi, R. Saidur, H.S.C. Metselaar, A review of nanofluid stability properties and characterization in stationary conditions, International Journal of Heat and Mass Transfer 54 (2011) 4051–4068.*

[2] *W. Yu, H. Xie, A Review on Nanofluids: Preparation, Stability Mechanisms, and Applications, Hindawi Publishing Corporation Journal of Nanomaterials Volume 2012, Article ID 435873.*

[3] *Y. Hwang, J.-K. Lee, J.-K. Lee, Y.-M. Jeong, S. Cheong, Y.-C. Ahn, S. H. Kim, Production and dispersion stability of nanoparticles in nanofluids, Powder Technology 186 (2008) 145 – 153.*

[4] *S. Mukherjee, S. Paria, Preparation and Stability of Nanofluids - A Review, IOSR Journal of Mechanical and Civil Engineering (IOSR-JMCE), e-ISSN: 2278-1684, p-ISSN: 2320-334X, Volume 9, Issue 2 (Sep. - Oct. 2013), PP 63-69.*

[5] *M.F. Zawrah, R.M. Khattab, L.G. Girgis, H. El Daidamony, R. E. A. Aziz, Stability and electrical conductivity of water – base Al2O3 nanofluids for different applications, HBRC Journal (2015).*

[6] *R. Mondragon, J. E. Julia, A. Barba, J. C. Jarque, Characterization of silica–water nanofluids dispersed with an ultrasound probe: A study of their physical properties and stability, Powder Technology 224 (2012) 138–146.*

[7] *A.Ghadimi, I. H. Metselaar, The influence of surfactant and ultrasonic processing on improvement of stability, thermal conductivity and viscosity of titaniananofluids, Experimental Thermal and Fluid Science 51 (2013) 1–9.*

[8] *M. J. Pastoriza-Gallego, C. Casanova, R. Páramo, B. Barbés, J. L. Legido, and M. M. Piñeiro, A study on stability and thermophysical properties (density and viscosity) of Al2O3 in water nanofluids, Journal of Applied Physics 106, 064301 (2009).*

[9] *S.J. Chung, J.P. Leonard, I. Nettleship, J.K. Lee, Y. Soong, D.V. Martello, M.K. Chyu, Characterization of ZnO nanoparticle suspension in water: Effectiveness of ultrasonic dispersion, Powder Technology 194 (2009) 75–80.*

[10] *J. Lee, K. Han, J. Koo, A novel method to evaluate dispersion stability of nanofluids, International Journal of Heat and Mass Transfer 70 (2014) 421–429.*

[11] *M.M. Heyhat, F. Kowsary, A.M. Rashidi, M.H. Momenpour, A. Amrollahi, Experimental investigation of laminar convective heat transfer and pressure drop of water-based Al2O3 nanofluids in fully developed flow regime, Experimental Thermal and Fluid Science 44 (2013) 483–489.*

[12] *N. A. C. Sidik, H.A. Mohammed, O. A. Alawi, S. Samion, A review on preparation methods and challenges of nanofluids, International Communications in Heat and Mass Transfer 54 (2014) 115– 125.*

[13] *S. Z. Heris, M. N. Esfahany, S.Gh. Etemad, Experimental investigation of convective heat transfer of Al2O3/water nanofluid in circular tube, International Journal of Heat and Fluid Flow 28 (2007) 203–210.*

[14] *B.A. Bhanvase, M.R. Sarode, L.A. Putterwar, Abdullah K.A., M.P. Deosarkar, S.H. Sonawane, Intensification of convective heat transfer in water/ethylene glycol based nanofluids containing TiO2 nanoparticles, Chemical Engineering and Processing 82 (2014) 123–131.*

[15] *J. Philip, P.D. Shima, Thermal properties of nanofluids, Advances in Colloid and Interface Science 183–184 (2012) 30–45.*

[16] *S. Kakaç, A. Pramuanjaroenkij, Review of convective heat transfer enhancement with nanofluids, International Journal of Heat and Mass Transfer 52 (2009) 3187–3196.*

[17] *A.Turgut, Investigation of Thermophysical Properties of Nanofluids, DokuzEylül University, Graduate School of Natural and Applied Sciences, PhD Thesis, 2010.*

[18] *E.F. Dilek, Nanoakışkanlarınhazırlanmasıveısıiletkenliklerininbelirlenmesi (Preparation of nanofluids and determination of thermal conductivities of nanofluids), MS Thesis, Graduate School of Natural and Applied Sciences, Atatürk University, 2008.*

[19] *M. Naraki, S.M. Peyghambarzadeh, S.H. Hashemabadi, Y. Vermahmoudi, Parametric study of overall heat transfer coefficient of CuO/water nanofluids in a car radiator, International Journal of Thermal Sciences 66 (2013).*

[20] *H. M. Ali, H. Ali, H. Liaquat, H. T. B. Maqsood, M. A. Nadir, Experimental investigation of convective heat transfer augmentation for car radiator using Zn-water nanofluids, Energy 84 (2015).*

[21] *Wang X.-J., Li H., Li X.-F., Wang Z.-F., Lin F., Stability of TiO2 and Al2O3 Nanofluids, Chin. Phys. Lett. Vol. 28, No. 8 (2011) 086601.*

[22]   *G. Xia, H. Jiang, R. Liu, Y. Zhai, Effects of surfactant on the stability and thermal conductivity of Al2O3/de-ionized water nanofluids, International Journal of Thermal Sciences 84 (2014) 118-124.*

[23]   *M. Karimzadehkhouei, S. E. Yalçın, K. Şendur, M. P. Mengüç, A. Koşar, Pressure drop and heat transfer characteristics of nanofluids in horizontal microtubes under thermally developing flow conditions, Experimental Thermal and Fluid Science 67 (2015) 37–47.*

First Order Integral Sliding Mode Control Of The Magnetically Levitated 4-Pole Type Hybrid Electromagnet

H.Fatih Ertugrul[1]*, Kadir Erkan[2]

[1]TUBITAK, Energy Institute, 41470, Gebze/Kocaeli, Turkey.

[2]Yildiz Technical University, Department of Mechatronic Engineering, 34220, Esenler/İstanbul, Turkey.

*Corresponding Author email: hasan.ertugrul@tubitak.gov.tr

Abstract

In this study, 4-pole type yoke hybrid electromagnet is modeled with respect to motion dynamics of the system. The hybrid electromagnet inherently has a non-linear characteristic and from the point view of controllability, it is unstable. This paper concerns the design of robust controller using first order integral sliding mode control method. Thus, the system becomes stable and robust against parametric uncertainties, nonlinearity, unmodeled uncertainties and external disturbance. Magnetic levitation system includes sensors that only measure the air gap. In order to estimate other states of the system, the full order disturbance observer is designed and integrated into the control loop. The estimated disturbance value is factored by the appropriate conversion gain and added to the input signal of the plant. The efficiency of control algorithm will be given in the paper by computer simulations.

Key words

Magnetic levitation, Integral Sliding mode control, Disturbance observer

1. INTRODUCTION

The non-contant magnetic levitation systems can operate without mechanical problem such as vibration, noise, abrasion, friction and so on. They also meet high accuracy and precision specifications. Because of these advantages, they are used in passenger transport vehicles, vibration isolation systems, biomedical devices, wind turbine, space studies and clean rooms as a key technology [1, 2].

The U and E-shaped electromagnets are often used in magnetic levitation systems, but they have only one degree of freedom control.4-Pole type hybrid electromagnet, which proposed by Koseki et al, has 3 degree of freedom. Each pole includes a coil (to control the field intensity) and a laminate permanent magnet leading to hybrid structure as shown in Fig.1.

The hybrid electromagnet inherently has a non-linear characteristic and from the point view of controllability it is unstable. In order to run such a system, it is required to actively control the hybrid electromagnet in multi axes. Several approaches have been proposed in the literature to control 4-pole type hybrid electromagnet [1-3]. In this paper, a sliding mode based control algorithm is proposed.

Conventional sliding mode control method does not guarantee robustness throughout the entire system. The control system response is sensitive against uncertainty during the reaching phase. After sliding mode occurs, the system response remains insensitive to variations of system parameters and external disturbance. By adding the integral component to sliding mode control, which is named integral sliding mode control (ISMC),the system response is became robust in both the reaching and sliding phase. In addition, ISMC can be used to eliminate the control chattering, which is the high-frequency vibrations (oscillations) of the control signal [4].

The performance of feedback control algorithm is associated with the measurement of the state variables of the system model. However, in practice, all the state variables are not measurable or the measurements of the state variables can be costly because of the high price of the sensors [5]. In order to obtain all state variables, the observer can be designed.

This paper is organized as follows. First, the mathematical model of the system is briefly derived. Then, integral sliding mode control and disturbance observer are introduced and designed using pole placement method. Finally simulation results verify the effectiveness of controller.

2. 4-POLE TYPE HYBRID ELECTROMAGNET

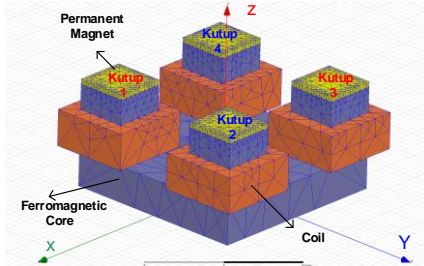4-pole type hybrid electromagnet has three degrees of freedom of movement (along Z plus rotation around X and Y).

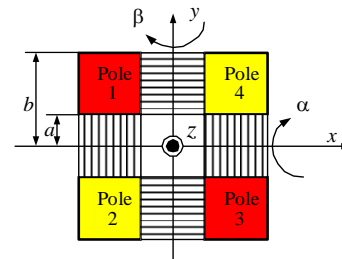*Figure 1. Basic structure of 4-pole hybrid electromagnet*

Figure 2. 4-pole hybrid electromagnet movement axis.

Independently control of each pole air gap is one of the way that can be followed to active control of the system. However, the implementation of this approach is difficult for controlling inclination axis motions and for compensating the unbalanced load. For this reason, system dynamics are developed independently using coordinate transformation. 4-Pole winding currents (i_1, i_2, i_3, i_4) are transformed virtual axis currents to provide control of each axis separately. Three virtual winding currents (i_z, i_α, i_β) are employed to control motion of vertical direction z, and inclinations α,β respectively.The relationships between virtual currents of the each degree of freedom and actual winding currents are represented by (Eq.1-2).

$$i_z = \frac{1}{4}(i_1 + i_2 + i_3 + i_4)$$
$$i_\alpha = \frac{1}{4}(-i_1 + i_2 + i_3 - i_4)$$
$$i_\beta = \frac{1}{4}(-i_1 - i_2 + i_3 + i_4)$$

$$\begin{bmatrix} i_1 \\ i_2 \\ i_3 \\ i_4 \end{bmatrix} = \begin{bmatrix} 1 & -1 & -1 \\ 1 & 1 & -1 \\ 1 & 1 & 1 \\ 1 & -1 & 1 \end{bmatrix} * \begin{bmatrix} i_z \\ i_\alpha \\ i_\beta \end{bmatrix}$$

(1)

In considering figure-2, the axial displacements are subjected to the following conversion.

$$z = \frac{1}{4}(z_1 + z_2 + z_3 + z_4)$$
$$\alpha = \frac{1}{2b}(\frac{z_1 + z_4}{2} - \frac{z_2 + z_3}{2})$$
$$\beta = \frac{1}{2b}(\frac{z_1 + z_2}{2} - \frac{z_3 + z_4}{2})$$

$$\begin{bmatrix} z \\ \alpha \\ \beta \end{bmatrix} = \frac{1}{4} \begin{bmatrix} 1 & 1 & 1 & 1 \\ 1/b & -1/b & -1/b & 1/b \\ 1/b & 1/b & -1/b & -1/b \end{bmatrix} * \begin{bmatrix} z_1 \\ z_2 \\ z_3 \\ z_4 \end{bmatrix}$$

(2)

Controller output signals are transformed to pole coil signals using H transformation matrix which is obtained from (Eq.1). Similarly, pole displacements are transformed to axial displacements using T transformation matrix which is obtained from (Eq.2). This axial transformation is shown in Fig. 3.
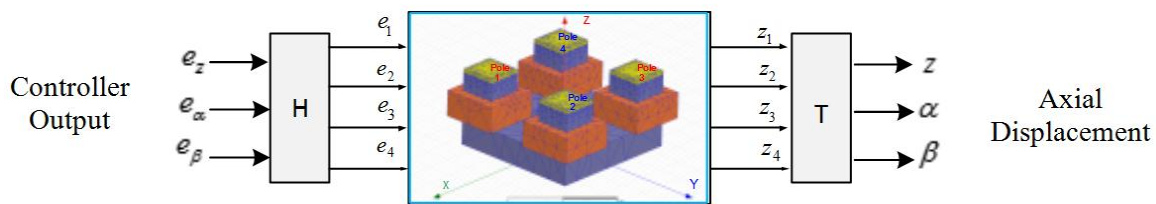

Figure 3. Axial transformation schematic.

The linearized mechanical system dynamics is given in below equation for z-axis motion [1-3].

$$Z(s) = \frac{K_B}{ms^2 - K_A} I_Z(s) - \frac{1}{ms^2 - K_A} F_d(s) \tag{3}$$

In the above equation, electrical input is the current form. In general, the voltage source is used to energize the coil of the magnetic levitation system.

$$I_Z(s) = \frac{1}{L_Z s - R_Z} \left[E_Z(s) - \frac{K_A L_Z}{K_B} s Z(s) \right] \tag{4}$$

The linearized system block diagram is shown in Figure 4(a) for z-axis motion. Changes are only encountered in the relevant parameters for inclination (α and β-axis) motion model (Figure 4(b)).
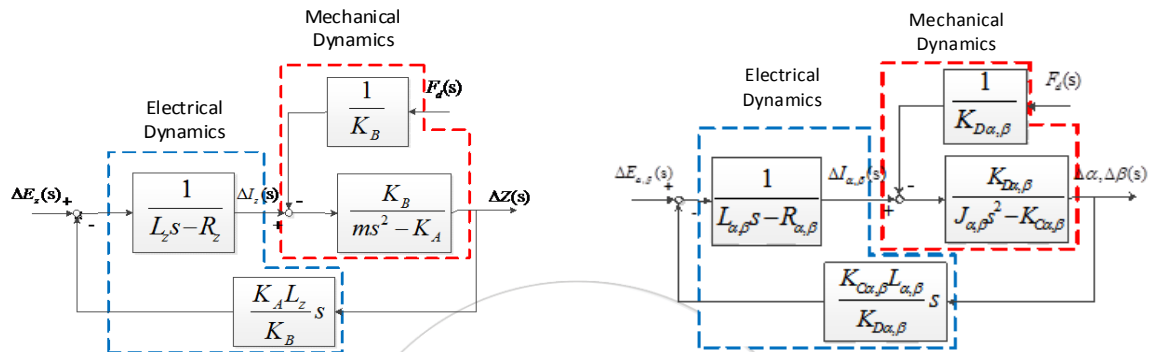

Figure 4. (a) System block diagram for z-axis motion.   *(b) System block diagram for α, β axis motions.*

The state-space representation of the system is given in below.

$$\dot{x}(t) = Ax(t) + Bu(t) + EF_d(t) \tag{5}$$

$$\frac{d}{dt}\begin{bmatrix} \Delta z(t) \\ \Delta \dot{z}(t) \\ \Delta i_z(t) \end{bmatrix} = \begin{bmatrix} 0 & 1 & 0 \\ \dfrac{K_A}{m} & 0 & \dfrac{K_B}{m} \\ 0 & -\dfrac{K_A}{K_B} & -\dfrac{R_z}{L_z} \end{bmatrix} \begin{bmatrix} \Delta z(t) \\ \Delta \dot{z}(t) \\ \Delta i_z(t) \end{bmatrix} + \begin{bmatrix} 0 \\ 0 \\ \dfrac{1}{L_z} \end{bmatrix} \Delta e_z(t) + \begin{bmatrix} 0 \\ -\dfrac{1}{m} \\ 0 \end{bmatrix} F_d(t)$$

3. DISTURBANCE OBSERVER-BASED INTEGRAL SLIDING MODE CONTROL

3.1. Integral Sliding Mode Controller Design

Sliding mode control signal is separated two components to achieve asymptotic output tracking; one is linear component u_l, and the other is nonlinear component u_{nl}.

$$u = u_l + u_{nl} \tag{6}$$

u_l component of the control signal drive the sliding variable (σ) to zero in finite time. The sliding starts after the sliding variable reaches zero at time t_r. After that time point, $\sigma = \dot{\sigma} = 0$ is valid for all time [6].

The sliding surface can be defined as follows:

$$\sigma = Sx = \begin{bmatrix} S_1 & S_2 \end{bmatrix} \begin{bmatrix} x_1 \\ x_2 \end{bmatrix} = 0 \qquad\qquad x_2 = \frac{-S_1}{S_2} x_1 \tag{7}$$

The sliding function is defined:

$$S = \begin{bmatrix} S_1 \\ S_2 \end{bmatrix} \qquad where \ \ k = S_2^{-1} S_1 \qquad\qquad S = \begin{bmatrix} S_2 k \\ S_2 \end{bmatrix} = S_2 \begin{bmatrix} k \\ 1 \end{bmatrix} \tag{8}$$

The sliding function (S) is obtained with selecting (S_2) parameter and calculating k. The integral of the position error is added to eliminate the error at the steady-state. The extended steady-space equation decomposed as follows

$$\frac{d}{dt}\begin{bmatrix} \int 0-\Delta z(t)dt \\ \Delta z(t) \\ \Delta \dot{z}(t) \\ \Delta i_z(t) \end{bmatrix} = \begin{bmatrix} 0 & 0 & 0 & 0 \\ 0 & 0 & 1 & 0 \\ 0 & \frac{K_A}{m} & 0 & \frac{K_B}{m} \\ 0 & 0 & -\frac{K_A}{K_B} & -\frac{R_z}{L_z} \end{bmatrix} \begin{bmatrix} \int 0-\Delta z(t)dt \\ \Delta z(t) \\ \Delta \dot{z}(t) \\ \Delta i_z(t) \end{bmatrix} + \begin{bmatrix} 0 \\ 0 \\ 0 \\ \frac{1}{L_z} \end{bmatrix} \Delta e_z(t) \tag{9}$$

The (Eq.10) can be obtained from the (Eq.8) and (Eq.9):

$$\dot{x}_1 = A_{11}x_1 + A_{12}x_2 = (A_{11} - A_{12}S_2^{-1}S_1)x_1$$
$$= (A_{11} - A_{12}k)x_1 \text{ where } k = S_2^{-1}S_1 \tag{10}$$

Since (A_{11}, A_{12}) is controllable, pole placement method is used to select the gain k[7,8]. Kessler canonical form (KCF) approach is used to obtain the gain k. KCF is an effective method to find the coefficients of characteristics polynomial of the SISO system. The basic idea behind this approach is to determine proper and stable characteristic polynomial using stability index and equivalent time constant [10].The equivalent time constant specifies the output response speed while stability index determines robustness, stability and output response of the system against parameter changes.

The characteristic equation of the closed-loop control system is given as:

$$P(s) = a_3 s^3 + a_2 s^2 + a_1 s + a_0 \tag{11}$$

Stability index (γ) and equivalent time constant (τ) can be described as follows:

$$\gamma_i = \frac{a_i^2}{a_{i+1}a_{i-1}} \quad (i = 1,2,3) \qquad\qquad \tau = \frac{a_1}{a_0} \tag{12}$$

In 1960s, Kessler has proposed that values of the γ_i should be two. In 1980s, Manabe proposed small modification of making $\gamma_1=2.5$ instead of 2 to obtain no overshoot condition.It is practically acceptable to take the equivalent time constant smaller than 0.1[s] in the magnetic levitation based system[1,2].

$$\frac{P_3(s)}{a_0} = \frac{a_3}{a_0}s^3 + \frac{a_2}{a_0}s^2 + \frac{a_1}{a_0}s + \frac{a_0}{a_0} = b_3 s^3 + b_2 s^2 + b_1 s + b_0$$

$$b_0 = 1 \qquad\qquad b_1 = \frac{a_1}{a_0} = \tau$$

$$\frac{b_1^2}{b_2 b_0} = \frac{\tau^2}{b_2} = \gamma_1 \qquad\qquad b_2 = \frac{\tau^2}{\gamma_1}$$

$$\frac{b_2^2}{b_3 b_1} = \gamma_2 \qquad\qquad b_3 = \frac{b_2^2}{b_1 \gamma_2} \tag{13}$$

The characteristic equation is solved to obtain desired poles of the system. In this study, pole placement is performed with the following MATLAB command.

$$ \tag{14} $$
$$k = ac\ker(A_{11}, A_{12}, [p1 \quad p2 \quad p3])$$

Thus, the sliding function S is obtained from (Eq.14) u_{nl} and selecting S_2.

The linear component of control signal u_l can be calculated by:

$$\dot{\sigma} = S\dot{x} = S(Ax + Bu_l) = 0$$

$$u_l = -(SB)^{-1} SAx \tag{15}$$

The nonlinear component of control signal is selected as follows:

$$u_{nl} = -(SB)^{-1} \rho \, \text{sgn}(\sigma) \quad \text{where } \rho \succ 0 \tag{16}$$

To show stability of system, a positive definite Lyapunov function is selected as [9]:

$$V = \frac{1}{2} \sigma^2 \tag{17}$$

The time derivative of Lyapunov function is negative definite:

$$\dot{V} = \sigma\dot{\sigma} = \sigma S(Ax + Bu)$$

$$= \sigma SAx + \sigma SB[-(SB)^{-1} SAx - (SB)^{-1} \rho \, \text{sgn}(\sigma)] \tag{18}$$

$$= -\rho\sigma \, \text{sgn}(\sigma) < 0 \qquad\qquad \text{where } \sigma \neq 0$$

Hence, the system becomes asymptotically stable.

In nonlinear component of control signal u_{nl} contain signum function which cause chattering problem because of the discontinuity. In practical case, the sigmoid function is used instead of signum function to eliminate chattering problem [6].

$$\text{sgn}(\sigma) \approx \frac{\sigma}{|\sigma| + \varepsilon} \tag{19}$$

where ε is a small positive scalar. u_{nl} is commonly selected by:

$$u_{nl} = -\rho \, \text{sgn}(\sigma) \approx -\rho \frac{\sigma}{|\sigma| + \varepsilon} \tag{20}$$

where ρ is a design parameter.

3.2. Disturbance Observer Based Design

Pole assignment is a basic design method for linear state feedback control system. In this method, it is assumed that all state variables are available for feedback. However, some state variables are not measurable directly or refrain from using of sensor because of noise occurring during the measurement. In order to estimate all state variables, the observer can be designed.

Disturbance force is added as a variable to obtain expanded system model (Eq.21). The disturbance force is generally step input in magnetic levitation system, so a zero line is added the system model. The expanded state equation is completely observable, thus observer can be designed. Figure 5 shows the block diagram of disturbance observer.

$$\frac{d}{dt}\begin{bmatrix} \Delta z(t) \\ \Delta \dot{z}(t) \\ \Delta i_z(t) \\ F_d \end{bmatrix} = \begin{bmatrix} 0 & 1 & 0 & 0 \\ \dfrac{K_A}{m} & 0 & \dfrac{K_B}{m} & -\dfrac{1}{m} \\ 0 & -\dfrac{K_A}{K_B} & -\dfrac{R_z}{L_z} & 0 \\ 0 & 0 & 0 & 0 \end{bmatrix} \begin{bmatrix} \Delta z(t) \\ \Delta \dot{z}(t) \\ \Delta i_z(t) \\ F_d \end{bmatrix} + \begin{bmatrix} 0 \\ 0 \\ \dfrac{1}{L_z} \\ 0 \end{bmatrix} \Delta e_z(t) \tag{21}$$
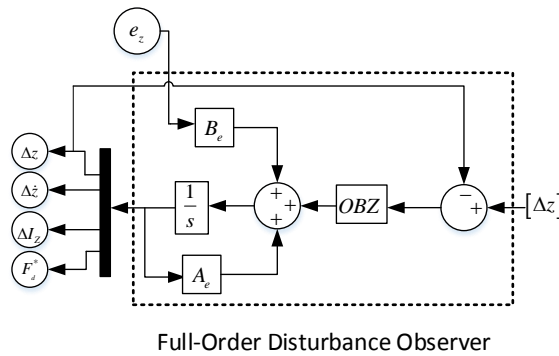
Full-Order Disturbance Observer

Figure 5. Full-Order Disturbance Observer Block Diagram.

Due to the separation principles, observer and controller can be designed independently of each other. The pole placement method is used to design full order disturbance observer similar to the controller design. Desired poles of the controllers and observers are decided by using Kessler's canonical form. However, the observer poles must be three to eight times faster than the controller poles to make sure the observation error converges to zero quickly [5].

Disturbance compensation gain is given as follows [2].

$$K_{Fd} = \frac{\Delta e_z(\infty)}{F_d} = \frac{R_z}{K_B} \tag{22}$$

Disturbance compensation gain is used to convert estimated force (N) into the control voltage (V). Figure 6 shows the Simulink model of the disturbance observer based integral sliding mode controller.
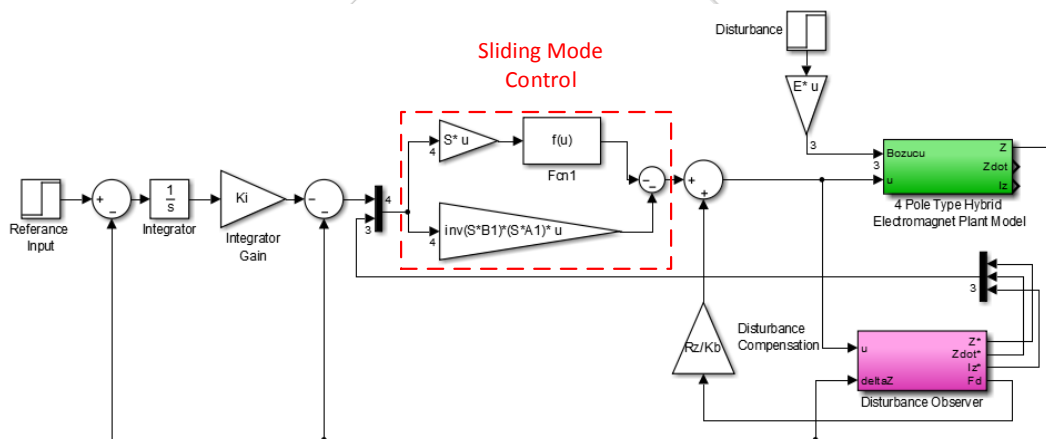
Figure 6. Simulink Model of the Control System

4. SIMULATION RESULTS AND EVALUATION

The effectiveness of integral sliding mode controller and disturbance observer, as discussed in the previous section, are shown using MATLAB environment. The simulation parameters for the 4-pole hybrid electromagnetic levitation system are shown in Table 1.

Table 1. System Parameters

Size / Unit	Value	Size/ Unit	Value	Size / Unit	Value
m [kg]	10	z_0 [mm]	4.3	α_0, β_0[rad]	0.0
$J_{\alpha,\beta}$[kg.m^2]	0.3	i_{z0} [A]	0.0	$i_{\alpha0}, i_{\beta0}$ [A]	0.0
k [N^2/A^2]	$6.84*10^{-6}$	K_A[N/m]	20991	K_C[Nm/rad]	106.43
I_m [A]	13.44	K_B[N/m]	14.87	K_D [Nm/A]	3.13
$R_{z,\alpha,\beta}$ [Ω]	1.50	$L_{z,\alpha,\beta}$[H]	0.016	E_{pm}[AT]	2689

Figure 7-8 show z-axes position and control signal waveform when a reference input is applied at 0.5 sec. of simulation time and 1.5 kg mass loads to the 4 pole type hybrid electromagnet at 2 sec. In Figure 7, the system can track step reference input with zero steady-state error. The disturbance compensator does not have much effect on the system response. This result indicates that proposed controller is insensitive to disturbance input. In Figure 9-10, the results show that the sliding mode control approach is achieved not only for vertical axis but also for inclinations. The chattering occurs particularly as shown on the control signals when a reference input and disturbance are applied. ρ parameter in (Eq.20) is used to adjust chattering effect. The higher value of ρ causes the high frequency chattering. The actual and observed disturbance values are shown in Figure 11.
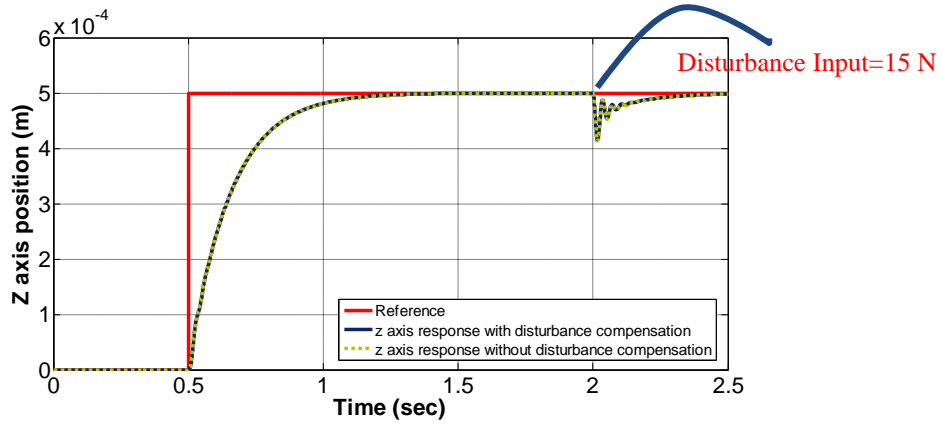

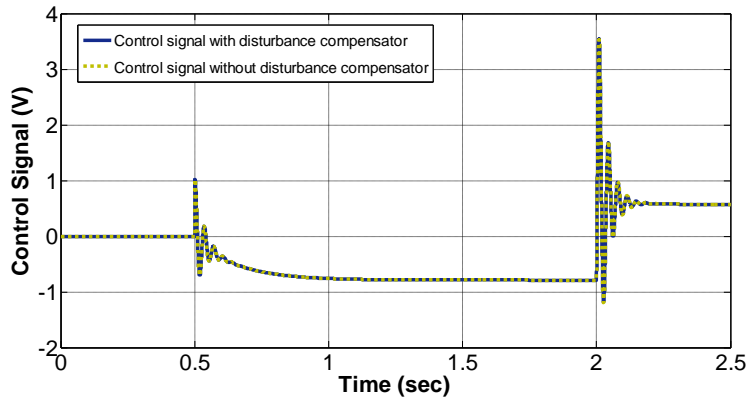*Figure 7. z-axis response for the step reference input and disturbance.*
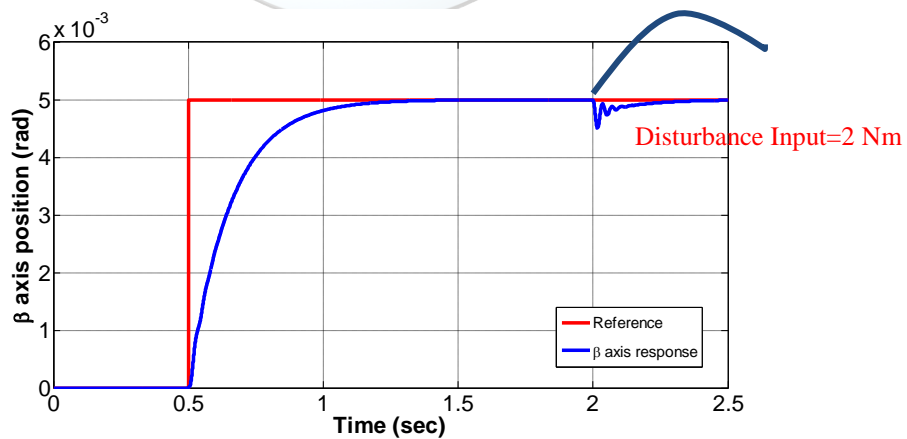

Figure 8. Control signal for z axes response.

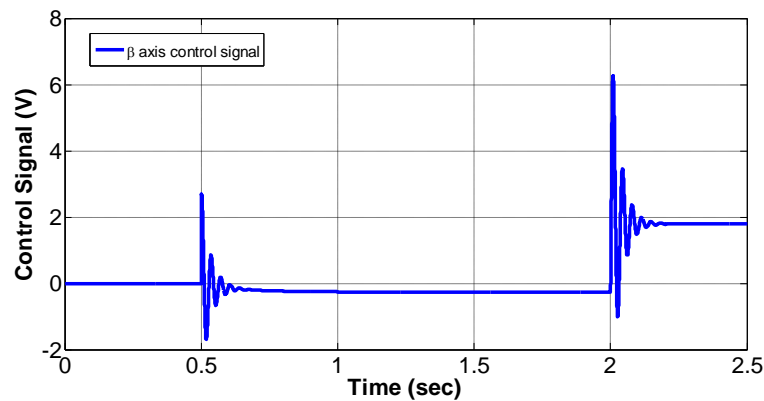*Figure 9: β-axes response for the step reference input and disturbance.*
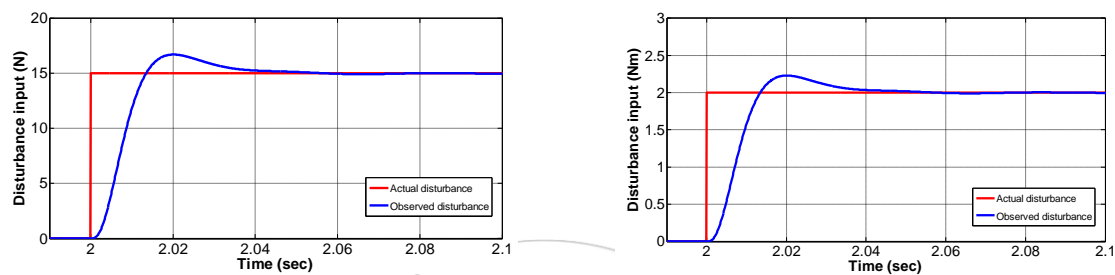
Figure 10. Control signal for β axes response.

Figure 11. Actual and observed disturbance value for z and β axis.

5. CONCLUSION AND FUTURE WORK

In this paper, firstly, fundamentals of modeling of 4-pole hybrid electromagnet have been given and control methods of 4-pole hybrid electromagnet were explained by using virtual axis currents. Then, designing of a sliding mode controller and disturbance observer have been outlined. To clarify the effectiveness of the proposed design approach simulation studies was conducted in MATLAB environment. In the near future, we are planning to implement the controller on the experimental setup.

ACKNOWLEDGMENT

REFERENCES

[1]. Y. Yakushi, T. Koseki and S. Sone, **"**3 degree-of-freedom zero power magnetic levitation control by a 4-pole type electromagnet", International Power Electronics Conference,vol.4, pp.2136-2141, April 3-7, 2000, Tokyo, Japan.

[2]. J. Liu, T. Koseki ,"Robust Control of a 4-Pole Electromagnet in Semi-Zero-Power Levitation Scheme with a Disturbance Observer" The Transactions of I.E.E. Japan, *A Publication of Industry Applications Society* Vol. 122-D, No. 1, pp. 7-15, January 2002

[3]. K. Erkan, B. Okur, T. Koseki, and F. Yigit, "Experimental evaluation of zero-power levitation control by transfer function approach for a 4-pole hybrid electromagnet," 2011 IEEE International Conference on Mechatronics, pp. 23–28, Apr. 2011.

[4]. Vadim Utkin, Juergen Guldner, Jingxin Shi, Sliding Mode Control in Electro-Mechanical Systems, Second Edition, CRC Press, 2009.

[5]. Katsuhiko Ogata, Modern Control Engineering, 5th Edition, Prentice Hall, 2009.

[6]. Shtessel, Y., Edwards, C., Fridman L., Levant A., "Sliding Mode Control and Observation (Control Engineering)",2013th Edition

[7]. J.-H. Lee, P. E. Allaire, G. Tao, and X. Zhang, "Integral sliding-mode control of a magnetically suspended balance beam: analysis, simulation, and experiment," IEEE/ASME Transactions on Mechatronics, vol. 6, no. 3, pp. 338–346, 2001.

[8]. Lee, J.-H., "A Design of Integral Sliding Mode Suspension Controller to Reject the Disturbance Force Acting on the Suspension System in the Magnetically Levitated Train System" , Transactions of the Korean Society for Noise and Vibration Engineering, Volume 17, Issue 12 2007, pp.1152-1160

[9]. Zhen Gang Sun; Cheung N.C; Shi Wei Zhao; Wai-Chuen Gan, Integral sliding mode control with integral switching gain for magnetic levitation apparatus, 2009. PESA 2009. 3rd International Conference on Power Electronics Systems and Applications, 2009.

[10].Manabe, S."Coefficient diagram method", 14th IFAC Symposium on Automatic Control in Aerospace, Aug. 24-28, 1998, Seoul, Korea, 199- 210. (1998).

Determination of Priority Contamination Factors in Lake of Manyas (Bird Paradise)

Elif Özmetin[1]*, Cengiz Özmetin[1], Yeliz Suzen[1], Mustafa Korkmaz[1]

Balıkesir University, Department of EnvironmentalEngineering, 10145, Çağış/Balıkesir, Turkey.

*Corresponding Author e-mail: eozmetin@balikesir.edu.tr

Abstract

Wetlands of which importance has been begun to understand better day by day, are rapidly contaminated as results of population growth, irregular urbanization, industrialization and agricultural activities. The Lake of (Bird) Manyas of Balıkesir, which is one of the most important wetlands protected with Ramsar Convention and hosts Bird Paradise National Park in is under the high pollution risks because of increasing industrial activities in its surrounding. Furthermore, in consequence of the lack of knowledge on the current pollution levels of the lake and the impact of industries on the lake, the management plans prepared to lake protection cannot be all got in the act and not be executed in a seriously. For this reason, by determining the general state of the lake, taking of measures to minimize pollution and ensuring of sustainability of the ecosystem is ofgreat importance. In this study, to determine pollution level of the Manyas Lake and sectoral effects on, in addition to conventional parameters, other pollution parameters determined by considering of the lake stress elements were examined. In the monitoring stage, from the previously determined sampling points of the lake and streams, water and sediment samples were taken by manual sampling method and analysed to determine the type, amount and change of contaminants. Results obtained from the monitoring studies carried out in last four years compared with Water Pollution Control Regulations (WPCR) of Turkey. It was concluded that the main pollution parameters of the lake were determined as Dissolved Oxigen (DO), Chemical Oxigen Demand (COD), Nitrate, Phosphate, Copper, Lead and Zinc. According to the specified pollutants, wastes from agricultural activities, mining activities, poultry farms and slaughterhouses mostly reach to the lake. It is concluded that these sectors are the major stress factors for the lake.

Key words

Bird Paradise, Contaminants, Manyas Lake, Monitoring, Wetlands

1. INTRODUCTION

The wetlands can be described as; "Natural or artificial, continuous or seasonal, drinkable, bitter or salty, calm or flowing water masses, marshes, peat bogs and sea water that not passing to six meter after tide of sea". The wetlands in the Mediterranean and its around are inlet, river delta, shore lagoon, lake, marshes and oasis, natural or artificial salty waters and dams [1]. The wetlands are ecosystems that have the highest biological variety after tropical forests. The wetlands that provide appropriate nourishment, reproduction, and accommodation media for the living creatures with rich variety, is not only rich museums of owner countries but also rich museums of the entire World [2].

The main reasons of the wetlands losses or damage in environmental quality level are that environmentalproperty and services of wetlands do not take part in economical system. Therefore, to realize the sustainable usage of the natural sources like wetlands, it is necessary to evaluate the positive or negative directions of every operation to be applied to this type sources in respect to community comfort [3]. The wetlands are underthreat due to humane usage. The some of factors causing species loss and ecosystem destruction are; spoil of water quality due to pollution causing from agricultural, municipal and industrial wastes, construction of dams on wetlands, changing of direction and extreme water supply,

extreme fish hunting, pulling water plants and burning the reed beds [4]. Turkey is assumed as the most important country in Europe and Middle East in respect to wetlands due to geographical and climate conditions. Turkey has about 300 wetlands that have totally two million hectare area. Of them, it is established that 135 piece has international importance [5].

The lake of Manyas comprise 20.400 hectare field that formed around the lake and its surroundings. The most important and rich region of the lake is the delta forming by Sığıcı Delta and Manyas Stream. The 64 hectare delta that is formed by Sığırcı Stream is declared as the National Park at 1959, 25.000 hectare field containing the lake and near surroundings is declared as Wild Life Protection Field at 1977 and the National Park and its surroundings are declared as first degree natural protection field at 1981. According to 2873 counted National Park law, the Bird Paradise is the unique natural sources that has simultaneously "Natural Protection Field" and "Wild Life Protection Field" properties. Together with becoming side of Turkey to Ramsar Aggreement, firstly 10.200 hectare field and then the whole of the lake were included to Ramsar Agreement at 1998 [6]. The reed bed field where the Sığırcı Stream comes together with the lake was taken to protection at 1959 as "Bird Paradise National Park". As Manyas is known as the first Bird Paradise field in Turkey has pioneered to known of wetlands, nature and birds. The lake of Manyas is rich in respect to water products and it has 23 different fish types. In addition, at the lake and its , there are 266 different bird types have beed determined and some are birds that their generation has come to an end [7].

The lake of Manyas is located in the border of Balıkesir City and Manyas District, at south of Marmara Sea and in a graben going over between Biga Peninsula and Ulu mountain. The average surface area of the lake of Manyas is 200 km^2 and at summer seasons this value decreases. The length and width of the lake are 20 km and 14 km, respectively and the lake has inclined shape. The lake has 14 km height from sea level and exhibits shallow property. The lake is nourished by Kocaçayand Sığırcı Streams. In addition, Dutludere, Köydereand other small several streams nourish the lake of Manyas. The extra water of the lake is transferred to Susurluk Stream by Karadere Stream [8].

In this study, the parameters causing stress on the Lake of Manyas that is important for Turkey were determined. In the samples taken from streams and the lakechemical analysis were done. The contaminating levels and seasonal changes of the parameters were examined. The pollutant sources and solution suggestions for decreasing of pollutants were taken hand.

Figure 1. (a) Lake of Manyas on Turkey Map   *(b) Lake Of Manyas (BirdParadise)*

2. MATERIALS AND METHODS

2.1 Sampling Points

Geographical location of the Lake of Manyas has 40° 11' 36" the North and 27° 58' 0" the Easth coordinates. Sea height changes between 14.5-17.5 meter based on water level. To determine the water quality in the Lake of Manyas, the water samples from the predetermined points was taken and their analysis were done. To determine the seasonal change of pollutants, samples were taken at rainless and rainy periods.While selecting the sampling points, the points that well represent the whole water sources were selected.

The volume of the Lake of Manyas is 800 million m^3. The water sources feeding the lake is KocaçayStream(74%), other streams and rainfall. The big portion of water reaches from Karadere to Susurluk stream and spills to Marmara Sea [8].

Therefore, samples were taken from Sığırcı, Kocaçayand Mürvetler Streams that feed the lake and from Karadere Stream that is unique water exiting points from the lake. The sampling points are shown in Figure 2.
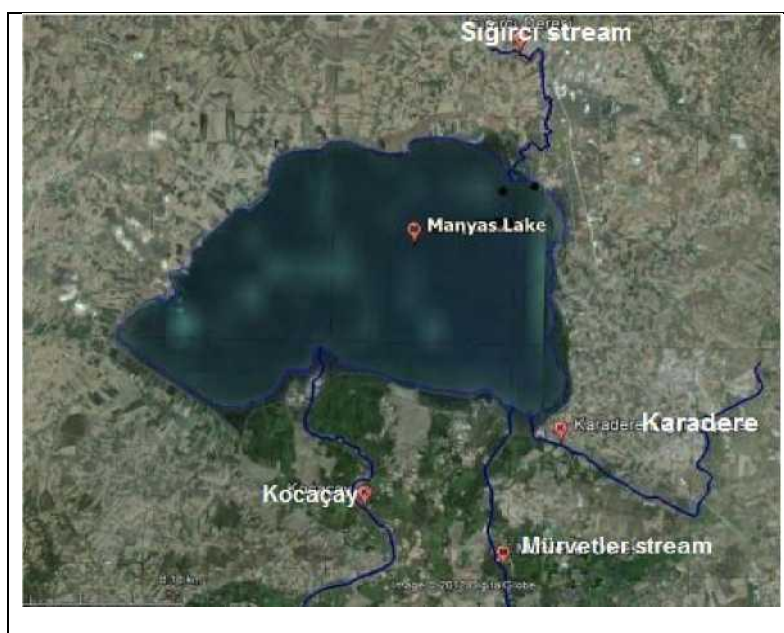
Figure 2.Sampling Points

While the water is being sampled, these criterions are taken into consideration; sampling points were determined at enough number so that they represent the water quality in sampling regions and characterize the water quality change. The waters entering the lake and exiting from the lake were taken into consideration, in addition, at least one sampling from interior of the lake was done. While samplings were being done interior of the lake, the points at which water flows and complete mixing occurs, were selected. At streams, the sampling points were selected at the near lake enter after last discharge point.

2.2 Analysis

The taken samples were protected by appropriate chemicals and stored at T<+4°C and the chemical using for protecting water is used according to parameter that would be analyzed. pH and dissolved oxygen measurements were done timely. All chemical analysis were done in Balıkesir University laboratories. On the other hand, the analysis results belonging to pat years were taken evaluation. All analysis were conducted based on Standard Methods [9].

3. RESULTS AND DISCUSSION

3.1. Analysis Results and Quality Classification

Description of water quality is made by Continent Interior Surface Waters Classification ofSurface Water Quality Control Regulation. Four main water quality classes (I- IV) that take part here, have been described with 45 parameters. The waters belonging to class I is the waters which can be used for drinking and and daily usage without any treatment and only should be disinfected. The waters belonging to class II is the waters which can be used as drinking and daily usage after treatment. The waters belonging to class (III) is the waters which can be used in the industries (except food, textile industries) for industrial water supply and cannot be used as drinking and use water. The waters belonging to class (IV) is low quality waters from class (III) and need a treatment [10].

The classification of the studied water sources according to Continent Interior Surface Waters Classification is given in the below Tables. In these tables, the I, II, III, and IV quality waters are indicated as *,**, *** and ****, respectively.

Table 1. Analysis Results forLake of Manyas

LAKE OF MANYAS						
PARAMETER	UNIT	2012	2013	2014	2015	2016
TEMPERATURE	(°C)	15,3*	10,5*	8,7*	8,6*	17*
pH		9,45****	9,26****	8,52**	8,08**	8,75**
DO	mg/L	7,23*	7,28*	-	-	12,66*
BOD	mg/L	5*	0*	-	-	5*
COD	mg/L	19*	58**	56**	34**	48,03**
NITRATE	mg/L	1,7*	4,52*	25,37****	1,3*	-

PHOSPHATE	mg/L	-	0,1293*	0,16**	0,03*	0,017*
COPPER	µg/L	1,55*	0,282*	0,003*	0*	<5,9*
LEAD	µg/L	0,24*	0,014*	0,006*	0*	<6,5*
MANGANESE	µg/L	-	0,041*	0,08*	-	-
IRON	µg/L	1,86*	0,167*	1,147*	0,03*	<4,1*
ZINC	µg/L	1,59*	0,17*	-	0,48*	<3,9*

Table 2. Analysis Results for Kocaçay

			KOCAÇAY			
		2012	2013	2014	2015	2016
PARAMETER	UNIT					
TEMPERATURE	(°C)	16*	12,2*	8,7*	12,1*	18*
pH		8,3**	7,77**	7,58**	7,82**	8,73**
DO	mg/L	5,79**	6,46**	-	-	12,44*
BOD	mg/L	2,5*	0,2*	-	-	5*
COD	mg/L	4,77*	16*	10*	17,82*	49,755**
NITRATE	mg/L	2,3*	10,54**	10,32**	6,6*	-
PHOSPHATE	mg/L	-	0,298**	0,1*	0,13*	0,07*
COPPER	µg/L	1,36*	0,020*	0,001*	158,8***	<5,9*
LEAD	µg/L	0,96*	0*	0,005*	23,76**	<6,5*
MANGANESE	µg/L	-	0,144*	0,167*	-	-
IRON	µg/L	1,71*	0,230*	0,288*	153,4*	<4,1*
ZINC	µg/L	<0,43*	0*	-	23,7*	<3,9*

Table 3. Analysis Results for MürvetlerStream

		MÜRVETLER STREAM				
PARAMETER	UNIT	2012	2013	2014	2015	2016
TEMPERATURE	(°C)	16,6*	11,7*	8,4*	9,8*	12,7*
pH		8,45**	8,29**	7,5**	8,06**	7,51**
DO	mg/L	8,75*	6,8**	-	-	8,62*
BOD	mg/L	3,1*	0,4*	-	-	3*
COD	mg/L	5,57*	4*	8*	31,16**	45,39**
NITRATE	mg/L	3,2*	2,9*	12,64**	2,9*	-
PHOSPHATE	mg/L	-	0,496***	0,2**	0,24**	0,135*
COPPER	µg/L	1,09*	0,017*	0,003*	495,2****	<5,9*
LEAD	µg/L	0,35*	0,004*	0,001*	2,3*	<6,5*
MANGANESE	µg/L	-	0,051*	0,022*	-	-
IRON	µg/L	1,71*	0,256*	0,201*	86,9*	<4,1*
ZINC	µg/L	<0,43*	0*	-	1*	<3,9*

Table 4.Analysis Results for Karadere

		KARADERE				
PARAMETER	UNIT	2012	2013	2014	2015	2016
TEMPERATURE	(°C)	20,5*	11*	8,2*	9,37*	16*
pH		8,19**	8,5**	7,15*	7,7**	9,2****
DO	mg/L	9,38*	7,46*	-	-	6,5**
BOD	mg/L	7,6**	0,3*	-	-	5*
COD	mg/L	11,95*	18*	22*	10,72*	28,82*
NITRATE	mg/L	11,3**	2,12*	9,78**	1,2*	-
PHOSPHATE	mg/L	-	0,193*	0,15*	0,05*	0,041*
COPPER	µg/L	1,62*	-	0,001*	432,6****	<5,9*
LEAD	µg/L	0,78*	-	0,003*	7,1*	<6,5*
MANGANESE	µg/L	-	-	0,217*	-	-
IRON	µg/L	1,71*	-	0,455*	232,4*	<4,1*
ZINC	µg/L	<0,43*	-	-	8,1*	<3,9*

Table 5.Analysis Results for Sığırcı Stream

		SIGIRCI STREAM				
PARAMETER	UNIT	2012	2013	2014	2015	2016
TEMPERATURE	(°C)	24*	11,3*	8,3*	8,9*	17,8*
pH		7,66**	7,93**	7,42*	8,6**	8,72**
DO	mg/L	5,63**	4,45**	-	-	12,52*
BOD	mg/L	25,8***	0*	-	-	6*
COD	mg/L	39,2**	12*	46**	23,16*	50,915**
NITRATE	mg/L	5,3*	6,44*	56,73****	7,7*	-
PHOSPHATE	mg/L	-	0,885****	1,03****	0,76****	0,022*
COPPER	µg/L	2,15*	0,094*	0,002*	194,8***	<5,9*
LEAD	µg/L	1,4*	0,006*	0,002*	0,3*	<6,5*
MANGANESE	µg/L	-	0,314*	0,316*	-	-
IRON	µg/L	1,71*	0,288*	0,267*	341,6**	<4,1*
ZINC	µg/L	<0,43*	0,593*	-	11,6*	<3,9*

When compared the Sığırcı Stream with other streams, it is seen that the organic load of the Sığırcı Stream is higher than other streams. Especially, COD, BOD, Nitrate and Phosphate levels are the high pollution parameters in the Sığırcı Stream.The agricultural industries and hen slaughters located at the north regions of Bandırma District are the main reason of organic pollution in the Sığırcı Stream. In addition, the municipal wastewaters of the vicinity villages are the other reason of the organic pollution in the Sığırcı Stream.

The lake waters is belonging to (II) and (III) classification according to BOD parameter and belonging to (I) and (II) classification according to COD parameter. If it is thought that the Sığırcı Stream is responsible for 3% of water feeding the lake, it is seen that Sığırcı Stream is important pollution source of the lake.

It is clear from the analysis results of Mürvetler Stream that its water quality is not of problematic contaminants for the Lake of Manyas. The reason of this is that there is not any industrial activity and discharge of municipal wastewater to

Mürvetler Stream. This has provided that the Mürvetler Stream remains over as clean when compared the other streams. KocaçayStream, the other water supplier of the lake, is the clean water source for the lake like Mürvetler Stream except high heavy metal concentration measured rarely.
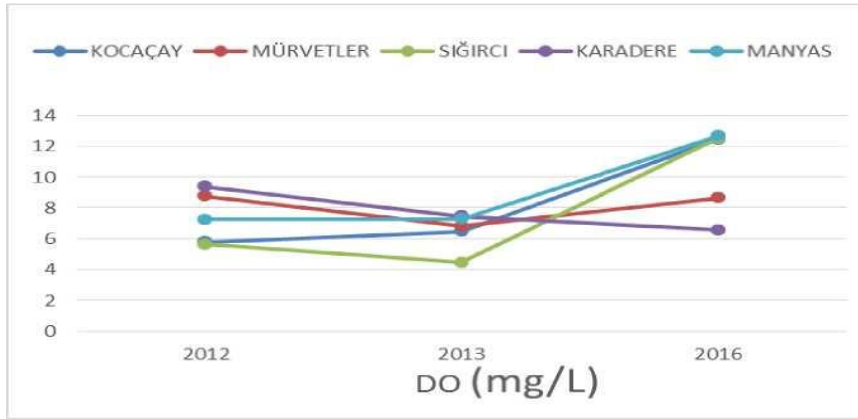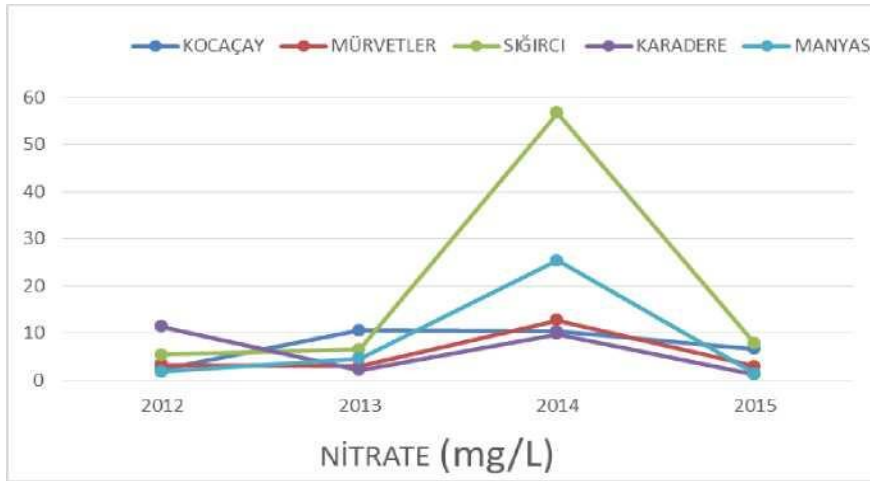

Figure 3. DO concentrationchangesbased on year

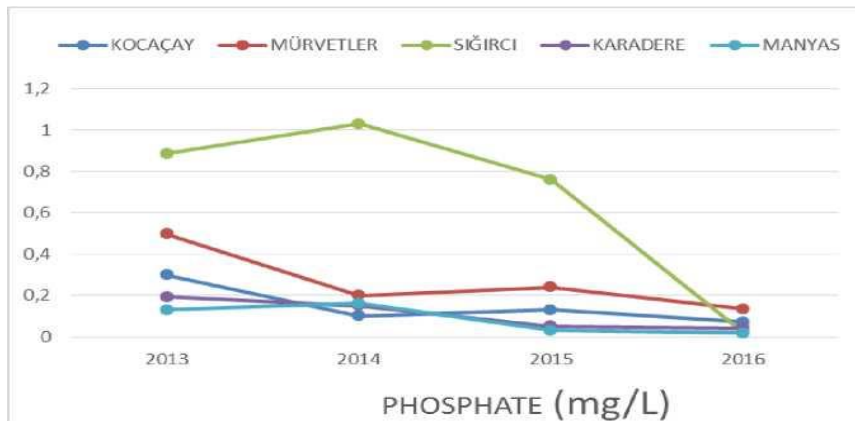*Figure 4. Nitrate concentration changes based on years*

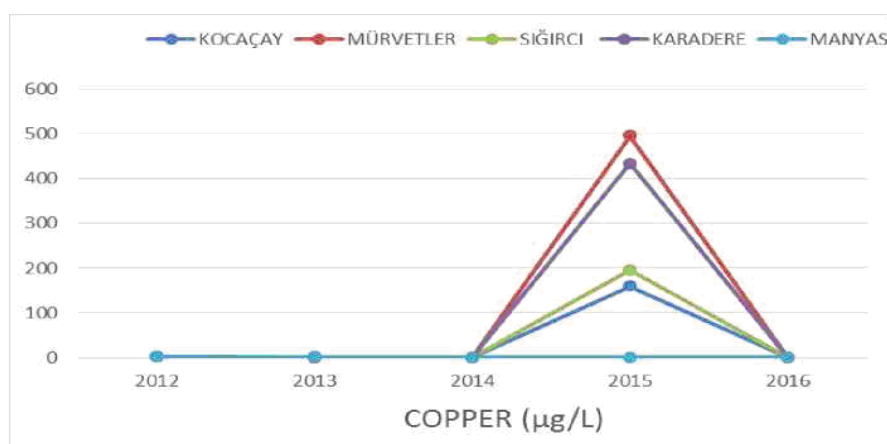*Figure 5. Phosphate concentration changes based on years*

Figure 6. Copper concentration changes based on years
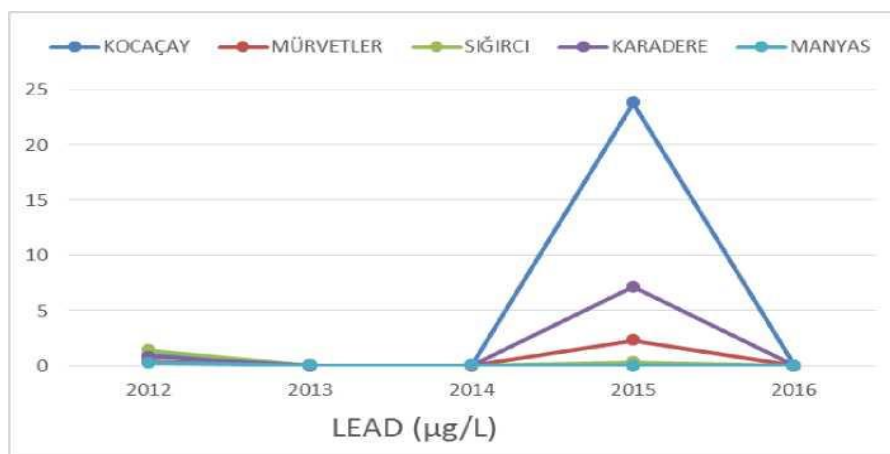
Figure 7. Lead concentration changes based on years

4. CONCLUSIONS

For the aim of prevention of pollution of the Lake of Manyas that is important natural source of Turkey, some precausions should be taken. These precausions can be summarized as follows:

• The industries in the lake regions must build the treatment systems and their operations should be controlled in respect to whether they are properly operated or not. When the treatment systems are not operated, strict sanction should be applied.

• The municipal wastewaters from houses around the lake should be treated.

• The water quality should be monitored by continuous monitoring devices at appropriated points and thus the controls will become continual.

• The flotation wastes which exist in the flood beds of Kocaçayand the stream connected to it should be collected from that region. Thus, the heavy metal transmigration to the lake should be prevented. At the same time, these wastes are economically valuable wastes as they are rich in zinc and lead.The alternatives that reduce the artificial fertilizer applications and enable to use of the mechanical agricultural struggle methods should be investigated and applied.

REFERENCES

[1] Doğa   Koruma   Derneği   website.   [Online].
    Available:http://dogakorumadernegi.org/index.php/component/content/article/47-biocesitlilik/102-sulak-alanlar, 2016

[2] Su Dünyası Dergisi,91.Sayı DSİ, 2011

[3] Gürlük, "Manyas Gölü ve Kuş Cenneti'nin çevresel değerlemesi üzerine bir araştırma," Phd. thesis, Uludağ Üniversitesi, Bursa, Türkiye, 2006.

[4] Orman   Su   İşleri   Bakanlığı   website.   [Online].
    Available:http://bolge9.ormansu.gov.tr/9bolge/AnaSavfa/fallivetlerimiz/sulakalanlar.aspx?sflang=tr, 2016

[5] "Kuş (Manyas) Gölü Sulak alan Yönetim Planı 2011-2015," Orman ve Su İşleri Bakanlığı, 2012.

[6] Dalkılıç, "Manyas (Kuş) Gölü Doğal Çevre Sorunları," M. Eng. Thesis, Ankara Üniversitesi, Ankara, Türkiye, 2000.

[7] Sulak Alanlar Kitabı, Orman ve Su İşleri Bakanlığı, Doğa Koruma ve Milli Parklar Genel Müdürlüğü, ,Ankara, 2013.

[8] Hoşcan, "Tarımsal Kullanımlar Yönünden Kuş (Manyas) Gölü Su Kalitesi," M. Eng. Thesis, Ankara Üniversitesi, Ankara, Türkiye, 1990.

[9] *Standart Methods for Examination of Water and Wastewater,* American Public Health Association (APHA), 17th ed, Washington, DC, 1992.

Yüzeysel Su Kalitesi Yönetimi Yönetmeliği, Orman ve Su İşleri Bakanlığı,Sayı : 28483, Ankara,2012.

Nonlinear Buckling Analysis of Cold-Formed Channel Sections

Mustafa Durmaz[1]*, Ayşe Daloglu[2]

[1]*Gümüşhane University, Department of Civil Engineering, 29100, Gümüşhane, Turkey.*

[2]*Karadeniz Technical University, Department of Civil Engineering, 61080, Trabzon, Turkey.*

*CorrespondingAuthor email: mustafadurmaz@gumushane.edu.tr

Abstract

The main objective of this paper is to provide an efficient and accurate finite element model to understand the behavior of cold-formed steel channel columns. The effects of initial local and overall geometric imperfections have been taken into consideration in the analysis. Failure loads and buckling modes as well as load-shortening curves of plain channel columns were investigated in this study. The nonlinear finite element model was verified against experimental results. The finite element analysis was performed on plain channels compressed between pinned ends over different column lengths, and column curves were obtained. An extensive parametric study was carried out using the finite element model to study the load eccentricity on the strength and behavior of channel columns. The column strengths predicted from the finite element model were compared with the design strengths calculated using the European Code, EN 1993-1-3 Eurocode 3: Design of steel structures - Part 1-3: General rules - Supplementary rules for cold-formed members and sheeting, for cold-formed steel structures.

1. INTRODUCTION

Finite element analysis (FEA) of cold-formed structures plays an increasingly important role in engineering practice, as it is relatively inexpensive and time efficient compared with physical experiments, especially when a parametric study of cross-section geometries is involved. Furthermore, it is difficult to investigate the effects of geometric imperfections and residual stresses of structural members experimentally. Therefore, FEA is more economical than physical experiments, provided that the finite element model (FEM) is accurate. Hence, it is necessary to verify the FEM with experimental results. In general, FEA is a powerful tool in predicting the ultimate loads and complex failure modes of cold-formed structural members. In addition, local and overall geometric imperfections, residual stresses and material non-linearity can be included in the FEM.

The purpose of the paper is to develop an accurate FEM to investigate the strengths of pin-ended cold-formed plain channel columns. The finite element analysis program ABAQUS 6.13 [1] was used for the numerical investigation. The FEM was verified against the cold-formed channel column tests conducted by Young and Rasmussen [2]. The FEM included geometric and material non-linearities.

2. EXPERIMENTAL TEST

The test program described in Young and Rasmussen [2] provided experimental ultimate loads and failure modes for cold-formed plain channel columns compressed between pinned ends. The test specimens were brake-pressed from high strength zinc-coated grade G450 structural steel sheets having nominal yield stress of 450 MPa and specified according to the Australian Standard AS 1397 [3]. The test program comprised two series of plain channels. The channel sections had a nominal thickness of 1.5 mm and a nominal width of the web of 96 mm. The nominal flange width was either 36 or 48 mm and was the only variable in the cross-section geometry. Accordingly, the two test series were labeled P36 and P48 where

"P" refers to "plain" channels. The average values of measured cross-section dimensions of the pin-ended test specimens are shown in Table 1 using the nomenclature defined in Figure 1. The specimens were tested at various column lengths ranging from 280 to 1565 mm. The measured cross-section dimensions of each specimen are detailed in Young and Rasmussen [2].

Table 1. Average measured specimen dimensions and material properties

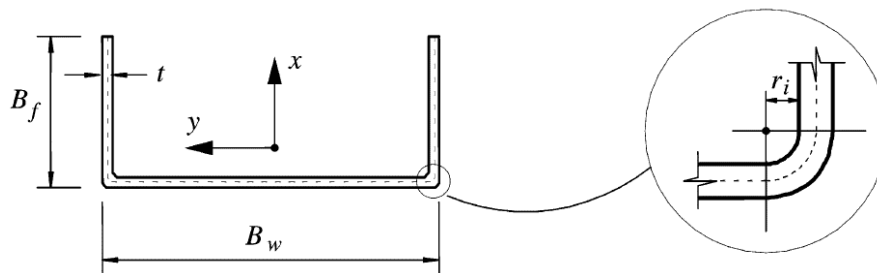| Test series	Specimen dimensions				Material properties			
	B_f (mm)	B_w (mm)	t (mm)	r_i (mm)	E (GPa)	$\sigma_{0.2}$ (MPa)	σ_u (MPa)	ε_u (MPa)
P36	36.8	96.9	1.51	0.85	210	550	570	10
P48	49.6	95.4	1.52	0.85	210	510	540	11

Figure 1. Definition of symbols

The material properties determined from coupon tests are also summarized in Table 1. The table contains the measured static 0.2% tensile proof stress ($\sigma_{0.2}$) and the static ultimate tensile strength (σ_u) as well as the Young's modulus (E) and the elongation after fracture (ε_u) based on a gauge length of 50 mm. The coupons were taken from the center of the web plate in the longitudinal direction of the finished specimens. The coupon dimensions conformed to the Australian Standard AS1391 [4] for the tensile testing of metals using 12.5 mm wide coupons of gauge length 50 mm. The coupons were tested in an Instron TT-KM 250 kN capacity displacement controlled testing machine using friction grips to apply loading at a constant speed of 1 mm/min. The static load was obtained by pausing the applied straining for one minute near the 0.2% proof stress and the ultimate tensile strength. This allowed the stress relaxation associated with plastic straining to take place. The stress–strain curves obtained from the coupon tests are detailed in Young and Rasmussen [2].

Residual stress measurements were conducted on a companion series of tests of lipped channel specimens by Young and Rasmussen [2, 5]. The plain and lipped channel specimens were cut from the same batch of structural steel sheets and break pressed from the same machine. The membrane and the flexural residual stresses were found to be less than 3% and 7% of the measured 0.2% tensile proof stress, respectively. Hence, the residual stresses were deemed negligible compared with the 0.2% tensile proof stress. Local and overall geometric imperfections were measured prior to testing for the tested columns. The measured maximum local imperfections were found to be of the order of the plate thickness at the tip of the flanges for the two test series. For the pin-ended specimens, the maximum overall minor axis flexural imperfections at mid-length were 1/2200 and 1/1500 of the specimen length for Series P36 and P48, respectively. The measured local and overall geometric imperfection profiles are detailed in Young and Rasmussen [2, 6].

A 250 kN servo-controlled hydraulic actuator was used to apply compressive axial force to the specimen. The tests were controlled by incrementing the shortening of the specimen. This allowed the tests to be continued into the post-ultimate range. Readings of the applied load were taken approximately 1 min after applying an increment of compression, hence allowing the stress relaxation associated with plastic straining to take place. Consequently, the loads recorded were considered to be static loads. The pin-ended bearings were designed to allow rotations about the minor axis while restraining major axis rotations as well as twist rotations and warping. Details of the test rig are given in Young and Rasmussen [7]. The experimental ultimate loads (P_{test}) of the test specimens are shown in Table 2. The test specimens were labeled such that the test series, type of boundary conditions and specimen length could be identified from the label. For example, the label "P36P0815" defines the specimen belongs to the test Series P36, the fourth letter "P" indicates that the specimen is pin-ended, and the last four digits are the specimen length of 865 mm.

Table 2. Geometric properties and failure loads of U-section members tested by Young and Rasmussen (1998).

Specimen	B_f (mm)	B_w (mm)	t (mm)	r_i (mm)	L (mm)	A (mm^2)	P_{test} (kN)
P36P0280	36,9	96,6	1,51	0,85	280	247	55,2
P36P0315	37,0	96,8	1,50	0,85	315	245	52,1
P36P0815	36,8	97,5	1,51	0,85	815	249	40,9
P36P1315	37,0	96,6	1,50	0,85	1315	245	27,0
P48P0300	49,6	94,8	1,51	1,46	300	279	45,2

P48P0565	49,8	94,5	1,53	1,48	565	283	38,6
P48P1065	50,0	94,2	1,52	1,48	1065	282	33,9
P48P1565	49,4	95,1	1,52	1,47	1565	281	31,2

3. FINITE ELEMENT MODELING

3.1. General

In this study, the finite element program, ABAQUS 6.13 [1] was used in the analysis of cold-formed plain channel columns tested by Young and Rasmussen [2]. The model used the nominal sizes, initial local and overall geometric imperfections and material properties. Finite element analysis for buckling requires two types of analyses. The first is known as eigenvalue analysis that estimates the buckling modes and loads. Such an analysis is a linear elastic analysis performed using the (*BUCKLE) procedure available in the ABAQUS library with the live load applied within the step. The buckling analysis provides the factor by which the live load must be multiplied to reach the buckling load. For practical purposes, only the lowest buckling mode predicted from the eigenvalue analysis is used. The second is called load-displacement nonlinear analysis and follows the eigenvalue prediction. It is necessary to consider whether the postbuckling response is stable or unstable.

3.2. Finite Element Type and Mesh

It is mentioned in the ABAQUS manual that the four-noded doubly curved shell element with reduced integration S4R is suitable for complex buckling behavior [1, 8, 9]. The S4R element has six degrees of freedom per node and provides accurate solutions to most applications. The element also accounts for finite strain and is suitable for large strain analysis. Since buckling of plain channel columns is very sensitive to large strains, the S4R element was used in this study to ensure the accuracy of the results. In order to choose the finite element mesh that provides accurate results with minimum computational time, convergence studies were conducted. It is found that a 10 mm x 10 mm (length by width) ratio provides adequate accuracy in modeling the channel columns.

3.3. Boundary Conditions and Load Application

Following the experimental tests, the ends of the columns were free to rotate and fixed to translate in any direction except for the displacement at the loaded end in the direction of the applied load. The nodes other than the two ends were free to translate and rotate in any direction. The load was applied in increments using the modified RIKS method available in the ABAQUS library. The RIKS method is generally used to predict unstable and nonlinear collapse of a structure such as postbuckling analysis. It uses the load magnitude as an additional unknown and solves simultaneously for loads and displacements. The load was applied as static uniform loads at each node of the loaded end which is identical to the experimental investigation. The nonlinear geometry parameter (*NLGEOM) was included to deal with the large displacement analysis.

3.4. Material Modeling

The material behavior provided by ABAQUS allows for a multilinear stress-strain curve to be used. The first part of the multilinear curve represents the elastic part up to the proportional limit stress with measured Young's modulus and Poisson's ratio equal to 0.3. Since the analysis of postbuckling involves large in-elastic strains, the nominal (engineering) static stress-strain curve was converted to a true stress and logarithmic plastic strain curve. The true stress (σ_{true}) and plastic true strain (ε^{pl}_{true}) were calculated using Equations 1. and 2.

$$\sigma_{true} = \sigma(1 + \varepsilon) \tag{1}$$

$$\varepsilon^{pl}_{true} = ln(1 + \varepsilon) - \sigma_{true} / E \tag{2}$$

whereE = Young's modulus, and σ and ε = measured nominal (engineering) stress and strain based on the original cross-section area of the coupon specimens as detailed in Young and Rasmussen [2]. The engineering stresses and strains were obtained from tensile coupon tests. The coupon specimens were loaded at a constant speed of 1 mm/min.

Figure 2 shows the measured engineering and true stress–strain curves for the test Series P36. The incremental plasticity model required the portion of the true stress–strain curve from the point corresponding to the last value of the linear range of the engineering stress–stain curve to the ultimate point of the true stress–strain curve, as shown in Figure 2. The Poisson's ratio was taken as 0.3 and the measured Young's modulus as shown in Table 1 was used in the FEM.
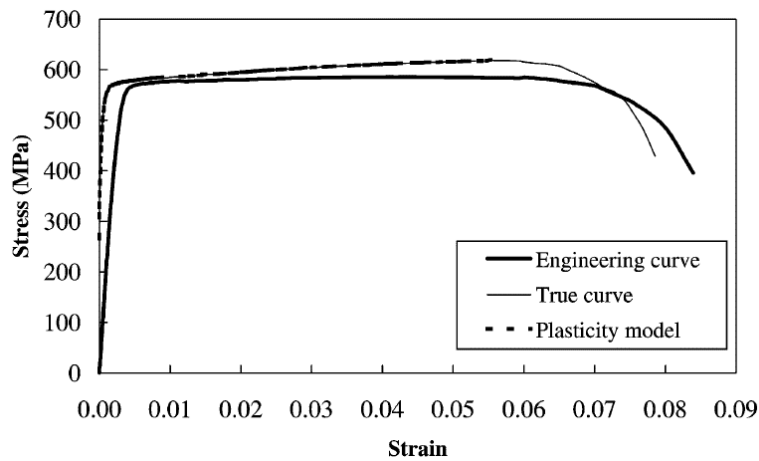
Figure 2. Modeling of material plasticity for test Series P36

3.5. Modeling of Initial Local and Overall Geometric Imperfections

The geometric imperfections were included in the FEM by using a linear perturbation analysis. The main purpose of the perturbation analysis was to establish probable buckling modes (eigenmode) of the column. The eigenmode was then scaled by a factor (scale factor) to obtain a perturbed mesh of the column for the non-linear analysis. Eigenmode 1 was used in the FEM, in which local or overall buckling mode was predicted from the analysis.

4. RESULTS AND DISCUSSIONS

4.1. Comparison of experimental results with finite element analysis results

In the verification of the finite element model, a total of 8 cold-formed steel plain channel columns were analyzed. The incremental plasticity models obtained from the true stress–strain curves were used in the FEM for the corresponding test series. A scale factor of 25% of the plate thickness was used in modeling the geometric imperfections of the columns. A comparison between the experimental results and the results of the finite element model is carried out. The main objective of this comparison is to verify and check the accuracy of the finite element model. The ultimate loads (P_{fem}) predicted by the FEA are compared with the experimental ultimate loads (P_{test}) as shown in Table 3 for Series P36 and P48, respectively. The mean values of the P_{test}/P_{fem} ratio are 1,014 and 1,046 with the corresponding coefficients of variation (COV) of 0,0016 and 0,0096 for Series P36 and P48, respectively. Generally, good agreement has been achieved for most of the columns. Three modes of failure were reported by Young and Rasmussen [7] and verified by the finite element model. The failure modes are the local buckling, flexural buckling and flexural-torsional buckling.

Figure 3 plotted the relationship between the ultimate load and the column effective length $L_{eff}=L$ for channels reported by Young and Rasmussen [2] where L actual column length. The column curves show the experimental ultimate loads together with that obtained by the finite element method. It can be seen that good agreement has been achieved between both results for most of the columns.

Table 3. Comparison between Test and FE Results

| Specimen	B_f (mm)	B_w (mm)	t (mm)	r_i (mm)	L (mm)	A (mm^2)	P_{test} (kN)	P_{fem} (kN)	P_{test}/P_{fem}
P36P0280	36,9	96,6	1,51	0,85	280	247	55,2	54,1	1,02
P36P0315	37,0	96,8	1,50	0,85	315	245	52,1	53,2	0,98
P36P0815	36,8	97,5	1,51	0,85	815	249	40,9	38,3	1,07
P36P1315	37,0	96,6	1,50	0,85	1315	245	27,0	27,3	0,99
Mean									1,014
COV									0,0016
P48P0300	49,6	94,8	1,51	1,46	300	279	45,2	47,0	0,96
P48P0565	49,8	94,5	1,53	1,48	565	283	38,6	39,5	0,98
P48P1065	50,0	94,2	1,52	1,48	1065	282	33,9	31,6	1,07
P48P1565	49,4	95,1	1,52	1,47	1565	281	31,2	26,6	1,17
Mean									1,046
COV									0,0096
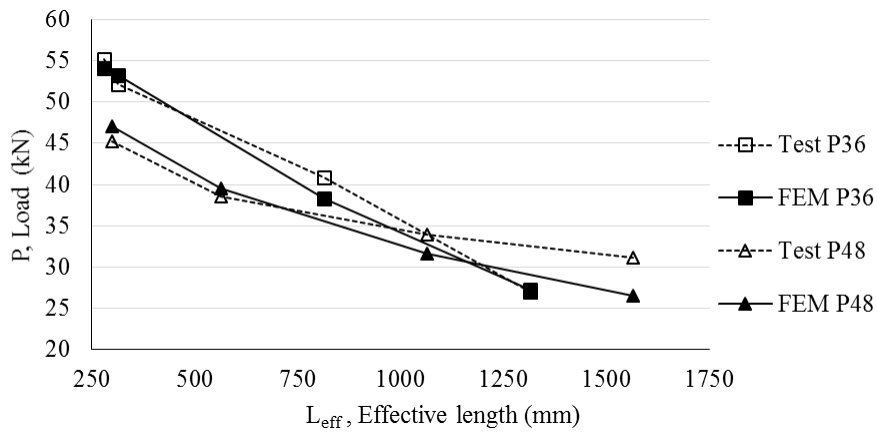
Figure 3. Comparison of experimental results with FEM results.

Figure 4 shows the ultimate load against the axial shortening behavior of column P48P0565 that has a length of 565 mm. The curve has been predicted by the finite element model and compared with the test results. The experimental ultimate load was 38,6 kN compared with 39,5 kN predicted by the finite element analysis. The failure mode of the test specimen P48P0565 was reported as a flexural buckling. The same failure mode has been confirmed numerically by the model as shown in Figure 5.
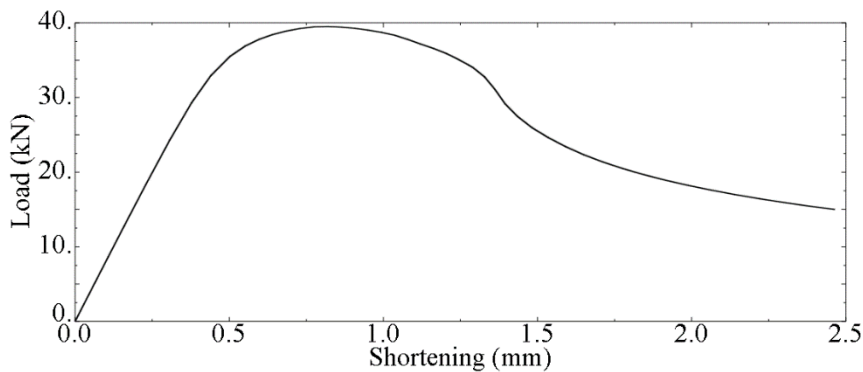

Figure 4. Load-axial shortening curve for P48P0565.
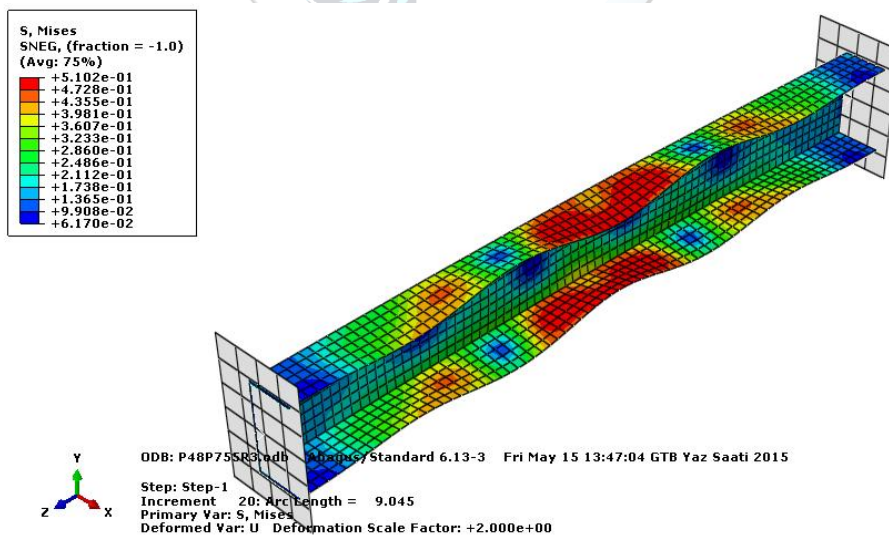

Figure 5. Failure mode of column P48P0565.

4.2. Design Rules

EN1993-1-3 [10] represents the unified European Code for cold-formed steel design, and contains specific provisions for structural applications using cold-formed steel products made from coated or uncoated thin gauge hot or cold-rolled sheet

and strip. In EN1993-1-3, cross sections subject to combined axial compression N_{Ed} and bending moments $M_{y,Ed}$ and $M_{z,Ed}$ should satisfy the criterion:

$$\frac{N_{Ed}}{N_{c,Rd}} + \frac{M_{y,Ed} + \Delta M_{y,Ed}}{M_{cy,Rd,com}} + \frac{M_{z,Ed} + \Delta M_{z,Ed}}{M_{cz,Rd,com}} \leq 1.0 \tag{3}$$

in which

N_{Ed} : design value of the compression force,

$N_{c,Rd}$: design compression resistance of a cross section,

$M_{y,Ed}$: applied bending moment about the major axis,

$M_{z,Ed}$: applied bending moment about the minor axis,

$M_{cy,Rd,com}$: moment resistances for the maximum compressive stress in a cross section that is subject only to moment about the y-y axis

$M_{cz,Rd,com}$: moment resistances for the maximum compressive stress in a cross section that is subject only to moment about the z-z axis

The additional moments $\Delta M_{y,Ed}$ and $\Delta M_{z,Ed}$ due to shifts of the effective centroidal axes should be taken as:

$$\Delta M_{y,Ed} = N_{Ed} \cdot e_{Ny} \tag{4}$$

$$\Delta M_{z,Ed} = N_{Ed} \cdot e_{Nz} \tag{5}$$

in which e_{Ny} and e_{Nz} are the shifts of y-y and z-z centroidal axis of the effective cross section relative to the gross cross section.

If $M_{cy,Rd,ten} \leq M_{cy,Rd,com}$ or $M_{cz,Rd,ten} \leq M_{cz,Rd,com}$ the following criterion should also be satisfied:

$$\frac{M_{y,Ed} + \Delta M_{y,Ed}}{M_{cy,Rd,ten}} + \frac{M_{z,Ed} + \Delta M_{z,Ed}}{M_{cz,Rd,ten}} - \frac{N_{Ed}}{N_{c,Rd}} \leq 1.0 \tag{6}$$

in which

$M_{cy,Rd,ten}$: design moment resistance of a cross section for maximum tensile stress if subject only to moment about the y-y axis,

$M_{cz,Rd,ten}$: design moment resistance of a cross section for maximum tensile stress if subject only to moment about the z-z axis.

4.3. Parametric Study and Discussions

It is shown that the FE model closely predicted the behavior of plain U-section columns compared with the test results. Hence parametric studies were carried out to study the effects of load eccentricity on the strength and behavior of U-section columns. A total of 8 plain U-section columns was performed in the parametric study. Two series of columns P36 and P48 were studied. All U-sections had same geometric properties as the test specimens. The load eccentricity with respect to the major principal axis, e_x were selected as 10.27 and 11.97 for series P36 and P48, respectively. P36 series of columns consists of four column lengths of 280, 315, 815, and 1315 mm, whereas P48 series of columns consists of four column lengths of 300, 565, 1065, and 1565 mm. A scale factor of 25% of the plate thickness was used in modeling the geometric imperfections of the columns. The residual stresses were not considered since its effect on the column capacity and load-shortening behavior is negligible. The measured stress strain curves of series P36 and P48 were used in all parametric studies. A summary of the parametric study results is presented in Table 4. Slenderness (λ) and the ultimate loads (P_{fem-e}) of the U-sections are given in Table 4.

The results of the parametric study are compared with the design strengths obtained using the European Code, EN1993-1-3. It can be seen that the EN1993-1-3 design strengths ($P_{EN-1993-1-3}$) are generally quite conservative for U-section columns as shown in Table 4.

Table 4. Parametric study results of eccentrically loaded U-sections.

Specimen	L (mm)	λ	e_x (mm)	P_{fem-e} (kN)	$P_{EN1993-1-3}$ (kN)	$P_{fem-e}/ P_{EN1993-1-3}$
P36P0280	280	42	10,27	25,50	12,1	2,11
P36P0315	315	45	10,27	25,20	12,1	2,08
P36P0815	815	90	10,27	18,60	12,1	1,54
P36P1315	1315	134	10,27	18,70	12,1	1,55
P48P0300	300	31	11,97	24,90	13,2	1,89

P48P0565	565	48	11,97	26,70	13,2	2,02
P48P1065	1065	80	11,97	16,80	13,2	1,27
P48P1565	1565	111	11,97	13,40	13,2	1,02

5. CONCLUSIONS

This paper provides an efficient nonlinear finite element model for understanding the behavior of eccentrically loaded single U-sections. Theoretical buckling and the experimental failure loads of pin ended, concentrically loaded U-sections were predicted by eigenvalue and load-deformation analyses of various models developed in ABAQUS 6.13. The U-sections were modeled by shell elements considering geometrically and materially nonlinear behavior. Initial imperfections, end support conditions, geometry and material property variation of the U-sections were included differently in each model. The load-carrying capacity of eccentrically loaded single U-sections are investigated by performing an extensive parametric study obtaining the most realistic estimations. The results of the parametric study are compared with the design strengths obtained using the European Code, EN1993-1-3. It is seen that the EN1993-1-3 design strengths are quite conservative for U-section columns.

ACKNOWLEDGMENT

REFERENCES

[1]. ABAQUS Standard User's Manual. (2013). Hibbit. Karlsson and Sorensen. Inc.. Vols. 1. 2 and 3. Version 6.13.

[2]. Young, B., & Rasmussen, K. J. (1998). Tests of fixed-ended plain channel columns. *Journal of Structural Engineering*, 124(2), 131-139.

[3]. Australian Standard. (1993). *Steel Sheet and Strip—Hot-dipped Zinc-coated or Aluminium/Zinc-coated*. AS 1397. Standards Association of Australia. Sydney. Australia.

[4]. Australian Standard. (1991). *Methods for Tensile Testing of Metals*. AS 1391. Standards Association of Australia. Sydney. Australia.

[5]. Young, B., & Rasmussen, K. J. R. (1995a). Compression Tests of Fixed-Ended and Pin Ended Cold-Formed Lipped Channels. Research Report-University of Sydney School of Civil and Mining Engineering R.

[6]. Young, B., & Rasmussen, K. J. R. (1995b). *Compression tests of fixed-ended and pin-ended cold-formed plain channels*. Research Report-University of Sydney School of Civil and Mining Engineering R.

[7]. Young, B., & Rasmussen, K. J. (1999). Behaviour of cold-formed singly symmetric columns. *Thin-walled structures*, 33(2), 83-102.

[8]. Nandula. R. (1998). *Finite Element Analysis of Eccentrically Loaded Angles*. M.S. Thesis. University of Windsor. Windsor. Ontario. Canada.

[9]. Young, B., & Yan, J. (2002). Finite element analysis and design of fixed-ended plain channel columns. *Finite elements in analysis and design*, 38(6), 549-566.

[10]. CEN (2006). *Eurocode 3: Design of steel structures. Part 1-3: General Rules. Supplementary rules for cold-formed thin gauge members and sheeting*, EN 1993-1-3:2006. European Committee for Standardization, Brussels, Belgium.

BIOGRAPHY

Assist. Prof. Dr. Mustafa DURMAZ was born on 1st September, 1977 in Gebze, Kocaeli. He studied his elementary studies at the Eşrefbey Primary School, his secondary school studies at the Sarkuysan Secondary School and completed his high school at the Gebze Technical and Industrial Vocational High School. Mustafa DURMAZ graduated from the Department of Civil Engineering in 2000 (B.Sc.) of the Karadeniz Technical University (KTU), and obtained his M.Sc. Degree from the Department of Civil Engineering in 2003. He obtained his Ph.D. in 2011 at the Department of Civil Engineering of the KTU. He started his academic career as Research Assistant in Department of Civil Engineering of KTU Engineering Faculty in 2000. In the Department of Civil Engineering of Gümüşhane University Engineering Faculty, he was promoted to the rank of Assistant Professor in 2012. He has been serving as Vice Head of Department at the Department of Civil Engineering since 2013. He is married and has two children.

Tribological Properties of Boron Carbide Reinforced Copper Based Composites

Huseyin Ipek[1*] , Hamdullah Cuvalci[1], Cemal Celebi[2]

[1]*Karadeniz Technical University,Department of Metallurgical and Materials Engineering 61080, Ortahisat/Trabzon, Turkey.*

[2]*Certificated Engineer 27100, Merkez/Gaziantep, Turkey.*

*CorrespondingAuthor email: hipek@ktu.edu.tr

Abstract

In this study, a boron carbide (B4C) reinforced copper based Metal Matrix Composites (MMCs) manufactured by powder metallurgy method and tribological behavior of compacted composites were investigated. B4C reinforcement was selected at different ratio from 2%wt to 10%wt. Powders was compacted under 735±1 MPa pressure in a die with cold pressing method. Sintering of the samples was performed at two different sintering time as 1 hour and 3 hours under Ar gas atmosphere at 900 °C. Tribological tests were performed by using a computer aided pin-on-disc experimental setup under dry sliding conditions. Tribological tests were performed from 1 hour to 5 hours. And wearing surfaces were investigated in a Scanning Electron Microscope SEM) and mechanisms of the wear were detected. In addition to that tribological behavior and porosity properties of the manufactured samples were investigated. It was found that the porosity of the samples was increased with increasing B4C content. Nevertheless, wear resistivity increased with increasing reinforcement content.

1. INTRODUCTION

Because of the unique properties of the Metal Matrix Composites (MMCs) have many application in industry [1, 2]. Most of the studies in industrial components should have good mechanical properties with better tribological properties [3]. The need for a recent wear resistant material for high performance tribological applications has been one of the major propellant power for the tribological development of ceramic particulate reinforced materials [4]. The introduction of hard, non-deformable ceramic particles into matrix alloy causes a loss in ductility and toughness of MMCs [5]. But the optimum ratio usage of the reinforcement particles could assist wear performance with a toughness. Matrix materials of the MMCs generally selected for their high thermal conductivity and ductility properties as copper, nickel and aluminum [6]. And reinforcement materials should be harder than matrix for the supporting the structure of composite as SiC, B4C Si3N4, Al2O3 and TiC [7].

In this study, copper and B4C was selected as a matrix and reinforcement materials, respectively. Copper-based materials are widely used in many industrial applications because of their good wear resistance and friction ductility, remarkable corrosion resistance, as well as self-lubrication properties, such as sliding bearings, sleeves, brushes and other components [8-10]. B4C reinforcement material was selected for its tribological and mechanical properties [4, 11]. Moreover, B4C particles have high impact and wear, low density, high melting point, and excellent resistance to chemical agents as well as high capability for neutron absorption make boron carbide attracting much attention as an acceptable reinforcement [12].

Wear and friction are the common problem in industry [13, 14]. And wear shows itself in two different way, abrasive and adhesive. [15, 16]. Adhesive wear cause surface deformation with separation of the surface by layers but the abrasive wear cause separation of the particles from surface by scratching [17]. Main motivation and the novelty of the study was determine of the wearing performance of the Cu-B4C MMCs with a pin-on-disc wearing test machine.

2. EXPERIMENTAL DETAILS

In this study, MMCs was manufactured. Copper as matrix and boron carbide (B4C) as reinforcement were selected at different ration (2%, 4%, 6%, 8% and 10%). 0,1mg precisions balance was used for weighting operations. Composites were mixed about 8-10 min. with mechanically. Mold was lubricated with a solid lubricant before molding. Manufacturing parameters and wearing parameter was given Table 1.

Table 1. Manufacturing and wearing parameters.

	Sintering Time (h)	Molding Pressure (MPa)	Sintering Temperature (ºC)	Wearing Time (h)	Wearing Load (N)
Cupper (pure)	1			-	-
	3				
Composites (2%, 4%, 6%, 8% and 10%)	1	735	900	1-5	50 ±5
	3				

Samples were sintered at 900 ºC. Argon atmosphere were selected for preventing the dirtiness during sintering process. Different sintering time and molding pressure were applied. Hardness of the samples was measured with Brinell Hardness method. Porosity of the samples was calculated with experimentally.

Samples experimental density was measured with formula 1.

$$\rho = m/V \qquad (1)$$

Where, ρ (g/cm3) density, m (g) mass and V (cm3) volume. Composites theoretical density was calculated with formula 2.

$$\rho T = [(\% \ wt \ Cu \ . \ \rho 1 \ ) + (\% \ wt \ B4C. \ \rho 2)] \qquad (2)$$

Where, ρT theoretical density, wt (g) mass, ρ1 and ρ2 (g/cm3) copper and B4C densities. Then formula 3 can be used for calculate the porosity of the samples.

$$\% \ porozite = (\Delta\rho/\rho0)x100 \qquad (3)$$

Where, Δρ difference between theoretical density and experimental density, ρ0 theoretical density.

Pin-on-disc wear method was run for wearing process. Samples were cut suitable for sample (pin) holder about 10mm x 10mm x40mm. Pin track diameter was selected as 100 mm. with 100 rpm working speed (≈0,5m/s). Cold work tool steel disc was used for wearing. Running in process was applied before wearing. Running in and experiments were carried out 50±5 N load.

3. RESULT AND DISCUSSION

3.1. 3.1. Structural Investigation

Structural investigations of the composites were performed with a Leica named optical system and the images of the structures were given in Figure 1. Figures show the different reinforcement ratio of the B4C.
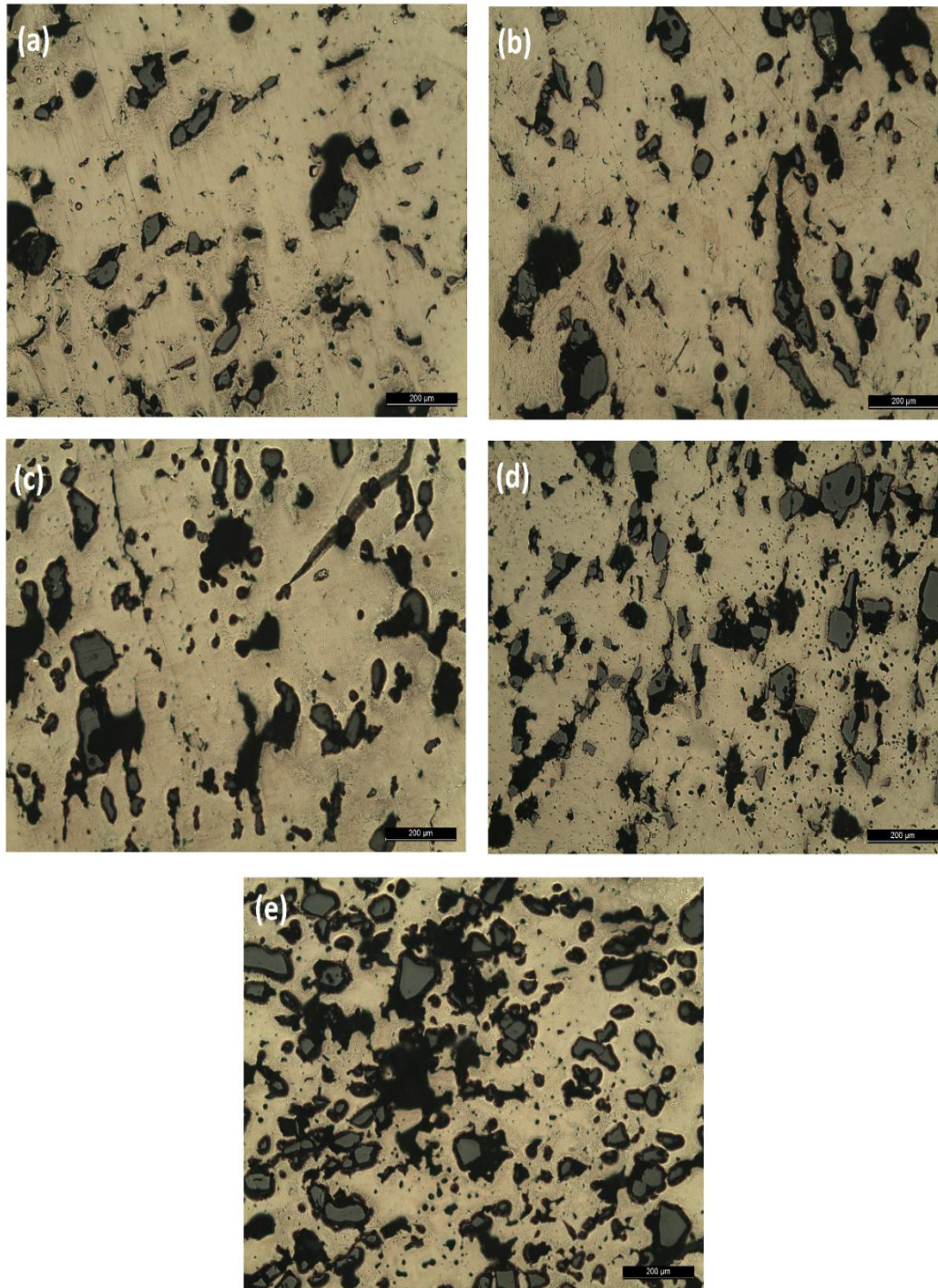
Figure 1. Optical microscope images of the composites (1 hour sintering time)(a-2%, b-4%, c-6%, d-8%, e-10%) (10x)

Investigated macrostructure images show that the effect of reinforcement. Images show that porosity (dark areas) was increased with increasing reinforcement B4C particles (grey areas).

3.2. SEM Investigation

Scanning Electron Microscope (SEM) investigations was imaged after wear tests. And Figure 2 shows the worn surface of the composites under dry sliding conditions.
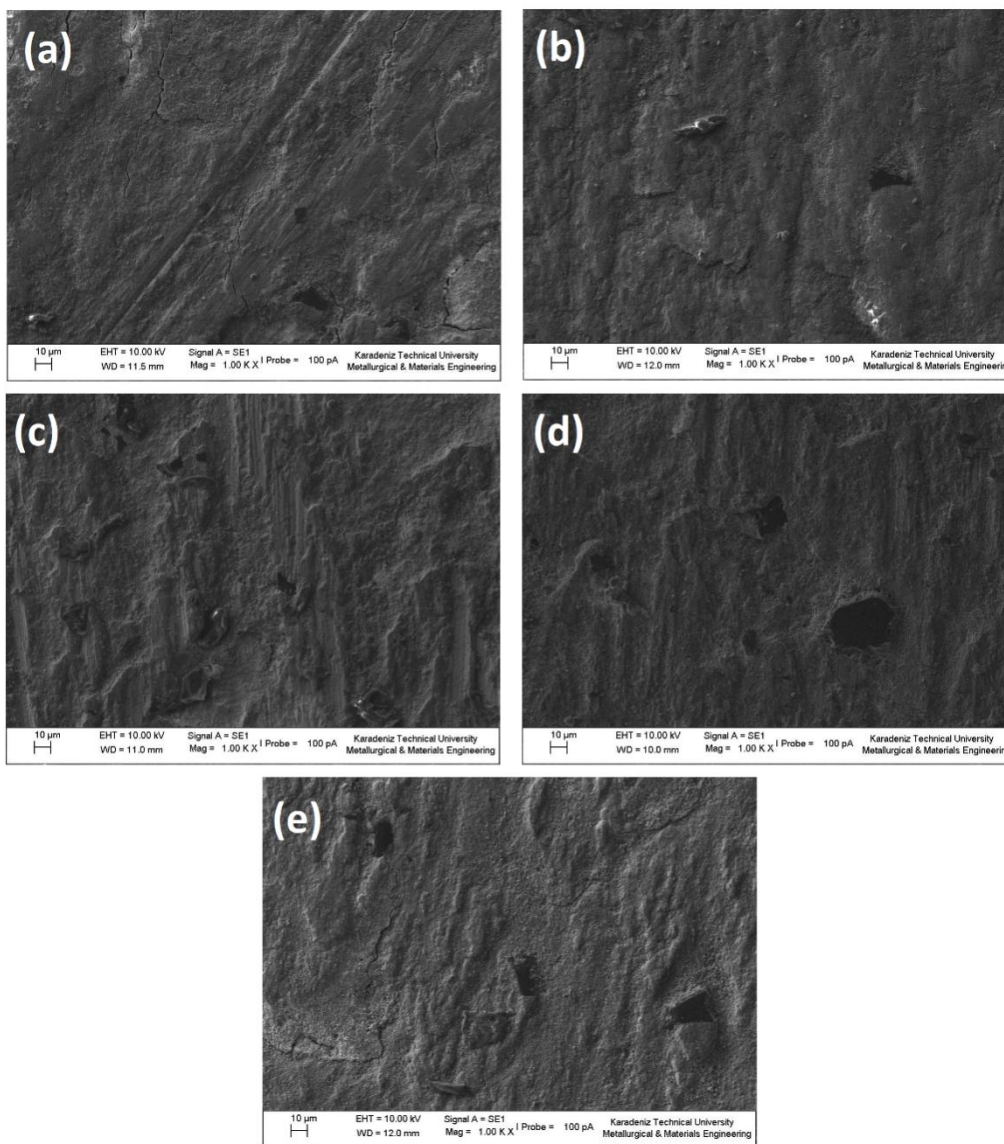
Figure 2. Worn surface of the composites which was manufactured with 1 hour sintering time (a-2%, b-4%, c-6%, d-8%, e-10%) (1000x)

3.3. Porosity

Porosity of the samples was calculated with formulas 1, 2 and 3. The graphical explanation was given in Figure 3.
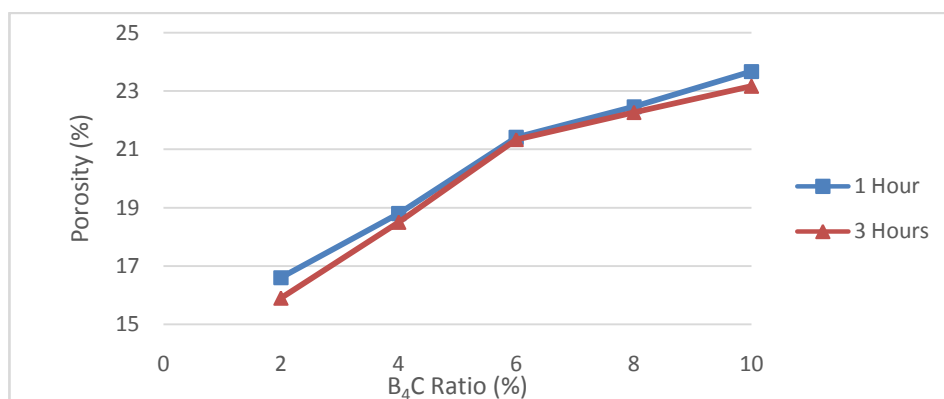

Figure 3. Porosity ratio of the samples

Porosity of the samples was increased with the increasing reinforcement ratio. And pure compacted copper porosity was calculated as 10.05%

3.4. Hardness

Hardness of the samples was measured with Brinell Hardness test method. And the hardness of the samples was given in Table 4.

Table 2. Hardness value of the samples

Sample	HB	
	1 hour sintering time	3 hour sintering time
Pure compacted copper	32	24
2 %	42	33
4 %	51	53
6 %	53	55
8 %	56	84
10 %	57	86

3.5. Wear Loss

The wear investigation of the samples was performed under dry sliding conditions. Wear loss was measured hour by hour and mass loss was found. Finding of the mass loss was converted to the wear rate. Wear rate formula was given in Formula 4.

Wear Rate $(mm^3 \, m^{-1})$ = mass loss (g) / [density (g/mm^3) x sliding distance (m)]   (4)

With the conversion of mass loss to the wear rate Figure 4 and 5 was obtained.
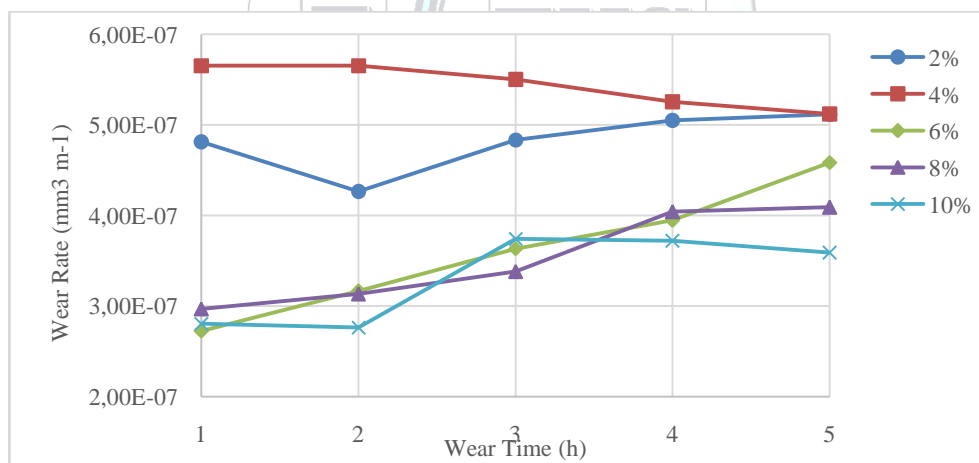
Figure 4.Effect of the sintering time to the wear rate (1 h sintering time)

Average wear rate of the samples was showed that minimum wear rate for 10% reinforced sample. 2% and 4% samples was showed higher wear rate and the ratio of the wear was decreased with increasing wear time. By the contrast with, samples which was reinforced in proportion as 6%, 8%, 10% showed that increasing wear rate with the increasing wear time. It means, B_4C particles was removed from surface with the vibration and cause some deep scratching and erosion.

Figure 5. Effect of the sintering time to the wear rate (3 h sintering time)

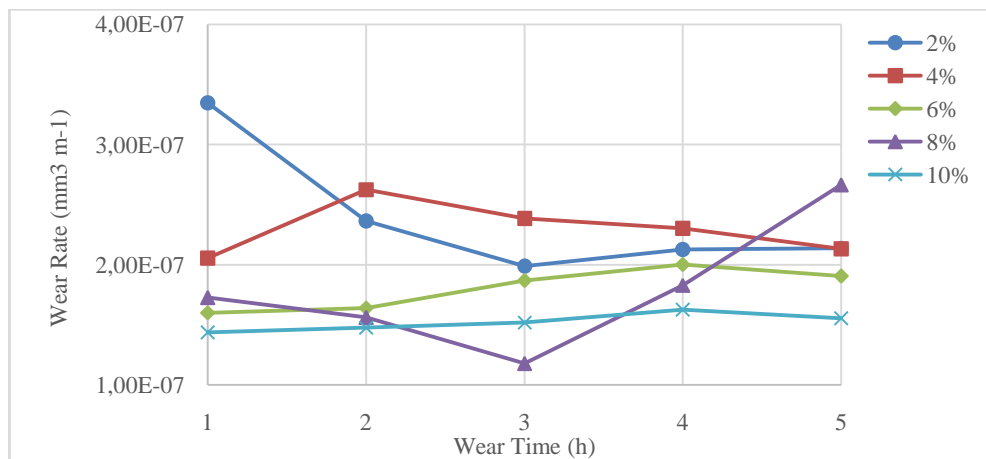Figure 5 shows that the sintering effect on the samples and it was detected decreasing wear rate with increasing sintering time. Average wear rate was showed minimum wear rate for 10% reinforced sample as Figure 4. But the average wear rate was less than Figure 4 about almost 46%. And all samples difference was less according the 1 hour sintered. Also Figure 3 showed that sintering effect on porosity. So increasing sintering time cause less pore, high hardness and high wear resistivity.

4. CONCLUSIONS

Copper and B_4C reinforced copper based metal matrix composites was manufactured with different sintering time. Hardness and porosity measurement was performed for all samples. But tribological tests was applied for the composites and the conclusion was found:

1.) Porosity of the composites were increased with increasing reinforcement ratio.

2.) Hardness of the composites were increased with increasing sintering time.

3.) Wear loss was decreased with increasing sintering time.

REFERENCES

[1] A. Baradeswaran, A.E.P., *Influence of B4C on the tribological and mechanical properties of Al 7075–B₄C composites.* 2013.

[2] Varol, T. and A. Canakci, *Effect of particle size and ratio of B₄C reinforcement on properties and morphology of nanocrystalline Al2024-B4C composite powders.* Powder Technology, 2013. **246**: p. 462-472.

[3] A. Baradeswaran, S.C.V.b., A. Elaya Perumal, N. Selvakumar, R. Franklin Issac, *Experimental investigation on mechanical behaviour, modelling and optimization of wear parameters of B₄C and graphite reinforced aluminium hybrid composites.* 2014.

[4] M. Uthayakumara, S. Aravindan b, K. Rajkumarb, *Wear performance of Al–SiC–B₄C hybrid composites under dry sliding conditions.* 2013.

[5] R. Sathıskumar, N.M., I.Dınaharan, S.J. Vıjay, *Fabrıcatıon And Characterızatıon Of Cu/B₄C Surface Dıspersıon Strengthened Composıte Usıng Frıctıon Stır Processıng.* 2014.

[6] Huiying Zhu, Y.N., Chucheng Lin, Liping Huang, Heng Ji, Xuebin Zhengn, *Microstructures and tribological properties of vacuum plasma sprayed B₄C–Ni composite coatings.* 2013.

[7] Gode, C., *Mechanical properties of hot pressed SiCp and B₄Cp/Alumix 123 composites alloyed with minor Zr.* Composites Part B-Engineering, 2013. **54**: p. 34-40.

[8] Canakci, A., et al., *Synthesis of novel CuSn10-graphite nanocomposite powders by mechanical alloying.* Micro & Nano Letters, 2014. **9**(2): p. 109-112.

[9] Sathiskumar, R., et al., *Characterization of boron carbide particulate reinforced in situ copper surface composites synthesized using friction stir processing.* Materials Characterization, 2013. **84**: p. 16-27.

[10] H.R. Akramifard, M.S., ⇑, M. Sabbaghian a,b, M. Esmailzadeh b,c, *Microstructure and mechanical properties of Cu/SiC metal matrix composite fabricated via friction stir processing.* 2014.

[11] L. M. Manocha, G.P., and S. Manocha, *Carbon-Ceramic Composites for Friction Applications.* 2014.

[12] Ali Mazahery, M.O.S., *Influence of the hard coated B₄C particulates on wear resistance of Al–Cu alloys.* 2012.

[13] Canakci, A., et al., *Microstructure and Abrasive Wear Behavior of CuSn10-Graphite Composites Produced by Powder Metallurgy.* Powder Metallurgy and Metal Ceramics, 2014. **53**(5-6): p. 275-287.

[14] Unal, H. and A. Mimaroglu, *Friction and wear performance of polyamide 6 and graphite and wax polyamide 6 composites under dry sliding conditions.* Wear, 2012. **289**: p. 132-137.

[15] Cuvalci, H. and H.S. Celik, *Investigation of the abrasive wear behaviour of ZA-27 alloy and CuSn10 bronze.* Journal of Materials Science, 2011. **46**(14): p. 4850-4857.

[16] Cuvalci, H. and H. Bas, *Investigation of the tribological properties of silicon containing zinc-aluminum based journal bearings.* Tribology International, 2004. **37**(6): p. 433-440.

[17] Patnaik, A., et al., *Tribo-performance of polyester hybrid composites: Damage assessment and parameter optimization using Taguchi design.* Materials & Design, 2009. **30**(1): p. 57-67.

Performance of Nitrogen and Phosphorus Removal of Moving Bed Biofilm Reactor Operated as Sequencing Batch

Muslun Sara Tunc[1]*, Ayhan Unlu[1]

[1]Fırat University, Department of Environmental Engineering, 23119, Elazığ, Turkey.

CorrespondingAuthor email:saratunc@firat.edu.tr

Abstract

In this study, nitrogen and phosphorus removal from municipal wastewater in moving bed biofilm reactor operated as sequencing batch was investigated. Kaldnes (K1) material as biofilm carrier media was used in the study. Operation consisted of anaerobic/aerobic/anoxic/aerobic phases with hydraulic residence times of 120 min/330 min/210 min/50 min. In the moving bed biofilm reactor with the filling ratio of 50% operated as sequencing batch, average effluent chemical oxygen demand (COD), ammonium-nitrogen (NH4-N), nitrite-nitrogen (NO2-N), nitrate-nitrogen (NO3-N) and phosphate-phosphorus (PO4-P) values after the cycle duration of 12 h were determined to be 27 mg/L, 0.7 mg/L, 0.04 mg/L, 0.6 mg/L and 0.7 mg/L, respectively. The average COD, NH4-N and PO4-P removal efficiencies were obtained as 92%, 97.5% and 91.3%, respectively.

1. INTRODUCTION

Nitrogen and phosphorus are commonly present in wastewater streams such as municipal, industrial and agricultural wastewaters [1]. When untreated or insufficiently treated wastewater discharges to water bodies such as lake and river, it causes several problems such as eutrophication and the depletion of dissolved oxygen [2]. Therefore, removal of these contaminants from wastewaters for reducing their damage to the environment is of great importance [3, 4].

In order to improve the quality of treated wastewater and meet the demands of environmental regulations, advanced treatment technologies have been developed [2]. The moving bed biofilm reactor (MBBR) having advantages of both attached and suspended growth systems is one of the advanced wastewater treatment process [5]. It is filled with carrier materials, on which biomass is attached, and freely move and circulate in the reactor by aeration in aerobic process or mechanical stirring in anoxic/anaerobic process. The carrier materials are kept inside the reactor by means of a sieve placed outlet of the reactor [6]. The MBBR relies on the attachment of biomass on plastic carriers, which allows retaining a significant amount of active biomass in the reactor regardless of the hydraulic conditions. This feature is very attractive for preventing washout of slow growing microorganisms like nitrifiers from the process [7]. It is a continuously operating, non-cloggable biofilm reactor with no need for backwashing, low head-loss and a high specific biofilm surface area [5]. It has some advantages such as a shorter hydraulic retention time (HRT), higher organic loading rates, a higher nitrification rate and larger surface area for mass transfer [8]. It has been widely applied to treat both municipal and industrial wastewaters due to the advantages of the attached growth process such as compact, stable removal efficiency and simplicity of operation without its limitations such as medium channeling and clogging [3, 9]. Also, it has been used for upgrading and retrofitting existing wastewater treatment plants due to having advantages of both suspended and attached growth systems [6, 10].

Nitrogen is removed by the combination of nitrification by autotrophs under aerobic conditions and denitrification by heterotrophs under anaerobic conditions. Phosphorus removal is achieved by its uptake into biomass which can be discharged from the system as a surplus sludge. It is possible that nitrification, denitrification and phosphorus removal are achieved in one reactor when a sequencing batch reactor system (SBR) is used [11]. SBR systems have been modified to

achieve nitrification and denitrification as well as COD and phosphate removal because of regulations on nutrient discharge limitations. When biological nutrient removal is desired, its cycle format can be flexibly adjusted to provide anaerobic, anoxic and aerobic phases in certain number and sequence [12]. Among various biological treatment systems, they have many advantages such as lower capital and operational costs and less bulking [1, 11, 13]. Over the years, many efforts have been made to modify the SBR system to improve the performance. Among others, the moving bed sequencing batch reactor (MBSBR) which incorporates both suspended-growth and attached-growth processes has attracted much interest among researchers in the field of wastewater treatment [1]. Nitrification and denitrification can also be successfully achieved in biofilm-based processes because nitrifiers, which are slow growing microorganisms, are retained by the biofilm [5].

In this study, removal of nitrogen and phosphorus from municipal wastewater was investigated in the moving bed biofilm reactor operated in the sequencing batch mode.

2. MATERIALS AND METHODS

2.1. Experimental Set-up and Operation

A schematic diagram of the experimental set up is depicted in Fig. 1. The reactor used in the study was made of plexiglass material and had a working volume of 1 L. The carrier elements, called K1, were used as support materials to provide a surface for biofilm growth in the moving bed biofilm reactor (MBBR). The reactor was filled with 50% carrier elements.
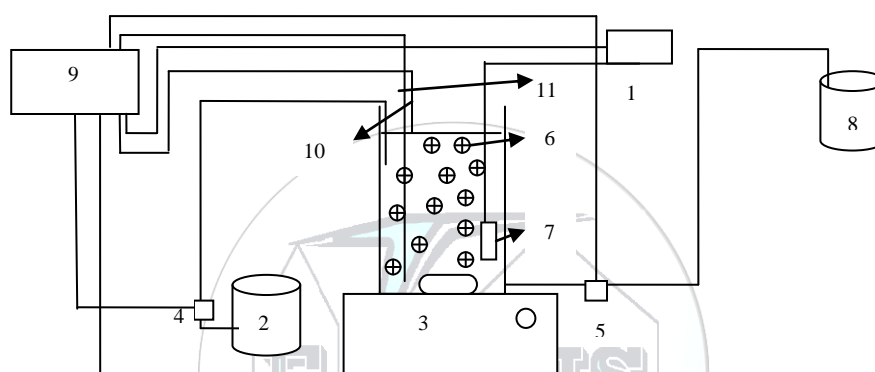

Figure 1. Schematic diagram of experimental set up. 1. air pump; 2. feed tank; 3. magnetic stirrer; 4. dosage pump, 5. drawing pump; 6. biofilm carrier materials; 7. air stone, 8. effluent tank; 9. programmable logic device; 10. filling level electrode; 11. drawing level electrode,

The reactor was inoculated with activated sludge taken from the secondary settling tank of the municipal wastewater treatment plant in Malatya, Turkey. The reactor was operated in a sequencing batch mode for COD, nitrogen and phosphorus removal. An operation cycle comprised a filling, reaction and drawing period. Reaction period consisted of anaerobic/aerobic/anoxic/aerobic phases with hydraulic residence times of 120 min/330 min/210 min/50 min. The filling plus drawing period was 10 minute. The MBBR was operated under hydraulic retention times of 12 h. The reactor was completely drained during drawing period at the end of each cycle. Aeration was supplied by air stone placed in the reactor by using an aquarium air pump. Airflow rate was controlled by rotometer. The alternation between aerobic, anoxic and anaerobic conditions was provided by the on and off control of the air pump. To make it work this way, the programmable logic device was used. The feed tank was filled periodically with the effluents collected from primary settler tank of the municipal wastewater plant in Elazığ, Turkey. Sufficient amount of ethanol solution was added in the reactor as an external carbon source at the beginning of the anoxic phase to reduce oxidized nitrogen (NO_2-N+NO_3-N) to nitrogen gas.

2.2. Biofilm Carrier

The carrier, called K1, was used in this study. The carrier was made from polyethylene with a density of 0.96 g/cm^3 slightly lower than the density of water and had an effective surface of 500 m^2/m^3. It was cylindrical with internal walls and external fins that protect the biofilm from abrasion. With a filling ratio of 50%, the available surface area (referred to the reactor volume) was 250 m^2/m^3.

2.3. Wastewater Characteristics

The study was carried out using wastewater collected from the primary settler tank of municipal wastewater plant in Elazığ, Turkey. The wastewater had chemical oxygen demand (COD) in the range of 328-336 mg/L, ammonium-nitrogen (NH_4-N) in the range of 17.3-21.7 mg/L, phosphate-phosphorus in the range of 8.7-10.8. The samples were stored in a refrigerator at 4 °C until use.

2.4. Analytical Methods

Samples were taken from the reactor at the beginning and at the end of anaerobic, aerobic and anoxic phases. To remove microorganisms from the mixed liquid medium, these samples were centrifuged at 5000 rpm for 10 min. Supernatants were analyzed for COD, ammonium-nitrogen, nitrite-nitrogen, nitrate-nitrogen and phosphate-phosphorus contents. The concentration of COD and total suspended solids (TSS) in the liquid phase was determined in accordance with Standard Methods for Examination of Water and Wastewater [14]. In order to determine the amount of the biofilm in the reactor, 10 carrier materials taken from reactor was dried at 70 ^{o}C for 48 h and weighed. The higher temperature was not used because of deformation risk of the carrier materials [15]. It was subsequently cleaned to remove the attached biofilm, followed by drying and weighing again. Then, biofilm amount was calculated taking into account the number of elements per liter. The nitrogen species (ammonium-nitrogen (NH_4-N), nitrite-nitrogen (NO_2-N) and nitrate-nitrogen (NO_3-N)) and phosphate-phosphorus (PO_4-P) were measured by standard test kits (Merck Spectroquant) using Nova 60 Spectroquant. The dissolved oxygen concentration and pH in the reactor were measured using an O_2 electrode and a pH electrode by a multimeter (Hach HQ40D).

3. RESULTS AND DISCUSSION

3.1. COD Removal

Effluent COD concentration and COD removal efficiency obtained in the moving bed biofilm reactor operated as the sequencing batch are depicted in Fig. 1. Effluent COD concentration obtained after 12-h cycle changed in the range of 16 to 32 mg/L. Average effluent COD concentration was 27 mg/L. COD removal efficiency changed in the range of 90.5-95.2%, with average removal efficiency of 92%. Effluent TSS concentration varied in the range of 220 to 280 mg/L. The average amount of biomass attached to the carrier materials was 3.1 kg/m^3.
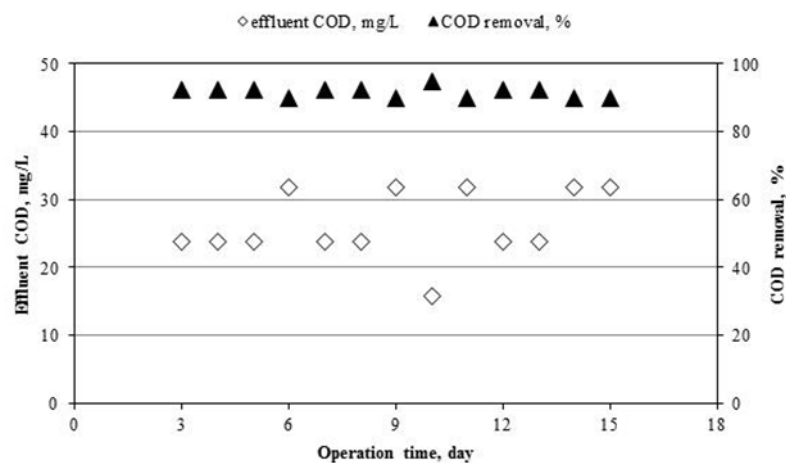
Figure 2. Effluent COD concentrations and COD removal obtained by MBBR operated as sequencing batch

3.2. Nitrogen Removal

Variation of effluent NH_4-N, NO_2-N and NO_3-N concentration and NH_4-N removal efficiency obtained is depicted in Fig 3. Effluent NH_4-N concentration varied between 0.1 and 0.8 mg/L, with average effluent level of 0.7 mg/L. Effluent NO_2-N and NO_3-N concentration changed in range of 0.01-0.1 mg/L and 0.1-1.8 mg/L, respectively. Average effluent level of NO_2-N and NO_3-N was observed to be 0.04 mg/L and 0.6 mg/L. NH_4-N removal efficiency varied between 96% and 99.5%, with average removal efficiency of 97.5%. As can be seen from the results obtained, nitrogen removal from the municipal wastewater can be removed by moving bed biofilm reactor operated in the sequencing batch mode with the cycle of 12 h.

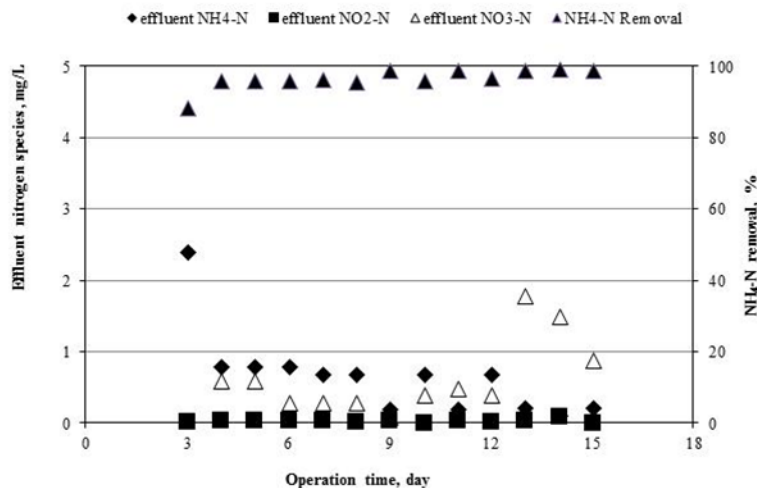*Figure 3. Concentrations of effluent nitrogen species and NH₄-N removal obtained by MBBR operated as sequencing batch*

Biological nitrogen removal from wastewater is achieved by nitrification under aerobic conditions and heterotrophic denitrification under anaerobic conditions [1, 16]. Nitrification is a process consists of two steps which ammonia is converted to nitrite by ammonia-oxidizing bacteria and then nitrite is converted to nitrate by nitrite-oxidizing bacteria. Nitrite and/or nitrate are reduced to nitrogen gas by heterotrophic bacteria during denitrification process [16, 17]. In the anaerobic, first aerobic (I), anoxic and last aerobic (II) phases of the cycle, variation of NH_4-N, NO_2-N and NO_3-N concentration is shown in Fig. 4. NH_4-N, NO_2-N and NO_3-N concentration at the beginning of the cycle was 21.7 mg/L, 0.05 mg/L and 0.4 mg/L, respectively. As can be shown from Fig. 4, NH_4-N, NO_2-N and NO_3-N were nearly constant during the anaerobic phase. NH_4-N was removed by assimilation and nitrification during the first aerobic phase. NH_4-N transformed to NO_3-N as result of nitrification in the end of the first aerobic phase and NO_3-N increased to 19.2 mg/L. NO_2-N did not accumulate in the reactor since the complete nitrification happened in the aerobic phases. In the anoxic and the last aerobic (II) phase, NH_4-N concentration was almost the same as NH_4-N concentration of aerobic (I). Adequate amount of ethanol solution was added into the reactor as a carbon source at the beginning of the anoxic phase to reduce the oxidized nitrogen (NO_2-N and NO_3-N) to nitrogen. As result of assimilation and denitrification, NO_3-N decreased to 0 mg/L in the anoxic phase in the present of the external carbon source added. Complete removal of the nitrogen species was achieved due to the addition of ethanol solution at thebeginning of the anoxic phase. Nitrogen gas generated in the anoxic phase as result of denitrification was removed in the last aerobic phase.
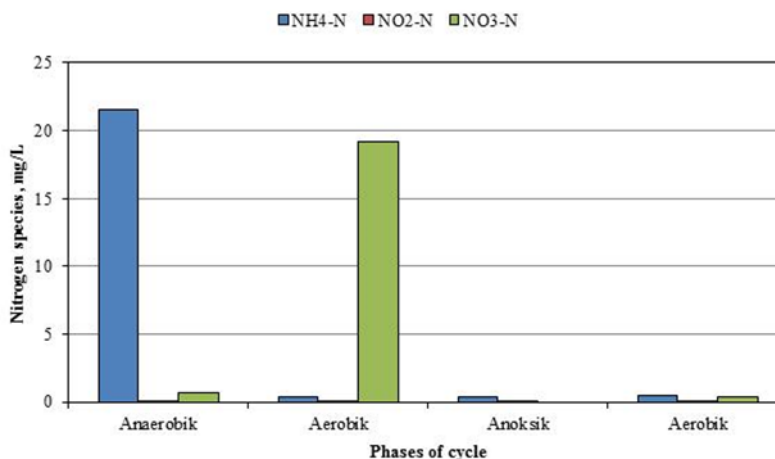

Figure 4. Concentrations of nitrogen species in phases of cycle in MBBR operated as sequencing batch

3.3. Phosphorus Removal

Variation of effluent PO_4-P concentration and PO_4-P removal efficiency obtained in the moving bed biofilm reactor operated as sequencing batch with the cycle of 12 h is depicted in Fig 5. Effluent PO_4-P concentration varied between 0.3

and 0.9 mg/L, with average effluent level of 0.7 mg/L. PO_4-N removal efficiency varied between 88.6% and 95.6%, with average removal efficiency of 91.3%. As can be seen from the results obtained, phosphorus from the municipal wastewater can be removed by moving bed biofilm reactor operated in the sequencing batch mode with the cycle of 12 h.
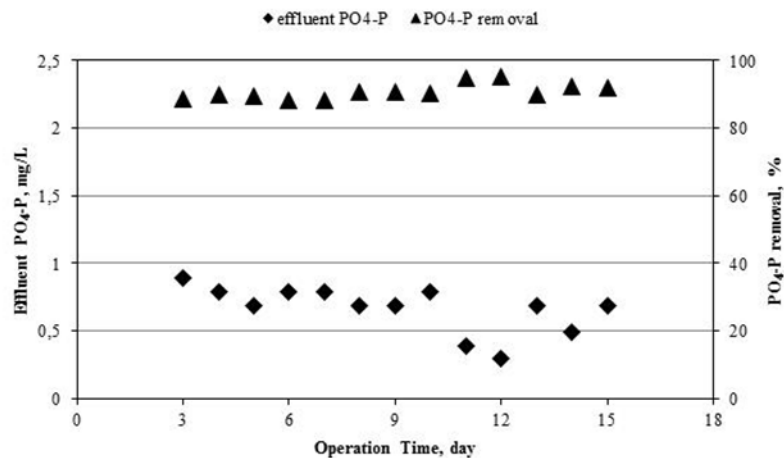
Figure 5. Effluent PO_4-P concentrations and PO_4-P removal in MBBR operated as sequencing batch

In the anaerobic, first aerobic (I), anoxic and last aerobic (II) phases of the cycle, variation of PO_4-P concentration is shown in Fig. 6. Initial PO_4-P concentration of 7.1 mg/L increased to 22.5 mg/L at the end of the anaerobic phase because of phosphate release by phosphorus accumulating organisms (PAOs). PO_4-P concentration decreased from 22.5 mg/L to 0.5 mg/L during the first aerobic phase due to phosphate uptake of PAOs. Phosphorus was significantly released by PAO during anaerobic phase while rapidly absorbed for PAOs growth and intracellular poly-P formation in aerobic phase [18, 19].
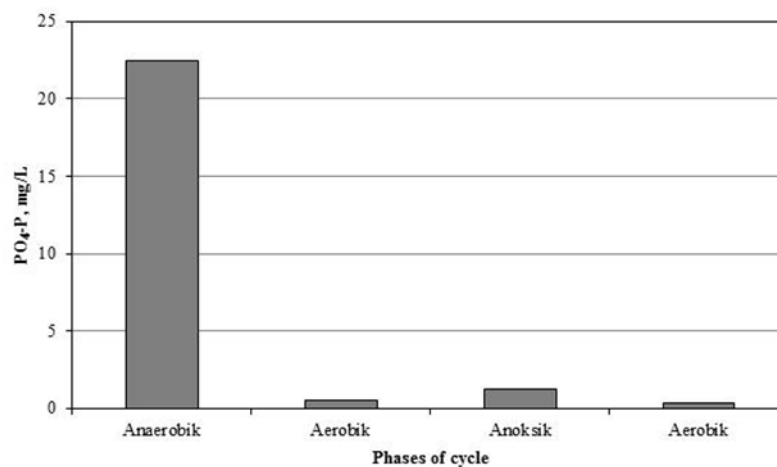
Figure 6. PO_4-P concentrations in phases of cycle in MBBR operated as sequencing batch

4. CONCLUSIONS

The moving bed biofilm reactor operated as sequencing batch with a cycle consist of anaerobic/aerobic/anoxic/aerobic showed good performance for removal of COD, nitrogen and phosphorus from the municipal wastewater. Effluent COD, NH_4-N, NO_2-N, NO_3-N and PO_4-P concentrations were on average 27 mg/L, 0.7 mg/L, 0.04 mg/L, 0.6 mg/L and 0.7 mg/L, respectively. When a cycle consists of anaerobic/aerobic/anoxic/aerobic with hydraulic residence times of 120 min/330 min/210 min/50 min, on average removal percentage of COD, NH_4-N and PO_4-P were obtained as 92%, 97.5% and 91.3%, respectively.

REFERENCES

[1]. J.-W. Lim, C.-E.Seng, P.-E.Lim, S.-L.Ng, and A.-N. A. Sujari, "Nitrogen removal in moving bed sequencing batch reactor using polyurethane foam cubes of various sizes as carrier materials," *Bioresource Technology*, vol. 102, pp. 9876-9883, 2011.

[2]. K. Calderón, J. Martín-Pascual, J.M. Poyatos, B. Rodelas, A. González-Martínez, J. González-López, Comparative analysis of the bacterial diversity in a lab-scale moving bed biofilm reactor (MBBR) applied to treat urban wastewater under different operational conditions, *Bioresource Technology*, vol. 121, 119-126, 2012.

[3]. X. J. Wang, S. Q. Xia, L. Chen, J. F. Zhao, N. J. Renault, and J. M. Chovelon, "Nutrients removal from municipal wastewater by chemical precipitation in a moving bed biofilm reactor," *Process Biochemistry*, vol. 41, pp. 824-828, 2006.

[4]. A. A. L. Zinatizadeh, and E. Ghaytooli, "Simultaneous nitrogen and carbon removal from wastewater at different operating conditions in a moving bed biofilm reactor (MBBR): Process modeling and optimization," *Journal of the Taiwan Institute of Chemical Engineers*, vol. 53, pp. 98-111, 2015.

[5]. A. Barwal, and R. Chaudhary, "To study the performance of biocarriers in moving bed biofilm reactor (MBBR) technology and kinetics of biofilm for retrofitting the existing aerobic treatment systems: a review," *Reviews in Environmental Science and Bio/Technology*, vol. 13, pp. 285-299, 2014.

[6]. B. L. Nogueira, J. Pérez, M. C. M. van Loosdrecht, A. R. Secchi, M. Dezotti, and E. C. Biscaia Jr., "Determination of the external mass transfer coefficient and influence of mixing intensity in moving bed biofilm reactors for wastewater treatment," *Water Research*, vol. 80, 90-98, 2015.

[7]. J. P. Bassin, B. Abbas, C. L. S. Vilela, R. Kleerebezem, G. Muyzer, A. S. Rosado, M. C. M. van Loosdrecht, and M. Dezotti, "Tracking the dynamics of heterotrophs and nitrifiers in moving-bed biofilm reactors operated at different COD/N ratios," *Bioresource Technology*, vol. 192, 131-141, 2015.

[8]. J. C. Leyva-Díaz, J. Martín-Pascual, M. M. Mu˜nío, J. González-López, E. Hontoriaa, and J. M. Poyatos, "Comparative kinetics of hybrid and pure moving bed reactor-membrane bioreactors," *Ecological Engineering*, vol. 70, pp. 227-234, 2014.

[9]. Y. Zhu, Y. Zhang, H.-Q. Ren, J.-J.Geng, K. Xu, H. Huang, and L.-L. Ding, "Physicochemical characteristics and microbial community evolution of biofilms during the start-up period in a moving bed biofilm reactor," *Bioresource Technology,* vol. 180, 345-351, 2015.

[10]. L. Chu, J. Wang, F. Quan, X.-H. Xing, L. Tang, and C. Zhang, "Modification of polyurethane foam carriers and application in a moving bed biofilm reactor," *Process Biochemistry*, vol. 49, 979-1982, 2014.

[11]. S. Yang, F. Yang, Z. Fu, T. Wang, and R. Lei, "Simultaneous nitrogen and phosphorus removal by a novel sequencing batch moving bed membrane bioreactor for wastewater treatment," *Journal of Hazardous Material*, vol.175, pp. 551-557, 2010.

[12]. F. Kargi, and A. Uygur, "Nutrient loading rate effects on nutrient removal in a five-step sequencing batch reactor," *Process Biochemistry*, vol. 39, pp. 507-512. 2003.

[13]. F. Kargi, and A. Uygur, "Effect of carbon source on biological nutrient removal in a sequencing batch reactor," *Bioresource Technology*, vol. 89, 89-93, 2003.

[14]. APHA, *Standard Methods for the Examination of Water and Wastewater*, 17th ed. APHA, AWWA, WPCF, American Public Health Association, Washington, DC, 1989.

[15]. B. Rusten, L.J. Hem, and H. ∅degaard, Nitrogen removal from dilute wastewater in cold climate using moving-bed biofilm reactors, Water Environmental research, vol. 67, pp.65-74, 1995.

[16]. P. Reboleiro-Rivas, J. Martín-Pascual, B. Juárez-Jiménez, J. M. Poyatos, R. Vílchez-Vargas, S. E. Vlaeminck, B. Rodelas, and J. González-López, "Nitrogen removal in a moving bed membrane bioreactor for municipal sewage treatment: Community differentiation in attached biofilm and suspended biomass," *Chemical Engineering Journal,* vol. 277, pp. 209-218, 2015.

[17]. J.C. Leyva-Diaz, A. Gonzalez-Martinez, J. Gonzalez-Lopez, M. M. Munio, and J. M. Poyatos, "Kinetic modeling and microbiological study of two-step nitrification in a membrane bioreactor and hybrid moving bed biofilm reactor-membrane bioreactor for wastewater treatment," *Chemical Engineering Journal,* vol. 259, pp. 692-702, 2015.

[18]. A. Oehmen, P.C. Lemos, G. Carvalho, Z. Yuan, J. Keller, L.L. Blackall, and M.A.M. Reis, "Review Advances in enhanced biological phosphorus removal: From micro to macro scale", Water Research, vol. 41, pp. 2271-2300, 2007.

[19]. W. Cai, B. Zhang, Y. Jin, Z. Lei, C. Feng, D. Ding, W. Hua, N. Chen, and T. Suemura, "Behavior of total phosphorus removal in an intelligent controlled sequencing batch biofilm reactor for municipal wastewater treatment," Bioresource Technology, vol. 132, pp. 190-196, 2013.

Investigation and Evaluation of Degradability of Ibuprofen from Wastewater by Using Fenton Process

Sevde Ustun Odabasi[1]*, Hanife Buyukgungor[1]

[1]Ondokuz Mayis University, Department of Environmental Engineering, 55200, Atakum/Samsun, Turkey.

*CorrespondingAuthor email: sevde.ustun@omu..edu.tr

Abstract

Pharmaceutical residues are considered as emerging environmental problem because of their potential toxicology risk on living organisms. Environmental problem of pharmaceuticals are persistence to the aquatic ecosystem even at low concentrations (µg/L-ng/L). Conventional wastewater treatment plants are not enough to remove an emerging solution. Ibuprofen (IBF), a non-steroidalanti-inflammatory drug (NSAID), is a most widely used medicine in almost part of world. In present study, under laboratory conditions, coagulation followed by advance oxidation, using H_2O_2 and $FeSO_4$ (Fenton process) is used to degrade the concentrations of ibuprofen from water were conducted. Fenton process is known to be most effective and common methods for the treatment of such wastewaters. In the present study H_2O_2 was used with $FeSO_4$ for the treatment ibuprofen and effects of H_2O_2, $FeSO_4$ concentrations COD and TOC removals. Experiments with optimal concentrations of H_2O_2 and $FeSO_4$ were carried out by chancing pH, temperature, stirring and residence time of solution (2-6), room temperature, (10,20,30 min) and (30,60,90 min) respectively. Concentration of $FeSO_4$ and H_2O_2 were selected as (30,75,150 mg/L). After processing, 150 ml of samples taken out from the upper layers of sample COD and TOC tests were conducted.

Key words

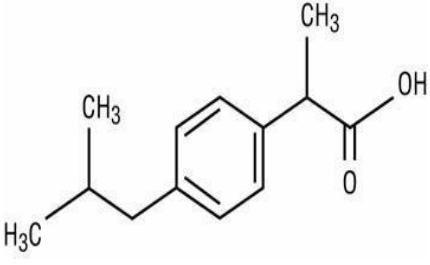Ibuprofen, Fenton Process, Pharmaceuticals, Water, Wastewater

1. INTRODUCTION

Pharmaceuticals are used for treatment of diseases. Pharmaceutical compounds at aquatic environment are a great interest for researchers worldwide [1]. It has been observed the pharmaceutical residues on ground and surface water, wastewater where they have been found at very low concentrations like ng/L to µg/L [2]. Ibuprofen (2-(4-2-methylpropyl)phenyl) propanoic acid) is non-steroidal anti-inflammatory drug (NSAID), consuming often both for human and veterinary practices[3].Properties of Ibuprofen (IBF) are shown Table 1.IBF leaves the body in the shape of metabolized and non-metabolized after excretion [4]. Therefore the form links up with other substances on water, the regenerated form may cause hazard for aquatic environments. As a result of common use of IBF, there exists very high concentration of IBF in wastewater. To say more clearly, after using IBF by patients, the disused parts are removed out of body by urine [5]. In this way, the residue of IBF goes through canalization and arrives treatment plant. It is not only way to survive of the contamination but also the other way to survive is cumulating in sediments. The water from treatment plant and sediment can be used for agriculture which has access to reach soil and ground water [5] [6]. Conventional treatment plants are not advanced to refine the water, classic physical-chemical techniques and conventional microbiological techniques cannot effectively treat micropollutants. To purify them, Advanced Oxidation Process (AOP) is usually used. Many advanced treatment technologies have been used in removal of micropollutants. These methods include membrane technologies, ozonation, ultraviolet, ultrasound, hydrogen peroxide-ultraviolet, and Fenton [7]. Among them fenton process has been commonly studied because of cost effectiveness and good efficiency compared with other advanced oxidation process [8].Fenton Processes, a branch of AOP, are seen as a good process for micropollutant removal, and also it is easy to apply,

works quickly [9]. The Fenton reaction iscomprised with highly reactive hydroxyl radicals (hydrogen peroxide) and ferrous ions in acidic [10], [11]. This reaction described by [12] in Eq (1).

$$Fe^{2+} + H_2O_2 \rightarrow Fe^{3+} + OH + OH^- \qquad (1)$$

With these qualifications, Fenton is most commonly used process for IBF removal. In this study the effectiveness of IBF degradation in drinking water uses Fenton process.

Table 1. Physico–chemical and pharmacological properties of IBF [13], [14].

Chemical structure	
Molecular formula,	$C_{13}H_{18}O_2$
Molecular weight	206,258 g mol−1
Water solubility	21 mg L−1 (20 °C)
Octanol-water partitioning	3,29-3,76
pKa	4,52
Usage	Analgesic, anti-inflammatory,antipyretic

2. MATERIALS AND METHODS

In the present study, under laboratory conditions, coagulation and advance oxidation, using H_2O_2 and $FeSO_4$ (Fenton process) is used to degrade the concentrations of ibuprofen from water were conducted. We have taken 25 mg/l ibuprofen synthetic solution. Biodegradability of the treated solutions (COD) and test with background constituents in the water matrix, like TOC will also observed. In the end of the experiments, to measure the efficiency of Fenton process, optimum pH, $FeSO_4$, H_2O_2, stirring time, residence time and temperature will be measured. Before starting our experiments we checked initial values of COD, TOC and amount of ibuprofen in untreated samples. Later, we selected different parameters like, pH values (2-6), $FeSO_4$ and H_2O_2 concentration (30-75-150 mg/l), stirring time (10, 20, 30 minutes), residence time (30, 60, 90 minutes) and room temperature that will be provided to our sample and optimal (high) values will be selected. After processing, 150 ml of samples was taken out from the upper layers of samples and COD and TOC tests were conducted.

A solution of IBF, obtained market was prepared in tap water to carry out advanced oxidation with Fenton process. In the experiments, Tablet was used to obtain 25 mg/L IBF content. For the preparation of sample, tablet containing 25 mg IBF tablet was first finely grinded to powdered form and then mixed with tap water in 1 liter flask to prepare 25 mg drug/liter solution.

We used in Fenton process 35% pure grade H_2O_2 hydrogen peroxide (Merck) , $FeSO_4.7H_2O$ iron sulphate (Sigma Aldrich), 98% pure grade H_2SO_4 sulfuric acid (Merck), NaOH sodium hydroxide (Merck). We used in COD process potassium dicromate K_2CrO_4 (Merck), Iron ammonium sulphate (Carlo Erba) 99% pure grade 1.10-phenanthroline and monohydrate (Sigma Aldich), mercury sulphate (Sigma Aldrich), silver sulphate (Sigma Aldrich), thermo reactor (Spectroquant TR 320).Physical measurements of synthetic wastewater are done by turbidimeter (Hach), TDS (Selectra), dissolved oxygen (Hach) and pH meter (Ohasus). We used in TOC analyze Apollo 9000 combustion TOC analyzer.The purpose of this study is to analyze the optimum degradation of IBF by using different parameters like pH, temperature, stirring time, waiting time, amount of Iron sulphate and hydrogen peroxide.

3. RESULTS AND DISCUSSION

Before starting the analysis, initial physicochemical properties of synthetic wastewater prepared from tap water were recorded and are given in Table 2.

Table 2. Physicochemical properties of synthetic wastewater with DFC.

Parameters	Units	Results
pH	pH birimi	6,85
TDS	µS/cm	402
Turbidity	NTU	1,3
Temperature	ºC	23,1
Dissolved oxygen	mg/L	6,99

In this context, first of all experiment with different pH like 2,3,4 and 6 was performed with concentrations: 75mg/l; $FeSO_4$, 75ml/l; H_2O_2 , stirring time;20 minutes, waiting time 60 minutes. After measuring COD and TOC optimum pH was observed to be in between 3 and 4. Because the value was closer to 3 and after consulting literature further experiments were decided to carry out by taking 3.5 pH as optimum [15], [16]. Values and results of TOC and COD can be cross checked from Figure 1.
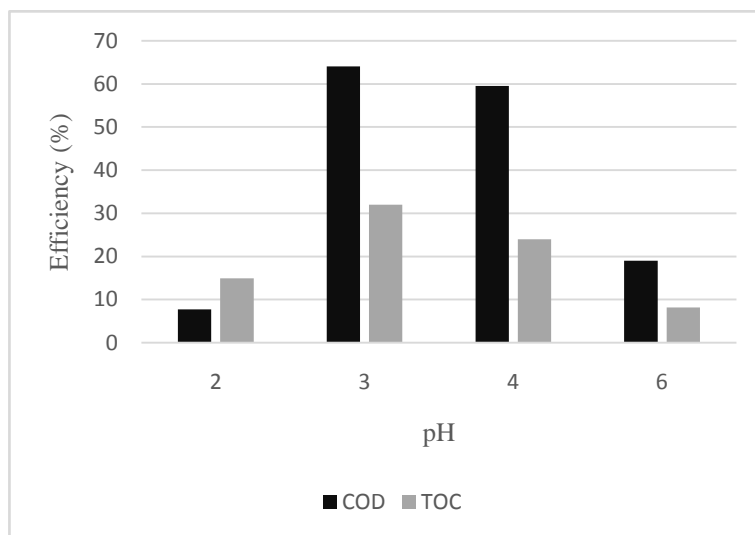
Figure 1. IBF removal with Fenton process. Efficiency with COD and TOC.

In the second step optimum concentration of $FeSO_4$ required for the degradation of drug was analyzed. For this purpose with optimum pH of <3.5, 75 mg/L; H_2O_2, stirring time;20 minute, waiting time 60 minute, different concentrations of $FeSO_4$ like, 30-75-150 mg/L were tried to select optimum amount to carry out further series of steps. As per the observed results of COD and TOC best value of $FeSO_4$ was 150 mg/L. Values and results of TOC and COD can be seen in Figure 2.
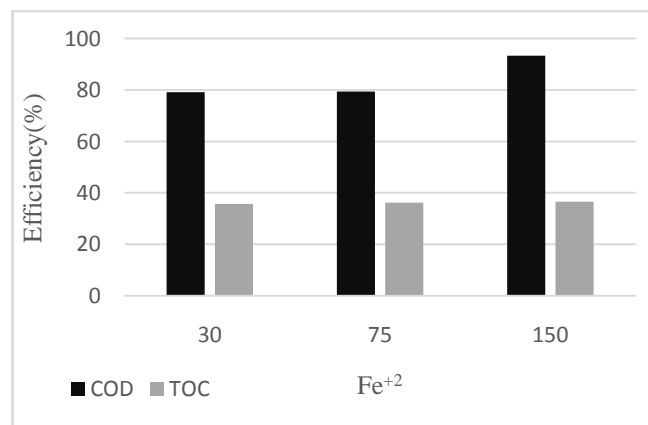
Figure 2.IBF removal with Fenton process.Efficiency with COD and TOC.

The purpose of third step was selection of optimum value of H_2O_2. In this step different concentrations of H_2O_2 like 30-75-150 mg/L were tried with optimum pH<3.5, optimum value of $FeSO_4$ 150 mg/L along with stirring time; 20 minute, waiting time 60 minute. According to the observed values of COD and TOC optimum value of H_2O_2 was selected as 150 mg/L. Published literature has shown that degradation of drugs increases with the increase amount of H_2O_2, hence increased amount of H_2O_2 means good degradation [16], [17]. After these results we assumed that our research is on right track. Observed TOC and COD values and results are shown in Figure 3.
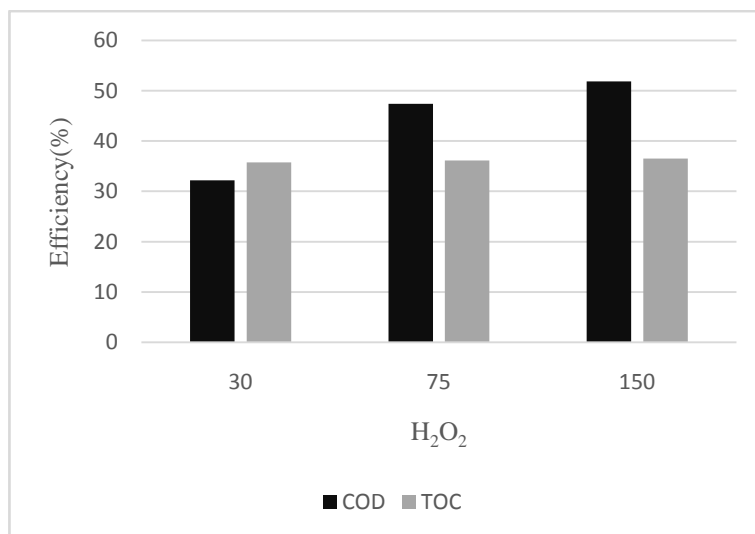
Figure 3.IBF removal with Fenton process.Efficiency with COD and TOC.

In the fourth step the optimum stirring time was figured out by applying different stirring times of 20-30-60 minutes to the solution under optimized parameters: pH<3.5, 150 mg/L; $FeSO_4$, 150 mg/L; H_2O_2, waiting time 60 minute. COD and TOC showed that 10 minute is the best optimum stirring time. Values of TOC and COD are showed in Figure 4.
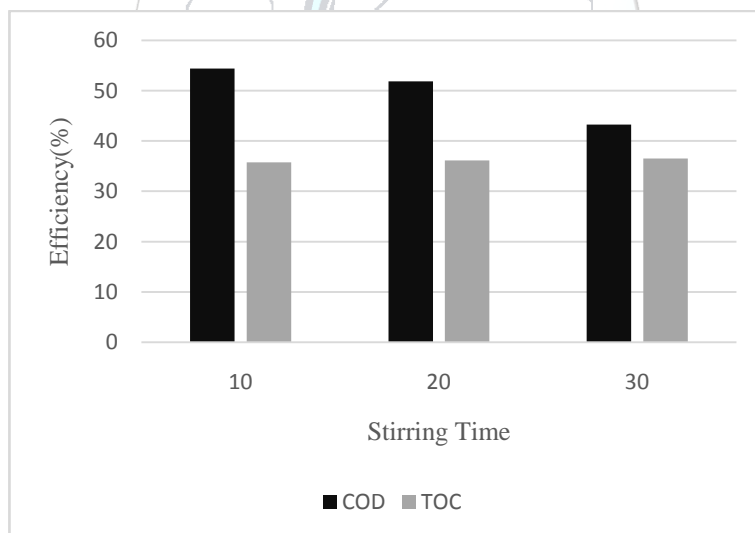
Figure 4.IBF removal with Fenton process.Efficiency with COD and TOC.

Fifth step was to optimize the waiting time, for this purpose time directions 30-60-90 minutes were provided to solution with other already optimized parameters as described above. Final optimized waiting time was cross checked by performing COD and TOC tests and it was finalized that waiting time of 90 minute was best optimum time. Observed TOC and COD values and results are shown in Figure5.
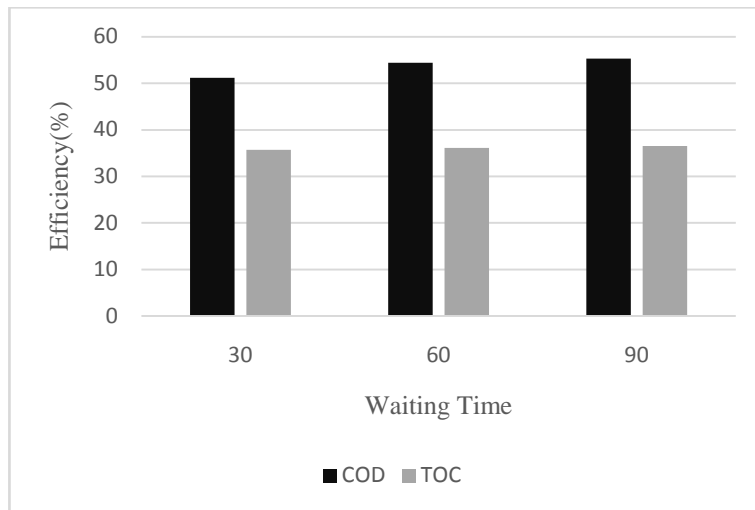
Figure 5.IBF removal with Fenton process.Efficiency with COD and TOC.

Total results were shown in Table 3.

Table 3.Results of total analysis.

		COD results (mg/l)	COD removal (%)	TOC results (mg/l)	TOC removal (%)
pH	**2**	262	7,74	66,57	14,95
	3	102	64,08	53,22	32,01
	<3,5	58,60	79,36	49,98	36,15
	4	115	59,50	59,23	23,95
	6	230	19,01	71,88	8,17
Fe^{+2} (mg/l)	**30**	59,43	79,07	50,30	35,74
	75	58,60	76,36	49,98	36,15
	150	19,20	93,23	49,68	36,53
H$_2$O$_2$ (mg/l)	**30**	48	83,09	53,04	32,20
	75	32	88,73	41,18	47,39
	150	16	94,36	37.70	51,83
Stirring Time (min)	**10**	6,4	97,74	35,69	54,40
	20	16	94,36	37,70	51,83
	30	20	92,95	44,70	43,28
Waiting Time (min)	**30**	7,0	97,53	38,18	51,22
	60	6,4	97,74	35,69	54,40
	90	6,1	97,85	34,98	53,31

*(Initial pH; 6,85, COD value; 284 mg/l, TOC value; 78,28 mg/l)

4. CONCULSION

All the results for investigated tap water sample containing drug (IBF) are precisely described below: pH<3.5, FeSO$_4$; 150 mg/L, H$_2$O$_2$; 150 mg/L, stirring time; 10 minute, waiting time; 90 minute were optimized. According to these results highest removal efficiencies for COD and TOC are 97,85 and 55,31 % respectively. Observed values of pH and H$_2$O$_2$ are in agreement with the published literature. With this research optimum figures for the degradation of IBF in the tap water by Fenton process were questioned. According to the results of the analysis, it can be decline that the best solution for the removal of pharmaceutical pollution from wastewater or freshwater resources is Fenton process which is compared with others.

REFERENCES

[1]. D. P. Mohapatra, S. K. Brar, R. D. Tyagi, P. Picard, Surampalli R.Y.,"Analysis and Advanced Oxidation Treatment of A Persistent Pharmaceutical Compound in Wastewater and Wastewater Sludge-Carbamazepine,"*Science of the Total Environment*, vol 470-471, pp 58-75, October, 2013.

[2]. M.Markovic,M.Jovic, Stankovic, V. Kovacevic, G. Roglic, G. Gojgic-Cvijovic, D. Manojlovic,"Application of non-thermal plasma reactor and Fenton Reaction for Degradation of Ibuprofen", *Science of Total Environment*, vol:505, pp: 1148-1155,Nov. 2014.

[3]. M. Kwon, S. Kim, Y. Yoon, Y. Jung, T. Hwang, J. Lee, J. Kang, "Comparative evaluation of ibuprofen removal by UV/H$_2$O$_2$ and UV/S2O8 process for wastewater treatment", Chemical Engineering Journal,vol: 269, pp:379-390, February' 2015.

[4]. L. Lishman, S. A. Smyth, K. Sarafin' S. Kleywegt, J. Toito, T. Peart, B. Lee, M. Servas, M. Beland, P. Seto "Occurrence and reductions of pharmaceuticals and personal care products and estrogens by municipal wastewater treatment plants in Ontario, Canada", Science of the Total Environment, vol: 367, pp: 544-558, August, 2006.

[5]. K. Kummerer, "Drugs in the environment-. Emissions of drugs, diagnostic acids and disinfectants into wastewater by hospitals in relation to other sources-a review", Chemosphere, vol: 45, pp: 957-969, November, 2001.

[6]. T. Heberer, "Occurence, fate and removal of pharmaceutical residues in the aquatic environment; a review of recent research data,"ToxicologyLetters,vol 131, pp 5-17 May,2002.

[7]. H. A. Hasan, S. R. S. Abdullah, A. W. N. Al-Attabi, D. A. H. Nash, N. A. Rahman, H. S. Tiah, "Removal of ibuprofen, ketoprofen, COD and Nitrogen Compounds from Pharmaceutical wastewater using aerobic suspension-sequencing bath reactor (ASSBR)", Seperatıon and Purification Technology, vol 157, pp 215-221, November, 2015.

[8]. S. Loaiza-Ambuludi, M. Panizza, N. Oturan and M. A. Oturan, "Removal of the Anti-inflammatory Drug Ibuprofen from Water Using Homogeneous Photocatalysis, Catalysis Today,vol 224, pp 29-33, January, 2014.

[9]. E. Gilpavas, I. Dobrosz-Gomez, M. A. Gomez-Garcia, "Coagulation-Flocculation Sequential with Fenton or Photo-Fenton Processes as an Alternative for the Industrial Textile Wastewater Treatment", *Journal of Environmental Management,*vol 191, pp 189-197, January, 2017.

[10].A. Mirzaei, Z. Chen, F. Haghighat, L. Yerushalmi, "Removal of Pharmaceutical from Water by Homo/Heterogonous Fenton-Type Process- A Review," *Chemosphere,*vol 174, pp 665-688, January, 2017.

[11].V. Kavitha, K., Palanivelu, "The Role of Ferrous Ion in Fenton and Photo-Fenton Processes for the Degradation of Phenol," *Chemosphere,*vol 55, pp 1235-1243, December, 2003.

[12].C. Wailling, "Fenton's Reagent Revisted, "*Accounts of Chemical Research*, vol8, pp 125-131, April, 1975.

[13].T. Scheytt, P. Mersmam R., Lindstadt and T., Heberer," 1-Octanol / Water Partition Coefficients of 5 Pharmaceuticals from Human Medical Care: Carbamazepine, Clofibric Acid, Diclofenac, Ibuprofen and Propyhenazone," Water, Air and Soil Pollution, vol 165, pp 3-11, March, 2005.

[14].(2017) Chem Spider Search and Share Chemistry [Online]. http://www.chemspider.com/Chemical-Structure.3544.html#

[15].G. Sonmez, "Removal of some pharmaceutical residues by advanced chemical oxidation process", Aksaray University, Science Institute, November, 2015.

[16].S. Ustun Odabasi, B. Maryam, H. Buyukgungor, "Assessment and Investigation of Paracetamol from Wastewater By Using Oxidation Process and TOC,"*3rd International Conference on Recycling and Reuse*, 2015, pp161-166.

[17].Y.W. Kang, veK.. Hwang, "Effect of reaction conditions on the oxidation efficiency in the Fenton process", *Water Research,*vol10, pp2786-2790, Jully,2000.

Use Of a Novel Bioreactor Configuration in The Form of High Solid Digestion For Municipal Organic Wastes at Pilot Scale

Kubra Arslan[1], Tugba Keskin Gundogdu[2], Duygu Karaalp Yavuzyilmaz[2], Nuri Azbar[1,2]*

[1]Ege University, Environmental Sciences Departmant, 35100, Bornova/İzmir, Turkey.

[2] Ege University, Department of Bioengineering, 35100, Bornova/İzmir, Turkey.

*Corresponding Author email: nuri.azbar@ege.edu.tr

Abstract

The objective of this study was to investigate the performance and process stability of a novel dry anaerobic digestion system. For this purpose, a dry anaerobic digester (100 L) with percolate tank (200 L) was designed at pilot scale. Municipal solid wastes were fed into the dry fermentation unit and system was operated with intermittent recycling of leachate through percolation unit back to the dry fermentation unit twice a day. Gas production in both unit was recorded daily and gas content and leachate analysis were carried out periodically. A batch feeding of solid waste (17.5 kg waste) having less than 5 cm particle size with a dry matter of 13% and organic dry matter of 85% was carried out and process was operated for 60 days. Results indicated that 560 L methane per kg organic dry matter was produced. This corresponds to biogas production 119 m3 per ton of wet solid waste. It was also observed that the main gas production took place in percolate tank and the solid digester acted as a hydrolysis and acid reactor indicated by the low gas production and acidic leachate characteristics. There were also almost no digestate generation which eliminates costly post treatment units before the discharge of digestate, which is a critical problem for wet digestion counterpart.

Key words

Anaerobic digestion, high solid fermentation, methane, municipal solid waste

1. INTRODUCTION

Industrialization and rapid urbanization has increased significantly the generation of municipal solid wastes (MSW) and as in many developing countries it is a big environmental problem for Turkey. In 2014, MSW generation rate was 1.08 kg/cap.day, 28 million tons of MSW generated, and this waste was landfilled either in sanitary landfills (63.6%) or dumpsites (35.5%), composted (4%) and disposed with other ways (5%) [1]. Typical MSW composition in Turkey contains high biodegradable organic fraction (40-75%) as it can be seen in Table 1 [2].

On the other hand, MSW management has been a pressure point for Turkey while being a candidate country for EU accession and EU 27 targets .In order to decrease the amount of organic biodegradable waste sent to landfill sites and to set up a waste management system, most of the EU waste management directives have been transposed into Turkey's national legislation. Therefore the reduction of biodegradable waste amounts which is landfilled and proper treatment of MSW is an important task for Turkey [3].

Table 1.Composition of MSW in Turkey

Components	Range in weight (%)
Organics	40-65
Paper/cardboard	7-18
Plastics	5-14
Metal	1-6
Glass	2-6
Others	7-24

Anaerobic digestion (AD) is a promising solution as it is a biological treatment capable to decompose the organic matter under oxygen free conditions [4]. Furthermore, the end product of AD includes biogas (60–70% methane) which is a renewable energy resources, and the effluent which is an organic residue rich in nitrogen can be used as soil conditioner or fertilizer [5,6]. AD process is based on four steps: hydrolysis, acidogenesis, acetogenesis and methanogenesis [7] and can be classified based on operating parameters and reactor design [4]. Depending on the total solid (TS) concentration of the feedstock the AD process can be divided into wet (<10% TS) and dry (>10% TS) digestion processes [8].

Compared to wet digestion, dry digestion, also known as ''high-solid'' anaerobic processes [8] is advantageous in terms of smaller reactor volume, lower energy consumption for heating, higher volumetric methane productivity [6], less wastewater generation, low-moisture digestate that is easier to handle and lower total energy loss [4]. However, in dry digestion due to the contact between microorganism and feedstock is poor the biogas yield is generally low and there is a high tendency to inhibition lead by accumulation of ammonia and volatile fatty acids (VFAs) [9]. The digestate or leachate of dry AD can be recycled to inoculate the fresh feedstock on the purpose of improving the biogas yield [10]. Systems that recycle leachate into the reactor vessel are called percolation systems. Leachate recycling approach provides a good transportation for microorganism throughout the digester and prevent the inhibition caused by accumulation of VFAs and ammonia [4].

The objectives of this study was to investigate the process performance and stability of a novel anaerobic digester configuration which employs dry fermentation of municipal solid wastes.

2. MATERIALS AND METHODS

2.1. Feedstock and Inoculum

MSW were obtained from Izmir Metropolitan City, Solid Waste Management Department in Izmir, Turkey and it mainly consisted of seasonal vegetable and fruits. The wastes were whittled to have a particle size around 5 cm before filled in reactor . Representative samples of MSW (small pieces taken from each fruit and vegetable) were crushed using an electrical blender and used to perform analytical analysis. Anaerobic inoculum was taken from an upflow anaerobic sludge blanket (UASB) reactor fed with wastewater of a beer factory located in Izmir.

2.2. Process Description

The process consist of a batch dry anaerobic reactor with 100 L total volume and a percolate tank with 200 L total volume. Inside the reactor there was a stainless steel basket which has holes at the bottom and the side and keeps the solid material inside reactor. On the top of the reactor the inoculum-percolate distribution device which is basically a perforated plate was placed and allowed the distribution of percolate over the feedstock. The temperature and humidity probe were also set on the top of the reactor.

In the beginning of the study the percolate tank was filled with the liquid anaerobic inoculum equipped with an agitator and a pump. Once a day this liquid inoculum was sprayed on the feedstock in the dry digester, passed through the substrate stack and reached into the percolate tank from the pipeline which is placed between the bottom of the dry digester and percolate tank (leachate circulation line). A sampling point was located on the leachate circulation line, every 2 or 3 days, samples from leachate were taken from this line and analyzed for VFA and total ammonia nitrogen (TAN).

The percolate tank and digester were heated by hot water through the heating pipe installed inside the tanks to keep the temperature at 37 °C and isolated for heat preservation. Biogas production was measured by a drum type gas meter for both dry digester and percolate tank, and biogas sampling was done from the line between reactor and gas meter.

2.3. Analytical Methods

VS and TS contents were analyzed according to the APHA Standard Methods for the Examination of Water and Wastewater. TAN was determined using a colorimetric method with an ammonia nitrogen kit, and a spectrofotmeter. VFAs in the AD leachate were measured using a gas chromatography (GC). Leachate samples were centrifuged then supernatant was filtered through 0,45 µm nylon syringe filter for GC analysis. The volume of biogas was measured by a drum type gas

meter (Ritter, Germany) and the composition of biogas (H_2, CH_4 and CO_2) was analyzed by Agilent gas chromatograph equipped with a flame ionization detector and a DB-FFAP 30 m × 0.32 mm × 0.25 mm capillary column.

3. RESULTS AND DISCUSSION

3.1. Characteristics of MSW

The characteristics of MSW and inoculum used in this study are shown in Table 2. As the content of MSW varied depending on different seasons, in summer MSW consist of mostly juicy fruits and vegetables therefore TS of the MSW used in this study was 13%, and VS was 85% of TS respectively.

Table 2.Characteristics of MSW

Parameter	MSW
TS (%)	13
VS (%TS)	85
NH4+-N(g/L)	0,1
pH	4.55

Fruit and vegetable wastes was characterized by an acid pH (pH of 4.55). It has been reported that due to the hydrolytic and fermentative/acidogenic processes are in action during storage in bin containers before its collection OFMSW has low pH values which is caused by the high VFA concentration [11].

3.2. Anaerobic Dry Digestion: Leachate Analyses

The dry fermenter was filled with the MSW and closed with gas tight cap. The inoculum was sprayed on MSW everyday for thirty seconds. A representative sample of leachate was taken periodically to perform the chemical characterization and a pH probe was placed in the circulation pipeline to monitor pH changes of leachate. Fig 1 shows the pH and total VFA trends in the leachate.
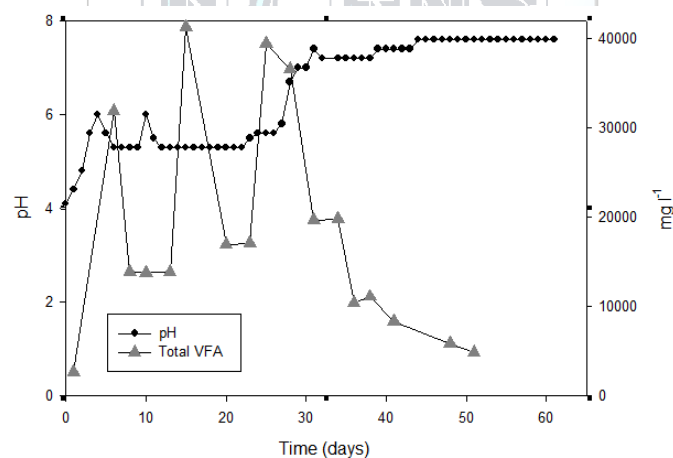
Figure 1. VFA and pH trends in the leachate

VFAs namely, acetic acid, propionic acid, butyric acid, isobutyric acid, valeric acid and isovaleric acid are intermediates produced during the hydrolysis and acidogenesis steps of anaerobic digestion [12]. The first leachate was characterized with low total VFA concentration. As the contact between microorganisms and substrate increase microbial activity was activated and in the sixth day of the process a sharp increase occurred in total VFAs with a concentration of 32000 mg l^{-1} and this VFAs consumed and flushed to percolate tank. However two other peaks in total VFAs occurred on day 15 and 25 with the concentration of 41000 mg l^{-1} and 40000 mg l^{-1}, respectively. The pH values of the leachate was around 4 in the beginning of the experiment. Afterward the pH value of leachate reached 5.5 in following four days and remained around 5.5-6 between days 4 and 28 due to the high VFA concentrations in leachate. From this moment the total VFA concentration in the leachate showed a decreasing trend and as total VFA concentrations decreased in the leachate the pH values of the leachate increased and reached to neutral values(7.0). The optimum pH of hydrolysis and acidogenesis has been reported as being between 5.5-6,0 and the optimum pH of methanogenesis is over 7.0 [12]. Due to the low pH values which is caused by high VFAs concentrations during the first 30 days of the process methanogenic activity in the dry digester might be inhibited and resulted with the low methane content of the biogas in dry digester It is reported that interactions between VFAs and pH may cause an inhibition where the process runs stably but with a lower methane yield[13].

The chemical compositions of the VFAs of the leachate is also shown in Fig 2. During the first days of the process, the leachate was rich in caproic acid, butyric acid, valeric acid and propiyonic acid. Acetic acid is the major substrate of the methane forming bacteria in an anaerobic digester [14] and it started to represented after the 30th day of the process by degredation of butyric, caproic and propionic acid [14] to acetic acid. Formic acid and heptanoic acid were also detected at relatively low concentrations.
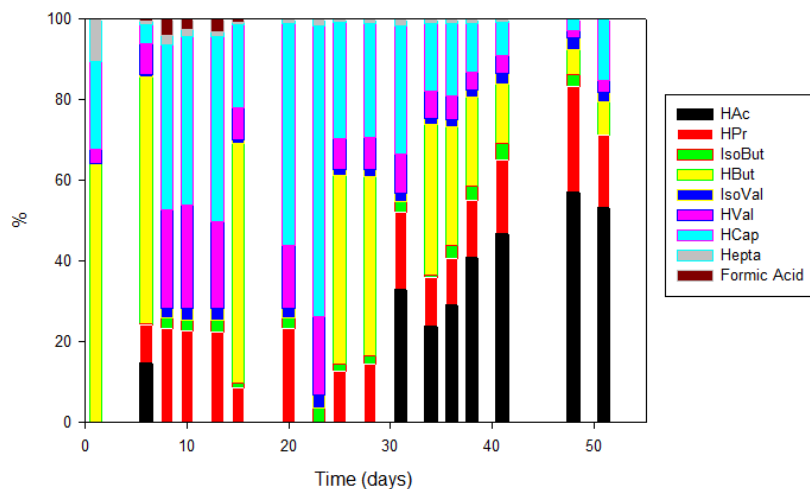
Figure 2. Individual VFA speciation ranges in the leachate

The TAN concentration of the leachate is shown in Fig 3. During the experiment TAN concentration remained under 150 mg l^{-1} which is reasonable for the AD process stability. It is reported that nitrogen is an essential nutrient for the anaerobic microorganisms and TAN concentrations below 200 mg l^{-1} are considered to be beneficial while concentrations exceeding 1500 mg l^{-1} can be moderately inhibitory [15]. As it can be seen in Fig 4 TAN concentrations stayed between beneficial range and no inhibition effect lead by ammonia accumulation occurred during the study.
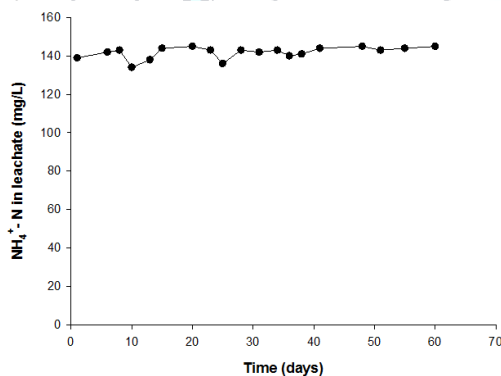
Figure 3. TAN concentration in leachate

3.3. Biogas and Methane Production

The start-up of the process followed different trends in percolate tank and dry digester (Figure 4). During first four days while big amounts of biogas was produced in percolate tank there was no biogas production in dry digester. The total biogas produced in percolate tank for first four days was 880 L which is the 50% of the total biogas production value reached after 60 days. It is reported that the fruit and vegetable waste has a big part of easily digestible fraction, which might produce excessive VFAs at the beginning of the dry digestion [16]. This soluble VFA leached from dry digester washed into the percolate tank and digested to biogas which might be the reason of high amount of biogas production in percolate tank in the first four days. However, the biogas production of the percolate tank decreased to a stable level after 10 days and after 40 days the biogas production progressively decreased and reached values around 5-3.
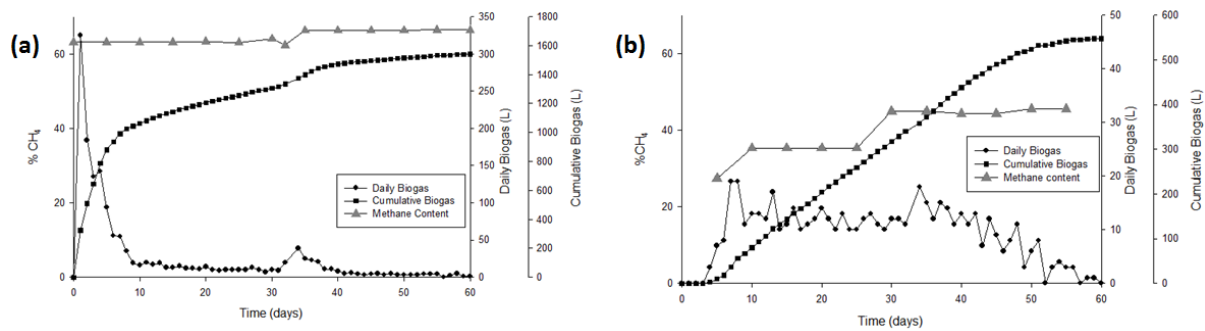
Figure 4. Daily and cumulative biogas production and methane content of biogas: (a)Percolate tank; (b) Dry digester

Fig. 4b shows that a lag phase of 4 days occurred at dry digester. The degredation of the feedstock depends on the connection between the substrate and microorganism and in the liquid digester, this movement is mainly done by mixing the whole substrate or by passing liquid substrate to microorganism surface [16]. In dry digester used in this study this connection was done by the percolate circulation and in the beginning hence the big particle size and highly porous structure of substrate stack the connection between microorganisms and feedstock was not done efficiently. It is reported that the percolate recirculation at a high flow rate allowed accelerating the solid–liquid mass transfer and increase the biogas production dramatically. It is also shown that increasing the percolate recirculation rate in intermittent and short recirculation operations improves the stability and speed of the dry anaerobic digestion [17]. Afterward the biogas production of the dry digester increased and reached to a stable level and the digester showed a steady biogas production for 40 days.

3.4. Overall Process Performance

The biogas and methane production of dry digester and percolate tank is shown in Table 3. Dry digester and percolate tank totally produced biogas of 2095 L, of which 550 L of biogas produced from dry digester, and 1545 L of biogas produced from the percolate tank which is the 75% of total biogas production.

These results indicated that a big amount of VFAs produced in dry digester and washed into the percolate tank with the recirculation of percolate and were digested into biogas. During the first 40 days, the process was separated into two-phase system of hydrolysis and acetogenesis in dry digester and methanogenesis in percolate tank. However, with recirculation of percolate the methanogens was irrigated into the digester and biogas and methane was produced both in percolate tank and dry digester. Depending on biogas and methane production values the AD efficiency of the percolate tank was much higher than dry digester. Some studies also reported the same results that two-phase dry AD has advantages of more stable processing [16,17].

Table 3. Biogas and Methane production of percolate tank and digester

	Biogas production (L)	CH_4 production (L)
Percolate Tank	1545	875
Dry Digester	550	210
Total	2095	1085

The specific biogas and methane yields reached after 60 days were 1085 L biogas kg^{-1} VS and 560 L CH_4 kg^{-1} VS, respectively. It is reported that the biogas yield of fruit and vegetable wastes varied from 650-700 L biogas kg^{-1} VS depending on different TS values [17]. It is also investigated that the methane yield of different content of solid organic wastes varied from 200-850 L CH_4 kg^{-1} VS [18]. Compared with literatures, the results showed that biogas yield in this experiment much more higher than literature values, methane yield was in an avarage range.

4. CONCLUSIONS

The objective of this study was to investigate the performance and process stability of a novel dry anaerobic digestion system and has demonstrated that the system is technically feasible for high solid anaerobic digestion of MSW.

The results also showed that the main gas production took place in percolate tank and the solid digester acted as a hydrolysis and acid reactor indicated by the low gas production and acidic leachate characteristics. There were also almost no digestate generation which eliminates costly post treatment units before the discharge of digestate, which is a critical problem for wet digestion counterpart.

ACKNOWLEDGMENT

the project above, however it is only the authors of this article who are responsible for the results and discussions made herein. The authors would also thank to Izmir Metropolitan Municipality and General Directory of IZSU for their supports.

REFERENCES

[1]. (2016) The TurkStat website. [Online]. Available: http://www.tuik.gov.tr/
[2]. N. G. Turan, S. Çoruh, A. Akdemir, O. N. Ergun, "Municipal solid waste management strategies in Turkey", *Waste Management*, vol. 29, pp. 465-469, 2009.
[3]. I. Bakas, L. Milios, " Municipal waste management in Turkey" , European Environment Agency, 2013
[4]. Y. Li, S. Y. Park, J. Zhu, "Solid-state anaerobic digestion for methane production from organic waste," *Renewable and Sustainable Energy Reviews*, vol. 15, pp. 821-826, 2011
[5]. I. M. Nasir, T. I. M. Ghazi, R. Omar, "Production of biogas from solid organic wastes through anaerobic digestion: a review,"*Applied Microbiology and Biotechnology*, vol. 95, pp. 321-329, 2012
[6]. T. Yang, Y. Li, J. Gao, C. Huang, B. Chen, L. Zhang, X. Wang, Y. Zhao, B. Xi, X. Li, "Performance of dry anaerobic technology in the co-digestion of rural organic solid wastes in China," Energy, vol. 93, pp. 2497-2502, 2015.
[7]. J. Fernández-Rodríguez, M. Pérez, L.I. Romero, "Dry thermophilic anaerobic digestion of the organic fraction of municipal solid wastes: Solid retention time optimization," *Chemical Engineering Journal*, vol. 251, pp. 435-440, 2014.
[8]. S. K. Cho, W. T. Im, D. H. Kim, M. H. Kim, H. S. Shin, S. E. Oh, " Dry anaerobic digestion of food waste under meshophilic conditions: Performance and methanogenic community analysis," *Bioresource Technology*, vol. 131, pp. 210-217, 2013.
[9]. X. Ge, F. Xu, Y. Li, "Solid-state anaerobic digestion of lignocellulosic biomass: Recent progress and perspectives," *Bioresource Technlogy*, vol. , pp. 239-249, 2016.
[10].J. Zhu, Y. Zheng, F. Xu, Y. Li, "Solid-state anaerobic co-digestion of hay and soybean processing waste for biogas production", *Bioresource Technlogy*, vol. 154, pp. 240-247, 2014.
[11].P. Michele, D. Giuliana, M. Carlo, S. Sergio, A., Fabrizio, "Optimization of solid state anaerobic digestion of the OFMSW by digestate recirculation: A new approach," *Waste Management*, vol.35, pp. 111-118, 2015.
[12].D. J. Lee, S. Y. Lee, J. s. Bae, J. G. Kang, K. H. Kim, S. S. Rhee, J. H. Park, J. S. Cho, J. Chung, D. C. Seo, " Effect of volatile fatty acid concentration on anaerobic degredation rate from field anaerobic digestion facilities treating food waste leachate in South Korea, " *Journal of Chemistry*, vol. 2015, 2015
[13].I. Angelidaki, L. Ellegaard, B. K. Ahring, "A mathematical model for dynamic simulation of anaerobic digestion of complex substrates: focusing on ammonia inhibition," *Biotechnology and Bioengineering*, vol. 42, pp. 159-166, 1993.
[14].M. G. Herardi, *The Microbiology of Anaerobic Digester*, 1st ed., Hoboken, New Jersey: John Wiley &Sons, 2003
[15].M.Y. Qian, R. H. Li, J. Li, H. Wedwitschka, M. Nelles, W. Stinner, H.J. Zhou, "Industrial scale garage-type dry fermentation of municipal solid waste to biogas," *Bioresource Technology*, in press, 2016.
[16].C. Rico, J. A. Montes, M. Munoz, J. L. Rico, "Thermophilic anaerobic digestion of the screened solid fraction of dairy manure in a solid-phase percolating reactor system," *Journal of Cleaner Production*, vol. 102, pp. 512- 520, 2015.
[17].D. Y. C. Leung, J. Wang, "An overwiev on biogas generation from anaerobic digestion of food waste," *International Journal of Green Energy*, vol. 13:2, pp.119-131, 2016
[18].A. Khalid, M. Arshad, M. Anjum, T. Mahmood, L. Dawson, "The anaerobic digestion of solid organic waste," *Waste Management*, vol. 31, pp. 1737-1744, 2011.

BIOGRAPHY

Kubra Arslan was graduated from Ege University Bioengineering Department in 2014. She has been doing her MSc degree at Ege University Environmental Sciences Department. She is currently working under a project which is supported by TUBITAK. Her research interest focuses on environmental biotechnology, solid-state anaerobic digestion and biogas production

Process Design for the Recycling Of Tetra Pak Components

Mustafa Karaboyaci[1]*, Gozde Gizem Elbek[1], Mehmet Kilic[1], Aziz Sencan[1]

[1]*SüleymanDemirelUniversity, Department of Chemical Engineering, 32260, Çünür/Isparta, Turkey*

**Corresponding author mustafakaraboyaci@sdu.edu.tr*

Abstract

The Tetra Pak packaging which was originally designed and developed for milk is widely used in the packaging of many foods and beverages. It is important to recycle and recovery of Tetra Pak's due to the different types of recyclable materials included 75% paper, 20% polyethylene and 5% aluminum. There are serious problems in recycling of composite beverage cartons that completed their lifetime and became a waste. A larger part of this packaging waste is disposed in landfills. Therefore, our priority should be performing scientific studies for management of this waste and operating with appropriate management alternatives. In this study, assessment methods and processes of waste composite drinks cartons are researched, and an alternative way is shown which separately recovers cartons, paper, aluminum and polyethylene. Tetra Pak films were cut into over 40 mm pieces, and charged to the reactor with stirring with chloroform. Thus paper, aluminum and polyethylene dissolves in chloroform. The resulting polyethylene and solvent liquid was transferred to distillation unit. The mixture of aluminum and paper remaining in the reactor was boiled and stirred until it turns into a pulp. Filtration of water is ensured by waiting the pulp on the fine sieve and the percentage of remaining solid is determined by analysis at the end of this waiting period. Thus only aluminum is remaining in the reactor. With the designed system, the waste amount of countries going to the solid waste storage areas will decrease and the protection of our environment will be provided. Tetrapak recovery will be a long-term economic investment. Recycling sector will be a step more advanced. The study will also result in allowing new technologies and reducing raw material needs.

Key words

Tetra pak, Recycle, Process design

1. INTRODUCTION

One of the most significant components, that threatens the future of the world are solid wastes. Unfortunately growing population and technological developments has resulted in an increase in solid wastes. In addition, the changes in consumption habits affect the composition of the waste.

Composite cartons which containing layers of paper, plastic and aluminum, especially preferred for storage of beverage packaging type.

There are serious problems in recycling of composite beverage cartons that completed their lifetime and became a waste. A larger part of this packaging waste is disposed in landfills. Therefore, our priority should performing scientific studies for management of this waste and operating with appropriate management alternatives.

Materials that are made by the macro-level unification of two or more materials from the same or different groups in order to merge their best characteristics or to bring out a new characteristic are called "Composite Materials." It can also be termed as the bonding of different materials or phases of materials with the objective of strengthening each other's weaknesses and attaining a superior characteristic [2].

The purpose of using different materials together is to increase durability and flexibility and to combine the unique characteristics of each material. The predominantly paper-cardboard composite packages known as Tetrapak are especially preferred in the conservation of liquid food products and are commonly used throughout the world.

The composite drinking cartons used in the food sector especially for long-term conservation of liquid food products are made up of 75% paper, 20% polyethylene and 5% aluminum [3].

Its layers from the outside inwards is as follows;

1. Polyethylene: Protection against external effects and moisture

2. Printing Ink

3. Cardboard: Stability / Strength

4. Polyethylene: Adhesion layer

5. Aluminum Foil: Oxygen, flavor, light and ultraviolet radiation barrier

6. Polyethylene: Adhesion layer
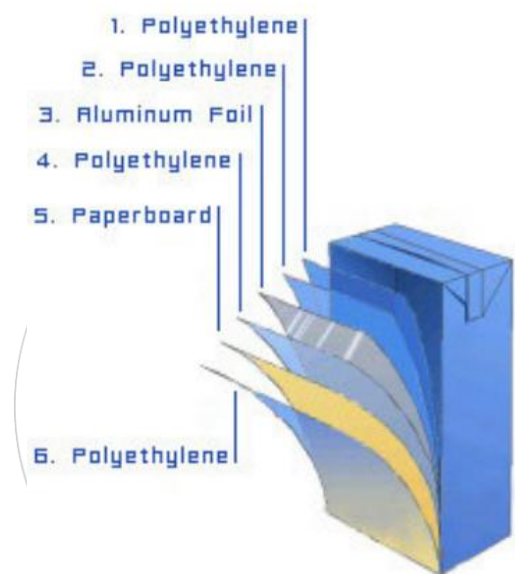
7. Polyethylene: Liquid sealing layer

Figure 1.The six layers (Tetra Pak) [2]

Tetra Pak was founded by Ruben Rausing and Erik Wallenberg in 1951 in the Swedish city of Lund. As of January 2013, the company Tetra Pak has supplied approximately 173, 234 million packages so that 77,307 million liters of milk, juice, nectar and other products could be delivered to consumers around the world[5].

The efficient separation of the 3 components found in composite drinking cartons is done by a company named Alcoa Aluminio in Brazil using plasma technology. The facility was established in 2006 with a setup cost of 40 million dollars. After the separation of paper fibers using the hydropulping method, the aluminum and the plastic mixture is heated to 15.000°C and as a result of this process, pure grade aluminum and paraffin oil to be used in the petrochemical industry is produced. The amount of energy required in the facility to produce 1 ton of aluminum is 400-500 kWh. The plasma plant processes 8.000 tons of aluminum and plastic mixture in a year, which corresponds to 32.000 tons of aseptic material; but it is known that this method is very costly.

In Germany, the plastic and aluminum mixture is used as alternative fuel in cement kilns, functioning as a catalyst.

In the company called Corenso in Finland, the gasification method is applied. The aluminum and plastics separated from the paper fibers in the facility are sent to the Ecogas plant. At this stage, while aluminum is recovered in granular form, gas is obtained from polyethylene. The steam produced in the recycling process in gasification is used in paper production. The facility, which began operation in 2001, processes 85.000 tons of carton boxes a year; of which 50.000 tons comes from Germany, a couple of thousand tons comes from Holland, and the rest comes from Finland.

The first method used in the recycling of composite drinking cartons was the particle board method. The boards manufactured from processing the product without separating it into its components (thermal compression) were used in furniture, civil construction, and packaging industries. In later years, the recycling of paper (hydropulping) began, in which the paper fibers that constituted 75% of the composite drinking cartons were recovered. The remaining polyethylene and aluminum parts left after the composite drinking cartons undergo hydropulping is subjected to plastic product

transformation, energy recovery, pyrolysis and plasma technologies; but the cost of these technologies are quite high, and the processes are complex.

Nowadays, the collected tetrapaks are accumulated in certified collection and separation facilities, in landfill areas, or burned in cement plants.

With this project, the paper, aluminum and polyethylene in waste tetrapaks shall be recycled, and the recovered materials shall be used to reduce the raw material needs of various facilities. Thus, the natural balance shall be protected against the increase in consumption that rises in parallel with the increase in human population.

At the same time, with the selling of the recovered materials as raw materials to related facilities, businesses be able to ensure high levels of energy saving. There are many establishments that can utilize paper, aluminum, and polyethylene as a source of raw material.

MATERIALS AND METHODS

Tetrapak films are cut in approximately 40mm sizes, and a 2 gr sample is mixed in a reaction flask with 40 ml (1 to 20) of chloroform in 65°C for 2 hours. As a result of this process, paper, aluminum and polyethylene dissolved in the chloroform is produced in the flask. The dissolved polyethylene in the chloroform is transferred to the distillation unit, and solid polyethylene is obtained after the solvent is evaporated. As the solvent condensed in the distillation unit can be re-used in the reaction flask, its continuous use makes it economical. Water is added (1 to 20) to the aluminum and paper left in the reaction flask to be boiled and mixed until it turns into paper-mache (pulp). The paper pulp is separated from the aluminum by watering and filtering it. The paper pulp is then placed on a fine sieve to allow the water to filter down; after the waiting period, the solid material content percentage is determined with analyses. Similar to the solvent, the re-use of the water is possible and is used when necessary. Thus, only the aluminum remains in the reaction flask.

RESULTS AND DISCUSSION

Experiments were performed in SuleymanDemirel University and it is altitude is over 1065 meter and so atmospheric pressure is over 674 mm Hg. So boiling point of the water is over 96,5 ºC. So dissolution of composite compounds takes more longer time than expected. Separation of all aluminum part from paper takes over 2 hours. After all aluminum separates from paper this means all polyethylene is dissolved. After this stage, the pulp is separated by filtration from polyethylenecontainingchloroform. After evaporation of chloroform 0,36 grams of polyethylene was obtained. In the literature it has been reported that tetra pak includes over 20 percent of LDPE. [1]. 0,36 gran is about %19 percent and it is consistent with the literature. After evaporation % 92 of solvent was recycled.

Filtered aluminum-paper mixture started to boil with 40 mL water. About 2 hour's paper start to divide to its fibers and being a pulp. Following this step, the paper is diluted by addition of water and a miscible fluid consistency. The liquid paper pulp filtered from aluminum with 10 mesh size filter. After filtering and drying 1,52 gram of paper pulp was obtained. In the literature it has been reported that tetra pak includes over 75 percent of paper [4]. 1,52 gran is about %76 percent and it is consistent with the literature.As in [6], they pyrolysis tetra pak composite for to obtain aluminum and they obtain about %7 of aluminum from waste tetra pak. In this study 0,12 gram aluminum obtained and it is %6 of the total weight and consistent with the literature.
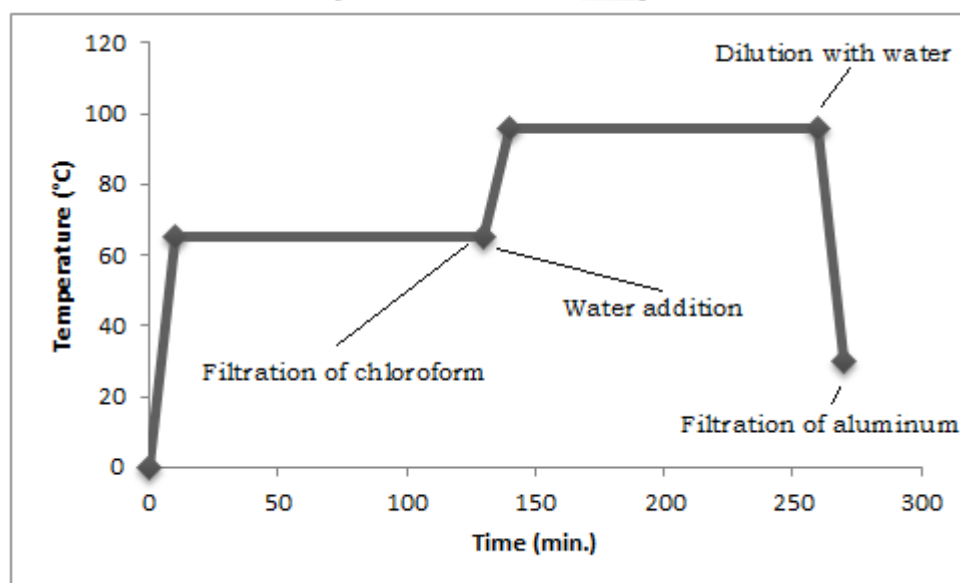

Figure 1. Process steps of tetra pak recycling

Figure 1 shows the details of Tetra Pak recycling process. As seen from the figure recycling process is easy to application. It takes about 4 hours to separate all compounds of the composite and all solvents are recyclable.

Figure 2 shows the disassembled components of the composites. First picture (a) is polyethylene, second picture (b) is dried paper pulp and third picture (c) is recycled aluminum.
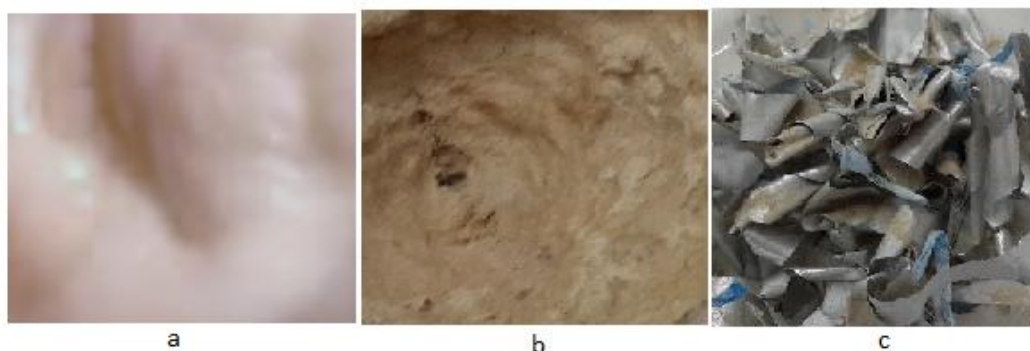

Figure 2.Separated components of Tetra Pak

CONCLUSIONS

Tetrapak films were put in reaction with chloroform under heat and pressure. The products of this reaction were paper, aluminum, and polyethylene dissolved in chloroform. Polyethylene was easily recovered in the distillation unit, and the chloroform from the distillation unit was re-used in the system. High-grade aluminum and paper were obtained by introducing water to the reaction flask. It was concluded that in terms of obtaining high-grade Tetrapak components, use of chloroform under heat and pressure was an interesting method as it resulted in requiring less duration and reaction times. Thus, the Tetrapak package that consisted of starting materials with different compounds was easily recycled. As a result of recycling, the damage to the environment and pollution due to increasing consumption habits will be prevented.

At the same time, with the selling of the recycled materials as raw materials to related facilities, businesses be able to ensure high levels of energy saving. There are many establishments that can utilize paper, aluminum, and polyethylene as a source of raw material.

The greatest reason why paper and carton (cardboard) manufacturers prefer recycled paper as raw materials is because they are able to obtain the cellulose necessary for paper for much cheaper. The paper that will be obtained in the envisaged project is in the form ofpaper-mache (pulp), which will be a reason for preference as it will not require any additional pulpification.

Aluminum, on the other hand, is used in many different industries in the manufacturing of millions of different products. Aluminum production from recycled aluminum required 95% less energy in comparison to aluminum production from raw materials. When 1 kg of aluminum is recycled, 8 kg of bauxite mineral, 4 kg of chemicals, and 14kWh of energy is preserved. When all these are considered, the importance of aluminum recycling is evident.

ACKNOWLEDGEMENTS

REFERENCES

[1]. Abreu M., Recycling ThaFibresOn Tetra Pak Cartons. Tetra Pak Canada Inc. 2000.
[2]. Pietikäinen, V., Collection and recycling of beverage cartons at AIT. Project report. 2008.
[3]. Ayrılmış, N., Candan, Z., Hızıroğlu, S. "Physical And Mechanical Properties Od Cardboard Panels Made From Used Beverage Carton With Veneer", Materials & Design, 29, 1897-1903. 2008
[4]. Ayrılmış, N., Kaymakçı, A., Akbulut, T., Elmas, G. M. "Mechanical Performance Of Composites Based On Wastes Of Polyethylene Aluminum And Lignocellulosics" Composites: Part B, 47, 150-154.
[5]. Tetra Pak Global Site. "Recycling And Recovery". [Online]. Available: http://www.tetrapak.com/environment/recycling-and-recovery/aluminium-and-polyethylene,
[6]. Korkmaz, A., Yanık, J., Brebu, M., Vasile, C. "Pyrolysis Of The Tetra Pak", Waste Management, 29, 2836-2841. 2009.

Performance of Dual Axis Solar Tracking System Using Fuzzy Logic Control: A Case Study in Pinarhisar, Turkey

Hayrettin Toylan[1]*

[1]KirklareliUniversity, Department of MechatronicEngineering, 39100, Kirklareli, Turkey.

*CorrespondingAuthor email: hayrettintoylan@klu.edu.tr

Abstract

Generating electrical via solar energy is one of the most popular renewable energy source. Modular structured solar panels that work according to photovoltaic principles convert solar radiation into electrical energy. There are some ways of increasing the power produced by the photovoltaic panels. One of the most effective ways is to minimize the angel of rays from sun to panel surface by taking the right position according to the angle of the sun. This paper proposes an intelligent control method for solar tracking. This method uses a fuzzy logic controller applied to the DC motors in solar tracking system (STS). STS is designed and developed as dual axis. Fuzzy logic algorithm used in STS was applied separately in order to control DC motors which determine the azimuth and zenith angels of the system. Position error which is obtained by the help of encoders tied to the motors and error variation were taken as input of fuzzy logic algorithm, applied voltage to the motor was taken as output of fuzzy logic algorithm. Finally, results of the photovoltaic panel on the STS controlled by fuzzy logic are compared to those obtained by the photovoltaic panel system without STS according to instantaneous power performance throughout the day in Pinarhisar, Turkey. Experimental results show that the STS which uses fuzzy logic controller increases the efficiency of energy production from PV.

1. INTRODUCTION

Energy is an important factor in industrialization, urbanization and financial growth and social life quality of a country [1]. That is why energy demand worldwide is increasing and this condition is most likely to continue in the future [2,3]. This demand increase lead people towards renewable energy sources such as wind, geothermal, and solar energy sources since fossil fuels are exhaustible. In Turkey, according to final data in 2014, when distribution of renewable sources in total of 69519,8 MW established power is analyzed, shares of wind, geothermal and solar energy are seen to be respectively 3629,7 MW, 404,9 MW and 40,2 MW [4]. In Turkey, %5,86 of the electricity produced is gained from wind, geothermal and solar energy (Figure 1.1). Nevertheless, with the use of renewable energy sources, share of electricity production shows an increasing trend in an annual basis.
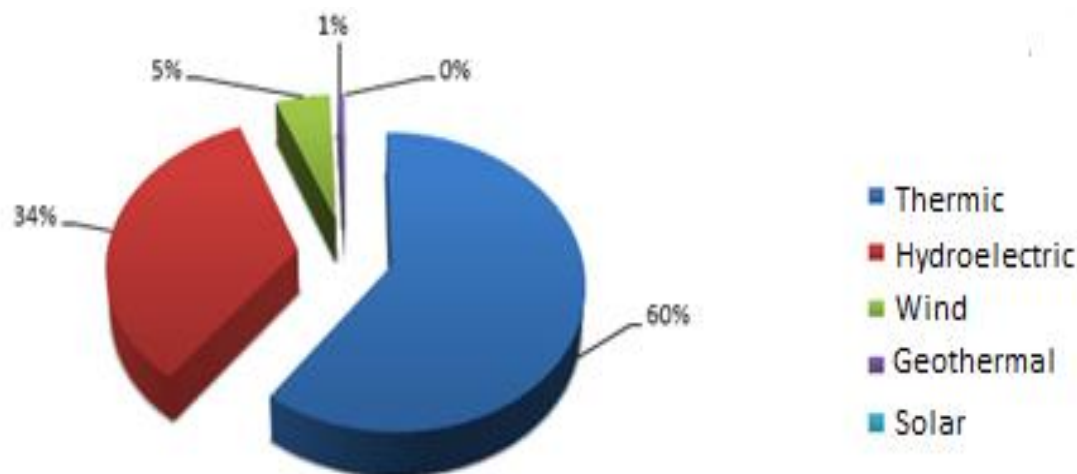
Figure 1. Distribution according to installed power capacity of energy types in Turkey [4]

One of the most important renewable energy sources is surely solar energy. Even though electricity energy produced out of it is lower when compared to other energy sources, thanks to advancements in solar energy industry, with decrease in the initial investment costs and increase in the efficiency, there is no doubt that its contribution rate will be increasing every year. Owing to the geographical position of our country, it can be said that it is in a lucky position in terms of receiving sun when compared to many other countries. Therefore, benefiting from infinite and free solar energy in maximum level will support the interests of our country which is dependent on foreign countries for energy.

Photovoltaic systems enable solar power to turn into electricity energy. Power that these systems produce depend on a variety of factors including the amount of energy they receive from sun rays. In order to increase the efficiency of photovoltaic systems, scientists and engineers have made many researches. In general, there are three ways to increase the efficiency of photovoltaic systems. First method is to increase power production efficiency of solar cells [5,6]. Second one is related to increasing the effectiveness of control algorithm for energy conversion systems that include maximum power point tracking [7,8]. Third approach is to use solar tracking system in order to make maximum use of solar energy [9].

There are a number of works proposed by many researchers to solar tracking. In their work, Sefa et al. have done the design and application of PC-based one axis solar tracking system. The reason why they have used one axis is that they thought system's total weight of 3500 kg would make double axis tracking harder [10]. M.J. Clifford and D. Eastwood have designed a one axis solar tracker that is, in other words, appropriate for use only in Ecuador regions [11]. Tiberiu and Liviu have used one-axis solar tracker and opted to manually adjust the other axis throughout the year with regular intervals [12]. WafaBatayneh et al. designed dual-axis solar trackers which are driven by a DC motor for each axis of tracking. They presented a fuzzy logic based controller for controlling the DC motors. They used four small PV cells as sensors to find solar position. [13]. While choosing the mechanical system of solar tracking systems, its cost analysis should be made. Cost of the tools to be used in the system and power consumption should be taken into consideration.

In this study, the effect of solar tracking system, which is controlled with fizzy logic at Kirklareli University Pinarhisar Vocational School, upon the performance of solar panels have been put under the scope. A comparison is made between the daily energy productions of fixed positioned PV panels and PV panels that are positioned on solar tracking system.

2. MATERIALS AND METHODS

2.1. Page Layout Sun Tracking System Design and Control

In the electro-mechanical system of solar tracking system, there are 2 DC motors, 2 reducers, 2 encoders, 1 double channel motor driver, daq card and a computer. In the mechanical structure of STS, PV panels have the motion ability with two double axis, and are positioned with direct current (DC) motors. By providing the revolution of panels in Azimuth and Zenith angles, sun can be tracked in a way that enables sunrays to fall onto panels with vertical angle.
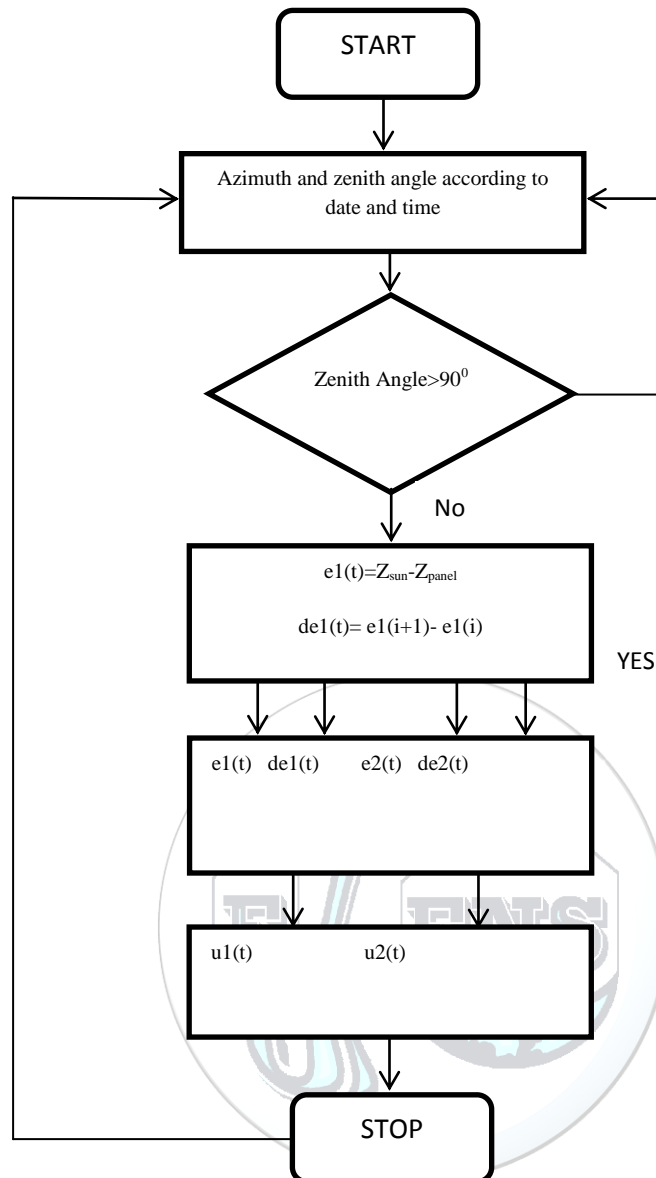
Figure2. Flow chart of the fuzzy controller

As shown in Fig 2, Azimuth and Zenith angle of Sun is calculated according to time/date and geographical information. If the Zenith angle is more than 90 degrees, sun is set. Running solar tracking system is needless. In the other condition, pulse signals coming from the encoder bound to motors, and consequently the errors and rate of changes of errors are calculated. For each motor, error (e) and change of error (de) are applied to Fuzzy Controller as input. The output of the fuzzy controller will be the motor's speed needed to move the panel.

2.2. STS using Fuzzy Logic

Fuzzy logic controller, which was first created in 1965 by Zateh [14], is a system defined via fuzzy rules and created by the professional experience. It is a system that includes the linguistic variables instead of the mathematical model of a dynamic system. It has four main parts: (i) Fuzzification (ii) Rule base, (iii) Inference (iv) Defuzzification interface The proposed system for two DC motors in this study consist of two input variables: error (e) and change of error (de), and one out variable: duty ratio (u), as shown in Fig. 3
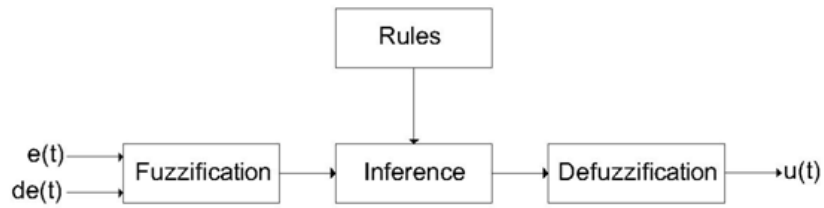
Figure3. General diagram of a fuzzy controller

Fuzzification

In the fuzzification process, membership function values are assigned to the linguistic variables. In order to carry out this process, the input variable range is transformed to the convenient universal cluster and by this way the input values are transformed to the convenient verbal values. In this study have five fuzzy subsets: NB (negative big), NS (negative small), ZE (zero), PS (positive small), and PB (positive big). In the fuzzification process various membership functions are used. In this study, triangle function is used as the membership function.
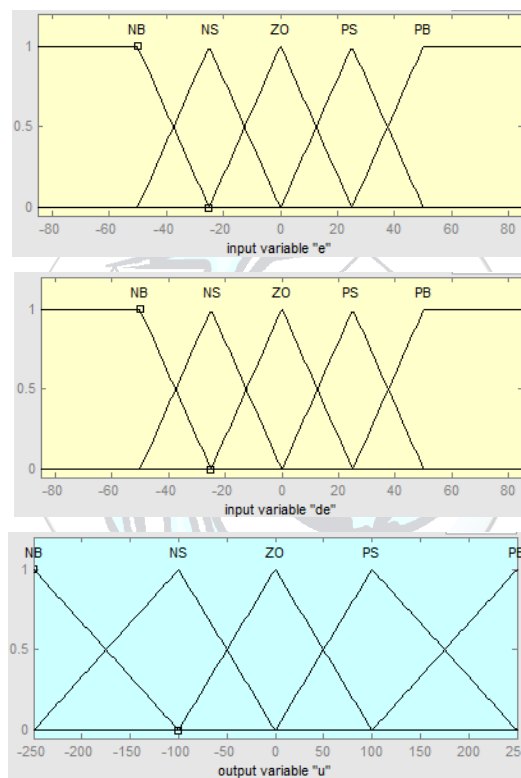
Figure4. Fuzzy logic membership functions for inputs and output variable of zenith angle.
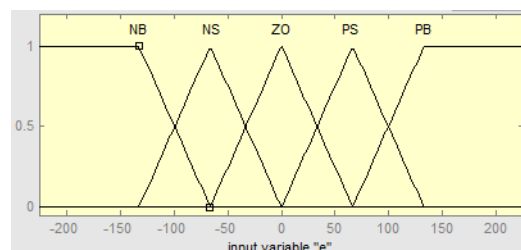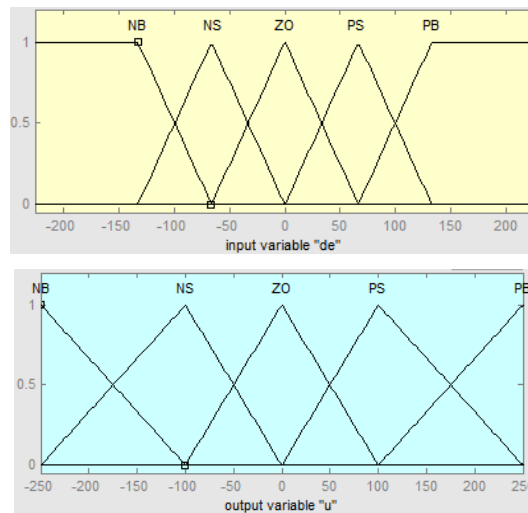
Figure5. Fuzzy logic membership functions for inputs and output variable of azimuth angle.

Rule base

Rule base, holds the knowledge in the form of a set of rules, of how best to control the system. In this study, 25 number "if-in that case" rules have been created. The result of rules and motor PWM values are determined. In table 1, a part of rule table which is created for the input variables takes place.

Table 1.Fuzzy controller rules

e/de	NB	NS	ZE	PS	PB
NB	NB	NB	NB	NS	ZE
NS	NB	NB	NS	ZE	PS
ZE	NB	NS	ZE	PS	PB
PS	NS	ZE	PS	PB	PB
PB	ZE	PS	PB	PB	PB

Inference

The data coming to system in the blurring rule base are processed by the inferring mechanism after they are ready to be processed. In this study, Mamdani method, which is one of the inferring method, has been used. While the threshold values of rules are measured in Mamdani inferring method, firstly " and (intersection)" then "or (combination)" processors are used.

Defuzzification

In the defuzzification process, the process of transforming the fuzzy set obtained in the fuzzy inferring motor to a definite value is carried out. In order that the obtained fuzzy set is to be applied the real life, there must be a numerical value. In this study, center of gravity method has been used. The center of gravity of the inferred cluster, which has been created via this method, is found and the value coming to this center as a definite value is assigned.

3. RESULTS AND DISCUSSION

In this study, a dual axis solar tracking system based on fuzzy logic controller, which simultaneously carries four number of 120 W panels, has been designed. According to the researches, before deciding to use solar following systems, the first thing that must be done is to take into account the initial investment cost and energy waste. In order to decrease the initial investment cost, two number of DC motor instead of servo motor have been used in order to move panels in azimuth and zenith angles. Angle position information of panels has been found with pulse signals read with the help of reed sensor instead of industrial encoder. Again in order to decrease the cost, Arduino Mega 2560 model has been chosen instead of industrial daq card.

We use fuzzy logic to control the speeds of the two motors based on date/time aiming at increasing the efficiency of the solar panels. Two different fuzzy logic algorithms have been applied to two motors that control Azimuth and Zenith angles (Figure 6). In both algorithms, the number of rules was 5 and fuzzy logic membership function parameters were determined with the help of experiences.
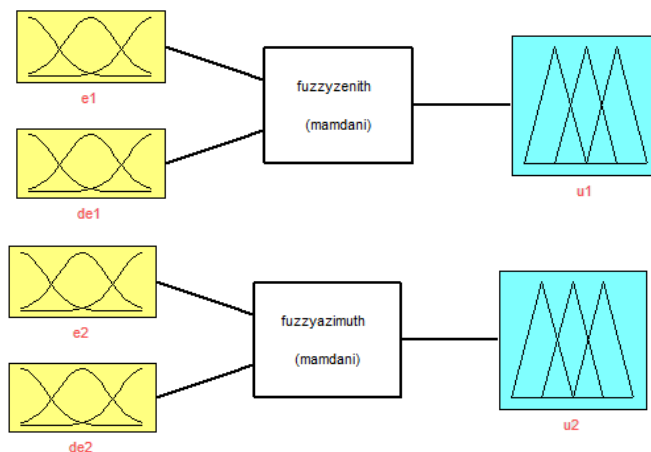
Figure 6.Fuzzy logic controller.

The dual axis solar tracking system presented here is tested experimentally. The experimental study is realized at Pinarhisar Vocational High School in Kirklareli, Turkey. STS has the capacity of carrying four panels, but measurements have been made over a 120 W panel. For performance evaluation, a comparison has been made between all-day productions of fixed panel and the panel positioned on STS. Installation angle of fixed panels have been determined as 38 degree south by considering the latitude angle of Kırklareli University Pinarhisar Vocational School taking into account that they will be used in summer and winter conditions.

Performance analysis of STS located at Kirklareli University Pinarhisar Vocational High school and fixed panel was made on the 17.09.2015.
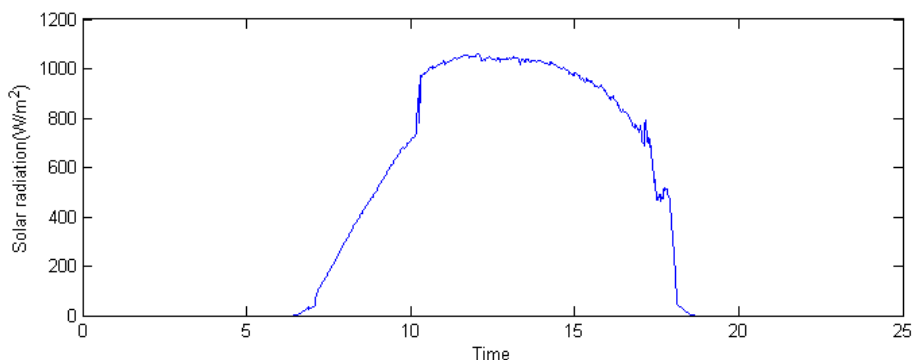
Figure 7. The results solar radiation amount on the 17th of September 2015.
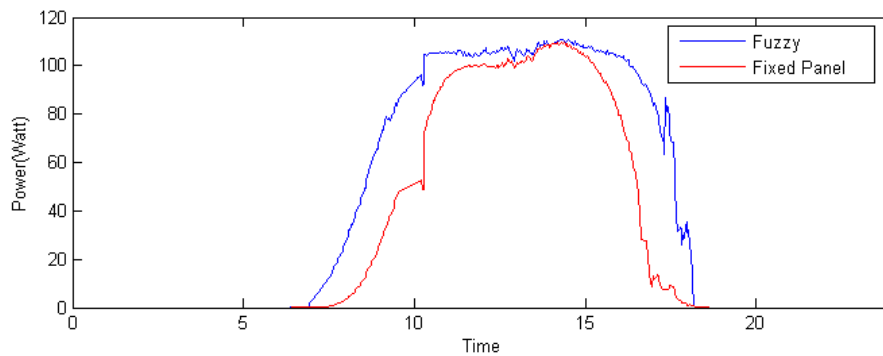
Figure 8. Power output values seems of the fixed panel and the PV panel using STS in Pinarhisar, Turkey. The results presented are on the 17th of September 2015.

It can be seen that throughout the whole day, the PV panel on STS has the highest power output due to highest solar irradiance exposure. The fixed PV panel has a lower output power compared to the panel on STS due to low solar irradiance. In Pinarhisar on the specified date it was found that the daily output power of the STS used with Fuzzy logic was 35.6% higher than the fixed PV panel

4. CONCLUSIONS

In this paper the speed of DC motors in dual axes solar tracking system is controlled using fuzzy logic controller. Results of the photovoltaic panel on the STS controlled by fuzzy logic are compared to those obtained by the photovoltaic panel system without STS according to instantaneous power performance throughout the day in Pinarhisar, Turkey. Experimental results show that the STS which uses fuzzy logic controller increases the efficiency of energy production from PV.

ACKNOWLEDGMENT

REFERENCES

[1]. V. Khare, S.Nema, and P.Baredar,"Status of solar wind renewable energy in India," Renewable and Sustainable Energy Reviews, vol. 27, pp. 1–10, Nov.2013

[2]. V. Subramanian, "Renewable energy in India: status and future prospects," Ministry of New and Renewable Energy, 2007

[3]. S. K. Sahoo, "Renewable and sustainable energy reviews solar photovoltaic energy progress in India: A review," Renewable and Sustainable Energy Reviews, vol. 59, pp. 927–939, June.2016

[4]. (2016) Theteias website. [Online]. Available: http://www.teias.gov.tr/yukdagitim/kuruluguc

[5]. S. Sun, J. Brooks, T. Nguyen, A. Harding, D. Wang, and T. David, "Novel Organic and Polymeric Materials for Solar Energy," Energy Procedia, vol.57, pp.79 – 88, 2014.

[6]. P. Oelhafen and A. Schuler, "Nanostructured materials for solar energy conversion," Solar Energy, vol.79, pp.110–121, August. 2005.

[7]. R. Pradhan and B. Subudhi, "Design and real-time implementation of a new auto-tuned adaptive MPPT control for a photovoltaic system," Electrical Power and Energy Systems, vol. 64, pp.792–80, 2015.

[8]. S. Daraban, D. Petreus, and C. Morel, "A novel MPPT (maximum power point tracking) algorithm based on a modified genetic algorithm specialized on tracking the global maximum power point in photovoltaic systems affected by partial shading," Energy, vol.74, pp.374-388, Sep.2014.

[9]. I. Stamatescu, I. Făgărăşan, G. Stamatescu, N. Arghira, and S.S. Iliescu, "Design and Implementation of a Solar-Tracking Algorithm," Procedia Engineering, vol.9, pp. 500-507, 2014.

[10].İ. Sefa, M. Demirtas, and İ. Çolak, "Application of one-axis sun tracking system, Energy Conversion and Management, vol. 50, pp. 2709–2718 Nov. 2009.

[11].M.J. Clifford and D. Eastwood,"Design of a novel passive solar tracker", Solar Energy, vol. 77, pp. 269–280, Sep.2004.

[12]. T. Tudorache, L. Kreindler, "Design of a Solar Tracker System for PV Power Plants,"ActaPolytechnicaHungarica, vol. 7, no. 1, 2010.

[13].W. Batayneh, A. Owais, and M. Nairoukh, "An intelligent fuzzy based tracking controller for a dual-axis solar PV system," Automation in Construction, vol. 29, pp.100–106, 2013.

[14]. LA Zadeh, "Fuzzy sets," Information and Control, vol.8, pp.338-353, Jun.1965.

Biodiesel Production Using Wet and Dry Purification Methods

Veli Gokhan Demir[1]*, Hakan Serhad Soyhan[2]

Balikesir University, Department of Mechanical Engineering, 10100, Balikesir,Turkey.

[2]SakaryaUniversity, Department of Mechanical Engineering, 54187, Sakarya, Turkey.

*CorrespondingAuthor email: veligokhandemir@balikesir.edu.tr

Abstract

In biodiesel production via transesterification, after removing glycerol from crude biodiesel, purification process must be performed before using biodiesel as a fuel that meets the EN 14214 standard. In the literature, various processes are presented for purification of biodiesel however; dry and wet washing methods are mostly recommended because of their higher efficiencies and easier applicabilities. In this study, methyl esters (biodiesel) derived from waste frying oil (WFO) and sunflower oil were generated using transesterification technique in the presence of KOH and methanol in a novel microwave assisted biodiesel reactor. For purification of crude biodiesel, two different methods; washing with distilled water as wet washing, and with magnesol as dry washing were carried out and compared. According to the results, dry washing method improved biodiesel yield and ester content, it also reduced the purification process time considerably.

1. INTRODUCTION

The chemical process, transesterification includes a TAG (triglycerides) reaction with a short chain monohydric alcohol in the presence of a catalyst to obtain biodiesel which is defined as fatty acid alkyl esters (FAAE), and by-product glycerol. Three moles of alkyl esters and one mole of glycerol are formed for every mole of TAG that undergoes complete conversion reaction [1]. In transesterification reactions, presence of sufficient amount of methanol is essential to break the glycerol-fatty acid linkages [2]. Methanol is the most commonly used alcohol in commercial biodiesel production via transesterification, since it is generally less expensive than other alcohols. There are different types of catalysts used in chemical reactions, among them; homogenous alkali catalysts (sodium or potassium hydroxide or methoxide etc.) are inexpensive catalysts generally used in commercial biodiesel production from refined or treated oils. Beside of the economic issues and concerns, homogenous alkali catalysts are more preferred than acid catalysts and enzymes due to their high reactivity and short reaction time requirements [1, 3]. Also, another reason for widely using alkali catalyzed biodiesel production techniques is this method's being less corrosive than others [4].

At the end of the alkali transesterification reactions, the by-product glycerol is removed from the crude alkyl ester-glycerol mixture. In addition, crude ester must be purified to obtain high quality biodiesel which must meet international standard specifications (EN14214, ASTMD6751 etc.) by removing excess contaminants (methanol, catalyst etc.) and impurities (soap, wax etc.) [5]. In commercial biodiesel production, purification method is called as washing process, and it is categorized into 2 techniques as: wet and dry washing [6]. Besides these, alternative washing method, membrane extraction has been investigated [7].

1.1. Wet Washing

Wet washing method is more traditional and widely used for removing containing the unreacted oil, excess catalyst and alcohol, salts, soaps, organic impurities etc. from crude biodiesel. In wet washing process, water is used for purification. Water has the ability to provide a means for addition of acid to neutralize the unreacted alkali catalyst. Wet washing

method simplifies removal of the salt products formed in transesterification reaction. The unreacted (excess) alcohol after transesterification should be removed before the washing process to decrease the amount of alcohol in the residual wastewater. Also, some researchers such as Van Gerpen et al. suggest removing process of excess alcohol after the end of wet washing [8, 9]. The researchers prevented precipitation of saturated fatty acid esters using distilled water (≈50-60°C). Emulsion generation is retarded when gentle water washing is applied fostering rapid and complete phase separation [8] The washing with hot distilled water results in the biodiesel purity of 99% [10]. Both of the dry and wet washing methods are used in commercial biodiesel production, however, it is claimed that only wet washing process can purify the biodiesel in desired levels, and the purified biodiesel meets the EN14214 standards [6].

Beside the advantages of wet washing, Low et al. [11] declared that this method has some drawbacks such as long separation time and loss of product yield. The loss of biodiesel yields in the rinsing water increases the formation of polluted liquid effluent [12]. In addition, the large amount of biodiesel wastewater formed after wet washing process causes an enormous problem for the biofuel industry and environment. Veljkoviˊc et al. [13] reported that the generated biodiesel wastewater was about 28 million m^3 in 2011 in the world.

1.2. Dry Washing

Using absorbents is another method of treating crude biodiesel. Dry washing technique generally uses ion exchangers or a magnesium silicate powder as absorbents [6]. These materials are utilized to replace the usage of distilled water in order to remove the impurities and purify crude esters. At the end of the dry washing, filtration is ordinarilycarried out for improving efficiency of the process. The advantages of dry washing can be described as: no waste water is generated and the total surface area coverage of the wash tank is minimized. Besides, this washing method has important advantages such as: strong affinity to polar compounds, easy to install into biodiesel processer plant, dramatically lower washing time, solid waste can be used in various ways, saves space etc. The main preferred absorbents in biodiesel production are defined as magnesol, ion exchange resin, activated carbon, activated fiber etc. [14].

Magnesol is used in many investigations and suggested by the authors. Sabudak and Yildiz[15] made a comparison of hot water washing (50%-V/V and 50°C) and dry washing with magnesol (1 wt%) according to the ester contents of methyl esters. They produced biodiesel from waste cooking oil by 3 different processes. In the event of one step alkali transesterification, they achieved 80.8% and 84.9% ester contents with wet washing and dry washing, respectively. In two step alkali transesterification, 91.0% ester content was obtained by wet washing while 92.3% by dry washing. In the third process (two step acid-alkali transesterification), 95.6% and 96.9% ester contents were measured at the end of the wet and dry washing processes, respectively. As a result, it was found that dry washing enhanced the ester content of crude biodiesel more than wet washing, in addition, only the samples purified by dry washing fulfilled with EN14214 ester content standards (min.96.5%). Berrios and Skelton [6]purified crude biodiesel samples using 0.25, 0.50, 0.75 and 1.00% magnesol concentrations at the temperature of 60 °C. 10 min and 20 min washing time were experimented while standard washing time is known as 30 min. A vacuum filtration and a water ejector were performed in separating process. With the exception of the experiments with 0.25% (wt/wt) magnesol concentration, all the experiments remove in satisfactory way the glycerol content in 10min of reaction. The same happened in the soap removal. They specified that min 0.75% magnesol concentration is needed with a washing time of 10 min; and it is necessary a previous methanol removal to avoid the saturation of the adsorbents. Also, none of the experiments decreased the methanol content below the defined level of the EN14214 Biodiesel Standards, and the best result was obtained using with 1%(wt/wt) magnesol concentration at 60°C temp. Bryan [16] applied dry washing technique in the presence of magnesol (1%) on both soybean and yellow grease crude biodiesels, also he used wet washing technique to compare those two methods clearly. The physicochemical properties of purified methyl esters (soybean&grease based) by dry washing method were fulfilled with EN 14214 and ASTM D6751standards. Moreover, the researcher claimed that magnesol treated sample of yellow grease derived methyl esters met all ASTM standards while the water washed and dried sample did not. The author remarked that magnesol has a strong affinity for polar compounds, thereby actively filtering out metal contaminants, mono and di-glycerides, free glycerin, and excess methanol as well as free fatty acids and soap.

1.3. Objectives

As it is seen in section *1.1.*and*1.2.,* conflicting outcomes exist in the literature about dry and wet washing purification methods. Thereby, the main objective of the study has been determined as comparing the wet washing method with hot distilled water and dry washing method with magnesol based on the obtained ester content amounts and yields of purified biodiesel samples. In the experiments, the biodiesel samples were produced via alkali catalyzed transesterification in various reaction conditions.

2. MATERIAL AND METHOD

2.1. Materials

In the experiments, methanol and KOH were used as an alcohol and a catalyst. The raw materials were determined as waste frying oil (WFO) with an FFA value ≈0.2% which was collected from local restaurants in Balıkesir, Turkey, and sunflower oil was supplied from an oil production plant. Methanol and KOH were purchased from Sigma–Aldrich, and magnesol ($MgO:SiO_2$ (1:2.7)) from Dallas Group of America.

2.2. Equipment

Biodiesel reactor:

The biodiesel processor system has 60 L capacity and it is composed of a reactor tank, a microwave heating system, a mechanic stirrer, a circulation pump, and a PLC circuit and software to control reaction parameters (temp, mixing rate etc.).

Wet washing:

The distilled water was produced from a water distillation system, and the washed crude biodiesel samples were settled in separatory funnels.

Dry washing:

In order to heat crude biodiesel samples filled into the beakers, the magnetic hotplate stirrer (Dragon-MS-H280-Pro) was used. In the filtering process, a vacuum pump and filters (pore sizes: 10 µm and 1.2 µm) were utilized.

2.3. Biodiesel Production

Reaction parameters:

In order to achieve maximum conversions, 6:1 molar ratio of methanol to oil is recommended in the literature[17]. Thereby, 6:1 molar ratio was fixed in all experiments we carried out. The catalyst loadings were defined as 1 wt% KOH for sunflower oil, and 1 wt% and 1.5 wt% for waste cooking oil. Because, the FFA of waste oils are higher than vegetable oils and free fatty acids can react with alkali catalysts to soap and water formation, and saponification consumes alkali catalysts [3]. In all the experiments, reaction temperature was set to 60°C.

Methyl ester formation:

Methyl ester production was realized in our novel microwave assisted biodiesel reactor in the defined production conditions, and two washing methods were performed to the same products after the settling processes. The main steps of biodiesel production are shown in Figure 1.
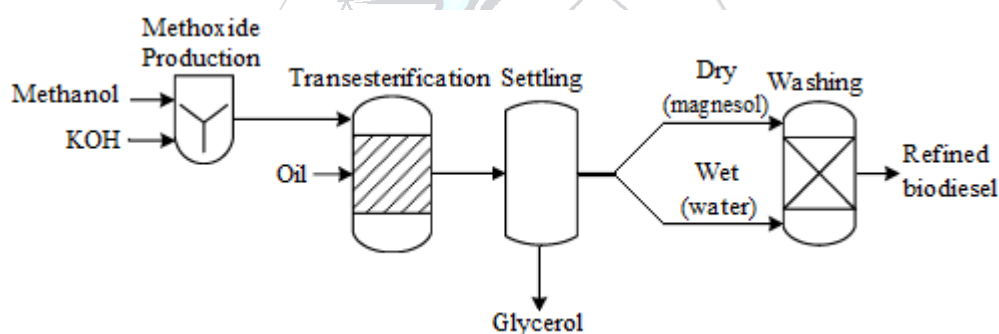
Figure 1. Schematic diagram of the biodiesel productions

Firstly, some physical and chemical properties of oils were determined (Table 1). Fatty acid compositions of oils were analyzed (IUPAC IID19) using Gas Chromatography (GC), and the average molecular weight of oils were calculated. Then the amounts of methanol and KOH were defined for each experiment. The density (EN ISO 3679), kinematic viscosity (EN ISO 3104), and methyl ester content (EN 14103) tests were performed on biodiesel or oils by using a pycnometer, a viscometer (AKV-202-TANAKA), and the ester contents were measured in İnönü University Fuel / Oil Analysis Laboratory in Malatya, Turkey.

Table 1. Some properties of WFO and Sunflower oil

Properties	Unit	WFO	Sunflower Oil
Density (15℃)	g cm^{-3}	0.925	0.921
Viscosity (40℃)	mm^2 s^{-1} 36.47		32.57
Acid value	mg KOH g^{-1}	0.69	0.26
Avr. molecular weight	g.mol^{-1}	879.14	879.82

In the first step of methyl ester production, methanol and KOH were added into the methoxide tank and the methoxide solution was formed. Then the methoxide was transferred to the reactor, into the preheated oil. Transesterification reactions were carried out at 60°C and the crude biodiesel samples were taken at different time intervals, and they were placed in the

separatory funnels. After the settling processes, two layers were observed as it is seen in Figure 2 (the upper layer is the biodiesel phase, the lower layer is the crude glycerol), and the glycerol layers were removed. Finally, the crude biodiesel samples were purified by two different methods.

Figure 2. Crude biodiesel and glycerol layers

2.4. Purification Process

As regards previous investigations about biodiesel production from WFO, the optimum result (by wet washing) was achieved with 20 min transesterification reaction while max reaction time was defined as 90 min. However, when sunflower oil was used as raw material, it was observed that the reaction was completed in a very short time, and at the end of the 20 min, 98.30% ester content was achieved. Thereby, the purification techniques were applied to the crude biodiesel samples produced in 20 min and 90 min.

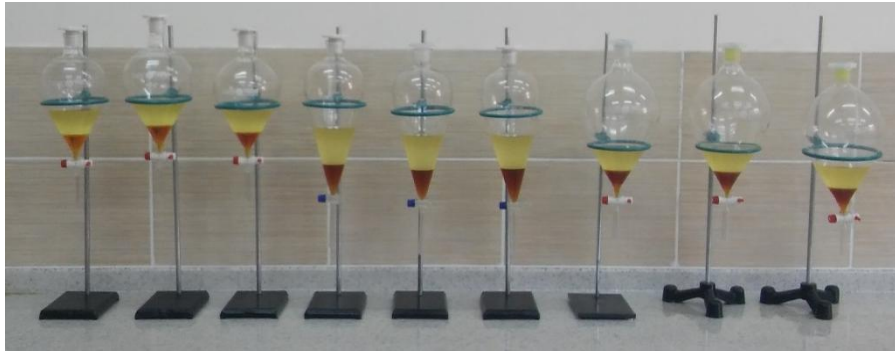### 2.4.1. Wet washing (water)

After removing the glycerol layers from the separatory funnels, warm distilled water at 55⁰ C was added into the each crude biodiesel samples, and the water-biodiesel mixtures were gently shaken. Then they were waited for settling, and two layers occurred as it is seen in Figure 3a and Figure 3b (the upper layer is washed biodiesel, the lower layer is waste water). The down layers were removed and the biodiesel layers were washed three times more. In the first three washing processes, the settling time was defined as 60 min while in the final washing the sedimentation time was performed as 360 min to provide the separation exactly. In order to remove undesired components such as the excess methanol or existing water, the washed biodiesel samples were dried at 110 ⁰ C until they were appeared crystal clear. At least, the final products were filtered using filter paper.

(a)   (b)
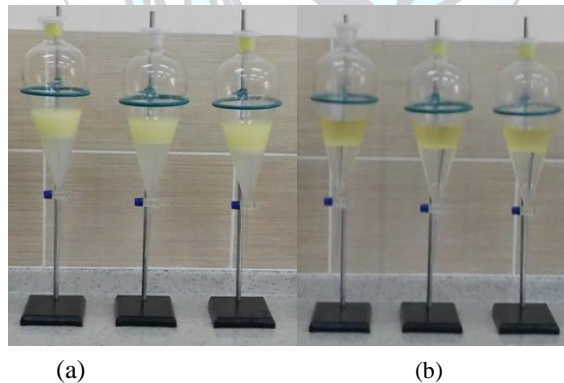
Figure 3. Biodiesel and wastewater layers: (a)1ˢᵗ wash, (b) 4ᵗʰ wash

2.4.2. Dry washing (magnesol)

In the dry washing processes with magnesol; at first, the glycerol layers were removed from biodiesel layer as same as the section 2.4.1. The crude biodiesel samples were transferred to the beakers and they were heated to 65⁰ C. The magnesol absorbents (1 wt%) were filled into the beakers and the mixtures were stirred for 30 min at constant 65⁰ C (Figure 4a). At the final stage, the mixtures were filtered in two steps (10 µm and 1.2 µm) under vacuum (Figure 4b). The initial and final appearance of used magnesol is shown in Figure 5. In this study, the experiments containing dry washing method, crude biodiesel samples were purified directly, however, one sample was dried at 110⁰ C to evaporate existing methanol and water before the purification process to observe the difference.
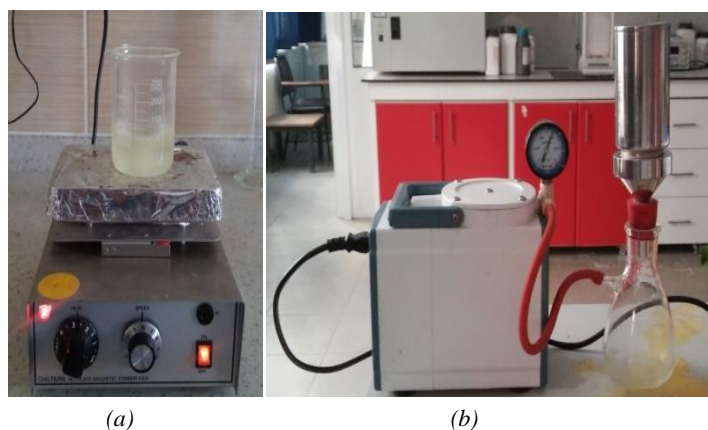
Figure 4. (a) Stirring process of crude biodiesel-magnesol mixture, (b)Filtering process using vacuum pump

Figure 5. The magnesol absorbent before and after the purification process

3. RESULTS AND DISCUSSION

Ester content (purity) is the main biodiesel property to analyze the transesterification efficiency and completion rate. Moreover, the purity level of biodiesel has a strong effect on fuel properties and on engine life. On the other hand, the main goal of transesterification reaction is decreasing the high viscosity value of oil, and density of biodiesel is a significant property affecting combustion process with viscosity. Thereby, these three main biodiesel properties were measured and analyzed, and wet and dry washing techniques were compared according to these values. In table 2 and 3, the differences of fuel properties and product yields related to used washing methods and raw materials are shown clearly.

Table 2. Fuel properties of the WFO based biodiesel samples.

Reaction time	Purification Processes	Density (15^0C)	Viscosity (15^0C)	Ester content	Product yield $(m_{biodiesel}/m_{oil})$
		(kg/m^3)	(mm^2/s)	(%m/m)	(%)
20 min	Wet washing	882	4.592	94.41	97.45
20 min	Dry washing	886	4.642	94.51	97.51
20 min *(1.5%KOH)*	Wet washing	874	4.784	94.27	94.64
20 min *(1.5%KOH)*	Dry washing	889	4.845	94.49	96.62
90 min	Wet washing	878	4.568	94.41	94.54
90 min	Dry washing	888	4.852	95.12	94.56
90 min	*2 step process:* 1st Wet washing 2nd Dry washing	870	4.566	95.76	92.31

Table 3. Fuel properties of the sunflower based biodiesel samples.

Reaction time	Purification Processes	Density (15⁰C)	Viscosity (15⁰C)	Ester content	Product yield ($m_{biodiesel}/m_{oil}$)
		(kg/m^3)	(mm^2/s)	(%m/m)	(%)
20 min	Wet washing	877	4.628	98.30	96.92
20 min	Dry washing	871	4.611	98.52	96.99
20 min	*2 step process:* 1st Wet washing	868	4.618	98.82	95.17
90 min	Wet washing	875	4.711	96.85	92.14
90 min	Dry washing	880	4.687	98.28	96.06
90 min	Dry washing (*After evaporating methanol*)	873	4.655	99.73	94.63
90 min	*2 step process:* 1st Wet washing	881	4.723	98.63	89.26

According to the results; 20 min WFO based and 90 min sunflower based biodiesel productions, dry washing method using magnesol increased the ester content compared to wet washing at the ratios of 0.22% and 1.43%, respectively. Also, the dry washing method performed after evaporating process gave the best ester content value in all experiments. This method increased the ester content ratios at the range of 1.45% (90 min transesterification) compared to the dry washing method. Absence of methanol and water in crude biodiesel must have contributed to enhance the efficiency of magnesol in absorbing the impurities (soap, glycerol etc.). When these two methods were applied consecutively, the increments in the ester contents were achieved as: ≈1.3% in WFO based biodiesel production (90 min), ≈0.5% in sunflower oil based biodiesel production (20 min) compared to wet and dry washing. In addition, the increments of 1.78% and 0.35% (90 min) were measured compared to wet washing and dry washing in sunflower oil based biodiesel production, respectively. In terms of product (purified biodiesel) yields, dry washing method gave the best results, and the two step purification techniques caused poor yield ratios. Regarding the density and viscosity properties, all the purification methods gave the suitable results according to the EN14214 standards. As seen in Table 2 and 3, the densities varies at the range of 868-888 kgm^{-3}, the viscosity values varies at the range of 4.568-4.726 mm^{2}s^{-1} while the EN14214 limits are 860-900 kgm^{-3} for density and 3.5-5 mm^{2}s^{-1} for viscosity of biodiesel.

According to the washing methods' practicability and fastness, dry washing method becomes prominent by reducing purification time dramatically. It minimized the process time up to 30 min from 540 min compared to wet washing method, moreover it does not require a washing tank and a water distiller system.

4. CONCLUSION

As a result of this study, it is observed that dry washing method is a more practical and efficient technique compared to wet washing (water) method. Dry washing method takes about less than 18 times than wet washing method; also it increases ester content and yield of biodiesel. In addition, evaporating methanol and water before dry washing improves purity (ester content) of biodiesel a little more. Applying wet and dry washing processes together increases ester content in comparison to wet washing and dry washing method however, it does not increase the ester content noticeably and it reduces product yield. This study shows that the optimum method for purifying crude biodiesel is dry washing.

ACKNOWLEDGMENT

BIOGRAPHY

Veli Gökhan DEMiR graduated from mechanical engineering at Sakarya University in 2008. He has a master degree in mechanical engineering from Balıkesir University and he has been a Ph.D. student since 2011. In his Ph.D. work, he has investigated about production of biofuels and their combustion efficiencies. Currently, he is a research assistant in mechanical engineering at University of Balikesir.

REFERENCES

[1]. B.R. Moser, "Biodiesel production, properties, and feedstocks," *In Vitro Cellular & Developmental Biology-Plant*, 45(3). p. 229-266, 2009.

[2]. M.I. Al-Widyan and A.O. Al-Shyoukh, "Experimental evaluation of the transesterification of waste palm oil into biodiesel," *Bioresource technology*, 85(3). p. 253-256, 2002.

[3]. Y. Zhang, M. Dube, D. McLean and M. Kates, "Biodiesel production from waste cooking oil: 1. Process design and technological assessment," *Bioresource technology*, 89(1). p. 1-16, 2003.

[4]. M. Jayed, H. Masjuki, R. Saidur, M. Kalam and M.I. Jahirul, "Environmental aspects and challenges of oilseed produced biodiesel in Southeast Asia," *Renewable and Sustainable Energy Reviews*, 13(9). p. 2452-2462, 2009.

[5]. N.M. Daud, S.R.S. Abdullah, H.A. Hasan and Z. Yaakob, "Production of biodiesel and its wastewater treatment technologies: A review," *Process Safety and Environmental Protection*, 94. p. 487-508, 2015.

[6]. M. Berrios and R. Skelton, "Comparison of purification methods for biodiesel," *Chemical Engineering Journal*, 144(3). p. 459-465, 2008.

[7]. D.Y. Leung, X. Wu and M. Leung, "A review on biodiesel production using catalyzed transesterification," *Applied energy*, 87(4). p. 1083-1095, 2010.

[8]. I. Atadashi, M. Aroua and A.A. Aziz, "Biodiesel separation and purification: a review," *Renewable Energy*, 36(2). p. 437-443, 2011.

[9]. J. Van Gerpen, B. Shanks, R. Pruszko, D. Clements and G. Knothe, *Biodiesel Production Technology, National Renewable Energy Laboratory Subcontractor Report NREL*. 2004, SR-510-36244.

[10]. F. Karaosmanoglu, K.B. Cigizoglu, M. Tüter and S. Ertekin, "Investigation of the refining step of biodiesel production," *Energy & Fuels*, 10(4). p. 890-895, 1996.

[11]. S. Low, G. Gan and K. Cheong, "Separation of methyl ester from water in a wet neutralization process," *Journal of Sustainable Energy & Environment*, 2(1), 2011.

[12]. S. Kumjadpai, K. Ngamlerdpokin, P. Chatanon, P. Lertsathitphongs and M. Hunsom, "Management of fatty acid methyl ester (fame) wastewater by a combined two stage chemical recovery and coagulation process," *The Canadian Journal of Chemical Engineering*, 89(2). p. 369-376, 2011.

[13]. V. Veljković, O. Stamenković and M. Tasić, "Wastewater management in biodiesel production," *Reporting For Sustainability*. p. 471-475, 2013.

[14]. I. Atadashi, M. Aroua, A.A. Aziz and N. Sulaiman, "Refining technologies for the purification of crude biodiesel," *Applied energy*, 88(12). p. 4239-4251, 2011.

[15]. T. Sabudak and M. Yildiz, "Biodiesel production from waste frying oils and its quality control," *Waste management*, 30(5). p. 799-803, 2010.

[16]. T. Bryan, Adsorbing It All. (2016); Available from: http://www.biodieselmagazine.com/articles/239/adsorbing-it-all.

[17]. R. Turck, *Method for producing fatty acid esters of monovalent alkyl alcohols and use thereof*. 2003, Google Patents;L. Meher, D.V. Sagar and S. Naik, "Technical aspects of biodiesel production by transesterification—a review," *Renewable and sustainable energy reviews*, 10(3). p. 248-268, 2006.

Prediction of Dam Reservoir Volume Fluctuations Using Adaptive Neuro Fuzzy Approach

Fatih Unes[1]*, F. Gokhan Gumuscan[1], Mustafa Demirci[1]

[1]*Iskenderun Technical University Civil Engineering Department / Hydraulics Division, Iskenderun / Hatay – Turkey.*

*Corresponding Author email: fatih.unes@iste.edu.tr

Abstract

Determination of reservoir volume fluctuations is important for the operation of dam reservoir, design of hydraulic structures, the hydropower for the energy production, flood damage reduction, navigation in the dam reservoirs, water quality management in reservoir and the safety of dam. In this study, reservoir volume variations were estimated using average monthly precipitation, monthly total volume of evaporation, dam discharge volume, and released irrigation water amount. In the present paper, adaptive-neuro-fuzzy inference system (ANFIS) was applied to estimating of reservoir volume fluctuations. ANFIS results are compared with conventional multi-linear regression (MLR) model. The results show that reservoir volume was successfully estimated using fuzzy logic model with low mean square error and high correlation coefficients.

1. INTRODUCTION

A dam reservoir is an artificial lake, storage pond or impoundment from a dam which is used to store water. Water structures such as dams are very expensive to build, and therefore, they must be well planned and management. Dam reservoir water volume predicting for different time intervals using the records of past time series is an crucial issue in water resources planning and management. Since predicting reservoir volume variations in a dam is affected by many environmental factors such as precipitations, the influence of adjacent catchments, evaporation, air and water temperature variations in catchments and reservoir surface, it is difficult to prediction of reservoir volume. Determining accurate volume of reservoir is important due to the design and operation of the hydraulic structures, the water supply, the irrigation and drainage, the energy production, flood planning and management, navigation in the dam reservoirs, water quality management and modeling in the reservoir.

Recently, the artificial intelligence techniques have been used in hydrology and water resources systems. Adaptive neuro-fuzzy inference system (ANFIS) which is one of them has been widely applied in water resources. ANFIS is a combination of an adaptive neural network and a fuzzy inference system. The parameters of the fuzzy inference system are determined by the NN learning algorithms. Since this system is based on the fuzzy inference system, reflecting amazing knowledge, an important aspect is that the system should be always interpretable in terms of fuzzy IF–THEN rules. ANFIS is capable of approximating any real continuous function on a compact set to any degree of accuracy [1].

ANFIS identifies a set of parameters through a hybrid learning rule combining backpropaga-tion gradient descent error digestion and a least-squared error method. There are two approaches for fuzzy inference systems, namely the approach of Mamdani [2] and the approach of Sugeno [3]. The neuro-fuzzy model used in this study implements Sugeno's fuzzy approach [3] to obtain the values for the output variable from those of input variables.

Keskin et al. [4] used fuzzy models to estimate daily pan evaporation in Western Turkey. Kazeminezhad et al. [5] applied ANFIS to forecast wave parameters in Lake Ontario and found ANFIS superior to the Coastal Engineering Manual methods. Kisi [6] investigated the ability of ANFIS techniques to improve the accuracy of daily evaporation estimation. Kisi and

Ozturk [7] used ANFIS computing techniques for evapotranspiration estimation. Demirci and Baltacı [8] estimated suspended sediment of Sacremento river in USA using fuzzy logic. Unes [9] predicted plunging depth of density flow in dam reservoir using the ANN technique. Unes [10], Unes at al. [11] used ANN model and Unes at al. [12] used generalized neural network (GRNN) model for predicting reservoir level fluctuation. Shiri et al. [13] used ANFIS for predicting short-term operational water levels.

The present study investigates the abilities of ANFIS and multi-linear regression (MLR) techniques to forecast daily reservoir volumes. Here, ANFIS has some daily input variables (basin rainfall, evaporation from reservoir, dam spillway release, and volume of irrigation water) and one output, reservoir volumes at the following day(s).

2. CASE STUDY

Yarseli Dam in Hatay region (Mediterranean part of Turkey) was selected for this study. Yarseli Dam was constructed Beyazçay river in Hatay, Turkey, and dam location can be seen in Figs. 1 and 2. The dam was built for the irrigation and the energy purpose and is located on the border of Hatay (Fig. 1). It is an earth fill dam having 55 million m^3 maximum reservoir volume, and 42 m height from the river bed. The data, which contains the time period between 2002 and 2012 on a daily basis, were obtained from Turkish General Directorate of State Hydraulic Works (DSI) and Turkish General Directorate of State Meteorology (MGM). The data sample consists of 10 years of daily records of basin rainfall (R), volumes of inflow river water (IR), evaporation from Reservoir (E), Dam Spillway Release (SR), volume of Irrigation water (IRGW) and change Reservoir Volume (CVO). These selected parameters are the most effective variables for reservoir volume fluctuation and measured in the field conditions and, therefore, are used in this work.

Based on these data both model development and validations are performed. Therefore, the first 3015 daily data are used for training the model, and the remaining 1004 daily data are used to test the model. Table 1 gives the statistical parameters of the used data set during the study period. In Table 1, x_{max}, x_{min}, and x_{avg} represent the maximum, minimum, and average values of the parameters within the time period, respectively. The values of s_x and c_{sx} are standard deviation and skewness coefficients respectively.

Table 1. Statistical summaries of all data of Yarseli Dam

Data	Statistical Parameters	R (mm)	IR ($10^3 m^3$)	E ($10^3 m^3$)	SP ($10^3 m^3$)	IRGW ($10^3 m^3$)	CVO ($10^3 m^3$)
1	2	3	4	4	5	6	7
	x_{max}	177	11883.0	50.00	9777.00	985.00	57104.0
Whole	x_{min}	0.0	-2935.0	0.00	0.00	0.00	4960.0
Data	x_{avg}	2.11	167.56	9.87	10.87	132.46	26549.(
	s_x	7.96	346.00	12.21	163.39	199.15	17690.9
	c_{sx}	7.45	11.85	0.92	53.54	1.23	0.34

R: Average Daily Precipitation; **IR**: Total Daily inflow river water; ;**E**: Total Daily Evaporation **SP**: Total Daily Volume Released from Spillway; **IRGW**: Total Daily Irrigation Volume; **CVO**: Total Daily Reservoir Volume.

Since the range of the variables is large, all the variables were normalized between 0.1 and 0.9 using the Equation 2 before training and testing phases.

$$x_{min} = 0.1 + 0.8\left(\frac{x_i - x_{min}}{x_{max} - x_{min}}\right) \tag{1}$$

Figure 1. The location of Yarseli dam in Turkey.


Figure 2. General view of Yarseli dam

3. APPLICATION AND RESULTS

MLR Results

Conventional multiple linear regression (MLR) technique were also used to define reservoir volume. These techniques assume a linear relationship among variables. Although a nonlinear approach is needed for the solution of reservoir volume problem, a multi_linear regression model was compared with field measurement and ANFIS model results. The MLR predicted and observed volumes are given for testing periods in Fig.3. A statistical analysis is performed between the estimated and the recorded test data to find out how well the ANFIS models perform. Performance evaluation measures, the mean square error (MSE) and the coefficient of correlation (R) between estimated and observed volume values of this statistical analysis are given Table 2. It can be seen from Fig.3 and Table.2 that MLR performance for testing and training stages is not quite satisfactory although the performance criteria have moderate values. The model estimates were quite scattered. The correlation coefficient between the predicted and the observed testing data is 0.74. The general shape of the recorded reservoir volume is not captured by MLR.

Table.2 Performance of different methods in terms of MSE, MAE and R

Method	MLR	ANFIS
MSE (Test)	0.043	0.032
MAE (Test)	0.170	0.130
R (Test)	**0.74**	**0.83**
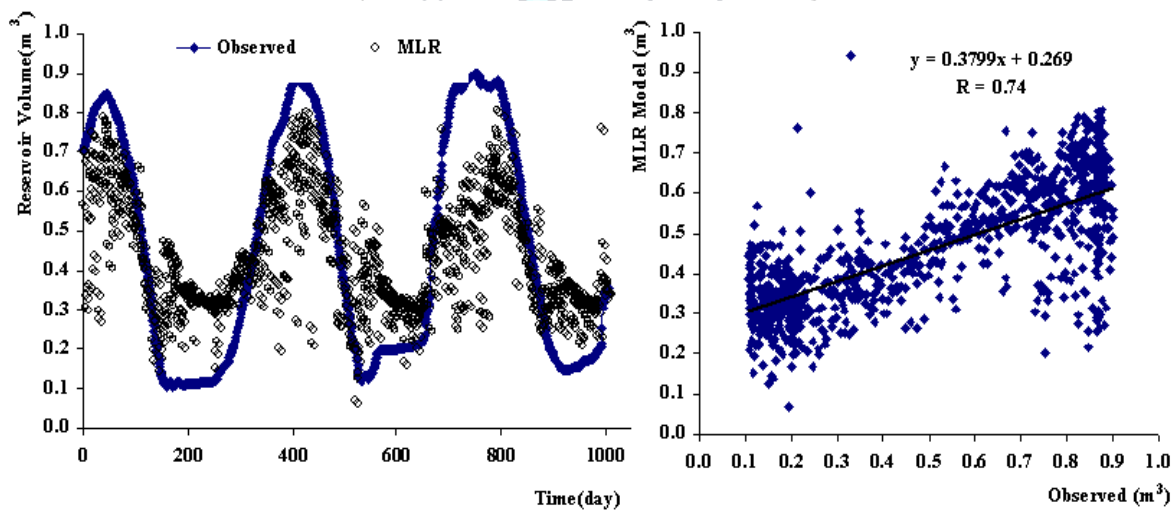
Figure 3.Observed and MLR model predicted reservoir volumes for Yarseli Dam in the test period

ANFIS Results

The back-propagation ANFIS network was applied in MATLAB code for forecasting reservoir volumes using the recorded aforementioned daily reservoir data. The testing statistics of ANFIS models in term of R, MAE and MSE are presented in Table 2. The results show that low MSE, MAE and high correlation coefficients (0.032 and 0.130 respectively) can be obtained using ANFIS. Fig. 4 shows model performance of the ANFIS. As it is seen Fig.4, ANFIS model performs better than the other MLR model in terms of the R in the test period. ANFIS model has also less scattered predictions than the other models and provided the highest R coefficient (0.83) for the input combination.
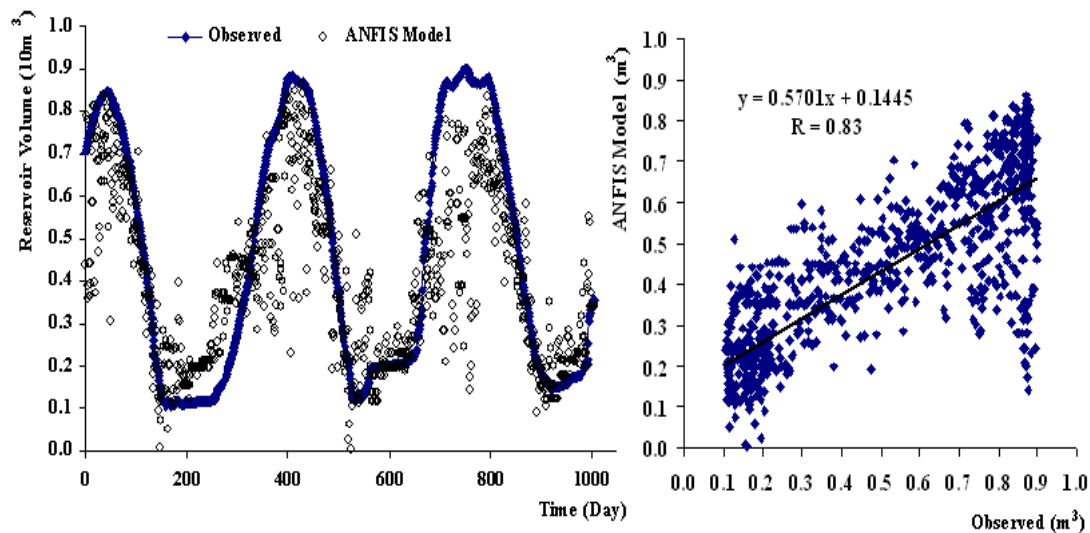
Figure 4.Observed and ANFIS model predicted reservoir volumes for Yarseli Dam in the test period

4. CONCLUSIONS

In this study, Yarseli dam reservoir volumes are predicted based on several parameters: the rainfall, the inflow river volume the spillways discharge, the irrigation, and the evaporation. The monthly reservoir volume estimations can be quite informative for the determination of the periodic water supply strategies, the hydroelectric energy computations and the flood management studies. ANFIS and MLR model used to estimate the dam reservoir volume. As a result of the study in this paper it is possible to derive the following conclusions.

- The presented ANFIS provides better estimates of the dam reservoir volume fluctuations than the conventional MLR model.

- MLR model describes empirical relations, but could not reach the desired accuracy in the same problem due to nonlinearity in the density flow behavior.

- Once an ANFIS model is developed for a specific region, the model can be quite helpful in the water resources management studies. The daily reservoir volume fluctuation prediction can be quite informative for the determination of the periodic water supply strategies, the hydroelectric energy computations and water resources management.

REFERENCES

[1]. J.S.R. Jang, C.T. Sun, and E. Mizutani, *Neurofuzzy and Soft Computing, A Computa-tional Approach to Learning and Machine Intelligence.* Prentice-Hall, New Jersey, 1997.

[2]. E.H. Mamdani, and S. Assilian, "An experiment in linguistic synthesis with a fuzzy logic controller", *International Journal of Man Machine Studies, 7,* 1–13, 1975.

[3]. T. Takagi, and M. Sugeno, "Fuzzy identification of systems and its application to modeling and control", *IEEE Transactions on System, Man and Cybernetics,* 15, 116–132, 1985.

[4]. M.E. Keskin, O. Terzi, and D. Taylan, "Fuzzy logic model approaches to daily pan evaporation estimation in Western Turkey", *Hydrological Sciences Journal,* 49, 1001–1010, 2004.

[5]. M.H. Kazeminezhad, A. Etemad-shahidi, and S.J. Mousavi, "Application of fuzzy inference system in the prediction of wave parameters", *Ocean Engineering*, 32, 1709–1725, 2005.

[6]. O. Kisi, "Daily pan evaporation modeling using a neuro-fuzzy computing technique", *Journal of Hydrology* , 329, 636–646, 2006.

[7]. O. Kisi, and O. Ozturk, "Adaptive neurofuzzy computing technique for evapo-transpiration estimation", *Journal of Irrigation and Drainage Engineering*, 133, 368–379 , 2007.

[8]. M.. Demirci, and A. Baltacı, "Prediction of suspended sediment in river using fuzzy logic and multilinear regression approaches", *Neural Computing and Applications*, 23,145-151, 2013.

[9]. F. Üneş, "Dam reservoir level modelıng by neural network approach. A case study", *Neural Network World,* 4, 461-474, 2010a.

[10].F. Üneş, "Prediction of density flow plunging depth in dam reservoir: An artificial neural network approach", *Clean - Soil, Air, Water*, 38, 296 – 308, 2010b.

[11].F. Üneş, M. Demirci, and Ö. Kişi, "Prediction of millers ferry dam reservoir level in usa using artificial neural network", *Periodica Polytechnica Civil Engineering*, 59, 309–318,2015a,.

[12].F. Üneş, and M. Demirci, "Generalized Regression Neural Networks For Reservoir Level Modeling", *International Journal of Advanced Computational Engineering and Networking* , 3, 81-84, 2015b.

[13]. J. Shiri, and O. Kisi, "Comparison of genetic programming with neuro-fuzzy systems for predicting short-term water table depth fluctuations", *Computers & Geosciences*, 37, 1692-1701, 2011.

Temporal Variation of Organic and Inorganic Carbon Transport from the Southeastern Black Sea (Trabzon Province) Rivers

Sinan Nacar[1*], Uğur Satilmis[1]

[1]*Karadeniz Technical University, Faculty of Engineering, Department of CivilEngineering, 61080, Trabzon,Turkey.*

Abstract

The input of organic carbon being an indicator of organic pollution as well to the oceans provides crucial sources in food web of estuarine ecosystems. The Black Sea surrounded by six countries is the world's largest land-locked inland sea and its total length of the coastal zone is 4,340 km, of which 1,400 km is shared by Turkey. The Black Sea receives annually a considerable freshwater input from the rivers carrying substantial loads of organic matter, nutrients and anthropogenic pollutants and the coastal parts are highly affected by eutrophication. The aim of this study is to determine the temporal variability of total carbon (TC), total organic carbon (TOC) and total inorganic carbon (TIC) carried from the eight Turkish streams to the Black Sea. The streams included in this study are Ağasar, Fol, Galanima, Değirmendere, Yomra, Karadere, Manahoz and Solaklı, within the boundaries of Trabzon Province, the most densely populated city located in the coast of Southeastern Black Sea. The water sampling studies have been monthly conducted in one station, which was selected at the point where the stream is discharged into the Black Sea, for each stream during a period of twelve months between March 2015 and February 2016.Considering the mean values for each stream, TOC concentration fluctuated from 1.59 to 25.90 mg/L and the Stream Yomra being under immense pressure due to various kinds of anthropogenic activities among which sand and gravel mining is the most disastrous one was the most critical one. The streams showed high TC and TIC yields during the summer and autumn months, corresponding to the seasonal trend of stream discharge. It was also found that TIC comprised the majority of the total carbon concentration, with mean percentages ranging from 68.9% to 84.06% in all of the streams.

Keywords

Black Sea, Total OrganicCarbon, Trabzon streams

1. INTRODUCTION

Water plays a vital role in all aspects of human and ecosystem survival. Unconsciously pollution of water of the rivers, lakes, seas and drinking water supplies are endangering life on earth day by day. Human activities like improper disposal of municipal and industrial effluents and indiscriminate applications of agrochemicals in agriculture are the main factors contributing to the deterioration of water quality [1]. An estimated 2 million tons of sewage and other effluents are discharged into the world's waters every day. In developing countries where over 90% of raw sewage and 70% of untreated industrial wastes are dumped into surface water sources the situation is worse [2].

The Black Sea has been increasingly threatened by nutrients carried by rivers over the past decades as a result of discharge of domestic wastes from coastal settlements and industrial areas [7]. The major rivers following into the Black Sea and their discharges are: Danube (203 km^3/yr), Dniper (54 km^3/yr), Dniesta (9.3 km^3/yr), Don (28 km^3/yr) and Kuban (13 km^3/yr). In addition to these rivers, a large number of smaller rivers along the Turkish and Bulgarian coasts contribute another 28 km^3/yr to the water budget of the sea [4]. There are several studies were made by researchers on the effect of different domestic and industrial discharges on the water quality of the Black Sea Coast of Turkey [3], [5], [6], [8], [9], [11], [13], [16], [17]. Also variation in the quality and quantity of river water has been studied worldwide in recent years [10], [14], [15].

The TC, TIC and TOC in surface waters and wastewaters are important analytical parameters describing the total content of all substances containing carbon. In practice, the TOC originated from natural and anthropogenic sources, and even if it is not directly responsible for dangers on human health, its determination is important for any kind of water that is used by public [19]. Researchers must consider that TOC depends on the kind of the measured water, but it is also affected by several parameters such as temperature, salinity, pH, microbial activity and surrounding vegetation [21].

The aim of this study is to determine the TC, TIC and TOC carried by streams located within the boundaries of Trabzon, the biggest province of the Eastern Black Sea Basin (EBSB), into the Black Sea.

2. MATERIAL AND METHOD

2.1. Study Area

The Black Sea is a semi-enclosed sea, whose only connection to the world's oceans is the narrow Bosphorus Channel. The area of Black Sea is $4.2*10^5$ km^2 with maximum and average depths of 2200 and 1240 m, respectively. Ninety per cent of its water mass is anoxic, thus it contains the world's largest anoxic water mass [18]. To the south, it is connected to the Mediterranean through the Bosphorus, which is the world's narrowest strait, with an average width of 1.6 km, depth of 36 m and a total length of 31 km. To the north, the Black Sea is connected with the Sea of Azov through the shallow Kerch Strait, which has a depth of less than 20 m. The Black Sea is surrounded by six countries located in Europe and Asia: Bulgaria, Georgia, Romania, Russia, Turkey and Ukraine (Figure.1). In fact, the Black Sea is influenced by 17 countries, 13 capital cities and some 160 million people [3].
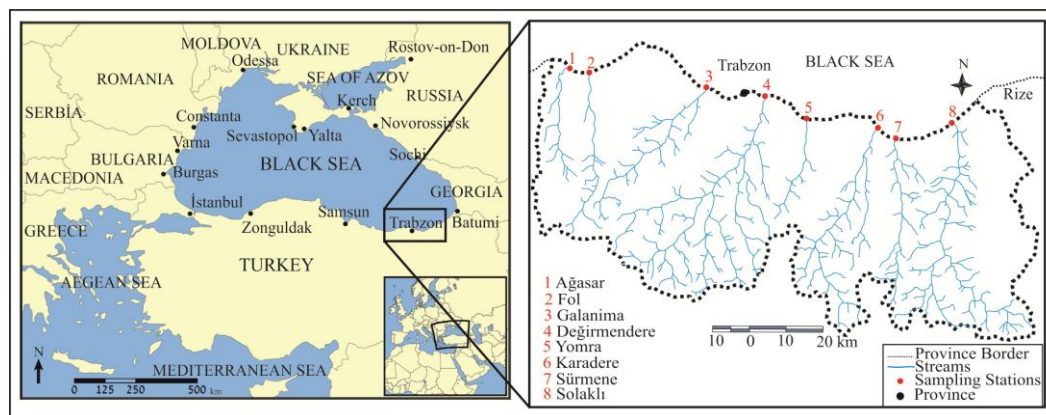

Fig.1. Study area and locations of the sampling stations

The ESBS is one of the most important hydrological basins in Turkey, and it is a major part of Caucasus Ecological Region together with Çoruh and Aras Basins [19]. Trabzon, the biggest province located in the ESBS of Turkey, lies between the 38° 30' and 40° 30' eastern longitudes and 40° 30' and 41° 30' northern latitudes. Trabzon with the area of 4,664 km^2 is a coastal city situated on the slope of the hills. The climate characteristic of the northeast coastal region of Turkey is rainy and humid. Trabzon has a typically moderate climate that is neither too warm in summers and nor too cold in winters [20].

There are many streams flowing in the boundaries of Trabzon into the Black Sea. A total of eight streams and one monitoring station for each stream were selected along the coast of Trabzon Province at the Eastern Black Sea Region of Turkey. The streams studied from the west to the east are Ağasar, Fol, Galanima, Değirmendere, Yomra, Karadere, Manahoz and Solaklı, respectively. These streams drain the major rural, agricultural, and urban of the Eastern Black Sea Region of Turkey and discharge into the Black Sea. The main nutrient loads include domestic wastewaters, agricultural runoff and industrial effluents. The Coordinates for each station are given in Table 1.

Table 1. Coordinates of stations

Station	N			E		
Ağasar	41˚	03'	26.14"	39˚	13'	07.51"
Fol	41˚	02'	48.69"	39˚	16'	40.22"
Galanima	41˚	01'	07.80"	39˚	35'	46.20"
Değirmendere	41˚	00'	06.00"	39˚	45'	25.80"
Yomra	40˚	57'	10.80"	39˚	52'	03.00"
Karadere	40˚	56'	05.40"	40˚	03'	38.40"
Sürmene	40˚	54'	52.80"	40˚	06'	41.40"
Solaklı	40˚	56'	35.40"	40˚	16'	01.80"

2.2. Water Sampling

Water samples were collected at all eight monitoring stations monthly from March 2015 to February 2016. The surface water samples were collected in 1.0 L polyethylene bottles. Plastic sample bottles, pre-cleaned with 1M HNO$_3$ and rinsed

with double-distilled water, were used to collect the water samples. At the point of collection, bottles were rinsed several times with water of streams and transferred to the laboratory in coolers containing icecap to reducing the degradation of samples before analysis. At the laboratory located in Karadeniz Technical University, Hydraulic Laboratory, the water samples were immediately analyzed within 12 h of sampling.

2.3. Water Analysis

TC, TIC and TOC content of the water samples were determined with a UV-vis spectrophotometer (DR 5000) by using its cuvette-test (LCK 380, TC), according to Standard Methods [22]. TOC is calculated as the difference between the TC and TIC values. These analyses were carried out in triplicate in room temperature ($21 \pm 2°C$) and their mean values were presented.

3. RESULTS AND DISCUSSION

The basic statistics of TC, TIC and TOC content (mg/L) for each studied stream are given in Table 2.

3.1. The Ağasar Stream

The TC levels of the Ağasar Stream show that the content varies between 19.10 mg/L in November and 41.90 mg/L in October. The TIC content changed between 14.20 mg/L in April and 34.60 mg/L in October. Also, the TOC content of the Ağasar Stream changed between 1.59 mg/L in November and 9.06 mg/L December. TC and TIC concentrations were highest during a three-month period from August to October.

3.2. The Fol Stream

For the Fol Stream, the content of TC varies between 22.60 mg/L in April and 41.60 mg/L August. The TIC levels of Fol Stream show that the content varies between 16.60 mg/L in April and 34.30 mg/L in October. The minimum TC and TIC content were determined in April. The TOC levels of the Fol Stream show that the content varies between 6.04 mg/L in May and 15.40 mg/L in February. TC and TIC content of the Fol Stream were highest during a three-month period from August to October. Also, the lowest content of TC, TIC and TOC were determined from March to May.

3.3. The Galanima Stream

Considering the yearly mean values for the Galanima Stream, the TC concentration was determined as 42.44 mg/L with a range of 27.40-61.60 mg/L, and TIC concentration 35.68 mg/L with a range of 24.40-55.50 mg/L. The lowest TC concentration was observed in April and the highest TC concentration was observed in August. The lowest TIC concentration was observed in April and the highest TIC concentration was observed in August. The TOC concentration of the Galanima stream was measured as 6.77 mg/L and, the lowest TOC concentration (1.60 mg/L) were observed in November and the highest TOC concentration (12.70 mg/L) were observed in December. TC, TIC and TOC concentrations were lowest during a three- month period from March to May. Considering the all streams, it was seen that the Galanima Stream had maximum TC and TIC concentrations.

3.4. The Değirmendere Stream

For the Değirmendere Stream, the yearly average TC content was determined as 38.76 mg/L with a range of 20.50 mg/L (June)-57.50 mg/L (January). Yearly average TIC concentration was 29.43 mg/L with a range of 17.20 mg/L (May-June) - 48.30 mg/L (September). The yearly average TOC content of the Değirmendere Stream was determined as 9.33 mg/L. The minimum TOC concentration (3.25 mg/L) was measured in June and, the maximum TOC (21.85 mg/L) concentration was measured in January. TC and TIC content of the Değirmendere Stream were highest during a three-month period from August to October. Also, the lowest content of TC, TIC and TOC were determined from April to Jun.

3.5. The Yomra Stream

The TC levels of the Yomra Stream show that the content varies between 16.20 mg/L in July and 73.10 mg/L in September. The TIC content changed between 10.50 mg/L in July and 52.60 mg/L in Jun. Also, the TOC content of the Yomra Stream changed between 4.06 mg/L January and 25.90 mg/L in March. TC and TIC content of the Değirmendere Stream were highest during a three-month period from August to October. Considering the all streams, it was seen that the Yomra Stream had maximum TOC concentration.

3.6. The Karadere Stream

For the Karadere Stream, the yearly average TC concentration was determined as 24.64 mg/L with a range of 15.10 mg/L (April)-35.70 mg/L (October), and yearly average TIC concentration 19.88 mg/L with a range of 12.50 mg/L (April)-30.80 mg/L (October). The yearly average TOC concentration value of the Karadere Stream was measured as 4.76 mg/L and, the lowest TOC concentration value (2.26 mg/L) were observed in May and the highest TOC concentration value (8.08 mg/L) were observed in December. TC, TIC concentrations were highest during a three month period from August to October. Also, TC, TIC and TOC concentration were lowest during a three-month period from April to Jun.

3.7. The Sürmene Stream

For the Sürmene Stream, the yearly average TC value was determined as 17.53 mg/L with a range of 14.50 mg/L (February)-24.30 mg/L (October). Yearly average TIC concentration value was 13.59 mg/L with a range of 10.50 mg/L (May) - 20.70 mg/L (October). The yearly average TOC content of the Sürmene Stream was determined as 3.96 mg/L. The minimum TOC concentration (2.20 mg/L) was measured in March and, the maximum TOC (5.44 mg/L) concentration was determined in December. TC, TIC concentrations were highest during a three month period from August to October. Considering the all streams, it was seen that the Sürmene Stream had minimum TC, TIC and TOC concentrations.

3.8. The Solaklı Stream

The TC levels of the Solaklı Stream show that the content varies between 14.20 mg/L (April) and 27.90 mg/L (October). The TIC content changed between 11.40 mg/L in April and 22.90 mg/L in October. Also, the TOC content of the Solaklı Stream changed between 2.75 mg/L April and 6.05 mg/L March. TC, TIC and TOC concentration were highest during a tree-month period from August to October and lowest during a three month period from April to Jun in the Solaklı Stream.

Table 2. Basic statistics of TC, TIC and TOC content monitored for the Southeastern Black Sea Streams

		Ağasar	Fol	Galanima	Değirmendere	Yomra	Karadere	Sürmene	Solaklı
TC (mg/L)	Mean	27.18	32.84	**42.44**	38.76	38.93	24.64	**17.53**	20.89
	Min	19.10	22.60	27.40	20.50	16.20	15.10	14.50	14.20
	Max	41.90	41.60	61.60	57.50	73.10	35.70	24.30	27.90
	SD	7.05	7.07	8.65	12.72	17.88	5.84	2.93	4.39
TIC (mg/L)	Mean	20.60	24.50	**35.68**	29.43	26.83	19.88	**13.59**	16.75
	Min	14.20	16.60	24.40	17.20	10.50	12.50	10.50	11.40
	Max	34.60	34.30	55.50	48.30	52.60	30.80	20.70	22.90
	SD	6.50	6.15	7.48	9.64	13.14	5.05	2.97	3.76
TOC (mg/L)	Mean	6.58	8.34	6.77	9.33	**12.14**	4.76	**3.96**	4.13
	Min	1.59	6.04	1.60	3.25	4.06	2.26	2.20	2.75
	Max	9.06	15.40	12.70	21.85	25.90	8.08	5.44	6.05
	SD	2.06	3.09	3.18	5.18	6.77	1.68	1.03	1.07

4. CONCLUSION

In this study the temporal variability of TC, TIC and TOC carried from the eight streams namely Ağasar, Fol, Galanima, Değirmendere, Yomra, Karadere, Manahoz and Solaklı, within the boundaries of Trabzon Province, to the Black Sea was investigated. The water sampling studies were monthly conducted in one station, which was selected at the near point where the stream is discharged into the Black Sea, for each stream during a period of 12 months between March 2015 and February 2016. The TC, TIC and TOC content of the water samples collected from eight stations along the coast of the Southeastern Black Sea were determined and evaluated. It was found that:

- The minimum TC concentration is determined in Solaklı Stream in April and the maximum concentration is determined in September in Yomra Stream. The minimum TIC concentration is determined in Yomra and Sürmene Streams and the maximum concentration is determined in August in Galanima Stream. Also the minimum TOC content was determined in November in Ağasar Stream and maximum content was determined in March in Yomra Stream.

- In all station, TC and TIC content show a similar trend throughout the year; start to decrease on spring, then rise during the summer and then it reached its peak in the autumn.

- TC and TIC content of stream water were highest during a three-month period from August to October for all streams while lowest from March to May for Ağasar, Fol and Galanima and from April to Jun for Değirmendere, Karadere and Sürmene streams.

- The maximum TC and TIC content are recorded in summer and autumn seasons, due to the low precipitation, where the lowest levels are determined in winter and spring because of the heavy rainfall causing dilution. But the maximum TOC content is recorded in spring.

- Considering the yearly mean values minimum TC, TIC and TOC concentration value are determined at Sürmene Stream and maximum TC and TIC value are determined in Galanima Stream, maximum TOC concentration is determined in Yomra Stream.

- Because of being under immense pressure due to various kinds of anthropogenic activities among which sand and gravel mining the TOC concentration of Yomra was recorded very high in all months.

- It is recognized that TIC generally constitutes the majority of the TC concentration with mean percentages ranging from 68.9% to 84.06% in all streams.

REFERENCES

[1]. Azizullah, A., Khattak, M. N. K., Richter, P., &Häder, D. P., Water pollution in Pakistan and its impact on public health—a review. Environment International, 37(2), 479-497, 2011.

[2]. Anonymous. World Water Day 22.03.2010; 2010. Retrieved from www.worldwaterday2010.info, United Nations.

[3]. Bakan, G., &Büyükgüngör, H., The black sea. Marine Pollution Bulletin,41(1), 24-43., 2000.

[4]. Balkas, T., Dechev, G., Mihnea, R., Serbanescu, O., &Unlueata, U., State of the marine environment in the Black Sea Region. UNEP Regional Seas Reports and Studies,124, 47., 1990.

[5]. Bayram, A., Onsoy, H., Bulut, V. N., &Akinci, G., Influences of urban wastewaters on the stream water quality: a case study from Gumushane Province, Turkey. Environmental Monitoring and Assessment, 185(2), 1285-1303., 2013.

[6]. Boran, M., &Sivri, N., Trabzon (Türkiye) İl SınırlarıİçerisindeBulunanSolaklıveSürmeneDerelerindeNütrientveAskıda Katı MaddeYüklerininBelirlenmesi. E.U. Journal of Fisheries & Aquatic Sciences, 18,(3-4): 343 – 348, 2001.

[7]. Bozcaarmutlu, A., Sapmaz, C., Aygun, Z., &Arinç, E., Assessment of pollution in the West Black Sea Coast of Turkey using biomarker responses in fish. Marine Environmental Research, 67, 167−176., 2009.

[8]. Gültekin, F., Ersoy, A. F., Hatipoğlu, E., &Celep, S., Trabzon İli AkarsularınınYağışlıDönem Su KalitesiParametrelerininBelirlenmesi. Ekoloji,21(82), 77-88., 2012

[9]. Koklu, R., Sengorur, B., &Topal, B., Water quality assessment using multivariate statistical methods—a case study: Melen River System (Turkey).Water Resources Management, 24(5), 959-978., 2010.

[10].Kumarasamy, P., James, R. A., Dahms, H. U., Byeon, C. W., & Ramesh, R., Multivariate water quality assessment from the Tamiraparani river basin, Southern India. Environmental Earth Sciences, 71(5), 2441-2451., 2014.

[11].Tuncer, G., Karakas, T., Balkas, T. I., Gökçay, C. F., Aygnn, S., Yurteri, C., &Tuncel, G., Land-based sources of pollution along the Black Sea coast of Turkey: concentrations and annual loads to the Black Sea. Marine Pollution Bulletin, 36(6), 409-423., 1998.

[12].TSWQR, Turkish Surface Water Quality Regulation. Official Gazette. no: 29327, Turkey, (in Turkish)., 2015.

[13].Varol, M., Gökot, B.,Bekleyen, A., &Şen, B., Water quality assessment and apportionment of pollution sources of Tigris River (Turkey) using multivariate statistical techniques—a case study. River Research and Applications, 28(9), 1428-1438., 2012.

[14].Vieira, J. S., Pires, J. C., Martins, F. G., Vilar, V. J., Boaventura, R. A., &Botelho, C. M., Surface water quality assessment of Lis river using multivariate statistical methods. Water, Air, & Soil Pollution, 223(9), 5549-5561., 2012.

[15].Wan, J., Bu, H., Zhang, Y., &Meng, W., Classification of rivers based on water quality assessment using factor analysis in Taizi River basin, northeast China. Environmental Earth Sciences, 69(3), 909-919., 2013.

[16].Bulut, V. N., Bayram, A., Gundogdu, A., Soylak, M., &Tufekci, M., Assessment of water quality parameters in the stream Galyan, Trabzon, Turkey. Environmental Monitoring and Assessment, 165(1-4), 1-13., 2010.

[17].Alkan, A., Serdar, S., Fidan, D., Akbas, U., Zengin, B., &Kilic, M. B.,Physico-Chemical Characteristics and Nutrient Levels of the Eastern Black Sea Rivers. Turkish Journal of Fisheries and Aquatic Sciences, 13, 847-859., 2013.

[18].Sorokin, Y. I.,The Black Sea. In Estuaries and Enclosed Seas. Ecosystems of the World, Vol. 26, ed. B. H. Ketchum, pp. 253 – 291. Elsevier, Amsterdam., 1983.

[19].Bayram, A., Onsoy, H., Akinci, G., &Bulut, V. N., Variation of total organic carbon content along the stream Harsit, Eastern Black Sea Basin, Turkey. Environmental Monitoring and Assessment, 182(1-4), 85-95., 2011.

[20].Demirci, E., &Cuhadaroglu, B., Statistical analysis of wind circulation and air pollution in urban Trabzon. Energy and Building, 31, 49–53., 2000.

[21].Visco, G., Campanella, L., & Nobili, V., Organic carbons and TOC in waters: an overview of the international norm for its measurements. Microchemical Journal, 79(1), 185-191., 2005.

[22].APHA, Standard methods for the examination of water and wastewater, 18th ed. Washington, DC:American Public Health Association., 1992.

Mapping with the Image Processing Method of Damage Regions with Respect Composite Laminates Subjected to Low Velocity

Memduh Kara[1], Yusuf Uzun[2], Huseyin Arikan[1]*

[1]*Necmettin ErbakanUniversity, Department of A.C. Engineering Faculty, 42370, Seydişehir/Konya, Turkey*

[2]*Necmettin ErbakanUniversity, SeydisehirVocational High School, 42370, Seydişehir/Konya, Turkey*

**CorrespondingAuthor email: harikan@konya.edu.tr*

Abstract

In this study , uni-directionaly reinforced laminates that arranged e-glass / epoxy composite samples in the form [+ 45 / -45 / 90/0]$_s$ and [+ 45 / -45 / 90/0]$_{2s}$ was applied low-velocity impact tests at impact energies of 10, 20 and 30 J has been obtained 8 and 16 laminated sample. Low-velocity impact tests were performed with the drop weight test device. Low-velocity impact damage was created on the samples depending on the different impact energies as a result of experiments conducted with hemispherical various impactor. The impactor mass was 6.350 kg. Digital imaging process method was applied images of the samples subjected to impact damage and damage maps for each damage zone were extracted. Also, change graph of damage area depending on the impact energies has been omitted. Changing damage zones were extracted. Also, change graph of damage area depending on the impact energies has been omitted.

1. INTRODUCTION

Composite materials have been used as a valid advantageous alternative for structural materials, replacing not only steel but even light alloys in the construction of some parts of vehicular body, spaceship, and aerodynamic structures and so forth. These materials are subjected to a wide spectrum of loadings during in-service use. Dynamic impact loadings, particularly in impact type events, represent a serious design condition for use of laminated composites for in-service applications, for example, dropping of tools during maintenance of the aforementioned industries. One of the properties of the laminated composite structures is that they are more susceptible to impact damage than similar metallic structures. If a composite laminate is subjected to normal low-velocity impact, invisible damage consisting of internal delamination might be induced [1]. Understanding the damage involved in the impact of composite targets is important in the effective design of a composite structure. For these reasons, numerous experimental and analytical techniques have been developed to study the dynamic response of composite structures subjected to transient dynamic loading. Some of the prominent work in this area is briefly mentioned in the following [2]. Damage mechanisms in composite materials are fairly complex, involving the interaction of matrix cracking, fiber matrix debonding, fiber pullout, delamination and fiber breakage. Generally, they occur simultaneously making the stress and failure analysis more difficult [3]. Impact failure in composites consists of various fracture modes which combine giving rise to a quite complex three-dimensional pattern [4–6]. Due to thecomplex features of damage mechanisms, more than one method is usually required for a complete non-destructive evaluation of impact induced damage. Advantages and disadvantages of different available techniques depend on the type of damage to be detected and on the test conditions in which sophisticated laboratory techniques can give highly accurate results, but may not be able to assess the state of the structure under in-service conditions [7]. There are various investigation techniques for determination of damages on composite materials. These are acoustic emission, thermography, dye penetrant, stereo X-ray radiography and ultrasonics. [8–10]. Unlike these methods, Image processing techniques are used in this study for determination of damages on composites. Delamination is observed to be the major failure mode. There for delamination areas are determined using image processing.

2. MATERIALS AND METHODS

2.1. Materials and specimens

In this study unidirectional E-glass/epoxy composite laminates were used. The laminates were cut into specimens of 140x140 mm in dimension with an average thickness of 1.6 and 3.2 mm. Stacking sequence of 8 laminated sample is [+45/-45/90/0]$_s$ and 16 laminated sample is [+45/-45/90/0]$_{2s}$.

2.2. Low velocity impact tests

The impact tests performed at impactor mass (6.35 kg) for three different impact energies (10, 20 and 30 Joule) were conducted with a drop weight testing machine (Figure 1). The radius of the impactors with a hemispherical nose was 6 and 12 mm. The composite specimen with dimensions of 140 mm by 140 mm was clamped on a fixture along a square circumference having a 100 mm side. The center of each plate was exposed to impact loading. The differences in the impact responses of specimens with varying width are characterized.
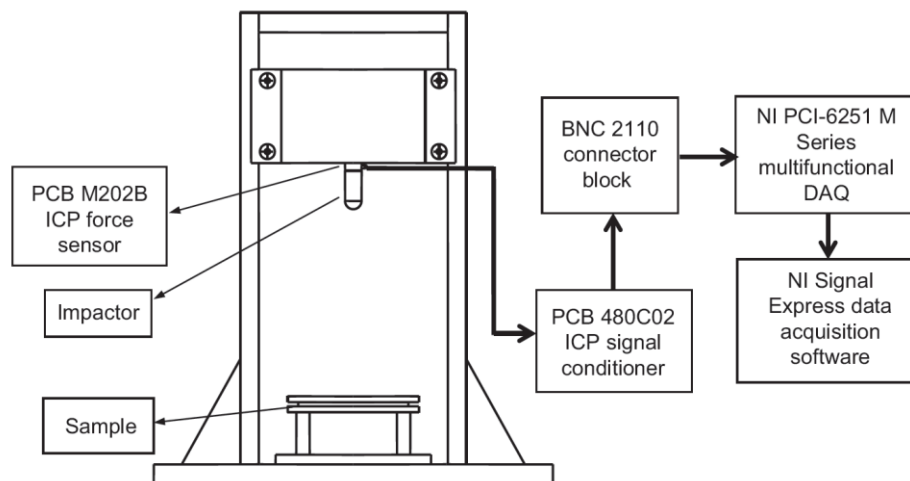

Figure 1. The Test rig [11]

2.3. Image Processing

Image processing involves processing or altering in an existing image. An image consists of a two-dimensional array of numbers. The color or gray shade displayed for a given picture element (pixel) depends on the number stored in the array for that pixel. The simplest type of image data is black and white. It is a binary image since each pixel is either 0 or 1. The next, more complex type of image data is gray scale, where each pixel takes on a value between zero and the number of gray scales or gray levels that the scanner can record. Most gray scale images have 256 shades of gray. The most complex type of image is color. Color images are similar to gray scale except that there are three bands, or channels, corresponding to the colors red, green, and blue. Thus, each pixel has three values associated with it [12].

Edge detection is one of the fundamental operations in image processing. The edges of items in an image hold much of the information in the image. The edges tell you where items are, their size, shape, and something about their texture.

Image segmentation is the process of dividing an image into multiple parts. This is typically used to identify objects or other relevant information in digital images. In segmentation, the computer attempts to find the major objects in the image and separate or segment them from the other objects [13].

Color mapping is a function that maps the colors of one (source) image to the colors of another (target) image [14]. A colormap is matrix of values between 0 and 1 that define the colors for graphics objects such as surface, image, and patch objects. MATLAB draws the objects by mapping data values to colors in the colormap.

3. EXPERIMENTAL STUDY

In this study, an image processing approach to detect damage regions with respect composite laminates subjected to low velocity impact was proposed. The process steps of the proposed approach are given bellow;

Colormaps can be any length, but must be three columns wide. Each row in the matrix defines one color using an RGB triplet. An RGB triplet is a three-element row vector whose elements specify the intensities of the red, green, and blue components of the color. The intensities must be in the range [0,1]. A value of 0 indicates no color and a value of 1 indicates full intensity. For example, this is a colormap with five colors: black, red, green, blue, and white [13].

Figure 2. Colormap(jet) function used in the study

To create a custom colormap, specify map as a three-column matrix of RGB triplets where each row defines one color. An RGB triplet is a three-element row vector whose elements specify the intensities of the red, green, and blue components of the color. The intensities must be in the range [0,1].

It basically represents a walk on the edges of the RGB color cube from blue to red (passing by cyan, green, yellow), and interpolating the values along this path [13].
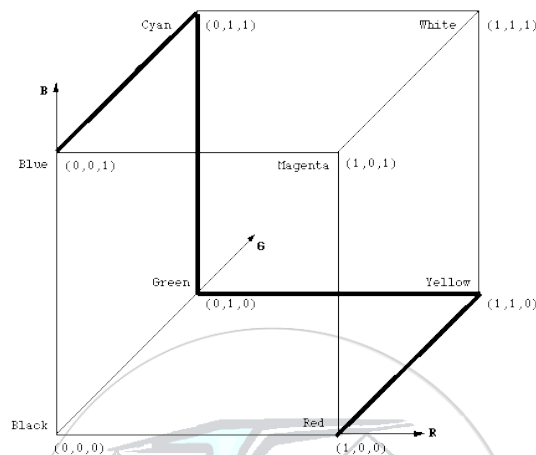

Figure 3. RGB color triplet cube

The RGB triplet values for common colors are shown in Table 1.

Table 1. The RGB triplet values for common colors

Color	RGB Triplet
Yellow	[1,1,0]
Magenta	[1,0,1]
Cyan	[0,1,1]
Red	[1,0,0]
Green	[0,1,0]
Blue	[0,0,1]
White	[1,1,1]
Black	[0,0,0]

4. EVALUATION OF THE STUDY

The damages on glass/epoxy and Kevlar composite samples can be observed by directing light beam from the back of the damaged areas. The size and nature of layer separation together with the existing matrix cracks can be determined with naked eyes [15]. After impact at various impact energy levels, high-resolution photographs of the damaged areas at the front of the test samples were taken using a simple backlighting method [1]. Image processing approach was applied these high-resolution photographs to detect damage regions with respect composite laminates. Figures 4–7 just show damaged areas of the specimens obtained using backlighting for specimens and photographs which were applied image processing, respectively.
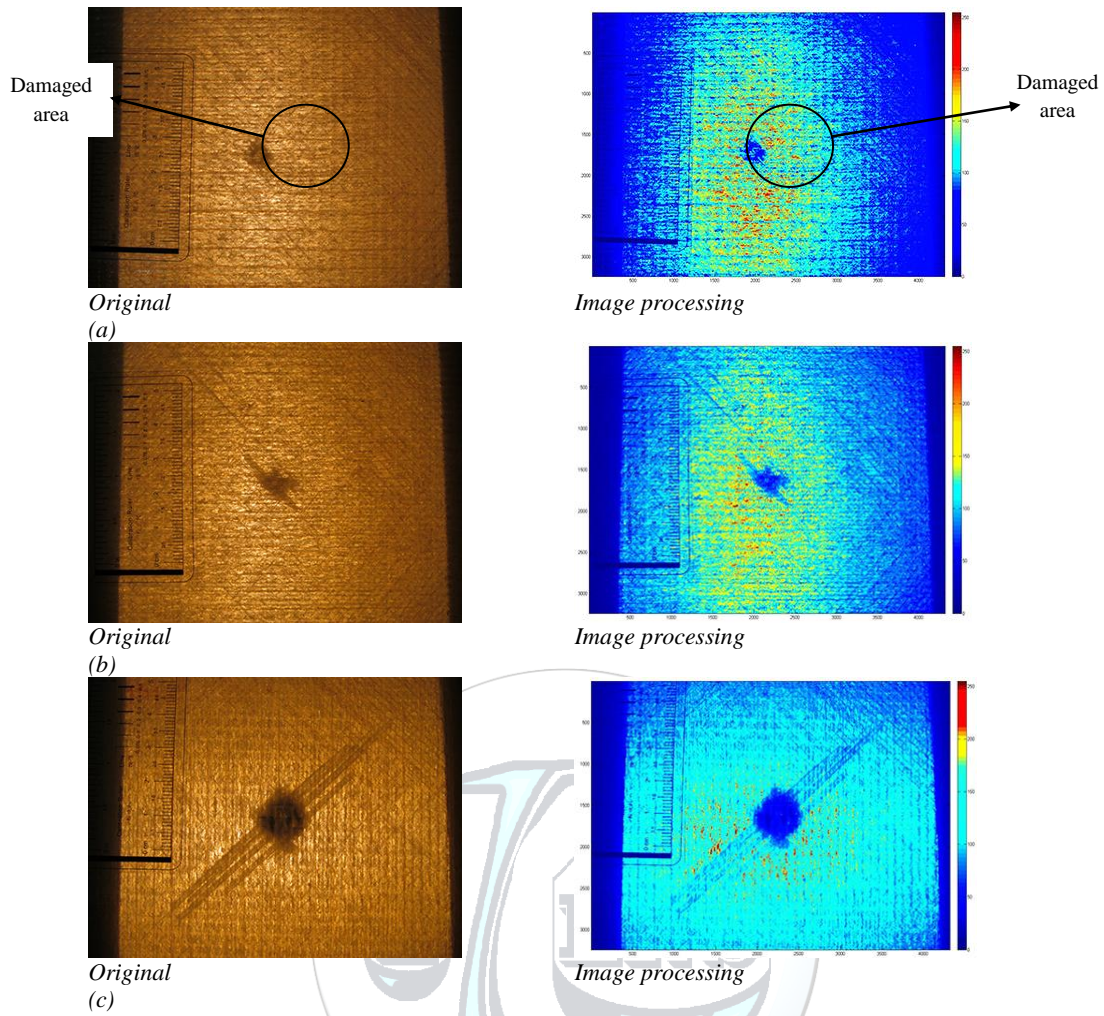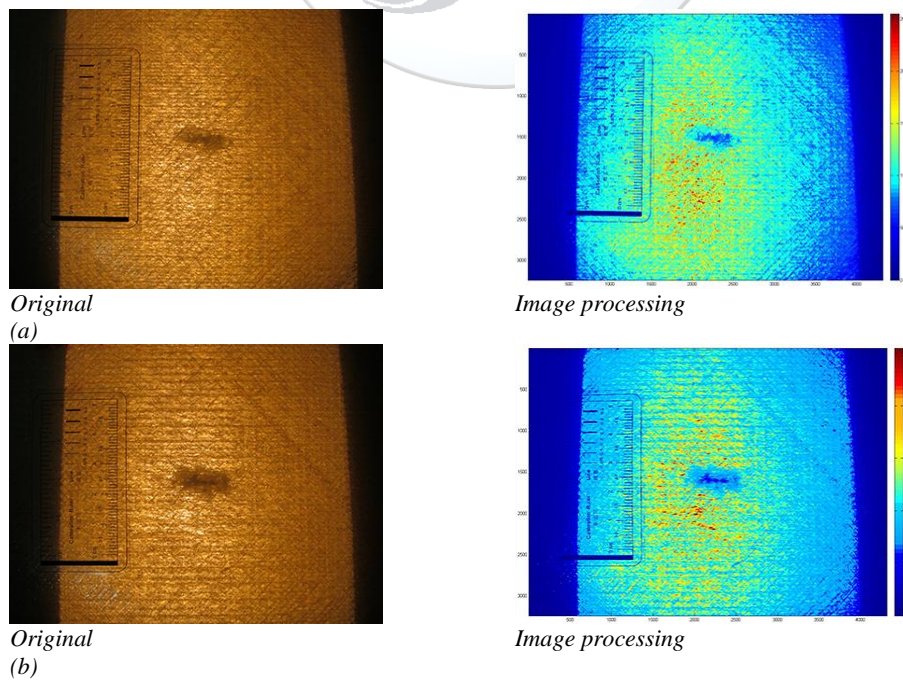
Figure 4. Original and image processing view of 8 laminated sample subjected to (a) 10, (b) 20, and (c) 30 J impactenergy levels. (12 mm in diameter hemispherical impactor)

Original
(c)

Figure 5. Original and image processing view of 8 laminated sample subjected to (a) 10, (b) 20, and (c) 30 J impactenergy levels. (24 mm in diameter hemispherical impactor)

Original
(a)

Original
(b)

Original
(c)

Figure 6. Original and image processing view of 16 laminated sample subjected to (a) 10, (b) 20, and (c) 30 J impactenergy levels. (12 mm in diameter hemispherical impactor)

Original
(a)

Image processing

Original
(b)

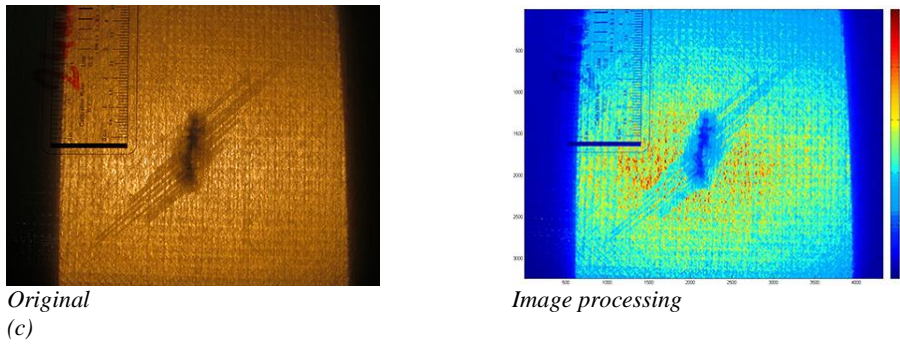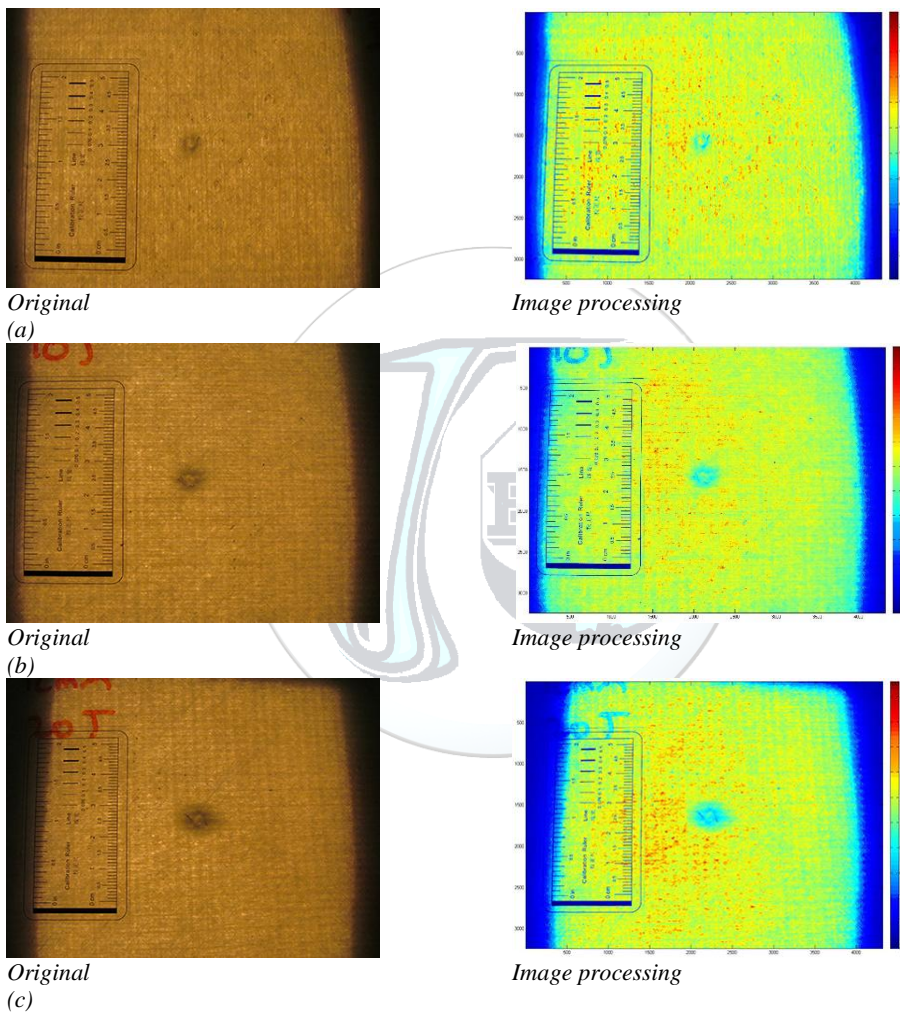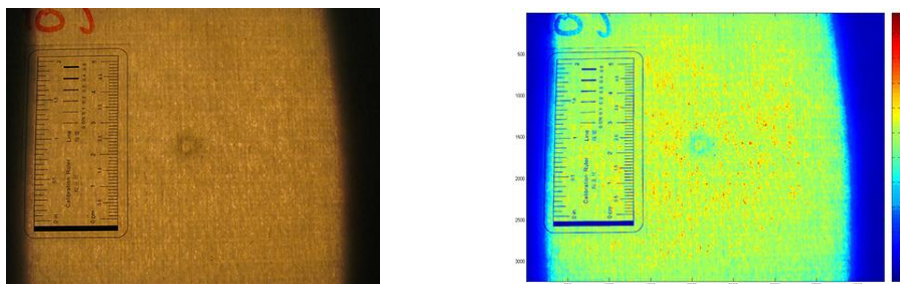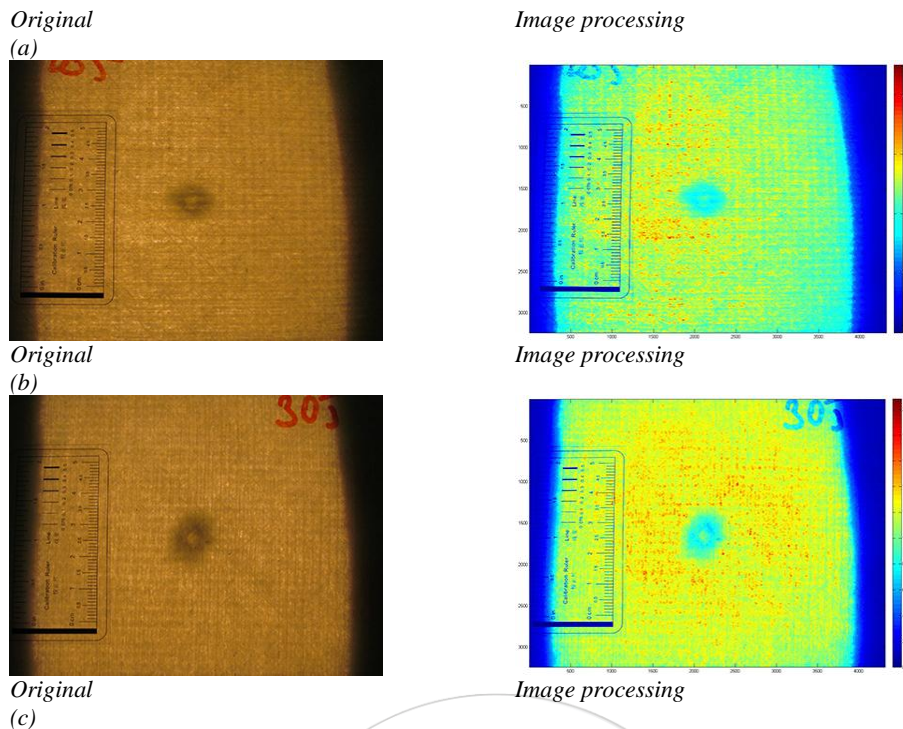Image processing

Original
(c)

Image processing

Figure 7. Original and image processing view of 16 laminated sample subjected to (a) 10, (b) 20, and (c) 30 J impactenergy levels. (24 mm in diameter hemispherical impactor)

5. CONCLUSIONS

The Image processing technique was used to detect and map damaged area. Practical results obtained from this study;

- Using image processing techniques, it was possible to quantify the damage areas.

- The result shows that for low velocity impact tests, as the impact energy increased the damage in the composite laminated increased.

- Dimensions of sample, especially thickness of the specimen in this study, have significantly affected the damage area that increases as the thickness of the specimen increases.

- In the tests conducted with various hemispherical taps, as the radius of the tap increases the damage area increases for the same energy level.

REFERENCES

[1].   M. Uyaner and M. Kara, "Dynamic response of laminated composites subjected to low-velocity impact." *Journal of Composite Materials*, 2007, 41(24), p. 2877-2896.
[2].   M. Uyaner, M. Kara and N. Ataberk, "Impact behavior of e-glass/epoxy laminated composite", *7th. International Fracture Conference*, Kocaeli, Turkey, 2005, p:813-821.
[3].   M. V. Hosur, C. R. L. Murthy, T. S. Ramamurthy and A. Shet, "Estimation of impact-induced damage in CFRR laminates through ultrasonic imaging", *NDT & E International*, 1998, 31(5), p. 359-374.
[4].   K. Srinivasan, W. C. Jackson, B. T. Smith and J. A. Hinkley, "Characterization of damage modes in impacted thermoset and thermoplastic composites", *Journal of reinforced plastics and composites*, 1992, 11(10), p. 1111-1126.
[5].   R. J. Chester and G. Clark, "Modelling of impact damage features in graphite/epoxy laminates", *In Damage detection in composite materials*. ASTM International, 1992
[6].   F. Aymerich, A. Bucchioni and P. Priolo, "Impact behaviour of quasi-isotropic graphite-peek laminates", *In Key Engineering Materials*, Trans Tech Publications, 1997, vol. 144, p. 63-74
[7].   F. Aymerich and S. Meili, "Ultrasonic evaluation of matrix damage in impacted composite laminates", *Composites Part B: Engineering*, 2000, 31(1), p. 1-6
[8].   J. Summerscales (Ed.), "Non-destructive testing of fibre-reinforced plastics composites", *Springer Science & Business Media*, Vol. 2, 1990
[9].   X. E. Gros, "Review of NDT techniques for detection of low-energy impacts in carbon reinforcements", *Sampe Journal*, 1995, 31(2), p. 29-34.

[10]. S. L. Gao and J. K. Kim, "Three-dimensional characterization of impact damage in CFRPs", *In Key Engineering Materials*, Trans Tech Publications, 1997, vol. 141, p. 35-54

[11]. M. Uyaner and M. Kara, "Experimental study of the impact behavior of laminated composites stricken by sharp impactors", *Science and Engineering of Composite Materials*, 2012, vol:3, p. 307-313

[12]. D. Phillips, "*Image Processing in C*", 2000, Second Edition, ISBN 0-13-104548-2

[13]. (2016) MathWorks web site. [Online.] Available: http://www.mathworks.com

[14]. (2016) Wikipedia web site. [Online]. Available: https://en.wikipedia.org/wiki/Color_mapping

[15]. S. Abrate, "*Impact on composite structures*" Cambridge university press, 2005

Moving Object Detection Using an Adaptive Background Modeling in Dynamic Scene

M.Fatih Savas[1*],HuseyinDemirel[1],Bilgehan Erkal[1]

[1]*Karabuk University, Faculty of Engineering, Electric-Electronic Engineering Department, 78050, Karabuk, Turkey*
CorrespondingAuthor email: muratfatihsavas@gmail.com

Abstract

Determination of moving foreground objects in dynamic scenes for video surveillance systems is still a problem can not be resolved exactly. In the literature; pixel-based, block-based and texture-based methods have been proposed to solve this problem. The method we propose will be block-based method which can be applied to real time in dynamic scenes. We have created non-overlapped blocks with the averages the pixels in the gray level. We used this average value to generate the background model based on a modified original KDE (Kernel Density Estimation) method. To determine the moving foreground objects and to update background model, we use an adaptive parameter which is determined according to the number of changes in the state of this pixel during the last N frames. Performance evaluation of the proposed method is tested by background methods in literature without applying post-processing techniques. Experimental results demonstrate the effectiveness and robustness of our method.

1. INTRODUCTION

Background modeling, which aims to classify each pixel as foreground and background, is one of the important processes of video surveillance system. It is a difficult process to determine moving objects in outdoor scenes such as waving trees, rippling water, moving shadow, illumination changes, camera jitters. Most of the studies conducted in recent years aim to minimize the effect of these changes which make difficult to detect efficient moving foreground. Wren et al [1]. have updated the parameters of the function regularly by creating a background model with single gaussian structure. However, this method is inadequate for dynamic background conditions. Gaussian mixture model (GMM) was proposed by Friedman and Russell [2]. and they updated the estimates by using incremental EM. In order to deal with complex scene changes, Stauffer and Grimson [3].expressed GMM with online k average approach. KaewTraKulPong and Bowden's [4].approach based on Mixture of Gaussians (MOG) improves adaptive background mixture model. To cope with background noise and illumination changes problems, Yan et al [5]. proposed a dynamic learning object determination which synthesizes the methods of background subtraction and adjacent frame difference.

Kim et al [6]. offered a structure called the codebook for real-time applications in one of the studies aimed at coping with the multimodal backgrounds. In this structure, by quantizing sample background values of each pixel into the codebook, he updated these codes in certain periods. In this structure, the codes which couldn't be reached for a long time are removed from the code table. To reduce the number of process, by using the color difference, Tu et al [7].modelled the background with boxed based codebook method. Although codebook structure offers an effective solution for dynamic background modeling, it is not fast while modelling. Maddalena et al [8]. proposed an adaptive learning rate in a neural network background modeling, a self-organizing method that does not contain a prior knowledge and model automatically background.

Elgammal et al [9]. proposed a non-parametric structure by the certain number of framers he accumulated for background modeling that expresses the color distribution of pixels with gaussian function . To eliminate the disadvantages of this structure, adaptive and less computational burden of parzen window structure is used. Ianasi, et al [10].proposed recursive density estimation with mean shift based mode to reduce the complexity of nonparametric kernel density estimation method. Tanaka et al [11]. proposed a fast PDF calculation function of structure by updating the PDF which partially

estimated from the previous frame. By using HSV color values and gradient information, Park et al [12]. created the classification of background or foreground with Bayesian decision rule. Cuevas et al [16]. proposed a real-time spatial-temporal non-parametric method. To create background modeling in this method, by using both spatial and temporal data of pixels, they increased system's immunity to noise. Hoffman et al [13]. proposed the Pixel-Based Adaptive Segment (PBAS) structure by updating the background model which was created as non-parametric, with learning parameters.

Recently, Heikkila et al [10]. have proposed the texture-based background model by using local binary pattern. Although this method is effective against illumination changes, it is not strong in the uniform region. To eliminate the disadvantages of LBP method, which is inadequate in uniform regions.Yao and Odobez [14].created background modeling by RGB color feature.

2. PROPOSED METHOD

Memory burden and process time are the problems that must be solved in Real-time applications [23]-[24]-[25]. Lee and Park [15].modified the KDE model to solve this problem. In our study, we based on the modified KDE model for background model.

Moving objects such as sudden illumination change, waving trees, rippling water in the dynamic scenes create too much noise for the background model. To reduce the amount of noise and the computational burden, we connected the pixels by averaging pixels as nxn blocks. These pixel blocks are used for the background model and adaptive parameters. To build an adaptive parameter, we used the counter structure which adaptive Casares et al [16]. used in their studies. By this parameter, the foreground determination and the background update was made. While updating the model, each block is continually involved in background model. Then, normalization process was performed to equal the area to 1, which is under the model's probability function.

2.1. Background Subtraction Method

In background determination algorithms, authors mostly focused on the models such as efficient usage of storage space, reducing process time. Two problems must be solved to use the background model in real-time applications. These problems are; storage space and processing time. In real-time applications, to reduce the processing burden and to use the storage space efficiently, pixels are used as gray level and background model is updated as adaptive. But one of the disadvantages of processing at gray level is that it is open to the noise came up on stage.

A picture frame with the resolution of 160x120 size is made up of 19200 pixel. If these pixels are composed of RGB value, more time and more storage space is required. Processing on these pixels bring a lot of load on the system both in terms of time and the requirements for storage space. Therefore, to create a minimum level for processing time and storage space, the background model we propose was in gray level. However, in literature, to minimize the disadvantage of grayscale structure, kernel density estimation based model which offers an effective solution to background modeling was used.

Lee and Park [15] created the background model as pixel based. In our study, we put the average values created as 2x2 blocks in bins in background model. Instead of evaluating pixels' membership value for bins as 1 or 0, probability values are calculated according to the distance of bins from the center.

$I(x,y)$	$I(x,y+1)$
$I(x+1,y)$	$I(x+1,y+1)$

Figure 1. 2x2 block

$I(x, y)$represents the gray level value of each pixel in the image frame. Pixels in the image frame were joined by averaging as 2x2 non-overlap blocks. As computational, mean filter structure which requires less burden is used equation 1.

$$\mu(x,y) = \frac{1}{nxn} \sum_{x=1}^{n} \sum_{y=1}^{n} I(x,y) \tag{1}$$

where μ (x, y), is the average value of the pixels in nxn block.

The following figure shows the change of the pixel at location (39,80) in the time interval 0-30 seconds and shows the gray level changes of the pixels averaged at location (39 + x,80 + y) in the time interval 0-30 seconds from the Wallflower dataset's wavingtrees test sequences. Here x,y={0,1}
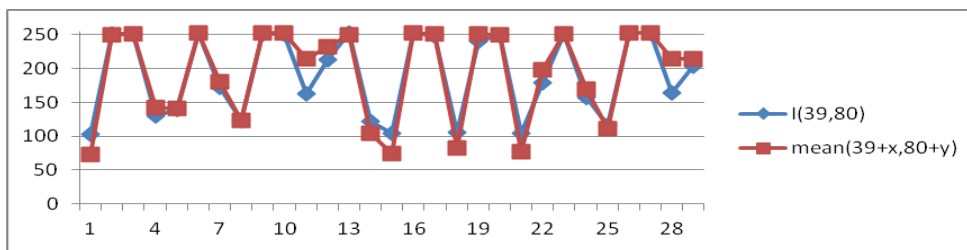
Figure 2.I(39,80) pixels and 39 + x ,80+ y block of pixels in the range of 0-50 times the change in gray level chart

The following equation 2.shows the function we used for the background model.

$$p_t(C_k) = \frac{1}{\sqrt{2\pi\left(B_d/2\right)^2}} exp\left(-\frac{1}{2}\left(\frac{C_k - \mu_t(x,y)}{B_d/2}\right)^2\right) (2)$$

In equation 2, for each block, the histograms are formed in the width of B_d by bins.C_k is the central point of kth bin which belongs to nxn block pixel, $p_t(C_k)$ is the probability value of block pixel at time index t.

2.2. Adaptive Threshold Parameter

Determining the fixed threshold used for the determination of moving objects in dynamic scenes is difficult. If less values are selected as the parameter, the image may contain a lot of noise, if a large value is selected as the parameter, some values from the image may be lost. To overcome this problem, we created threshold as adaptive in our study. Adaptive threshold is created by counter structure counting the change in each pixel. This counter structure was used to reduce the computational burden.

In this structure, the parameter of $\beta_x, x \in \{1,2,3\}$ is the maximum value of a counter can count that determined by the user. $CC_n, n \in \{1,2,3\}$ shows the number of counter belonging to a pixel. The value of a counter is incremented by 1 at change of each pixel's state. After counting the frame number to be counted, counter values are sequentially reset [16].The value of counters increase or decrease according to the rate of pixels' state changing. $\tau(x,y) = CC_1(x,y) + CC_2(x,y) + CC_3(x,y)$) is formed by the total value of counter of pixels. The parameter values of the pixels in moving regions take large τ value, τ values of the pixels in quasi-static area take small values. By this approach, at any time index t, we can determine the change number of pixels in past N frame.

2.3. Background Update

The following formulate is used for updating the background model. α is the fixed updating parameter. While updating , all C_k values aren't calculated, only bins interval $p_t(C_{(k-2)})$ and $p_t(C_{(k+2)})$ are updated by considering bins interval $p_t(C_{(k\pm2)})$ [15].The following equation 4.

$$p_t(C_k) = \hat{p}_{t-1}(C_k) + \left(\frac{1}{\alpha + 100.\tau}\right)\frac{1}{\sqrt{2\pi\left(B_d/2\right)^2}} exp\left(-\frac{1}{2}\left(\frac{C_k - \mu_t(x,y)}{B_d/2}\right)^2\right) (4)$$

2.4. Foreground Detection

Determination of moving objects in dynamic scenes depends on a robust background modelling structure and the value of parameter to be determined. While determining the foreground, the distance between the bin center which has the largest possibility value at histogram and $\mu_t(x,y)$ is taken into consideration.Equation 5.

$$Distance|C_k - \mu_t(x,y)| \leq threshold + \tau (5)$$

If the absolute value difference between C_k, which has the largest possibility value at histogarm and the average value calculated at t time of $\mu_t(x,y)$ is bigger than threshold, foreground is determined. Equation 6.

$$I(x,y)\begin{cases} ForegroundDistance|C_k - \mu_t(x,y)| \leq threshold + \tau \\ Backgroundotherwise \end{cases} (6)$$

3. RESULTS AND DISCUSSION

We tested the performance of our method by wallflower [17]. and Li [18]. datasets. We compared our proposed method with Mixture Of Gaussian V1BGS [4], Pixel Based Adaptive Segmenter [13]. and T2FGMM_UM [22].methods from BGSLibrary which was created by Andrews Sobral [19]. Three different binary classification measurement methods were used while comparing methods. These methods are precision, recall and F-measure. When the recall and precision values are high, it shows that the performance is high. F-measure is the weighed harmonic average of recall and precision [20]-[21].Equation 7.

$$reacll = \frac{TP}{TP+FN} \qquad precision = \frac{TP}{TP+FP} \qquad F-measure = \frac{2.recall \ .precision}{recall \ +precision}(7)$$
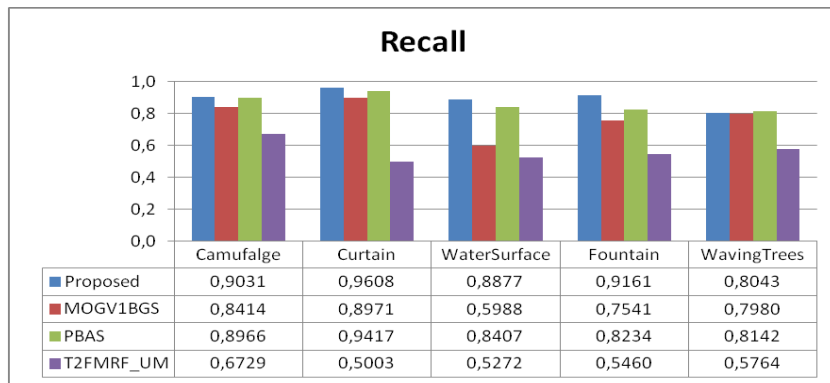

Figure 3.Experimental Results

Figure 4.The recall results obtained with the proposed scheme and other methods for the Li and wallflower dataset.
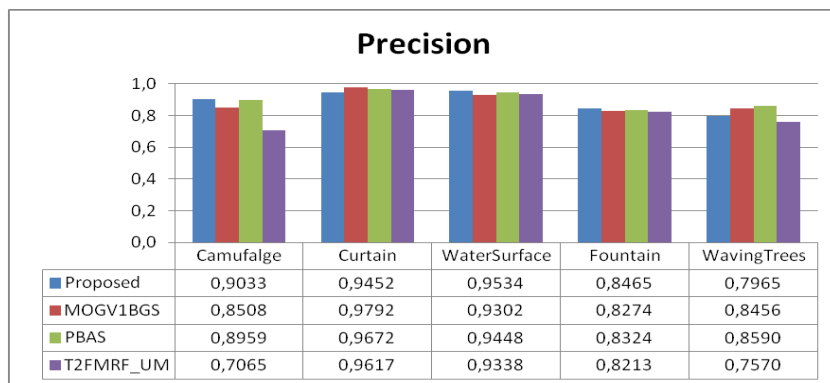

Figure 5.The precision results obtained with the proposed scheme and other methods for the Li and wallflower dataset.
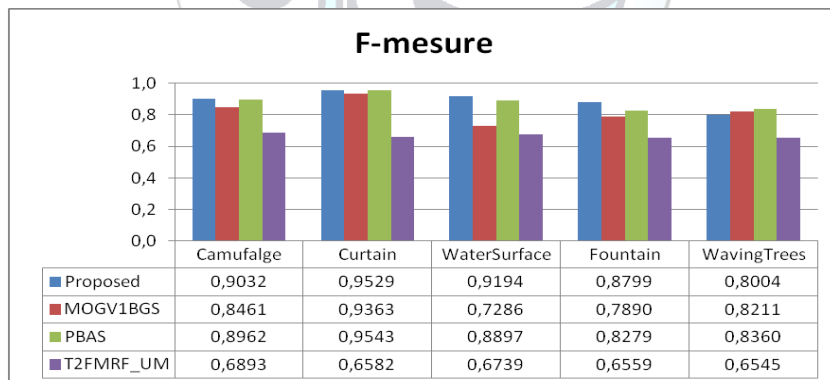

Figure 6.The f-measurement results obtained with the proposed scheme and other methods for the Li and wallflower dataset.

Recall, also known as detection rate, gives the percentage of detected true positives as compared to the total number of true positives in the ground truth, where TP is the total number of true positives, and FN is the total number of false negatives, which accounts for the number of foreground pixels incorrectly classified as background. Precision, also known as positive prediction, that gives the percentage of detected true positives as compared to the total number of pixels detected by the method, is generally used in conjunction with the recall. Where FP is the total number of false positives.

For five test videos, an evaluation was carried out between the models by calculating Recall, Precision and F measurement values. In test images, no post-processing technic application is performed. Test sequences are camouflage, curtain, water surface, fountain and waving trees. Some of these test sequences include continuously changing dynamic background, some of them include changing dynamic background at certain times. These test sequences have the frames with a size of 160 x 120 and 160x128.

The method we proposed in the measurements carried out with these test sequences, obtained robust results in most test data. When the waving trees scene was compared with other methods, the amount of noise was seen much more. These noises can be reduced according to the threshold parameter chosen in the process of determining foreground. On the contrary, reducing the noise can cause incorrectly classifying of some pixels belonging to foreground object. In

T2FGMM_UM method, the amount of noise was reduced, but pixels belonging to foreground object were evaluated as background. In water surface test sequence, as it is seen in the test data obtained via MOGV1BGS method, if the background model adapts to the scene very fast, the continuance of stopped objects moving at the scene on the screen will be less. The disadvantage of Pixel Based Adaptive Segmenter method which gets similar performance values as our proposed method, it contains too many parameters.

4. CONCLUSIONS

In our study, we created an effective model for real time applications by modifying KDE structure of Lee and Park [15]. By dealing with background model as gray level blocks nonoverlap, we reduced both the memory area requirement for model and the time needed for processing pixels. We determined the adaptive parameter by using counter structure of Casares et al. [16], and by determining the condition changing number of pixels in N frame that past at any t time. Thus we created an effective background modeling at grey level in dynamic scenes. The weak point of this method is, as a single band was used for background modeling it can't exactly discriminate the foreground and the background. As background model was created block-based, image belongs to foreground object is coarser than the pixel based methods. In future work, we are going to use this method for RGB band. Test data shows that, our study carried out for single color band is valid.

REFERENCES

[1]. C. Wren, A. Azarbayejani, T. Darrell, and A. Pentland, " Pfinder: Real-time tracking of the human body," *IEEE Trans. Pattern Anal*. 1997, vol.19, pp.780–785.

[2]. N. Friedman and S. Russell, "Image segmentation in video sequences: a probabilistic approach," *In Proceedings of the 13th Conference on Uncertainty in Artificial Intelligence, Morgan Kaufmann Publishers Inc.*, 1997, pp. 175–181.

[3]. C.Stauffer and W.E.L, Grimson, "Adaptive background mixture models for real-time tracking," *In Proceedings of IEEE Conference on Computer Vision and Pattern Recognition*, Santa Barbara, CA, USA, June 1998, pp. 246–252.

[4]. P,KaewTraKulPong and R,Bowden, " An improved adaptive background mixture model for real-time tracking with shadow detection," *In Proceedings of 2nd European Workshop on Advanced Video-Based Surveillance Systems(AVBS01)*, Sept. 2001.

[5]. R.Yan, X.Song and S.Yan, "Moving Object Detection Based on an Improved Gaussian Mixture Background Model", *Computing, Communication, Control, and Management,* 2009. CCCM 2009. ISECS International Colloquium on, pp. 12–15.

[6]. K.Kim, T.H,Chalidabhongse, D.Harwood and L.Davis, "Real-time foreground-background segmentation using codebook model," *Real-Time Imaging*, vol.11, pp.172–185, 2005.

[7]. Q.Tu, Y. Xu and M.Zhou, "Box-based Codebook Model for Real-time Objects Detection," *Intelligent Control and Automation, 2008*. WCICA 2008. 7th World Congress on,2008, pp. 7621-7625.

[8]. L.Maddalena and A.Petrosino,"A self-organizing approach to background subtraction for visual surveillance applications," *IEEE Trans. Image Process 2008*, pp. 1168–1177.

[9]. A.Elgammal, R.Duraiswami, D. Harwood and L.S.Davis, "Background and foreground modeling using nonparametric kernel density estimation for visual surveillance*," Proc. IEEE 2002*, vol.90, pp.1151–1163.

[10]. C.Ianasi, V. Gui, C. Toma and D.Pescaru, " A fast algorithm for background tracking in video surveillance, using nonparametric kernel density estimation*," FactaUniversitatis (NIS) Ser.: Elec. Energ.* ,vol.18, pp.127–144,2005

[11]. T.Tanaka, A.Shimada, D. Arita and R.I Taniguchi, "A Fast Algorithm for Adaptive Background Model Construction Using Parzen Density Estimation", *Advanced Video and Signal Based Surveillance, 2007. AVSS 2007. IEEE Conference on London. 2007*, pp.528 – 533

[12]. J.G.Park and C.Lee, "Bayesian rule-based complex background modeling and foreground detection, "*Optical Engineering*, vol.49 No.2, 2010.

[13]. M. Hofmann, P. Tiefenbacher, G. Rigoll, "Background segmentation with feedback: The pixel-based adaptive segmenter," *IEEE Computer Society Conference on Computer Vision and Pattern Recognition Workshops (CVPRW)*,2012, pp. 38–43.

[14]. J.Yao and J.M.Odobez, "Multi-Layer Background Subtraction Based on Color and Texture", *IEEE Conference on Computer Vision and Pattern Recognition, 2007.* ,pp. 1–8.

[15]. J.Lee and M.Park, "An Adaptive Background Subtraction Method Based on Kernel Density Estimation," *Sensors* , vol.12, pp.12279-12300,2012.

[16]. M.Casares, S.Velipasalar and A.Pinto, "Light-weight salient foreground detection for embedded smart cameras," *Computer Vision and Image Understanding*, pp. 1223–1237, 2010.

[17]. Wallflower dataset web site.[Online].Available: http://research.microsoft.com/en-us/um/people/jckrumm/WallFlower/ TestImages.htm

[18]. Li dataset web site.[Online]. Available: http://perception.i2r.a-star.edu.sg/bk_model/bk_index.html

[19]. Andrews Sobral web site.[Online]. Available: https://github.com/andrewssobral/bgslibrary

[20]. S.Brutzer, B.Hoferlin and G.Heidemann, "Evaluation of background subtraction techniques for video surveillance," in*: Proceedings of the CVPR, IEEE,* 2011, pp. 1937–1944.

[21]. EC Funded CAVIAR project/IST 2001 37540, web site.[Online]. Available: http://homepages.inf.ed.ac.uk/rbf/ CAVIAR/

[22]. Fida El Baf, T.Bouwmans, B.Vachon, "Type-2 Fuzzy Mixture of Gaussians Model: Application to Background Modeling," *Advances in Visual Computing*, vol. 5358, pp. 772-78,2008.

[23]. Demirel. H, *SayısalElektronik*, 2nd ed., İstanbul, BirsenYayınevi, 2015.

[24]. Topaloğlu. N, *Mikroişlemcilerve Assembly Dili, 6nd ed*., SeçkinYayıncılık, Ankara, 2015.

[25]. S.Savaş, N.Topaloğlu, B. Ciylan, "Analysis of mobile communication signals with frequency analysis method". *Gazi University Journal of Science*, Vol.25,No.2, pp.447-454,2012.

Research on Retinal and Iris Identification Systems

Yesim Ulgen Sonmez[1], Asaf Varol[2]*

[1] *Department of Software Engineering, Technology Faculty, Fırat University, Elazığ, Turkey, yesimulgen123@gmail.com*

[2] *Corresponding author: Department of Software Engineering, Technology Faculty, Fırat University, Elazığ, Turkey,*

*CorrespondingAuthor email: varol.asaf@gmail.com

Publication Info

Abstract

Biometrics is the science that analyzes biological data and also the technology that measures biological data. Biometric systems make identification or identity verification by using measurable, distinctive physical and behavioral properties of humans. The most widely used biometrics techniques rely on finger prints, palm, hand geometry, iris, retina, face, ear shape, vein, signature, hand writing and voice identification of an individual. Iris identification systems and retina identification systems are the most accurate and reliable identifying techniques. Iris is a circular structure surrounding the pupil, which determines eye color. The iris is a very rich tissue and it has a unique texture. This texture is different for each individual and it will stay same throughout their lives. Iris identification systems use the mathematical pattern-identification algorithms and statistical methods on individuals' captured iris images. Retina, similar to iris, is unique for each person and has an unchanging texture throughout the life, except for some side effects of diseases. Retina that is located in the back side of the eye is responsible for vision. The mesh of blood vessels in retina is very complicated and distinctive. In retina identification systems, firstly, infrared light is radiated into the eye and blood vessels create unique reflections of this light. Retina identification is used in many areas from security systems to medical applications. This study examines and presents similarities and differences between two ocular biometric systems which are iris identification systems and retina identification systems. Analysis has also been carried out suing the findings of this study.

Key words

1. INTRODUCTION

Biometric systems work with the principle of examining and identifying some unique physiological and behavioral characteristics of each person. The way the human brain works is taken as the basis of biometric systems. In such systems, there are two phases called identification and verification. In identification phase, data is collected and saved in the database as computer codes (which are digital codes). In the verification phase, the data collected is compared with the data of the person who requests access and a conclusion is reached by the system.

Iris and retina identification systems are among ocular identification systems. However, they do have different structures and they are different biometric systems. Iris and retina tissues are unique and distinctive for each and every human being. The structure of iris does not change from birth to death. Retina tissue also does not change, however it is affected by some diseases like diabetes, high blood pressure, MS and leukemia. Thus, iris and retina identification systems are the highest grade biometric systems in their field with the properties of uniqueness, accuracy, universality and permanence. The rich texture of iris is essential for the iris identification systems. The shape of capillaries is taken into account for retina identification systems.

This study examines and presents similarities and differences between two ocular biometric systems which are iris identification systems and retina identification systems. Analysis has also been carried out suing the findings of this study.

1.1. Biometric System Characteristics and Criteria

There are unique characteristics used in biometric systems which are unique for each and every human being. These can be finger prints, palm structure, hand shape, vein patterns, finger joint prints in hands, ear shape, teeth, tongue print in face area, retina, iris and sclera in the eyes, and as with biological properties go, DNA, bodily scent, heart sound, or behavioral features such as voice, signature, keystroke patters and style of walking. [1].

Biometric traits must have some criteria. These criteria can be listed as follows [1, 2].

- Universality: Every person should have that particular trait [1-5]. It should exist in every individual.

- Distinctiveness/Uniqueness: The trait should be effectively different for each person [1-5].

- Permanence: The characteristic should not change as time goes by, it should permanently stay the way it is [1-5].

- Collectability: The trait which will be measured should be easily acquired by suitable devices. [1-5].

- Measurability: The quantitative measurability of the trait.

- Performance: Performance is accuracy and speed, and also robustness of the technology used [1-4]. It is the relative success of defining the biometric trait [1].

- Acceptability:The approval rating of the technology used [1-5]. This can be defined as agreeable of acquisition and assessment of the biometric characteristic [1-5].

- Circumvention: The ease of using a substitute [1-4]. The biometric system can be fooled easily by unauthorized persons.

- If the human trait carries the permanence, universality, uniqueness, collectability criteria, it can be used for querying within a biometric system. If a system uses such a biometric trait and appropriate and robust technological equipment, it can be accepted as a reliable and powerful biometric system.

Table 1 shows the comparison of iris and retinal biometrics, according to biometric trait criteria, under suitable conditions [1, 2]. In the table, H means "high", L means "low" and M means mediocre.

Table 1. Comparison of iris and retina characteristics [1, 2, 6].

	Uniqueness	Universality	Permanence	Measurability	Performance	Acceptability	Circumvention
Iris	H	H	H	M	H	L	L
Retina	H	H	M	L	H	L	L

The measurements used in biometric systems are called biometric measurements. There are international standards for the use of these systems in passwords. These standards are set by INCITS, International Committee for Information Technology Standards [2, 7]. Thanks to these standards, any person with a bank account who can reach his account with iris or palm identification systems, can reach his bank account in his home country from anywhere around the world and make a transaction [2].

1.2. Comparison of Iris and Retinal Biometrics

In table 2, ease of use, possible problems, performance and security requirements of iris and retinal biometric systems under appropriate conditions have been compared.

Retina identification systems are systems with high accuracy and speed; however, because they need focus of the camera, they are not widely used biometrics [1, 4, 8].

Table 2. Comparison of iris and retina biometric systems [1, 8].

Biometric Trait	Ease of Use	Problems	Accuracy	Security Requirements
Retina	Low	Glasses	Very high	High
Iris	Medium	Light	Very high	Very high

1.3. Areas in Which Retina and Iris Biometrics are used

In table 3, the most common usage areas for iris and retinal biometrics have been listed. The most widely used biometric traits that are used for border security application are iris and retina. In ID cards and passports however, iris is used more in comparison to retina.

Table 3. Fields of application for iris and retinal biometrics [1, 9].

	Iris	Retina	Sclera
Border Security	x	x	
Forensics			
Identification of Criminals	x	x	
ID Cards	x		
Passports	x		
Computer Logon Processes	x		x
Access Control	x	x	x
Electronic Trade	x		x
Smart Phones			
Imaging Systems	x		
Watching Videos			
Missing Child Identification	x		
Crowd Tracking			
Electronic Banking			

2. OCULAR BIOMETRICS

Because of relatively more accurate and permanent characteristics of ocular biometric traits, many different approaches have been developed regarding ocular identification [1, 9]. The most important biometric traits in the ocular area are iris, sclera and retina. In iris based biometric systems, identification is done by benefiting from color, shape and the properties of iris tissue. Besides the distinctive property of iris, as these character based systems are relatively expensive and prone to attacks, they are not very widely used [1, 10].

In retina based biometric systems, the attributes of blood vessels which filter the light and optical field in retina are used as the distinctive traits [1, 9]. As the retina identification systems are expensive and it is rather difficult to obtain the data, they are not also widely used.

The sclera of the eye consists of blood vessels. The particular patterns of these blood vessels are used in sclera based biometric systems. [1, 9].

2.1. The Structure of the Eye and Eyesight

Eyes are very special and important organs which take in the light that is originated from the sun, and reflected from objects. The light that is visible to human eye is called visible light. It is the light in between wavelengths of 400 and 700 nanometers. Human eyes cannot perceive X rays, ultraviolet rays and infrared rays [11, 12]. Eye consists of two types of structures, one for sight, and others for the protection of these structures. The protective structures are the eyelids, eyebrows, eyelashes, lacrimal glands, and the muscles that connect the

eyes to their circular orbits and provide movement [11]. The structure of a human eye is made up of three layers. These layers are the sclera on the outer layer, choroid in the middle and retina in the inner layer [11].

Sclera is the white part of the eyeball. Sclera is a structure that surrounds and protects the eye. It becomes the transparent cornea on the front side of the eye and lets the light enter.

Choroid is beneath the sclera. Its exact place in the eye is shown in figure 1. It consists of blood vessels that feed the eye. It also absorbs excess light and prevents damage to the eye. Choroid gets thicker in the front side of the eye and becomes the round and colorful structure called iris [11].
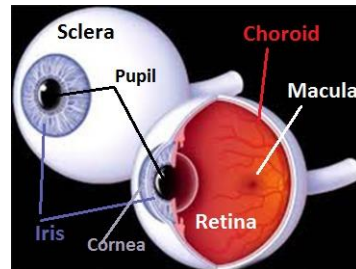

Figure 1. Anatomy of the eye [39]

Iris can be in different colors according to the color material that it possesses. Iris color can be black, brown, blue, green or hazel.

In the middle of iris is the pupil, which is a gap. The light enters the eye through this gap and goes to the back of the eye, to retina. As shown in figure 2, iris either enlarges or shrinks the pupil, according to the amount of light entering the eye. Thus, pupils constrict in bright light and they dilate in darkness.
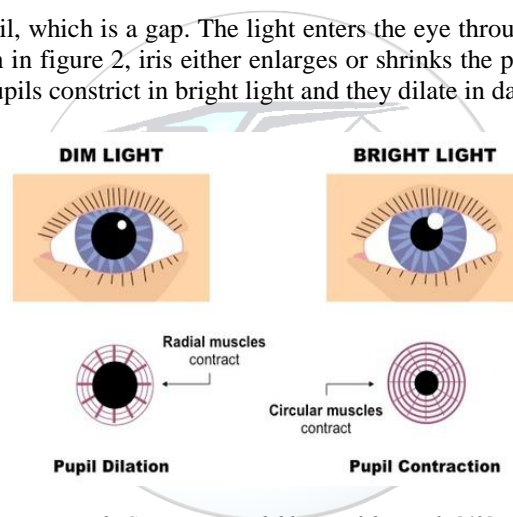

Figure 2. Constriction and dilation of the pupils [40].

Retina is the inner layer of the eye. It receives colors and impulses and provides vision. As there are networks of nerve endings in this layer, it is called the retina [11].

2.2. The phases in which the vision is realized

Vision starts with the rays of light coming from the sun which are reflected from the objects to come to our eyes. Any ray of light reflected from an object, gets refracted by the cornea and passes through the pupils and reaches to the lens [11].

The light that reached to the lens is refracted once again and passes on to vitreous body and reaches to the retina. The rays of light that reached the retina create electrical pulses on optic nerves. These electrical impulses allow the formation of a reverse image in the macula [11]. Optic nerve transmits this reverse image to the brain. The part of the brain which manages sight rotates the image and, thus seeing occurs.

Figure 3 shows how seeing works, how the light is refracted, where the vision is created, and how it is transmitted to the brain. The role of iris in seeing is to control the size of pupils and adjust the amount of light entering into the eye [13].
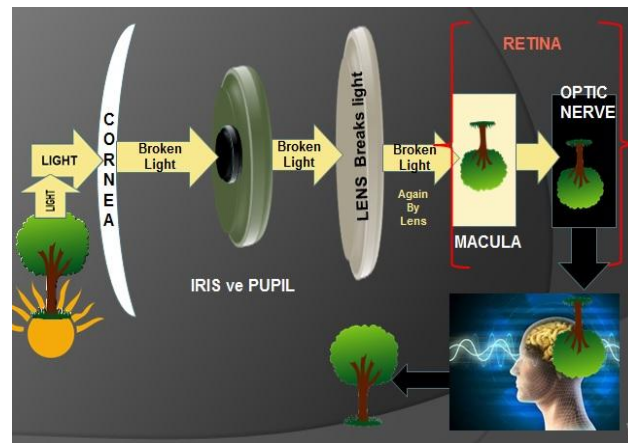
Figure 3. The phases of seeing

3. IRIS IDENTIFICATION SYSTEMS

Iris identification system is one of the most accurate and reliable biometric systems because it uses the unique and unchanging structure of iris. It was first introduced by John Daugman in 1993. J. Daugman, in 1994, introduced a prototype that delivers excellent results over databases with many different images and developed a human identification system based on iris analysis [13].

Iris identification is a highly reliable biometric method used for identification. The iris pattern of the person whose iris is scanned is mapped and converted into a digital code in various ways. This digital iris code is matched with the other ones in the database in order to make identification [14].

3.1. The Unique Structure of Iris

In 1985, Leonard Flom and Aran Safir have proven that iris pattern of each and every human being is different [14]. This part is also the part which gives the eye its color. The color of iris depends on cell density and pigment concentration. For example, brown eyes have more cell density and pigment count compared to blue eyes. The structure of iris is not hereditary, however its color is.
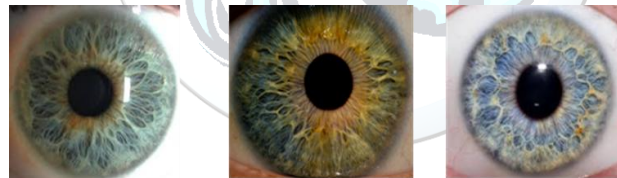

Figure 4. Different iris structures

The features related to the unique structure of iris which enables it to be a biometric trait are as follows;

- The structure of each person's irises is unique. Even though DNA structures in twins are the same, their irises are still different.
- There are even differences between the right and left irises.
- Iris is much less affected by genetic factors.
- Iris structure does not change with genetic diseases.
- Race, gender or skin color does not affect the characteristics of the iris.
- It is an internal organ which can be seen and measures externally.
- The structure of iris does not change. Due to its permanence, it is a secure biometric trait.
- Eye is the organ which loses its viability the quickest after death.

Figure 4 illustrates different iris tissues. Iris possesses the tissue properties of sclera and retina [13]. In biometric systems, this rich tissue's structure is converted into digital codes using various methods [14].

For a clear visibility of the iris tissue, the eye should be photographed using 750 nm infrared light. Because with visible daylight (400-700 nm), these tissues can't be seen clearly [14].

3.2. The Way the Iris Identification Systems Work

3.2.1. Photographing the Iris

There are stages of iris identification systems. In the first stage, digital photographs of the person who requests access to the system are taken using video cameras. This stage requires the person to willingly look at the camera. This biometric system is not intrusive as there is no contact with the eye by the camera, thus it is healthy. This way of it increases its adoption level by the people.

3.2.2. Localization – Locating the Iris and the Pupil

The captured image is processed using visual processing methods. Meanwhile, iris and pupil is distinguished in the image taken and the remaining parts are removed from the image. The purpose for doing that is to separate eyebrows, eyelashes etc. from the iris in order to create a code and make a healthy analysis. At this stage, the center of the pupil is also determined [13]. Various edge detection methods are applied in this stage.

3.2.3. Segmentation

At this stage, as shown in Figure 5, the circular edge between the iris and the pupil, and the circular edge between the iris and the sclera is determined.

Figure 5. Determining circular borders and noise [13, 41]

The noise on the iris image is removed using a variety of image processing techniques. The noises over the iris image are factors like eyebrows, eyelashes, eyelids and light reflections etc. The removal of such factors from the image is called noise detection [13, 45, 46]. In figure 5, the pupil, iris and sclera is separated from each other using circular edge detection methods.

3.2.3.1. John Daugman Segmentation Method

Daugman used circular edge detection methods to determine the borders of iris, pupil and sclera. Especially to separate sclera from the iris, he used maximum gradient integrodifferential equation in iris images [13].

$$max_{r,x_0,y_0} \left| \frac{\partial}{\partial r} G(r) * \oint_{r, \; x_0,y_0} \frac{I(x,y)}{2\pi r} \; ds \right| \qquad (1)$$

$$G(r) = \left(\frac{1}{\sqrt{2\pi} \, \sigma} \right) e^{-\left(\frac{(r-r_0)^2}{2\sigma^2} \right)} \qquad (2)$$

$G(r)$, is the radial Gaussian function. $I(x, y)$ is the input iris image. The firs equation looks for the maximum value with fuzzy partial derivative for increasing radius and $(0, 0)$ x_0, y_0 central coordinate. This method is also called active contour fitting [13, 15].

3.2.3.2. John Daugman Polar Conversion Method

The system generates a coordinate system on the localized iris image. The center of the coordinate system is the center of the circular pupillary boundary. Figure 6 shows the cartesian form of the iris image [13, 41].
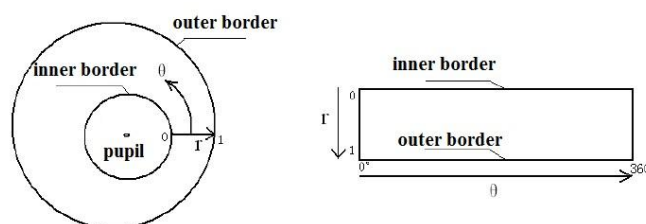

Figure 6.Cartesian form of the iris image, normalization and polar form [41, 42, 46].

3.2.4. Normalization - Polar Transformation

At this stage polar transformation is applied to the image and it is converted into dimensionless form polar from cartesian form. Daugman used radial scaling method for polar conversion [13, 46].

$$x(r,\theta) = (1-r)x_p(\theta) + rx_1(\theta) \qquad (3)$$

$$y(r,\theta) = (1-r)y_p(\theta) + ry_1(\theta) \qquad (4)$$

As shown in figure 6, the image is converted from (x, y) form into polar (r, θ) form, using image radial scaling and polar transformation [13]. Figure 7 shows (a) the image of iris area, (b) the iris image after the application of polar transformation and normalization. Daugman's polar transformation method is called Rubber Sheet model [42].
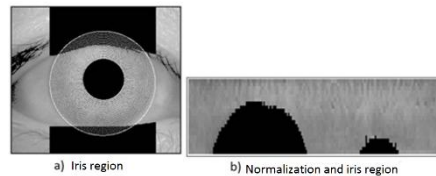

Figure 7. Normalized iris image [46].

In this stage, in order to compose a clearer iris code, histogram equalization and noise reduction methods are applied once again on the polar image.

3.2.5. Demodulation - Formation of Iris Code

After the normalization, feature vector (digital code) of the polar iris image is created during the demodulation stage. Pattern identification methods are used for image identification. In the first iris identification system, the digital code of the image is reduced to a size between 256 and 512 bytes, using a function called "2D Gabor wavelet transform" [13,16]. The created iris template in other words iris feature vector is matched with other iris templates in a huge database, for the identification and verification. During all these processes, the iris code is password protected and it is impossible to use them in any other way [16].

At this stage, feature extraction is performed using Gabor wavelet filter. Gabor wavelet filter is applied on the normalized image and a binary iris code like the one seen in figure 8 is created, which is in a fixed size and universal format.

Figure 8. Binary iris code [13, 44, 45].

In the field of iris identification, there are many different feature extraction methods in literature, for converting iris images into digital codes. Some of these methods are as follows [13];

- 1-D Gabor Wavelet Transform
- 2-D Gabor Wavelet Transform
- Correlation Filter
- Haar wavelet transform
- Dydatic wavelet transform
- Discrete Cosine transform
- Log Gabor wavelet transform
- Zero-Crossing wavelet transform

3.2.6. Iris Identification Methods According to Iris Encoding

Iris identification Methods according to Iris Encoding are separated into 4 different classes [13]. These classes are as follows;

- Phase based methods [17]
- Zero pass method [18, 19]
- Tissue analysis method [19, 20, 21,22]
- Density gradient analysis [23]

3.2.7. Comparison of Iris Codes

After the iris image of the person who demands access to the system passes the segmentation, normalization and demodulation processes, it is matched with the iris templates in the database and then identification is done. For this comparison, different methods and classifiers are used.

The comparison method of Daugman was Hamming Distance [13]. Hamming distance is the comparison of two binary codes XOR and AND. It calculates the difference between the bits of two iris codes [13, 43, 45].

$$HD = \frac{(IrisCodeA \oplus IrisCodeB) \cap MaskA \cap MaskB}{MaskA \cap MaskB} \tag{5}$$

Normalized Hamming distance

$$HD = \frac{1}{2048} \sum_{j=1}^{2,048} A_j \oplus B_j \tag{6}$$

System makes matching according to the results of the Hamming distance results. It reaches to yes or no decisions. Figure 9 shows the matching in between three iris samples. Hamming distances have been calculated. The iris with the smallest value of distance matches with the code [24]. It produces a "yes" result. Without any match, a "no" answer is produced.
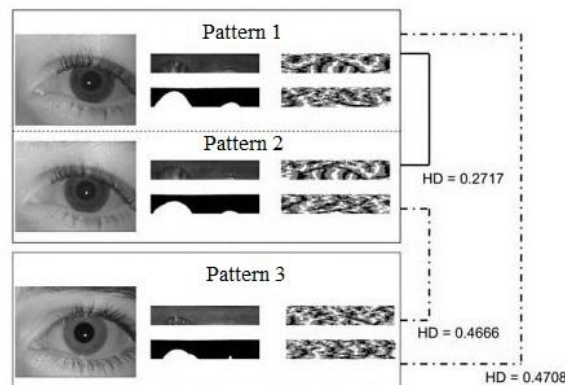

Figure 9. Hamming distance [24].

When the studies in the literature are examined, the classifiers used for the comparison of iris codes are as follows [13];
- Hamming Distance
- Euclid Distance
- Support Vector Machine (SVM)
- Artificial Neural Networks (NN)
- Nearest Neighbor Clustering (kNN)
- Self-Organized Feature Maps (SOM)
- Vector Quantization Learning (LVQ)
- Bayes Classifier

The iris codes derived from the iris images of a living eye are matched with another iris code which was previously saved in the database, within a few seconds. If there is any damaged bit on the iris code, the system detects it and only matches the valid ones [16].

4. IRIS IDENTIFICATION STUDIES IN LITERATURE

Wildes [21, 25, 26] used different methods from what John Daugman used for iris identification. Wildes first used a histogram based approach for the detection of circular edges of the iris and pupil, then, he used Hough transform [26]. Eyelids were identified as parabolic arcs.

$$H\ (x_0\ ,y_0\ ,r) = \sum_{j=1}^{n} h\ (\ x_j\ ,y_j, x_c, y_c\ ,r\ ) \tag{7}$$

$$h\ \left(x_j\, y_j\, x_0 y_0\ ,r\right) = \begin{cases} 1, & if\ \ g\left(x_j\, y_j\, x_0 y_0, r\right) \\ 0, & otherwise \end{cases} \tag{8}$$

$$g\ \left(x_j\ , y_j\, , x_0\ , y_0, r\right) =$$
$$= \left(x_j\ -\ x_0\ \right)^2\ +\left(y_j\ -\ y_0\ \right)^2\ -\ r^2 \tag{9}$$

Wildes uses image saving technique for the scaling and rotation.

$$\int_x \int_y \left(\ I_d\ (x,y) - I_a\ (\ x-u\ , y-v\ )\right)^2\ \mathrm{dxdy} \tag{10}$$

$$\begin{pmatrix} x' \\ y' \end{pmatrix} = \begin{pmatrix} x \\ y \end{pmatrix} - sR(\emptyset) \begin{pmatrix} x \\ y \end{pmatrix} \tag{11}$$

Matching function that minimizes the similarity transformation which transforms (x, y) coordinates into (x', y') is used [21, 25]. Instead of capturing the spatial details of the iris, isotropic band-pass derived with Laplacian of Gaussian is made. For the matching in between the obtained pattern and the patterns in the database, normalized correlation is used.

In the literature, in different stages of iris identification, there are studies carried out for the systems to perform better [13]. These are as follows;

- Systems have been developed which use iris code as biometric secret key. These keys were more secure than crypto-graph based keys [27].

- In order to improve real time localization (iris and pupil separation), methods which are based on particle swarm optimization have been developed [28].

- 2D Haar wavelet transform was used, which separates iris images into 4 different phases and this 4 phases of high frequency information was quantized in 87 bits code form. For classification, vector quantized learning (LVQ) has been applied [29]. In another study, iris identification systems have been produced which are based on the zero pass of wavelet transform [30].

- Iris identification systems combining wavelet transform and support vector machines have been developed. Support vector machine wavelet transform method reduced the error rates.

Methods using support vector machines have given much better results compared to methods using feed-forward artificial neural networks, nearest neighbor clustering, Hamming and Mahalanobis distance classifiers [13].

As a result of the research, it's been determined that Haar wavelet transform does better feature extraction compared to Gabor filter [20]. Image 10 shows the iris code with applied 5-D Haar wavelet transform. Haar WT is used in visible light photos.

Figure 10. Iris code with Haar wavelet transform applied [31].

5. RETINAL IDENTIFICATION SYSTEMS

Retinal identification systems are biometric systems which convert the retinal pattern which consists of capillaries, into a digital code.

5.1. The Unique Structure of the Retina

Retina is located behind the eyeball and is the most inner layer of the layers of the eye. It is rich in capillaries. These blood vessels absorb the excess light and protect the eye from damages. While working on ocular diseases in 1935, Dr. Carleton Simon and Dr. Isodure Goldstein found that each eye has a unique blood vessel structure [33]. Later on, it's also seen that although twins have the same genetic code, have different retinal patterns [34].

After the discovery that the retinal structure is unique and different for each and every human being, and is also universal, it's been understood that it could be used for identification and studies for a retinal identification system has been started. Retina can be affected by diseases like diabetes, high blood pressure, blood and cardio vascular diseases. This diminishes its reliability as a biometric system a little bit. In figure 11, (a) original photo of the retina, (b) blood vessel network of retina.
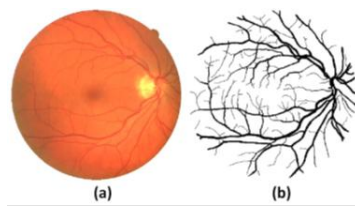

Figure 11. (a) Original retinal image (b) Blood vessels [34, 35].

5.2. Working Methods of Iris Identification Systems

Retinal identification system consists of the following stages: obtaining retinal image, segmentation, blood vascular pattern extraction, feature extraction and filtering, finally biometric pattern matching. The flowchart of retinal identification is given in figure 12.
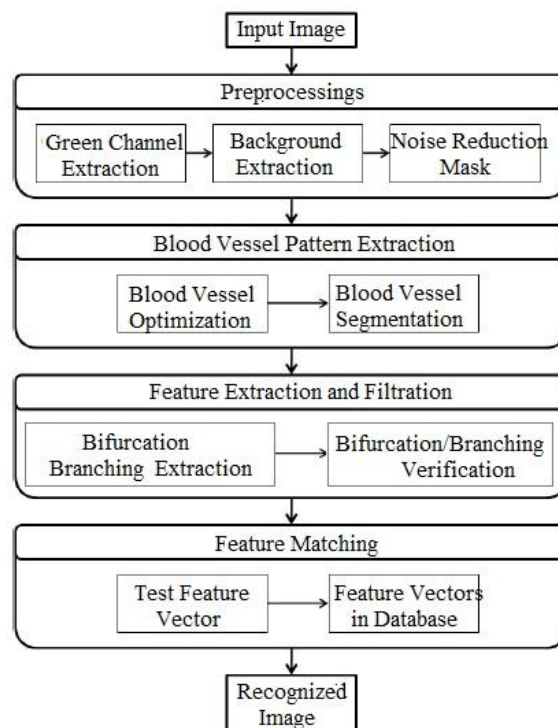

Figure 12. Flowchart of retinal identification system [32].

5.2.1. Obtaining the Retinal Image - Acquisition

The eye of the person who wants access to the system is photographed from close proximity. As the retina is behind the eye, the person has to stay close to the camera. The infrared ray of light is shone to the eye. This light passes the lens and follows the retinal path and reaches the capillaries in the retina. Meanwhile, the capillaries undergo changes as the light reaches them. They take different shapes and forms. These characteristic shapes are reflected to a video camera. System obtains the image from this reflection.

5.2.2. Preprocessing, Segmentation and Optimization

There are green, red and blue levels in digital photos. A photo can be viewed in different levels. Green channel has a higher density compared to red and blue channels. Thus green channel is extracted from the photo. The green channel is located with the following mathematical formula.

$$G = \frac{G}{R+G+B} \qquad (12)$$

R means the red channel, G means the green channel and B means the blue channel [38]. In figure 13, retinal images have been given according to the techniques applied in the preprocessing stage.
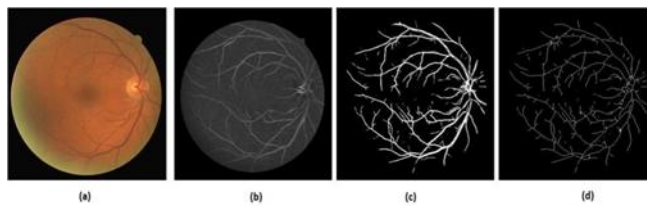

Figure 13. (a) green channel image (b) optimizedcapillaries (c) Segmented image (d) Refined capillaries [34, 35].

Preprocessing stage includes the detection of noise and separation of background from the retinal image and to highlight the blood vessel pattern. The correction of retinal identification depends on the extraction of the features of capillaries. The preprocessing includes the following actions;

- First, optimization of the image is done using wavelet transform in order to extract capillary pattern.
- A multi layered thresholding is applied on the optimized retinal image.
- Wavelet transform method is used for feature extraction. The used transform methods are as follows [34].
- Constant wavelet transform (CWT) $T\psi\ (\ b,\theta,a)$
- Fourier wavelet transform (FWT)
- 2-D Gabor wavelet transform

With Gabor wavelet transform, optimized vascular pattern can be obtained [34].

5.2.3. Feature Extraction and Bifurcation

Bifurcation means branching. The main features of vascular patterns are vascular endings and branching points [35]. The system uses the crossing number method which is shown in figure 14, for the extraction of the vascular endings and branching [35]. Figure 15 shows the vascular features and branching which are obtained using this method.
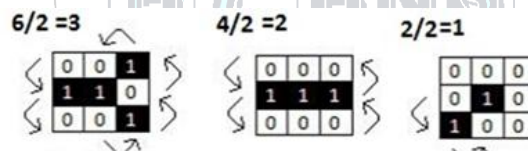
Figure 14. Crossing number method [36].

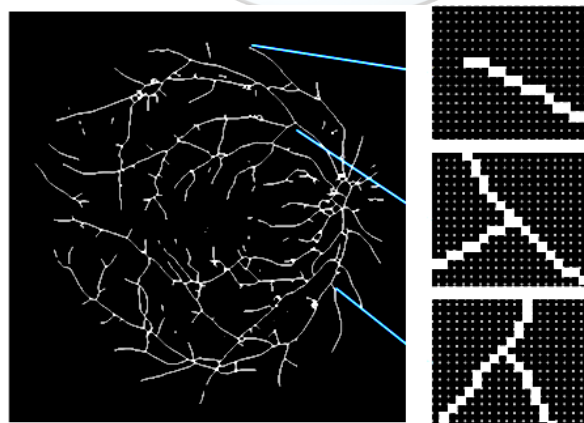*Figure 15. Vascular features, endings and bifurcation [34].*

The mathematical expression of this method:

$$C(p) = \frac{1}{2}\sum_{i=1}^{8}|g(p_{i\,mod\,8}) - g(p_{i-1})| \tag{13}$$

g is the refined retinal image and p represents each vascular pixel. Pixels between p_0 and p_7 are the pixels in clock wise which define the 8 neighboring of p and $g(p)$ is the pixel value [34]. For vascular pixels $g(p) = 1$,

for others $g(p) = 0$. $C(p) = 3$ and $C(p) = 1$ are branching and vascular endings. Feature spots obtained with this algorithm are the correct ones. In order to determine the wrong spots, 9x9 windowing method is used. Figure 16 shows the wrong spots like bling spots, breaks and short blood vessels.
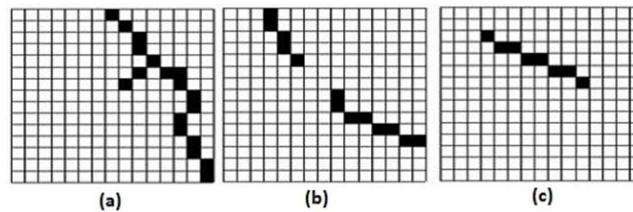

Figure 16. Wrong spots, (a) blind spots, (b) breaks, (c) short Blood vessels [36].

While obtaining the retinal vascular patterns, the purpose is to find the correct branching. After the blind spots, breaks and short blood vessels are found using windowing technique, these are eliminated [36]. Thus, correct endings and branching feature spots can be determined.

5.2.4. Comparison of Vascular Patterns

This is the identification phase. The retinal image taken from the person who wants access is processed using various processing, recognition etc. methods and feature vector (digital code) is generated for the retina. This digital template is matched with other retinal templates in the big database. This comparison can be made using various methods. These methods are as follows;
- Mahalanobis distance
- Vascular pattern correlation
- Matching which use branching spots.

6. PERFORMANCE CRITERIA OF BIOMETRIC SYSTEMS

Performance is an important concept for computerized systems. Any computerized system should operate fast and accurate. The most important performance criteria in biometric systems are total processing time, false acceptance rate (FAR) and false rejection rate (FRR) [2, 37, 45].

The total processing time is the time elapsed between the person's request to access, and the time the access is given. This should take 1-2 seconds in a good system [2, 37]. False acceptance rate is the possibility of access being granted for an unauthorized person, with a faulty decision. False rejection rate is the possibility of access not being granted for an authorized person. The aim for all biometric systems is to reduce both FARs and FRRs below 1%. [2, 37, 45].

7. RESULTS

In this study, different iris and retinal identification methods have been examined, and the similarities and differences of these systems have been identified. It's been seen that these systems are much more reliable, accurate and fast, compared to other biometric systems available. However, their high cost prevents them to be widely adopted.

The similarities between iris and retinal identification can be listed as follows;
- False acceptance rate is low in both.
- False rejection rate is very low, almost 0.
- Highly reliable, because the iris or retinal patterns are unique for everybody.
- Identification is very fast in both.

The differences between iris and retinal identification can be listed as follows;
- The accuracy of retinal scanning can be affected by various diseases, however, the rich texture of the iris is fixed for life and immutable.
- Iris scanning is not different from a normal photo shoot, shots are taken from a short distance. Retinal scanning requires the person to be much more close to the camera.
- Iris is an internal organ which can be seen externally, but retina is on the back of the eye. Therefore, photographs are taken from different distances.
- Iris scanning is more commercially accepted than retinal scans. Retinal scanning is considered to be harmful.
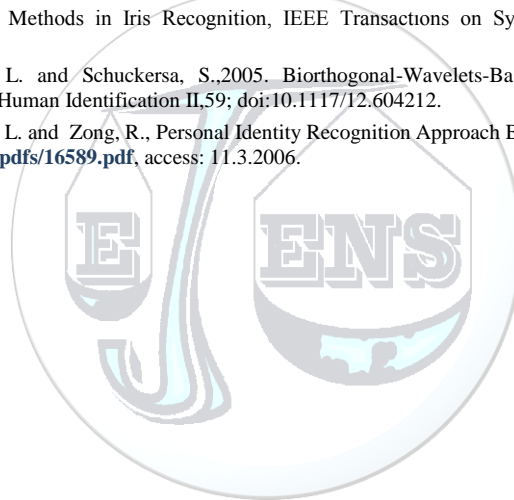
Retina and iris can be used in cryptography with their unique structures. With smart cards that carry both iris and retinal codes, both users and the system owners or institutions can have a more security.

When the properties of retinal and iris identification are analyzed, it is expected that these two systems can perform better compared to other biometric based systems like finger print, face or vascular identification systems. Apart from that, it's also been understood that with a combination of iris and retinal pattern prototype can be one of the most secure identification systems available.

REFERENCES

[1]. Turhan C., Ceyhan, E., Sağıroğlu Ş., Biyometrik Sistemlerde Güvenlik Üzerine Bir İnceleme, **www.iscturkey.org**, access: 03.03.2016.

[2]. Yalçın, N., Gürbüz, F., 2015. Biyometrik Güvenlik Sistemlerinin İncelenmesi, Düzce Üniversitesi Bilim ve Teknoloji Dergisi, cilt 3, no. 2, pp.

[3]. Elumalai, K., Kannan, M., 2011.Multimodal Authentication For High End Security, International Journal on Computer Science and Engineering (IJCSE), 3(2), 687-692.

[4]. Jain, K., Bolle, R., Pankanti, S., 1999. Biometrics: Personal identification in Networked Society, Springer Science and Business Media.

[5]. Ergen, B., Çalışkan, A., 2011. Biyometrik Sistemler ve El Tabanlı Biyometrik Tanıma Karakteristikleri, 6th International Advanced Technologies Symposium, Elazığ-Türkiye.

[6]. Jain, A.K., Ross, A., Prabhakar, S., 2004. An Introduction to Biometric identification, IEEE Transaction on Circuits and Systems for Video Technology, vol.14, no.1, pp.4-20.

[7]. Şamlı, R., Yüksel, M. E., 2009. Biyometrik Güvenlik Sistemleri, Akademik Bilişim, Şanlıurfa-Türkiye.

[8]. Liu, S., Silverman, M., 2001. A Practical Guide to Biometric Security Technology, IT Professional, vol. 3, no. 1, pp. 27-32.

[9]. Unar, J., Senga, W., Abbasia, A., 2014. A Review of Biometric Technology Along with Trends and Prospects, Pattern identification, vol. 47, pp.2673-2688.

[10]. Monrose, F., Rubin, A., 1997. Authentication via Keystroke Dynamics, 4th ACM Conference on Computer and Communications Security, Switzerland, pp. 48-56.

[11]. **http://www.biyolojisitesi.net/tum%20uniteler/denetleme_ve_duzenleme/gorme_nasil_gerceklesir.html, access: 6.1.2016.**

[12]. Yücel, E. Işık, Renk ve Elektromanyetk Spektrum,**http://www.akat.org/sizin_icin/elektromagnetik_tayf.pdf**, access: 6.1.2016.

[13]. Alkoot, Fuad M., 2012. A Review On Advances In Iris identification Methods, International Journal of Computer Engineering Research, vol. 3(1), pp. 1-9, Kuwait.

[14]. **http://www.biltek.tubitak.gov.tr/haberler/tip/s528_5.pdf**, access: 6.1.2016.

[15]. Tasyapi Celebi A., Güllü, Kemal M., Ertürk, S., 2009. Low-complexity Iris identification Using One-bit Transform and Angular Radial Partitioning, 2009 IEEE 17th Signal Processing and Communications Applications Conference.

[16]. **http://www.ergosis.com.tr/iris-tanima-teknolojisi.html**, access: 6.1.2016.

[17]. Daugman, J., 2003. Demodulation by Comlex-Valued Wavelets for Stochastic Pattern identification, Int. J. Wavelets, Multi-Res. and ınfo. Processing. 1(1): 1-17.

[18]. Daugman, J., Downing, C., 1995. Demodulation, Predictive Coding and Spatial Vision, J. Opt. Soc. Am. A 12: 641-660.

[19]. Sanchez-Avila, C., Sanchez-Reillo, R., 2002. Iris-Based Biometric identification Using Dyadic Wavelet Transform, IEEE Aerosp. Electron. Sys. Mag., 17:3-6.

[20]. Lim, S., Lee, K., Byeon, O., Kim, T., 2001.Efficient İris identification Through İmprovement of Feature Vector and Classifier, ETRI J. 23(2): 1-70

[21]. Wildes, R., Asmuth, J., Green, G., Hsu, S., Kolczynski, R., Matey, J., McBride, S., 1996. A Machine-Vision System for Irıs identification, Mach. Vis. Applic., 9: 1-8.

[22]. Zhu, Y., Tan, T., Wang, Y., 2000. Biometric Personal identification Based On Iris Patterns, Int. Conf. Pattern identification, II:805-808.

[23]. Ma, L., 2003. Personal identification Based On Iris identification, Ph.D dissertation, China.

[24]. Jain, A., Ross, A., Nandakumar, K., İntroduction to Biometrics, **https://books.google.com.tr/**, access: 6.1.2016.

[25]. Wildes, R., 1994. A System for Automated Iris identification, 2nd IEEE Workshop Applicat. Comput. Vision, pp.121-128.

[26]. Jones, M. J., Guo, G., 2008. Iris Extraction Based on Intensity Gradient and Texture Difference, IEEE Workshop on Applications of Computer Vision Conference.

[27]. Ziauddin, S., Dailey M., 2010. Robust Iris Verification for Key Management, Pattern identification Letters, 31(9).

[28]. Perez, C. A., Aravena, C. M., Vallejos, J. I., Estevez, P. A., Held, C. M. 2010.Face and Iris Localization Using Templates Designed by Particle Swarm Optimization, Pattern identification Letters, 31(9): 857-868.

[29]. Lim, S., Lee, K., Byeon, O., Kim, T., 2001. Efficient Iris identification Through Improvement of Feature Vector and Classifier. ETRI J. 23(2): 1-70.

[30]. Boles, W., Boashash, B., 1998. A Human identification Technique Using Images of Iris and Wavelet Transform, IEEE Transaction on Signal Processing, 46(4).

[31]. Murty, P. C., Reddy, E. S., Babu, I. R., 2009, Iris identification System Using Fractal Dimensions of Haar Patterns International, Journal of Signal Processing, Image Processing and Pattern identification, vol. 2, No.3.

[32]. Akram, U. M., Tariqy, A., Khan, S. A., 2011. Retinal identification: Personal identification using Blood Vessel, 6th International Conference on İnternet Technology and Secured Transactions, United Arab Emirates.

[33]. Simon, C., Goldstein, I., 1935. A New Scientific Method of identification, New York State Journal of Medicine, vol. 35, No. 18, pp. 901-906.

[34]. Qamber, S., Waheed, Z., Akram, U., 2012.Personal identification System Based on Vascular Pattern of Human Retina, Cairo International Biomedical Engineering Conference (CIBEC), Egypt.

[35]. Fatima, J., Syed, M., Akram, U., 2013. A Secure Personal identification System Based on Human Retina, 2013 IEEE Symposium on Industrial Electronics and Applications, Malaysia.

[36]. Fatima, J., Syed, M., Akram, U., 2013. Feature Point Validation for Improved Retina identification, IEEE Workshop on Biometrics Measurements and Systems for Security and Medical Applications, Italy.

[37]. http://elektroteknoloji.com/Elektrik_Elektronik/Teknik_Yazilar/Biyometrik_Sistemler_Fiziksel_Ozelliklerden_Yararla narak_Kimlik_Tespit_Etme_bilgisayar_destekli.html, access::6.1.2016.

[38]. Patwari, Manjiri B., Manza, Ramesh R., Rajput, Yogesh M., Saswade, M., Deshpande, M.,2014. Personal Identification Algorithm Based on Retinal Blood Vessels Bifurcation, 2014 International Conference on Intelligent Computing Applications, India.

[39]. http://www.evrenvebilim.com/kotu_tasarim_yanilgisi.html, access: 11.3.2016.

[40]. http://pmgbiology.com/2014/05/31/understanding-the-functioning-of-the-eye-to-a-biology-gcse-part-1/ access: 11.3.2016.

[41]. Rashad, M. Z. Shams ,M. Y., Nomir, O., El-Awady, R. M., 2011. Iris Recognition Based on LBP and Combıned LVQ Classıfıer, International Journal of Computer Science & Information Technology (IJCSIT), vol 3, No 5, DOI : 10.5121/ijcsit.2011.

[42]. Bendre, Sandip M., Shivarkar, Raosahe A., An Improved Approach for Iris Authentication System by Using Daugman's Rubber Sheet Model, Segmentation, Normalization and RSA Security Algorithm, International Journal of Computer Technology and Electronics Engineering (IJCTEE) vol. 1, Issue 3 102.

[43]. Latha, L., Thangasamy, S., 2010. A Robust Person Authentication System based on Score Level Fusion of Left and Right Irises and Retinal Features, Procedia Computer Science 2 (2010) 111–120.

[44]. Daugman, J., 2007. New Methods in Iris Recognition, IEEE Transactıons on Systems, Man, and Cybernetıcs—part b: Cybernetıcs, vol. 37, no. 5.

[45]. Abhyankar, A., Hornak, L. and Schuckersa, S.,2005. Biorthogonal-Wavelets-Based Iris Recognition, Proc.SPIE 5779, Biometric Technology for Human Identification II,59; doi:10.1117/12.604212.

[46]. Tian, Q., Qu, H., Zhang, L. and Zong, R., Personal Identity Recognition Approach Based on Iris Pattern,2011. http://cdn.intechweb.org/pdfs/16589.pdf, access: 11.3.2006.

Journal Homepage : http://dergipark.gov.tr/ejens

EJENS

European Journal of Engineering and Natural Sciences

DergiPark
AKADEMİK

CODEN: EJENS

Grounded and Floating Real Inductor Simulations and Experimentations using Second Generation Current Conveyors

Mehmet Demirtas[1]*, Salih Gunes[1], Saadetdin Herdem[1]

[1]*Selçuk University, Department of Electrical and Electronics Engineering, 42250, Selçuklu/Konya, Turkey*
*CorrespondingAuthor email: mdemirtas@selcuk.edu.tr

Abstract

Current Conveyors (CC) are active circuit elements which perform analog signal processing. CCs were developed as an alternative to the classical Operational Amplifiers (OPAMP). Unlike OPAMPs, CCs are current-based and they operate according to the principle of 'current conveying' from one terminal to another. As a modified version of the First Generation Current Conveyor (CCI), Second Generation Current Conveyors (CCII) is versatile and useful in designing analog circuits such as filters, amplifiers, inductor simulators etc. In this paper, one grounded and one floating inductor simulator designs are given. These simulator designs are based on CCII's and passive elements like resistors and capacitors. Both inductor simulator designs are lossy and simulate real inductors that have internal resistance. The simulators simulate an inductance in series with an internal resistance. Since inductors are non-ideal, noisy, bulky circuit elements, it is reasonable to simulate their behavior under certain frequency range using CCII's as active elements. In this study, inductor simulators are created first by BJTs & passive elements in SPICE environment and created inductor simulators are tested in a Low Pass Filter (LPF) for a frequency range up to 10MHz. Moreover, both simulators are realized for experimentation using commercially available Analog Device's AD844's which can perform as a CCII & using resistors and capacitors. Realized inductor simulators are tested in the same LPF. The gain of the filter is measured for 15 different frequency values which are located between 10 Hz-10MHz. Finally, both SPICE simulation and experimental results are compared for the same LPF which is constructed using ideal inductor. It is concluded that a lossy, real inductor can be simulated up to certain frequencies by using CCIIs both in simulation environment and experiment.

1. INTRODUCTION

1.1. Second Generation Current Conveyors

Second Generation Current Conveyors (CCII) are first proposed as a revised version of First Generation Current Conveyors (CCI) [1]. Compared to CCIs, CCIIs are more useful and versatile in analog signal processing implementations such as voltage/current sources, amplifiers, filters, differentiators, integrators and inductance simulations [2]. The main principle of current conveyors is conveying current from one terminal to another terminal.

In Figure 1, block diagram of a CCII is shown. Under ideal conditions, the principle of operation of CCII is as follows:

- If a V_y voltage is applied to the Y terminal, the same amount of voltage will appear at terminal X. Therefore, $V_x = V_y$ will be observed.

Figure 1. CCII Block Diagram

- There is no current flowing into to the Y terminal which makes $i_y = 0$ which is the only difference between CCI and CCII. In CCI, if there is a current flowing into the X terminal, the same amount of current will flow into the Y terminal.

- If there is a current flowing into the X terminal, the same current will also flow into the Z terminal which is $i_x = i_z$.

Under ideal conditions, Y terminal should not draw current from the circuit which means there is infinite impedance at that terminal. Also, since voltage at X terminal follows the voltage at Y terminal, the impedance at X terminal should be very low, ideally zero.

$$\begin{bmatrix} i_y \\ V_x \\ i_z \end{bmatrix} = \begin{bmatrix} 0 & 0 & 0 \\ 1 & 0 & 0 \\ 0 & \pm 1 & 0 \end{bmatrix} \begin{bmatrix} V_y \\ i_x \\ V_z \end{bmatrix} \tag{1}$$

The matrix which explains the relation between input and output characteristics of CCII in ideal conditions is as shown in (1). In hybrid matrix, ± 1 notation indicates the direction of the current at Z port. If it is +1, then CCII is called as positive type second generation current conveyor (CCII+). If it is -1, that type of CCII is called as negative type second generation current conveyor(CCII-).

1.2. Inductance Simulation

Inductors are non-ideal passive circuit elements. The reasons for their non-ideality are the length of wire to wrap up inductors, the internal resistance of that wire and parasitic capacitance which occurs between parallel wirings [3]. Moreover, inductors are bulky, expensive and noisy circuit elements which contain too much unwanted characteristics [4]. Because of these reasons, physical inductors are not generally preferred in integrated circuits. Instead of physical inductors, 'inductance simulator' circuits are used. Inductance simulator circuits operate like inductors under certain frequency range.
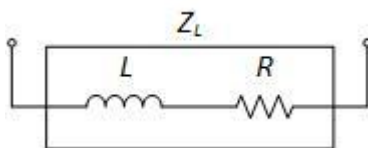
Figure 2. Real Inductor Model

In Figure 2, a real inductor model is shown. In this model, R in series with L is the resistance of the wire used to form inductor. The impedance observed between terminals of a real inductor is given as follow:

$$Z_L = R + sL \tag{2}$$

Using CCIIs and certain combination of passive elements like resistors and capacitors, it is possible to simulate both floating and grounded inductors.

2. MATERIALS AND METHODS

One grounded and one floating lossy, real inductor models are given. The proposed models use CCII's and passive circuit elements such as resistors and capacitors as seen in Figure 3 and Figure 9. Those models are tested in test circuits which behave as low pass filter. Also, Analog Device's AD844[5] integrated circuit is

used as CCII+ so that the test circuit is built and measured experimentally. For experimental testing, the gain is measured for 15 different frequency points to compare simulation and experimental results.

2.1. Grounded Inductance Model

In Figure 3, a grounded inductance simulation circuit which consists of one CCII+ and three passive elements is given [6]. This circuit simulates a real inductor which consists of a resistance and an inductor in series with each other. When the impedance is observed from Z_{in} point of view, considering the terminal equations of the CCII+ and passive element characteristics, the Z_{in} is calculated as follows:

$$Z_{in} = Z_1 + Z_2 + \frac{Z_1 Z_2}{Z_3} \qquad (3)$$

If Z_1 and Z_2 passive elements are selected as resistors R_1 and R_2 respectively and Z_3 is selected as capacitor C, the following input impedance equation that fulfills the requirement of a real inductor can be obtained:
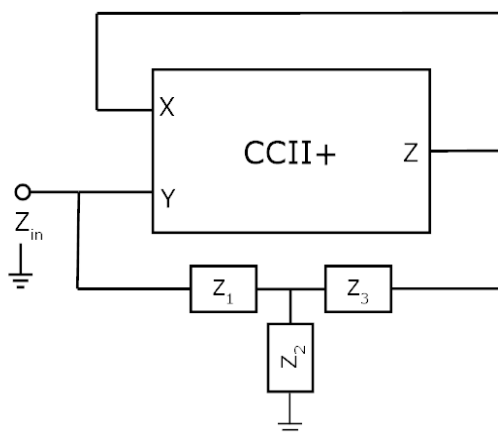
Figure 3. Grounded Inductance Simulator

$$Z_{in} = R_1 + R_2 + sCR_1R_2 = R_{eq} + sL_{eq} \qquad (4)$$

Therefore, a lossy (due to the resistance term in the equation) grounded inductance is simulated using one CCII+ with 2 resistors and 1 capacitor.

To model CCII+, Figure 4[7] is used along with NR200N and PR200N SPICE model parameters [8].
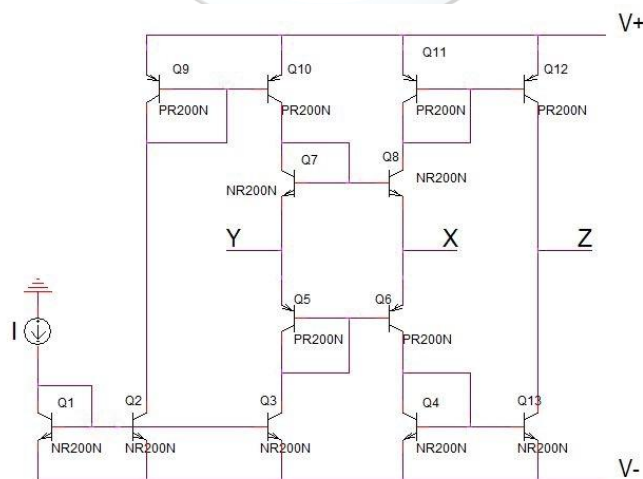
Figure 4. Schematic Implementation of CCII+

2.2. Grounded Inductance Model Experimental Setup

In order to test the suggested inductance model experimentally, an integrated circuit AD844 fabricated by Analog Devices which behave as CCII+ is used as shown in Figure 5. Since it is commercially available,

AD844 is useful in putting simulation level studies into practice. Therefore, experimental results can be obtained.

Figure 5. AD844 Block Diagram

For this grounded inductor simulator, if passive element are chosen such that $R_1 = 10\ \Omega$, $R_2 = 10\ \Omega$ and $C = 10$ µF then $R_{eq} = 20\ \Omega$ and $L_{eq} = 1$ mH is obtained. For the experimental setup, the circuit in Figure 6 is constructed using these resistor and capacitor values.
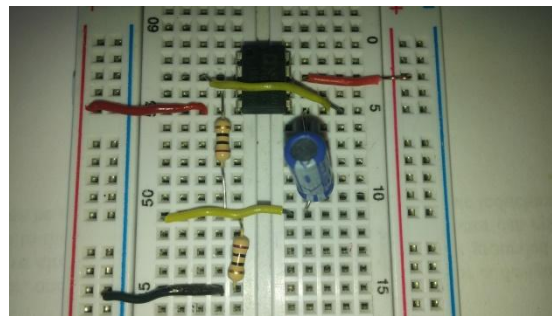
Figure 6. Grounded Inductance Simulator Experimental Setup

2.3. Grounded Inductance Model Test Circuit
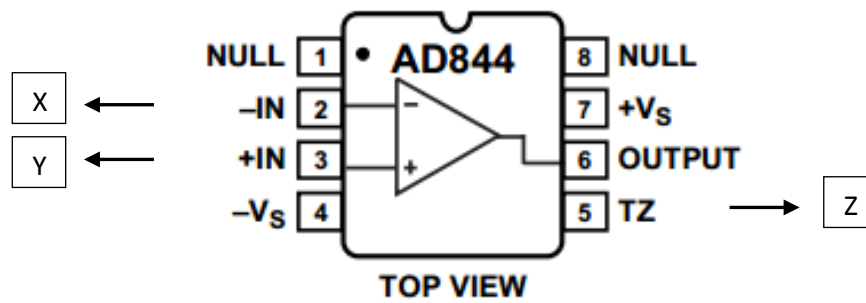
We can test this grounded inductance simulator designing a low pass filter as shown in Figure 7.
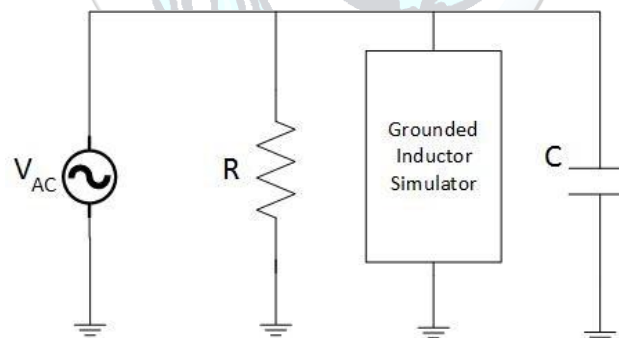
Figure 7. Grounded Inductance Simulator Test Circuit

The frequency response of the test circuit is observed from the current in the grounded inductor simulator point relative to the input current. Three different graphs are obtained as shown in Figure 8. The first graph is the ideal response as if using an ideal inductor in series with a resistor. The second one is simulation results which are obtained in SPICE environment. Second graph is obtained using Figure 4. schematic representation. The third graph is the experimental results. For 15 different frequencies in between 10 Hz-10MHz, experimental results are measured.

From Figure 8, it can be concluded that the cut-off frequency is found at 200 kHz for ideal situation while it is 7 MHz for the SPICE simulation. Experimentally it is found out to be 300 kHz. It is fair to say that SPICE simulated circuit operates very close to the ideal situation until 100 kHz. The experimental circuit can model the lossy inductor up to 40 kHz.
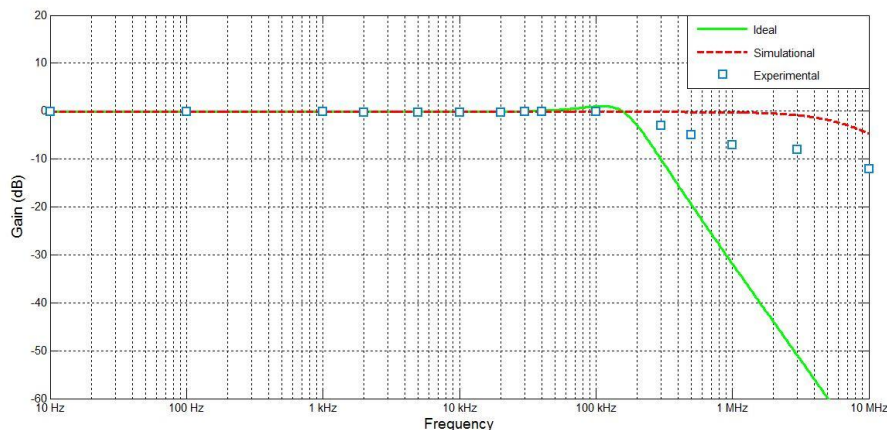
Figure 8. Simulation, Experimentation & Ideal Frequency Responses for Grounded Inductance Simulator

2.4. Floating Inductance Model

In Figure 9, a real/lossy floating inductance simulator that is built with 2 positive-type CCII's and 3 passive elements is given [9]. If Z_1 and Z_2 are chosen as resistor R and Z_3 is chosen as capacitor C; the impedance value between the terminals of the floating inductance simulator can be obtained as follows:

$$Z_L = R + sCR^2 \tag{5}$$
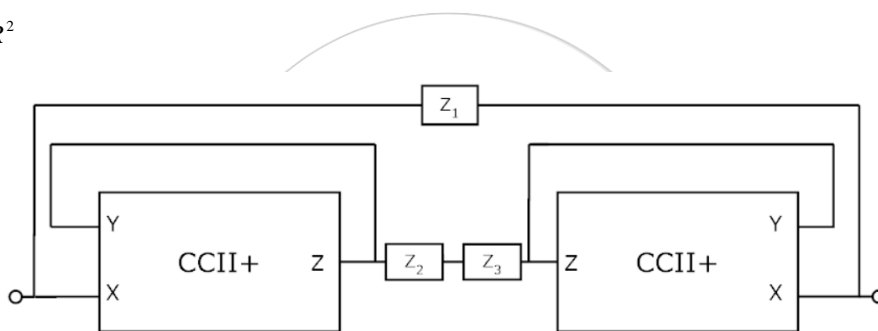
Figure 9. Floating Inductance Simulator

Therefore, the obtained impedance Z_L can model a lossy floating inductor. In order to test the designed floating inductance simulation a PSPICE simulation is run. To model the CCII+'s, NR200N and PR200N SPICE model parameters are used.

2.5. Floating Inductance Model Experimental Setup

For this model, if passive elements are chosen such that $R = 1\text{k}\,\Omega$ and $C = 1$ nF; then

$$Z_L = 1000 + s0.001\,\Omega \tag{6}$$

impedance value is found. This model simply simulates a 1 mH lossy inductor with 1000 Ω internal resistance. For the experimental setup, the circuit in Figure 10 is constructed using 2 AD844s, 2 1k Ω resistors and one 1 nF capacitor.
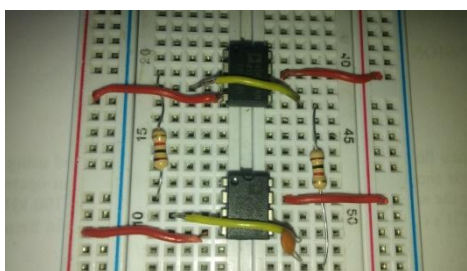
Figure 10. Floating Inductance Simulator Experimental Setup

2.6. Floating Inductance Model Test Circuit

In order to test the floating inductance simulation a test circuit is set as shown in Figure 11.
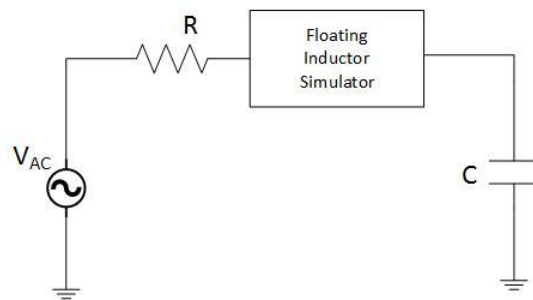
Figure 11. Floating Inductance Simulator Test Circuit

The frequency response of the voltage of capacitor in the test circuit is observed relative to the input voltage. The graphs of ideal, SPICE simulation and experimentation results are shown in Figure 12.
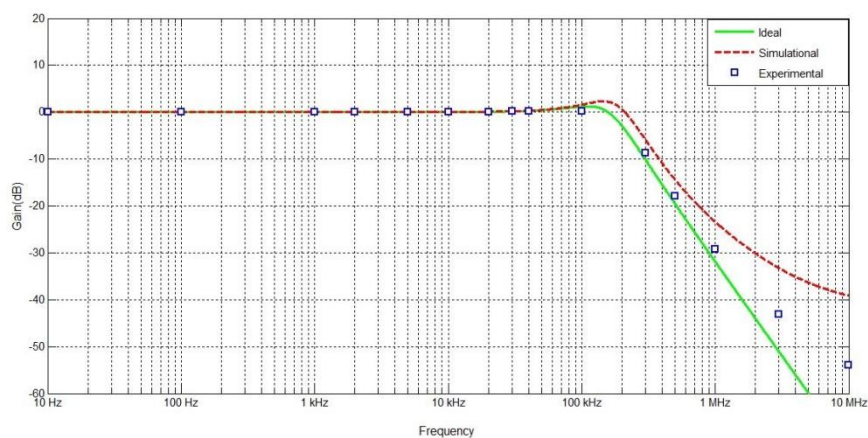
Figure 12. Floating Inductance Simulation, Ideal and Experimental Frequency Responses

In Figure 12, it can be seen that the cut-off frequency is found at 202 kHz for ideal situation while it is 256 kHz for the SPICE simulation. In experiments, the cut-off is found out to be 150 kHz. It can be said that this floating inductor simulator can operate close to the ideal situation up to 90 kHz for the SPICE simulation. Also, experimental results show that the circuit in Figure 11 can operate as if a lossy inductor up to 50 kHz.

3. RESULTS AND DISCUSSION

As a passive electronic circuit element, inductors have many applications. However, using physical inductors in circuit design is somehow problematic due to their size and cost. In order to overcome this issue, instead of physical inductors, inductor simulations could be utilized.

In this paper, two kinds of inductor simulators are given and tested both in simulation and experimentation. Grounded inductor simulator is designed with one CCII+, 2 resistors and 1 capacitor. This design can simulate a lossy inductor such that 1 mH inductance in series with 20 Ω resistance. CCII+ is first modeled by BJTs and simulation results are taken. Also, the same circuit is realized with AD844 and experimental data is obtained. Using the test circuit, the performance of those simulation and experimentation are compared to the ideal response. The simulator can perform up to 100 kHz similar to the ideal response. The experimental results also show that up to 40 kHz realized AD844 circuit can be used instead of a lossy inductor.

Floating inductor simulator is designed 2 CCII+'s, 2 resistors and 1 capacitor. This simulator can simulate an inductor 1 mH with a 1 kΩ internal resistance. The performance of the floating inductor simulator is tested in a test circuit. Simulation and experimentation data is taken and compared to ideal situation. The simulator can perform up to 90 kHz for simulation case and 50 kHz for experimentation very close to the ideal response.

4. CONCLUSION

In this paper, one grounded and one floating inductance simulator is designed and tested using CCII+'s and some passive circuit elements. It is shown that the simulator for grounded inductor can operate like a real inductor up to the 180 kHz, while the simulator for floating inductor can operate up to 100 kHz. With these results, it can be concluded that CCII's can be employed to simulate inductors up to certain frequencies.

REFERENCES

[1]. Smith, K.C. veSedra, A., 1968, The current conveyor: A new circuit building block. IEEE Proc., 56: 1356-1369.

[2]. Smith, K. C. veSedra, A., 1970, A second generation current conveyor and its applications. IEEE Trans. Circuit Theory, CT-17: 132-134.

[3]. Soliman, A. M., 1973, Inductorless realization of an all-pass transfer function using the current conveyor. IEEE Trans. On Circuit Theory, CT-20: 80-81.

[4]. Pal, K., Singh, R., 1982. Inductorless current conveyor allpass filter using grounded capacitors. Electronics Letters, 18(1): 47.

[5]. Analog Devices AD844, 1989, "60 MHz 2000 V/μs Monolithic Op Amp", Rev. 2009

[6]. Nandi, R., 1978, Active inductance using current conveyors and their application in a simple bandpass filter realization. Electronics Letters, 14: 373-375.

[7]. Fabre, A., Saaid, O., Wiest, F. veBoucheron, C., 1995. Current controlled bandpass filter based on translinear conveyors. Electronics Letters, 31(20): 1727-1728.

[8]. Frey D.R., 1993, "Log-domain filtering: An approach to current-mode filtering", IEEE Proceedings-G: Circuits, Devices and Systems, Vol. 140, pp. 406-416.

[9]. Senani, R., 1985. Novel high-order active filter design using current conveyors. Electronics Letters, 21(22): 1055-1056.

Evaluation of Commercial Type of Split Air Conditions by Using Condenser Waste Heat in a Boiler

Alper Ergun[1]*, Engin Gedik[1], Mehmet Ozkaymak[1], Bahtiyar Sansli[2]

[1]*Karabük University, Technology Faculty, Department of Energy Systems Engineering, 78050, 100. yıl/Karabük, Turkey*

[21]*Karabük University, Graduate School of Natural and Applied Sciences, 78050, 100. yıl/Karabük, Turkey*

CorrespondingAuthor email: alperergun@karabuk.edu.tr

Abstract

Air conditioners are used for reducing the ambient temperature and they are manufactured in different versions. Especially, split type air conditioners are used widely. Because of increasing use of air conditioners, energy consumption has also increased, so researchers have attracted to search for production of more efficient air conditioners. The main objective of this study is to investigate thermal performance of the whole split type air conditioner system. For this purpose, an experimental system was designed and manufactured by adding a boiler unit to the conventional split air conditioners condenser. At the end of the study, coefficient of performance (COP) of the system increased from 3.64 to 4.54. In addition, boiler which added to system increases temperature of water from 10ºC to 40 ºC. When economical benefit is considered, electrical consumption is decreased 0.61 $ supposing that the device works 10 hours in a day. Only 132.5 $ is paid for the device in addition to existing split air conditioners. Besides, domestic water at 40 ºC was produced.

1. INTRODUCTION

Cooling is a technique that is decreasing the temperature of substance or local environment below the surrounding volume temperature [1]. Recently, local cooling has been popular in order to supply thermal comfort conditions. Besides, the devices that work according to the vapor compressing cooling cycle has used. Home type split air conditioners that work using vapor compressing cooling cycle phenomena has widely been used nowadays. According to the researches, energy in the world is consumed about 16% to 50% by cooling and heating systems in buildings [2]. Energy consumption of residential buildings is 30% of the total energy consumption in Turkey and 80% of this consumption is related to the heating and cooling systems [3-5]. Thus, it can be seen that energy which is used to perform home cooling and prepare domestic hot water is massive. Nowadays, there are many studies has been carried out to improve the performance of split type air conditioners Martinez et al. [6] covered the condenser unit of split type air conditioner with evaporative cooling pads that have various thicknesses and examined the energy performance of this system. Sumeru et al. [7] used an ejector as an expansion element in order to perform experiments and numerical analysis. Padalkar et al. [8] changed the HCFC-22 refrigerant to HC-290 of a split type air conditioner and determined the performance of this new refrigerant. Kumlutaş et. Al [9] performed heat and flow analysis in internal unit of split type air conditioner. Jie and Lee [10] placed a storage-enhanced heat recovery room into the split type air conditioner. They used a capillary tube and expansion valve in order to determine the system performance. Besides, [11] they used phase changed material in storage-enhanced heat recovery room and performed the analysis of modified system.

In this study, energy analysis were performed by adding boiler unite onset of the condenser unit in split type air conditioner that works with R-22 refrigerant.

2. MATERIAL AND METHODS

In this study, split type air conditioner with boiler unit was designed and manufactured. The designed and produced system is shown in Figure 1. The system consists of compressor, evaporator, condenser, expansion valve and four way valve. The boiler unit was designed to prepare domestic hot water and placed in between condenser and four-way valve. Assembled boiler unit and built-in system can be seen in Figure 2.
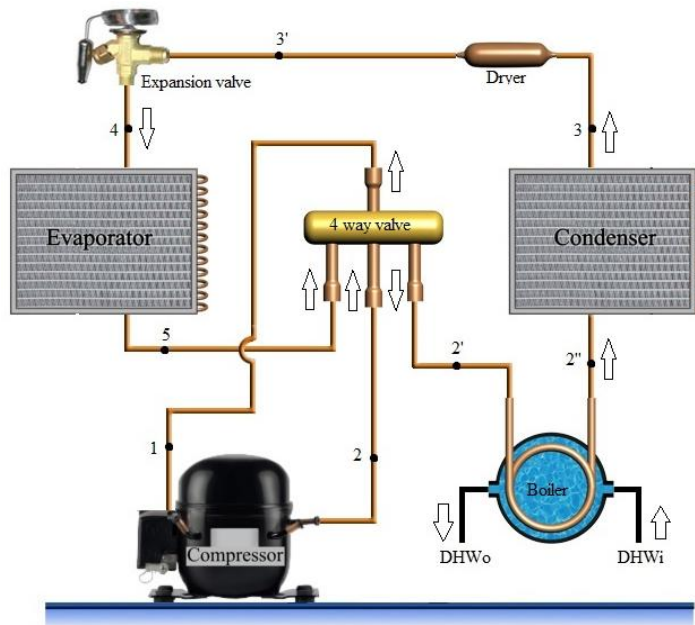
Figure 1. Schematic view of the experimental setup.

Figure 2. Designed boiler unit and assembled experimental setup

Designed boiler unit that have 40l volume and 3/8" copper pipe with 18m length was placed in. Boiler unit was covered with rubber isolation material that have 1cm thickness to prevent heat loses. In the unit, 0.15 gr refrigerant was added for each 1 m pipe length.

When high pressured refrigerant as superheated steam exited from outlet of the compressor, the heat of refrigerant is transferred to water in boiler unit instead of atmosphere air. The heat was sent to the boiler unit

water when the condensation pressure was about 4.5-5 bar. At this stage, there was no need to work condenser fan. If this heat transfer is higher than boiler capacity, condenser fan started. This system works with a thermostat that opens at 55°C and closes at 35°C to regulate condenser unit properly. When the refrigerant transferred its heat, the refrigerant was accomplished its cycle by passing expansion valve and evaporator. The system can be by-passed using boiler valves. Thus, the analysis can be performed with and without boiler unit in terms of comparison between both designs.

3. THERMODYNAMIC ANALYSIS OF SYSTEM

The coefficient of performance was calculated for boiler and without boiler conditions. Energy balance of steady-flow condition can be determined as follow;

$$q_{net} - w_{net} = \Delta h + \Delta ke + \Delta pe \tag{1}$$

Here, q_{net} and w_{net} are described heat and work input, Δh, Δke and Δpe are impressed changing of enthalpy, kinetic energy and potential energy respectively. The changing of kinetic and potential energies can be neglected. Thus, steady-flow energy equation on a unit-mass basis reduces to;

$$(q_i - q_o) + (w_i - w_o) = h_0 - h_i \tag{2}$$

In equation 2, q, w and h are the heat, work and enthalpy respectively while i and o describe the subtitle of input and output.

Compressor work, condenser load and evaporator load were calculated related to energy equations. Energy transfer was not occurred because of the fact that therewas not any enthalpy changes in expansion valve. When the loss of pressure in fittings equipment and loss of heat in pipes were ignored, the equation of conservation of energy principle can be expressed as follow;

$$W_{comp} + Q_{evap} = Q_{cond} \tag{3}$$

From this equation, compressor work, evaporator and condenser load can be calculated as follows;

Compressor work;

$$\dot{W}_{comp} = \dot{m}(h_2 - h_1) \tag{4}$$

Condenser load;

$$\dot{Q}_{cond} = \dot{m}(h_2 - h_3) \tag{5}$$

Evaporator load;

$$\dot{Q}_{evap} = \dot{m}(h_5 - h_4) \tag{6}$$

The most crucial parameter that determines the performance of vapor compressing cooling cycle is coefficient of performance (COP) and it can be calculated as follow;

$$COP = \frac{\dot{Q}_{evap}}{\dot{W}_{comp}} = \frac{h_5 - h_4}{h_2 - h_1} \tag{7}$$

The power of system (P) can be calculated as follow;

$$P = U \times I \tag{8}$$

In there, U is the voltage of the device (220V) and I is the current.

All the calculations were performed both boiler and without boiler unit conditions and analyzed.

4. RESULT AND DISCUSSIONS

The results were classified into two parts, with and without boiler cases.According to the inlet and outlet temperatures of each devices, the enthalpy values have been obtained from the thermodynamic tables of R-22

working fluid. Thermodynamic properties and energy values of both with and without boiler unit is given in Table 1 and Table 2 respectively.

Table 1. Thermodynamic properties and energy values for non-boiler unit condition

Point	Component	Temperature (°C)	Pressure (Bar)	Mass flow rate (kg/s)	Enthalpy (kj/kg)	Q (kW)
1	Compressor inlet	14	4.8	0.05151	415.777	21.4167
2	Compressor outlet	98	22	0.05151	459.992	23.6942
2'	Condenser inlet	95	22	0.05151	457.26	23.5535
3	Condenser outlet	43	21	0.05151	253.682	13.0672
3'	Expansion valve inlet	43	21	0.05151	253.682	13.0672
4	Expansion valve outlet	6	4.5	0.05151	253.682	13.0672
4'	Evaporator inlet	6	4.5	0.05151	253.682	13.0672
5	Evaporator outlet	12	4.5	0.05151	414.913	19.6572

Table 2. Thermodynamic properties and energy values for boiler unit condition

Point	Component	Temperature (°C)	Pressure (Bar)	Mass flow rate (kg/s)	Enthalpy (kj/kg)	Q (kW)
1	Compressor inlet	12	4.5	0.03878	414.913	16.089
2	Compressor outlet	90	22	0.03878	452.289	17.5383
2'	Boiler inlet	90	22	0.03878	452.289	17.5383
2"	Boiler outlet	43	21	0.03878	405.618	15.7286
2"	Condenser inlet	43	21	0.03878	405.618	15.7286
3	Condenser outlet	35	19	0.03878	243.101	9.42668
3'	Expansion valve inlet	35	19	0.03878	243.101	9.42668
4	Expansion valve outlet	4	6	0.03878	243.101	9.42668
4'	Evaporator inlet	4	6	0.03878	243.101	9.42668
5	Evaporator outlet	8	4	0.03878	413.048	16.0167

Compressor work, evaporator load and condenser load for boiler and non-boiler unit conditions are given in Table 3 by the helping of Table 1 and Table 2 data.

Table 3. Compressor work, evaporator load and condenser load for boiler and non-boiler unit conditions.

Device	W_{comp}	Q_{cond}	Q_{evap}
Boiler	1.449321	8.11164	6.59
Non-Boiler	1.807201	8.32085	6.59

The energy graphics of equipment of boiler and non-boiler unit conditions are shown in Figure 3.
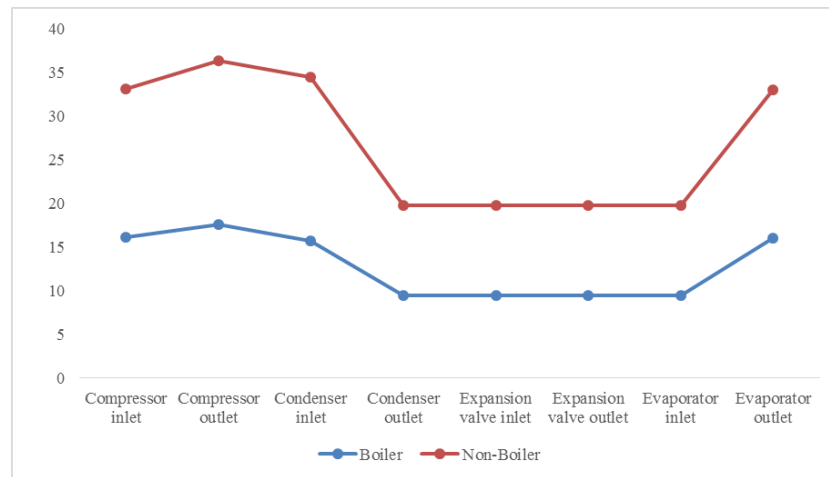
Figure 3. Energy graphics for Boiler and Non-Boiler unit conditions

COP values and operating currents for both conditions are given in Table 4.

Table 4. COP values and currents of systems

Device	COP Values	Current (A)
Boiler	4.54	8
Non-Boiler	3.64	10

It was determined that designed system with boiler unit operated 2A less current what it is compared with the system without boiler unit. From equation 8, it can be calculated that the power of system was decreased about 0.44kW. When the cost of electricity was taken into account, the electricity kW per an hour is 0.139 $ and it can be seen that if the designed system works during 10 hours per a day, the cost of electricity will decrease about 222.04$ per a year.

Moreover, designed system with boiler produce 40°C domestic hot water. When the boiler with 50LT consumes 1.5kW electricity per a day, it can be calculated that designed system with boiler has profits about 75.34$ per a year.

5. CONCLUSIONS

In this study, the boiler unit system was added to split type air conditioner with R22 refrigerant and the experimental results were analyzed thermodynamically. The results can be listed as follows;

- Using the boiler unit, the COP of the system was increased from 3.64 to 4.54.

- Compressor work and condenser load were decreased using boiler unit. Thus, the more efficient working condition was obtained.

- The operating current was decreased about 2A by means of boiler system.

- City water entered the boiler system about 10°C and exited from boiler about 40°C. Thus, domestic hot water at 40°C was produced without another energy sources.

- The consumed electricity of the system was decreased and the cost of electricity about 296.48$ as well.

REFERENCES

[1]. T. Menlik, A. Demircioğlu, and M.G. Özkaya, "Energy and Exergy Analyses of R22 and its Alternatives R407c and R410a in a Vapor Compression Refrigeration System", *Journal of Exergy,* vol. 12 (1), pp. 11-30, 2013.

[2]. R. Saidur, H.H. Masjuki and M.Y. Jamaluddin, "An application of energy and exergy analysis in residential sector of Malaysia", *Energy Policy,* vol. 35, pp. 1050–1063, 2007.

[3]. A. Ergün, T. Menlik, T. and M.G. Özkaya, "Energy and Exergy Analyses of the Heating System in a Multipurpose Building", *Gazi Journal of Engineering Science*, vol. 1, pp. 195-218, 2015.

[4]. A. Ergün, T. Menlik, T. and M.G. Özkaya, "First and Second Law Analysis of Central Cooling System of a Multipurpose Buildings", *International Symposium on Innovative Technologies in Engineering and Science,* vol. 12(A) pp. 1974-1983, Karabuk Turkey. 2014.

[5]. A. Ergün, "Energy and Exergy Analyses of a Shopping Center Which Needs 80.000 M^2 Heating and Cooling", Master Thesis, Gazi University Graduate School of Natural and Applied Sciences, Ankara, 2010.

[6]. P. Martínez, J. Ruiz, C.G. Cutillas, P.J. Martínez, A.S. Kaiser and M. Lucas, "Experimental study on energy performance of a split air-conditioner by using variable thickness evaporative cooling pads coupled to the condenser", *Applied Thermal Engineering*, In press (doi: 10.1016/j.applthermaleng.2016.01.06.) 2016.

[7]. K. Sumeru, S. Sulaimon, H. Nasution and F. N. Ani, "Numerical and experimental study of an ejector as an expansion device in split-type air conditioner for energy savings", *Energy and Buildings,* vol. 79, pp. 98–105. 2014.

[8]. A. S. Padalkar, K.V. Mali and S. Devotta, "Simulated and experimental performance of split packaged air conditioner using refrigerant HC-290 as a substitute for HCFC-22", *Applied Thermal Engineering,* vol. 62, pp. 277-284, 2014.

[9]. D. Kumlutas¸ Z. H. Karadeniz and F. Kuru, "Investigation of flow and heat transfer for a split air conditioner indoor unit", *Applied Thermal Engineering,* vol. 51 pp. 262-272, 2013.

[10]. J. Jia and W.L. Lee, "Experimental investigations on the use of capillary tube and thermostatic expansion valve in storage-enhanced heat recovery room air-conditioner", *Energy and Buildings,* vol. 101, pp. 76–83, 2013.

[11]. J. Jia and W.L. Lee, "Experimental investigations on using phase change material for performance improvement of storage-enhanced heat recovery room air-conditioner", *Energy*, vol. 93 pp. 1394-1403, 2015.

Chelate-Induced Phytoextraction Potential of *Brassica rapa* for Soil Contaminated with Nickel

Aydeniz Demir Delil[1]*, Nurcan Kokeli[1]

[1] *Mersin University, Faculty of Engineering, Department of Environmental Engineering, 33342 Mersin, Turkey*

*Corresponding Author email: aydenizdemir@mersin.edu.tr

Abstract

The aim of present study is to induce for phytoextraction of Ni by Brassica rapa from contaminated soil by application of EDTA. Brassica rapa seeds were planted in pots with Ni concentrations ranging from 0 to 2000 mg/kg in the absence or presence of 10 mg/kg EDTA. After 60 days of growth, Ni concentration of plants were observed. Brassica rapa showed the remarkable resistance to Ni toxicity with no visual toxic symptoms as chlorosis and necrosis. The addition of 10 mg/kg EDTA significantly increased both the plant growth and the Ni concentration, compared with the control. Especially the addition of 10 mg/kg EDTA and 500 mg/kg Ni produced fertilizer effect and maximum dry matter achieved to 1.96 mg/plant from 0.82 mg/plant. While Brassica rapa accumulated 3763 mg/kg Ni in the absence of EDTA, the addition of 10 mg/kg EDTA increased Ni accumulation to 3942 mg/kg Ni at Ni application dose of 2000 mg/kg. Experimental results indicated that Brassica rapa is Ni hyperaccumulator plant (>1000 mg/kg in shoots) both in the absence or presence of EDTA. The bioaccumulation coefficient (BAC) for Ni by Brassica rapa was greater than 1, providing further evidence for the transport of Ni from Ni contaminated soils.

1. INTRODUCTION

There is a great worldwide interest surrounding issues of soil contamination including heavy metals [1]. Soil contamination with Ni has become a worldwide problem [2]. Nickel (Ni) is an important heavy metal in soil and is an essential element required for nitrogen (N) metabolism. Nickel plays a role in the structure and activity of the urease and hidrogenaz enzyme in plants [3]. In recent years, Ni pollution has gained importance due to negative potential impact on agriculture and human health. Nickel contamination mainly results from volcanic eruptions, land fill, forest fire, bubble bursting and gas exchange in ocean, weathering of soils and geological materials, effluent disposal from mining and smelting, fossil fuel burning, vehicle emissions, disposal of household, municipal and industrial wastes, fertilizer application and organic manures [4-6].

Phytoextraction is a non-destructive, cost-effective and safe alternative to conventional clean up techniques of contaminated soils with heavy metals such as Ni [7].

Phytoextraction is either a continuous (natural) process (using metal hyperaccumulating plants, or fast growing plants), or an induced process (using chemicals to increase the bioavailability of metals in the soil) [8].

The success of phytoextraction, either natural or chemically assisted, is largely determined by plant biomass, metal concentration in the plant tissue, and the phytoavailable fraction of metals in the rooting medium [9]. Researchers initially applied hyperaccumulator plants to clean metal polluted soils. However, many such plants

have limited utility for phytoremediation, because of their slow growth, difficult propagation, seasonal growth, and low biomass [2]. Then, chelates such as EDTA, hydroxy ethylethylenediaminetriacetic acid (HEDTA), and ethylenebis-2(o-hydroxyphenyl) glycine (EDDHA) are used to enhance the phytoextraction of a number of metal contaminants including cadmium (Cd), chromium (Cr), cooper (Cu), lead (Pb), zinc (Zn) and Ni.

This chelate-assisted accumulation of toxic quantities of metal in a non-accumulator species is termed "chelate-induced hyperaccumulation" [10]. Chelate-induced phytoextraction is an innovative technique for cleaning metal contaminated soil [11]. Ethylenediaminetetraacetic acid is the most effective chelating agent for chelate-induced hyperaccumulation because it has a strong chelating ability for different metals and increases the bioavailability and uptake of metals in the plant from soil [11-12]. Several researchers have screened on chelate-induced hyperaccumulation of some fast-growing, high-biomass-accumulating plants, including agronomic crops, for their ability to tolerate and accumulate metals in their shoots [13]. Huang *et al.* [10] reported a 1000-fold increase of Pb in in agronomic crops such as corn (*Zea mays* L.) and pea (*Pisum sativum* L.) after HEDTA application in comparison to soil solution of a control (no HEDTA addition). Under these conditions Pb concentrations in the shoots of corn and pea increases from less than 500 mg/kg to more than 10.000 mg/kg within one week after HEDTA application.

Brassica species are well known as metal accumulators and are being used for phytoremediation of contaminated soils. However, the metal tolerance mechanism in the plant still remains unclear [14]. Purakayastha *et al.* [15] reported that in a pot culture experiment, five different species of Brassica (*Brassica juncea, Brassica campestris, Brassica carinata, Brassica napus, and Brassica nigra*) were grown for screening possible accumulators of heavy metals, viz. Zn, Cu, Ni, and Pb. Among all species, *Brassica carinata* showed the highest concentration (mg/kg) as well as uptake (μg/pot) of Ni and Pb at maturity. Grčman *et al.* [16] studied the effect on the uptake of Pb, Zn and Cd by *Brassica rapa* and found that the concentrations of Pb, Zn and Cd in shoots were detected, up to 104.6, 3.2 and 2.3-times as much as that in the control.

In a study performed by Putnik-Delic *et al.* [17] had been determined the biggest concentration of Ni (300 ppm), both in leaf and in stem, was in *B. rapa*, with 64.25 times increase in concentration compared with the control group, and 66.5 times in stem in comparision with the respective control group.

In this study, Ni was choosen as target metal because it is widespread on serpentine rocks and the area in which the study was performed. It is known that serpentine soils are high in several heavy metals (e.g. nickel, cobalt and chromium) and these high heavy metal concentrations are thought, in part, to lead to varying levels of plant adaptation and soil affinities (i.e. endemic vs. non-endemic plant species) [18]. Koleli *et al.* [19] defined common soil formations distinguished in this area as follows: brown forest soils, reddish Mediterranean soils and brown calcareous soils reported that the maximum concentrations of metals in 11 soil samples collected from Mersin-Findikpinari (as dry mass) were 909 mg/kg Cr, 3615 mg/kg Ni, 246 mg/kg Cu, 467 mg/kg Zn, 8.2 mg/kg Cd and 111 mg/kg Pb. As it can be seen from the results, Ni concentration is always higher than the other metals. Because of that reason in this study investigated only nickel.

The objectives of this study were to evaluate the effect of EDTA application on Ni phytoextraction by *Brassica rapa* growing in artificially Ni contaminated soil, and to evaluate EDTA application effects on toxicity symptom, dry matter production, Ni concentration, Ni content and BAC of the plant. *Brassica rapa* is preferred because of its high yield (1.5 tons‑ 4.0 tons per ha) and high oil content of 42-46% [20], resist to soil and climate conditions and efffective root depth is ~1-1. 20 cm.

2. MATERIAL AND METHODS

2.1. Soil Sample and Analysis

Surface soil sample (0-30 cm) was collected from the experimental farm on General Directorate of Agricultural Research, Tarsus-Mersin, Turkey. After collecting soil from the surface (0–30 cm), it was brought to a laboratory, air dried, ground to pass through a 2-mm sieve, and stored in plastic bags for analyses and pot experiments. The some initial physical and chemical properties of the soil used in pot experiment were measured with routine analytical methods. Soil organic matter was determined using the Walkley and Black

method [21]. Soil particle size distribution was estimated by the hydrometer method after pre-treating soil with H_2O_2 and dispersing overnight in sodium hexametaphosphate by the hydrometer method [22]. The carbonate content was determined by a calcimeter method, and the soil pH was measured at 1:1 soil:water ratio [23]. The concentrations of diethylenetriamine pentaacetic acid (DTPA)-extractable Ni were estimated using the method described by [24]. Total Ni concentrations in soil sample were digested according to [25] Anonymous (1995) with aqua regia method using inductively coupled plasma mass spectrophotometer (ICP-MS, Agillent 7500ce). Certified reference material (CRM 7003) was also analyzed in order to control the data quality. All results were given in terms of mg Ni per kg soil. All tests were performed in triplicates.

2.2. Artificial Soil Contamination
Two kg air-dried soils were weighed and loaded into a plastic bags and were contaminated by nickel nitrate $[Ni(NO_3)_2 \cdot 6H_2O]$ salt solution containing 0, 500, 1000, 1500 and 2000 mg Ni kg^{-1} onto it and spread uniformly on plastic sheet. Then, soil was thoroughly mixed to achieve uniformity with respect to metal spiking.

After contamination and mixing, soil was left on plastic sheet and allowed to equilibrate at room temperature for almost three months with frequent and thorough mixing and by adding distilled water to maintain water content in soil at 60% of water-holding capacity and to periodic alternating wetting and air-drying cycles.

2.3. Greenhouse Pot Experiments
Total 4 seeds were planted in plastic pots, each containing 2 kg soil supplemented with increasing supply of Ni (0, 500, 1000, 1500 and 2000 mg/kg soil) in the absence or presence of 10 mg EDTA per kg soil. Ethylendiaminetetraacetic acid was added in the form of Na_2EDTA $(C_{10}H_{14}N_2Na_2O_8 \cdot 2H_2O)$.

A basal treatment of 200 mg/kg N as $Ca(NO_3)_2$ and 100 mg/kg P as KH_2PO_4 was applied to all pots. After germination, the seedlings were thinned to 2 plants per pot. During this 60 days, soils in the pots were kept humid (~80% water holding capacity). After 60 days of growth in the greenhouse, only the shoots of the plants were harvested, and dried at 70 ^{o}C for the determination of dry matter production.

2.4. Plant Sampling and Analysis
The oven-dried shoot samples were first ground and digested using 2 mL 30% H_2O_2 and 5 mL 65% HNO_3 in sealed vessels of a microwave (MarsXpress) apparatus. The digested samples were then analyzed with ICP-MS for Ni. Certified reference materials (*SRM 1573A, SRM 1547*) were also used in order to check the accuracy of the extraction technique used in the study. All analyses were carried out in triplicates, and the results were presented in terms of mg Ni per kg biomass (DW) or μg Ni per plant biomass. In this study, Ni was choosen as target metal because phytoextraction efficiency is related to both plant metal concentration and dry matter yield. Thus, the ideal plant species to remediate a contaminated site should be a high yielding crop that can both tolerate and accumulate the target contaminants [26].

3.   RESULTS AND DISCUSSION

3.1. Some Initial Physical and Chemical Properties of the Soil Used in Pot Experiment

Some physical and chemical properties of the soil used in pot experiment are summarized in Table 1. The greenhouse pot experiments were performed using unpolluted agricultural soils with a clayey loam texture, a pH of 8.1, 26.2% $CaCO_3$ and 1.3% organic matter contents. The analysis of soils for total and DTPA-extractable Ni contents indicates Ni concentrations of 57.0 and 2.2 mg/kg soil, respectively.

In serpentine soils, Ni is not strongly held by clay and Fe-oxyhydroxide surfaces relative to other transition elements; consequently, Ni was more mobile than other metals in the serpentinitic landscape surrounding the study area. The soils derived from serpentine, displayed strong chemical fertility limitations due to a very low Ca/Mg ratio and limited available phosphorus [27]. Therefore, the application rate for 200 mg/kg N as $Ca(NO_3)_2$ and 100 mg/kg P as KH_2PO_4 amended in the study soil.

The total metal contents are much lower than the typical concentration ranges observed for unpolluted soils as set by the "Turkish Soil Contamination and Control Legislation", and were under the critical value (100 mg/kg) according to KabataPendias [28].

Table 1. Some initial physical and chemical properties of the soil used in pot experiment

Parameters	Tarsus Soil
pH (1:2)	8.1
Organic Matter (%)	1.3
$CaCO_3$ (%)	26.2
Particle Size Distribution	
Sand (%)	41
Silt (%)	36
Clay (%)	23
Texture Class	Clay Loam (CL)
Total Ni (mg/kg)	57
DTPA Extractable Ni (mg/kg)	2.2

3.2. Effect of EDTA on Ni Toxicity and Plant Growth

Following Ni application, visual symptoms were also monitored throughout the experiments. The toxicity effects were observed based on plant growth, chlorosis, and necrosis symptoms of the plant. Although *Brassica rapa* did not exhibit any significant symptoms as observed in a typical Ni toxicity including chlorosis and necrosis, increasing Ni application led to a visual reduction in the growth of plants, especially in absence of EDTA. Toxic effects of high concentrations of Ni in plants have been frequently reported as reductions in plant growth and adverse effects on fruit yield and quality ([2], [29]). Plants are known to tolerate metals to some extent, but high concentrations of available metals affect and induce disorders in the plant metabolism [30]. Plants can absorb and distribute metals internally in many different ways and may localize selected metals mostly in leaves and roots [31]. As a mechanism of metal tolerance or accumulation in plants, the response to metal stress is observed in both the leaves and roots. This response and accumulation of metals is more dependent on the type of metal rather than metal concentration [31].Fig. 1 shows the effects of Ni and EDTA application on dry matter production (shoot) after 60 days of growth. Application of 2000 mg/kg Ni decreased dry matter production of *Brassica rapa*. But the addition of 10 mg/kg EDTA significantly increased the plant growth compared with the control. The addition of EDTA promoted an increase in DW by *Brassica rapa*, up to 74% in the shoots. Especially the addition of 10 mg/kg EDTA and 500 mg/kg Ni produced fertilizer effect and maximum dry matter achieved to 1.96 mg/plant from 0.82 mg/plant. EDTA is a synthetic chelator. In this study, it has been studied in fairly low concentration against the possibility of damaging the soil structure. Increases in the doses of EDTA and DTPA applied increased the mobilization of heavy metals; however, environmental risk associated with synthetic chelators is consequently increased regardless of the EDTA and DTPA application rate under such saturation [27]. According to Chaturvedi *et al.* [32] considering the overall plant growth as it is highly essential for efficient phytoextraction we conclude that the low molecular weight organic acids (LMWOAs), such as citric acid, are a better and environmentally compatible alternative to synthetic chelators such as EDTA [32]. When our results are evaluated, we can conclude that EDTA is also used as a kind of plant micronutrient fertilizers. Because pot experiments data showing the effect of 10 mg/kg EDTA on soluble nickel levels at each of the soil concentrations would be benefical. A two-sided t-test with *p*-values less than 0.05 confirmed that the EDTA application had a positive effect on plant growth. The findings obtained were in agreement with the results obtained by Alam *et al.* [33]-[35]. This reduction in yield parameters might be attributed to poor plant development and reduced photosynthesis as a consequence of

reduction in photosynthetic pigments in the leaves of the Ni-treated plants which resulted in suppressed supply of nutrients and photosynthates to the reproductive parts that ultimately affected yield [36].
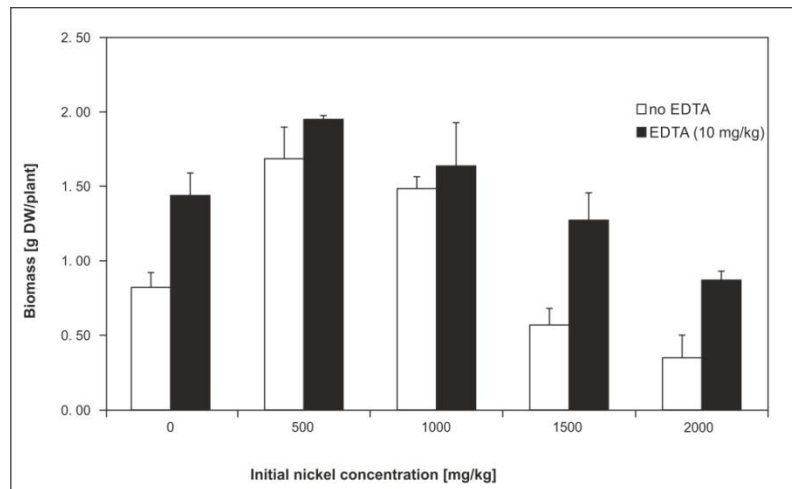

Fig. 1. *Effect of Ni and EDTA on dry matter production (shoot) of Brassica rapa.*

3.3. Effect of EDTA on Ni Concentration in Plant Shoots

The added EDTA remained most effective in increasing Ni accumulation in plants shoots and thus enhanced the phytoextraction [37]. The synthetic chelators EDTA was the most efficient amendments for increasing concentrations of Ni in soil solutions. In the present study, the concentrations of Ni in the soil solutions treated with EDTA were markedly higher than in the control soil.

As seen Figure 2 plots the Ni concentration in shoots in the control treatment and following the application of 0 and 10 mg/kg EDTA. Concentrations of Ni in the shoots of the control *Brassica rapa* varied between 23 and 61 mg/kg. This concentration according to Kabata and Pendias [28] was the pyhototoxic range of Ni (30 and 100 mg/kg). Experimental results indicate that the accumulation of Ni was significantly greater than those of control plants and the strong dependence of Ni concentration on initial Ni dose and EDTA concentration. *Brassica rapa* accumulated more Ni in the presence of EDTA. While *Brassica rapa* accumulated 3763 mg/kg Ni in the absence of EDTA, the addition of 10 mg/kg EDTA increased Ni accumulation to 3942 mg/kg at Ni application dose of 1500 mg/kg. (Fig.2) Experimental results indicated that applying 10 mg/kg EDTA could significantly increase the concentrations of Ni in the soil solution and remarkably enhance Ni accumulation in the shoots of *Brassica rapa*.

The addition of 10 mg/kg EDTA increased Ni uptake in the shoots from 61 mg/kg in the control to 3942 mg/kg. Shoots of *Brassica rapa* exceeded the Ni hyperaccumulation threshold value (>1000 mg/kg) according to the criteria described by [38]. Experimental results indicated that *Brassica rapa* is Ni hyperaccumulator plant (>1000 mg/kg in shoots) (Fig. 2). Nickel concentrations are >1000 mg/kg in shoots both the absence and presence of EDTA which these result confirm Ni hyperaccumulator of *Brassica rapa.* This result was higher than value reported Wenzel *et al.* [39] for *Brassica rapa*. Authors found that chelate effects were significant in the order EDDS > EDTA, control for *Brassica rapa and* EDDS enhanced only Ni content up to 10 mg/kg in *Brassica rapa* [40].

Chelating agents such as EDTA had positive effects on the enhancement of the bioavailability of heavy metals in soils, thereby increasing the amount of metals accumulated in the plants [41-43].

The amounts of metal removed from the soil via phytoremediation are affected by different factors. One important factor controlling the amount of Ni removed through phytoremediation is distribution of chemical

forms of this metal in the soil. As the proportion of Ni in insoluble forms increased, the amount of Ni removed via phytoremediation decrease [44]. The increase in Ni accumulation by plants can be explained through the formation of highly soluble and less toxic Ni-EDTA complexes. This finding is in agreement with the results obtained by Barona *et al*. Panwar *et al*. [45-46]. Nascimento *et al*. [47] reported that EDTA increased Ni concentration in plant shoots to maximum and is confirmed by high concentration of AB-DTPA-extractable Ni in the soil in EDTA treatment; this could be due to greater stability constants of Ni-EDTA.

Some investigations have used the *Brassica* species for phytoremediation of sites contaminated with heavy metals [11,14, 48]. But they have not examined the use of EDTA, to increase plant phytoextraction capacity. Kumar et al. [48] tested many fast growing Brassicas for their ability to tolerate and accumulate metals, including Indian mustard (*Brassica juncea*), black mustard (*Brassica nigra* Koch), turnip (*Brassica campestris* L.), rape (*Brassica napus* L.), and kale (*Brassica oleracea* L). Although all *Brassicas* accumulated metal, *Brassica juncea* showed a strong ability to accumulate and translocate Cu, Cr (VI), Cd, Ni, Pb, and Zn to the shoots. Kos *et al*. [49] studied that the Pb, Zn and Cd phytoextraction potential of 14 different plants including *Brassica rapa* was assessed in a chelate (as EDTA and ethylenediamine-disuccinic acid (EDDS) induced phytoextraction experiment. But they no study has been performed on this plant species to show whether the EDTA could efficiently improve its phytoextraction in Ni contaminated soil [6] (Muhammad *et al.* 2009). Statistical analysis (two-sided t-test) ($p < 0.05$) indicates that the differences obtained for Ni concentration in the absence and presence of EDTA are statistically significant.
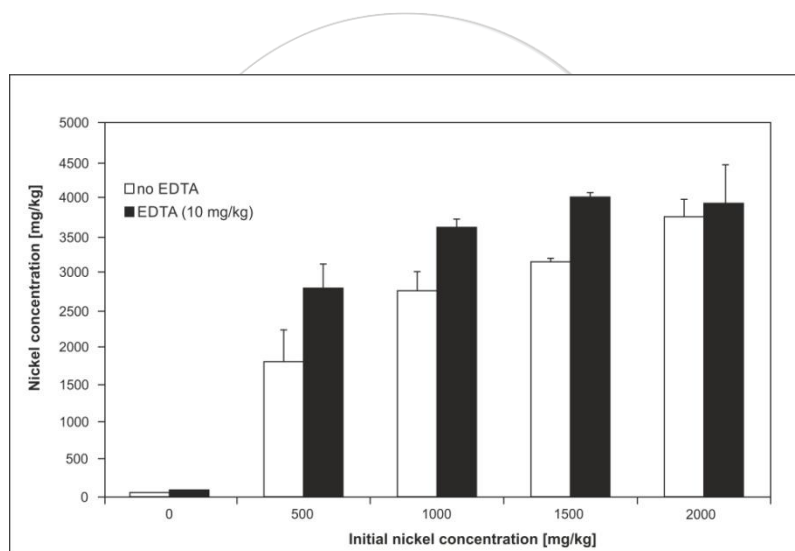

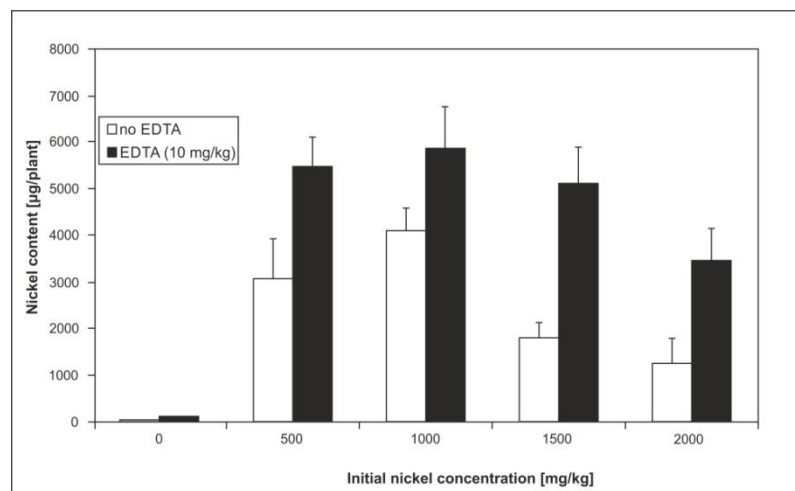**Fig. 2.** *Effect of Ni and EDTA on shoot Ni concentration (mg/kg) of Brassica rapa.*

3.4. Effect of EDTA on Ni Content in Plant Shoots

Plant Ni content (µg/plant) was calculated as dry weight (mg/plant) multiplied by Ni concentration (mg/kg). The maximum Ni content by *Brassica rapa* was 4111 µg per plant in the absence of EDTA, the addition of 10 mg/kg EDTA increased Ni uptake to 5878 µg per plant at an initial Ni application of 1000 mg/kg. Wenzel *et al.* [39] (2003) reported that overall extracted mass per plant varied between 7and 50 µg in the control, between 29 and 135 µg in the EDTA treated pots, which were not consistent with the our study. The enhanced Ni accumulation in the presence of EDTA indicates the formation of less toxic Ni-EDTA complexes, which led to an increase in plant growth. Nickel content by plants reached a maximum at an initial Ni application of 1000 mg/kg, and then decreased sharply with increasing initial Ni level due to the fact that excess Ni reduced the biomass of plant (Fig. 1), thereby decreasing the amount of Ni accumulation. EDTA at selected concentration (10 mg/kg) increased uptake of the heavy metals from the soils it also resulted in low plant biomass. Greater biomass production is a desired parameter for plants being used for phytoextraction so that these plants can extract more amounts of heavy metals from the soil. A decrease in biomass production might be due to

increased metal uptake because of the destruction of the physiological barrier by these acids in roots, which controls the uptake of solutes [37] (Sabir *et al.* 2014). In a study carried out Wu *et al.* [26] has shown EDTA increased shoot Cu and Pb concentrations in Indian mustard (*Brassica juncea*) plants growing in the soil. There were no visible symptoms of heavy metal toxicity in Indian mustard during germination and growth. However, 2–4 days after EDTA addition into the soil there were numerous brown dots on the leaves, and the whole leaf became yellow and died slowly, indicating phytotoxicity of EDTA metals [26].

These findings are consistent with the results of present study. In our study, after Ni content in plants reached 1000 mg/kg, it was observed that biomass of plant was decreasing sharply with increasing initial Ni concentration.

The correlation analyses were performed between Ni content and the plant growth and correlation was much stronger ($r > 0.95$, $p < 0.01$). This strong correlation can be explained through much higher affinity of *Brassica rapa* to accumulate Ni species as shown in Fig. 3. The enhanced Ni accumulation in the presence of EDTA indicates the formation of less toxic Ni-EDTA complexes, which led to an increase in plant growth (Fig. 1), thereby increasing both Ni tolerance and capacity for Ni transport to the shoot [50].

Fig. 3. *Effect of Ni and EDTA on Ni uptake by Brassica rapa plotted in terms of initial nickel dose versus shoot Ni content (µg/plant).*

According to Laurie *et al*. [51] and Molas and Baran [35], there are mainly two different patways for the uptake of metal ions from contaminated soils. The first path involves the transport of free metal ion (M^{2+}) to cell root across plasmalemma following the dissociation of metal-ligand complex in the diffuse layer. The second pathway, on the other hand, involves the absorption of metal-ligand complex by root cell membrane where the metal-ligand complex is either transported to root cells across plasmalemma, or dissociated in the cell membrane; free metal is then transported to cell, and the ligand goes back to solution [52] (Wang *et al.* 2007). Here, the increase in Ni uptake in the presence of EDTA may be explained through a mechanism similar to the second pathway mentioned above. Molas and Baran [35] suggests that Ni is absorbed by plants in the form of a free ion rather than a Ni-ligand complex.

3.5. Biological accumulation coefficient (BAC)
In addition to total Ni concentration and content, the BAC needs to be considered while evaluating hyperaccumulators. The BAC commonly used commonly to evaluate metal accumulating capacity of plants relative to the degree of soil contamination [53]. According to the criteria described by Brooks [38] to define hyperaccumulators, bioaccumulation coefficient (ratio of metal concentration in plant to soil) is greater than 1. Biological accumulation coefficient (BAC) was defined as the concentration of heavy metals in plant shoots divided by the heavy metal concentration in soil [BAC = [Metal] $_{shoot}$ / [Metal] $_{soil}$] [54] and indicate the ability of plants to tolerate and accumulate heavy metals.

The bioaccumulation coefficients of Ni in *Brassica rapa* growing in a artifically contaminated soil are shown in Table 2. *Brassica rapa* was between 1.9 and 5.6 for Ni, providing further evidence for the transport of Ni from Ni contaminated soils to plant shoots. Adding 10 mg/kg EDTA significantly increased the bioaccumulation coefficient of Ni in *Brassica rapa* shoots (Table 2). This information confirm also Ni hyperaccumulation of *Brassica rapa.*

Table 2. Bioaccumulation coefficients of Ni in Brassica rapa growing in a artifically contaminated soil

Application (mg/kg)		Bioaccumulation Coefficient
Ni	**EDTA**	
500	0	3.6
1000	0	2.8
1500	0	2.1
2000	0	1.9
500	10	5.6
1000	10	3.6
1500	10	2.7
2000	10	2.0

4. CONCLUSION

Greenhouse experiment was carried out to evaluate the potential for phytoextraction of Ni, with or without with the use of EDTA. Nickel hyperaccumulation was defined by [38] Brooks *et al.* (1989) as the accumulation of at least 1000 mg/kg Ni in the dry biomass of plants grown on a natural substrate. As indicated in the results, the pot experiment conducted with contaminated soils indicated that *Brassica rapa* had the capability to accumulate high levels of Ni. Ethylenediaminetetraacetic acid is a good chelating agent for enhancing phytoextraction of Ni by *Brassica rapa,* especially when 10 mg/kg EDTA is applied, because it exceeded the threshold value (1000 mg/kg) as a Ni hyperaccumulator [11, 55-56] (Baker and Brooks 1989; Alkorta *et al.* 2004; Gupta *et al.* 2011). Moreover, the BAC value were 1.9 and 5.7, respectively, which were higher than 1 with or without with the use of EDTA. Therefore, *Brassica rapa* might be useful for the remediation of soil contaminated with Ni. Since *Brassica rapa* is fast and easy growing a agronomic crop plant. In recent years, *Brassica rapa* is seen as a key and strategic crop for raw material supply in the biodiesel (green diesel) industry throughout the world and Turkey [20,57] (Baydar 2005; Mahasi and Kamundia, 2007). Therefore, the distribution of the accumulated Ni within the plant and whether the transport to *Brassica rapa* seeds of Ni should be also study in the future.

ACKNOWLEDGMENTS

REFERENCES

[1]. S. P. McGrath, E. Lombi, C. W. Gray, N. Calille, S. J. Dunham and F. J. Zhao, Field evaluation of Cd and Zn phytoextraction potential by the hyperaccumulators *Thlaspi caerulescens*and *Arabidopsis halleri*. Environ Poll 141:15-125, 2006.

[2]. C. Chen, D. Huang and J. Liu, Functions and toxicity of nickel in plants: recent advances and future prospects. Clean 37:304–313, 2009.

[3]. I.E. Akinci and U. Caliskan   Effect of Lead on Seed Germination and Tolerance Levels in Some Summer Vegetables. Ecology 19(74): 164-172, 2010.

[4]. M. S. Abdullahi, A. Uzairu , G. F. S. Harrison, M. L. Balaraabe and O. J. Okunola, Comparative study of tomatoes and onions from irrigated farmlands on the bank of river Challawa, kano, Nigeria. Int J Environ Res 2(1): 65- 70, 2007.

[5]. M. S. Abdullahi, A. Uzairu and O. J. Okunola, Quantitative determination of heavy metal concentration in onion leaves. Int J Environ Res 3(2): 271-274, 2009.

[6]. D. Muhammad, F. Chen, J. Zhao, G. Zhang and F. Wu, Comparison of EDTA- and citric acid-enhanced phytoextraction of heavy metals in artificially metal contaminated soil by *Typha angustifolia.* Int J Phytoremediat 11(6): 558-574, 2009.

[7]. G. Garg and S. .K. Kataria, Phytoremediation potential of *Raphanus sativus* (L.), *Brassica juncea* (L.) and *Triticum aestivum* (L.) for copper contaminated soil. E-Proceedings of International Society of System Sciences, Univertity of Queensland, Brisbane (Australia), July 12-17, 2010.

[8]. S. Greipsson, Phytoremediation. Nature Education Knowledge, 2(1): 7, 2011.

[9]. D. Aydin and O. F. Coskun, Effects of EDTA on Cr^{+3} Uptake, Accumulation, and Biomass in *Nasturtium officinale* (Watercress). Ecology 22 (87): 16-23, 2013.

[10]. J. W. Huang, J. J. Chen, W. R. Berti and S. D. Cunningham, Phytoremediation of lead contaminated soils: role of synthetic chelates in lead phytoextraction. Environ Sci Technol 31:800–805, 1997.

[11]. A. Gupta, S. Shaw-Wei and C. Zueng-Sang, Heavy-metal bioavailability and chelate mobilization efficiency in an assisted phytoextraction process by *Sesbania sesban* (L.) Merr, Commun Soil Sci Plant Anal 42 (2): 231-245, 2011.

[12]. D. E. Salt, R. D. Smith and L. Raskin, Phytoremediation. Annu Rev *Plant* Biol 49(1): 643-668, 1998.

[13]. M. N. V. Prasad and H. Freitas, Metal hyperaccumulation in plants-Biodiversity prospecting for phytoremediation technology. Electron J Biotechn 6:275-321, 2003.

[14]. M. Jahangir, I. B. Abdel-Farid, Y. H. Choi and R. Verpoorte, Metal ion-inducing metabolite accumulation
    in *Brassica rapa.* J Plant Physiol. 165(14): 1429-37, 2008.

[15]. T. J. Purakayastha, T. Viswanath, S. Bhadraray, P. K. Chhonkar, P. P. Adhikari and K. Suribabu, Phytoextraction of zinc, copper, nickel and lead from a contaminated soil by different species of Brassica. Int J Phytoremediat 10 (1):61-72, 2008.

[16]. H. Grčman, S. Velikonja-Bolta, D. Vodnik, B. Kos and D. Lestan, EDTA enhanced heavy metal phytoextraction: metal accumulation leaching and toxicity. Plant Soil 235:105–114, 2001.

[17] M. Putnic-Delic, I. Maksimovic, I. Gani-Novakovic, T. Zeremski and A. M. Jeromela, The Effect of Ni on Concentration of The Most Abundant Essential Cations In Several Brassica Species. Jour Nat Sci 126: 15-23, 2014.

[18]. G. A. Meindl, D. J. Bain and T. L. Ashman, Nickel accumulation in leaves, floral organs and rewards
    varies by serpentine soil affinity. AoB PLANTS 6, plu036;, 2014.

[19]. N. Koleli, A. Demir, M. Eke and O. Cakmak, Accumulation of Heavy Metals in Some Plants Grown on Serpentine Soils of Mersin-Turkey. Oral presentation, 2nd International Symposion on Sustainable Development (ISSD'2010), 8-9 June, Sarajevo, 2010, pp. 499-507, ISBN:978-9958-9965-7-3.Sarajevo, 2010.

[20]. M. J. Mahasi and J. W. Kamundia, Cluster analysis in rapeseed (*Brassica napus* L.). Afr J Agric Res 2 (9):409-411, 2007.

[21]. D. W. Nelson and L. E. Sommers, Total carbon, organic carbon, and organic matter. In: Page AL, Miller RH, Keeney DR, eds. Methods of Soil Analysis. Part 2. Chemical and Microbiological Properties. 2nd ed. Madison (WI): Agronomy Monograph, p. 539–577, 1982.

[22]. G. J. Bouyoucos, Hydrometer method improved for making particle size analysis of soil. Agron J 54 (5):466- 465, 1952.

[23]. E. O. McLean, Soil pH and lime requirement. In: Page AL, Miller RH, Keeney DR, eds. Methods of soil analysis. 2nd ed. Madison, (WI): Agronomy Monograph p. 595-624, 1982.

[24]. W. L. Lindsay, and W. A. Norvell, Development of DTPA soil test for zinc, iron, manganese and copper. Soil Sci Soc Am J 42:421–448, 1978.

[25]. Anonymous, Soil quality, extraction of trace elements soluble in aqua regia, DIN ISO 11466, Berlin, Germany, 1995.

[26]. L. H. Wu, Y. M. Luo, X. R. Xing and P. Christie, EDTA-enhanced phytoremediation of heavy metal contaminated soil with Indian mustard and associated potential leaching risk. Agric. Ecosyst. Environ. 102: 307–318, 2004.

[27]. Z. Y. Hseu, Concentration and distribution of chromium and nickel fractions along a serpentinitic toposequence. Soil Sci 171: 341–353, 2006.

[28]. A. Kabata-Pendias, Trace elements in soils and plants. 3nd edition, Boca Raton, USA, 2001.

[29]. H. Daghan and N. Koleli, Comparative Evaluation of Transgenic and Non Transgenic Tobacco for the Phytoextraction of Nickel-Contaminated Soils. Ecology 21(84): 90-97, 2012.

[30]. T. R. Guo, G. P. Zhang, Y. H. Zhang, Physiological changes in barley plants under combined toxicity of aluminum, copper and cadmium. Colloids Surf. B. 57, 182–8, 2007.

[31]. A. R. Memon, D. Aktoprakligul, A. Zdemur and A. Vertii, Heavy metal accumulation and detoxification mechanisms in plants. Turk. J. Bot. 25:111–21, 2001.

[32]. N. Chaturvedi, N. K. Dhal and H. K. Patra, EDTA and citric acid-mediated phytoextraction of heavy metals from iron ore tailings using Andrographis paniculata: a comparative study. Int. J. Min. Reclam. Env. 29(1): 33-46, 2015.

[33]. M. G. M. Alam, S. Tokunaga and F. Stagnitti, Removal of arsenic from contaminated soils using different salt extractants. J Environ Sci Health Part A 42 (4): 447-451, 2007.

[34]. P. M. Kopittke, C. J. Asher and N. W. Menzies, Toxic effects of Ni^{2+} on growth of cowpea (*Vigna unguiculata*). Plant and Soil 292:283-289, 2007.

[35]. J. Molas and S. Baran, Relationship between the chemical form of nickel applied to the soil and its uptake and toxicity to barley plants. Geoderma 122:247-255, 2004.

[36]. M. S. Ahmad, M. Hussain, R. Saddiq and A. K. Alvi, Mung Bean: A nickel indicator, accumulator or excluder? Bull Environ Contam Toxicol 78(5): 319-24, 2007.

[37]. M. Sabir, M. M. Hanafi, M. Zia-Ur-Rehman, H. R. A. Saifullah, K. R. Hakeem and T. Aziz, Comparisonof Low-Molecular-Weight Organic Acids and Ethylenediaminetetraacetic Acid to Enhance Phytoextraction of Heavy Metals by Maize. Commun Soil Sci Plant Anal 45(1): 42-52., 2014.

[38]. R. R. Brooks, Plants that Hyperaccumulate Heavy Metals: Their Role in Phytoremediation, Microbiology, Archaeology Mineral Exploration and Phytomining. CAB International, Wallingford, UK, 380 p, 1998.

[39]. W. W. Wenzel, R. Unterbrunner, P. Sommer and P. Sacco, Chelate assisted phytoextraction using canola (*Brassica rapa* L.) in outdoors pot and lysimeter experiments. Plant Soil 249:83-96, 2003.

[40]. E. Meers, A. Ruttens, M. Hopgood, E. Lesage and F. M. G. Tack , Potential of *Brassica rapa*, *Cannabis sativa*, *Helianthus annuus* and *Zea mays* for phytoextraction of heavy metals from calcareous dredged sediment derived soils. Chemosphere 61:561-572, 2005.

[41]. H. Y. Lai and Z. S. Chen, The EDTA effect on phytoextraction of single and combined metals-contaminated soils using rainbow pink (*Dianthus chinensis*). Chemosphere 60:1062-1071, 2005.

[42]. C. Luo, Z. Shen and X. Li, Enhanced phytoextraction of Cu, Pb, Zn and Cd with EDTA and EDDS. Chemosphere 59:1–11, 2005.

[43]. L. Jean, F. Bordas, C. Gautier-Moussard, P. Vernay, A. Hitmi and J. C. Bollinger, Effect of citric acid and EDTA on chromium and nickel uptake and translocation by *Datura innoxia*. Environ. Pollut. 153: 555-563, 2008.

[44]. B. H. Robinson, R. R. Brooks, P.E. H. Gregg and J. H. Kirkman, The nickel hytoextraction potential of some ultramafic soils as determined by sequential extraction. Geoderma. 87: 293–304, 1999.

[45]. A. Barona, I. Aranguiz and A. Elias, Metal associations in soils before and after EDTA extractive decontamination: implications for the effectiveness of further clean-up procedures. Environ Pollut 113:79-85, 2001.

[46]. B. S. Panwar, K. S. Ahmed and S. B. Mittal, Phytoremediation of nickel-contaminated soils by *Brassica* species. Environ Dev Sustain, 4:1-6.

[47]. C. W. A. Nascimento and B. Xing, Phytoextraction: A review on enhanced metal availabilityand plant accumulation. *Scientia Agriculture* 63, 299–311, 2006.

[48]. N. P. B. A. Kumar, V. Dushenkov, H. Motto and I. Raskin, Phytoextraction: The use of plants to remove heavy metals from soils. Environ Sci Technol 29:1232-1238, 1995.

[49]. B. Kos, H. Grčman and D. Lestan, Phytoextraction of lead, zinc and cadmium from soil by selected plants. Plant Soil and Environ 49(12):548–553, 2003.

[50]. J. Agrawal , I. Sherameti and A. Varma Detoxification of heavy metals: State of art. In: Sherameti I, Varma A, eds. Detoxification of heavy metals. Germany: Springer-Verlag. p.1-34. 2011.

[51]. S. H. Laurie, N. P. Tancock, S. P. McGrath and J. R. Sanders,Influence of complexation on the uptake by plants of iron, manganese, cooper and zinc: II. Effect of DTPA in a multi-metal and computer stimulation study. J Exp Bot 42(4):515–519, 1991.

[52]. H. Wang, X. Shan, T. Liu, Y. Xie, B. Wen, S. Zhang, F. Han and M. Van Genuchten, Organic acids enhance the uptake of lead by wheat roots. Planta 225:1483–1494, 2007.

[53]. M. Rafati, N. Khorasani, F. Moattar, A. Shirvany, F. Moraghebi and S. Hosseinzadeh, Phytoremediation potential of *Populus alba* and *Morus alba* for cadmium, chromium and nickel absorption from polluted soil. Int J Environ Health Res 5(4): 961-970, 2011.

[54]. Y. Q. Zu, Y. Li, J. J. Chen, H. Y. Chen, L. Qin and C. Schvartz, Hyperaccumulation of Pb, Zn and Cd in herbaceous grown on lead-zinc mining area in Yunnan, China. Environ Int 31: 755-762, 2005.

[55]. A. J. M. Baker and R. R. Brooks, Terrestrial higher plants which hyperaccumulate metallic elements-a review of their distribution, ecology and phytochemistry. Biorecovery 1:81-126, 1989.

[56]. I. Alkorta, H. Hernandez-Allica, J. M. Becerril, I. Amezaga, I. Albizu and C. Garbisu, Recent findings on the phytoremediation of soils contaminated with environmentally toxic heavy metals and metalloids such as zinc, cadmium, lead, and arsenic. Rev Environ Contam Toxicol 3:71–90, 2004.

[57]. H. Baydar, Yield and quality properties of canola (*Brassica rapa* L.) cultivars under Isparta condition. Dissertation, University of Suleyman Demirel, 2005.

PSIM Simulation of Flyback Converter for P&O and IC MPPT Algorithms

Harun Ozbay[1]*, Akif Karafil[1], Selim Oncu[2], Metin Kesler[3]

[1]*Bilecik Seyh Edebali University, Department of Electric, Vocational High School, 11210, Bilecik, Turkey.*
[2]*Karabuk University, Department of Electrical&ElectronicsEngineering, EngineeringFaculty, 78050, Karabuk, Turkey.*
[3]*Bilecik Seyh Edebali University, Department of ComputerEngineering, EngineeringFaculty, 11210, Bilecik, Turkey.*
*CorrespondingAuthor email: harun.ozbay@bilecik.edu.tr

Abstract

The output power of PV panels varies continuously depending on some environmental factors such as temperature, shading and solar radiation level and load conditions. PV panels have a nonlinear characteristic since they have different output power at different operating points. Therefore, dc-dc converters are required between PV panels and load to obtain the maximum power from the panels. In this study, the simulation of the flyback converter for two most commonly used MPPT algorithms specifically Perturb and Observe (P&O) method and Incremental Conductance (IC) method are achieved in PSIM and performance of the control techniques are compared. The simulation results of P&O and IC MPPT algorithms are compared for different solar radiation conditions.

1. INTRODUCTION

Electric energy demand has been increasing recently due to the increasing population and industrialization. However, a great part of the electric energy has been met by fossil fuels such as oil and coal. Renewable energy sources have gained importance since the fossil fuels give harm to the environment and they will be exhausted in the near future. Among the renewable energy sources solar energy has been more attractive since it is clean, free and infinite [1, 2]. Among the renewable energy sources, the solar energy has gained popularity for energy demand recently and has been prompted. Therefore, the costs have reduced and studies in this field have increased. Although generating energy using PV panels has many advantageous, the efficiency of the panels is low depending on some environmental factors such as temperature, radiation level, shading, and dirt. Therefore, it becomes important to extract maximum power from PV panels by MPPT dc-dc converter [3].

In literature, many MPPT techniques are used to determine the maximum power point (MPP). Some of these MPPT techniques are fractional open circuit voltage, fractional short circuit current, perturb and observe, incremental conductance, lookup table method, neural network and fuzzy logic controller. Fractional open circuit voltage and short circuit current methods adopt approximation methods. However, these methods give low accuracy at MPP. On the other hand, a large database is needed for some MPPT techniques such as lookup table method, neural network and fuzzy logic. However, this increases the implementation complexity of the system. P&O and IC techniques are among the most used MPPT techniques. These methods are simple, high efficient, panel independent and provide high accuracy at MPP [4, 5].

In literature, some flyback converter applications with P&O MPPT method [6, 7], artificial neural network (ANN) P&O MPPT method [8] and IC MPPT method [9] have been studied. In the study, two most common used MPPT algorithms specifically P&O and IC methods are compared for flyback converter in PSIM.

2. FLYBACK CONVERTER

Figure 1 shows the PSIM simulation schematic of the flyback converter. The circuit consists of a power switch (S_1), transformer (1:n), magnetizing inductor of the transformer (L_m), rectifying circuit (D), output filter capacitor (C) and load resistance (R_o) [10]. PV panel (Perlight PLM-100P/12) with 100 W maximum power is modeled at PSIM for the simulated flyback converter. Six PV panels are connected in series and total 600 W power is obtained. The standard test conditions for the PV panel are as follows: 17.7 V maximum voltage and 5.65 A maximum current. The flyback converter parameters: L_m 0.3 mH, C 10 µF, R_o 400 Ω and transformer turns ratio 1:4. The switching frequency is determined as 50 kHz.
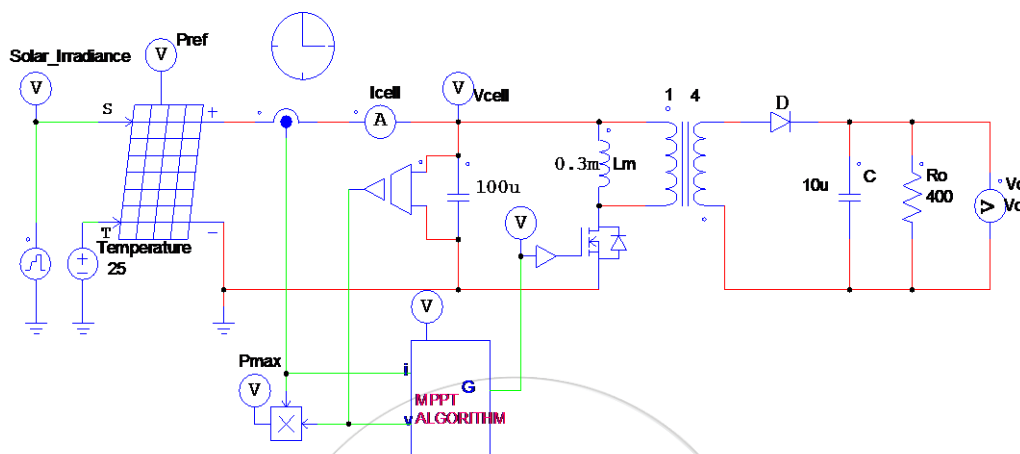

Figure 1.PSIM simulation schematic of the flyback converter

3. MPPT ALGORITHM METHODS

Load resistance must be equal to the optimal resistance in order to track the maximum power point. However, it is difficult to determine a fixed load corresponding this value. Therefore, a dc-dc converter is connected between PV panel and load to transfer maximum power from PV panel. The system is called as maximum power point tracking [11].

In literature, many MPPT techniques are used to determine maximum power point (MPP). P&O and IC methods are the most widely used MPPT techniques due to simplicity and low cost. However, in all MPPT techniques MPP is determined by changing the duty ratio (D) of the dc-dc converter [12].

3.1. P&O Method

P&O method is one of the most frequently used MPPT methods due to its simplicity, practicality and high efficiency. Moreover, the most important advantage of the method is that it is independent from some factors such as PV characteristic, temperature and radiation level in achieving MPP [13]. In P&O method, PV panel power is measured and compared with the previous one. If the power increases, perturbation direction is not changed. Otherwise, perturbation direction is reversed. Therefore, the operating point of the system moves towards MPP and oscillates around MPP under steady state conditions [14]. P&O simulation block diagram is shown in Figure 2.
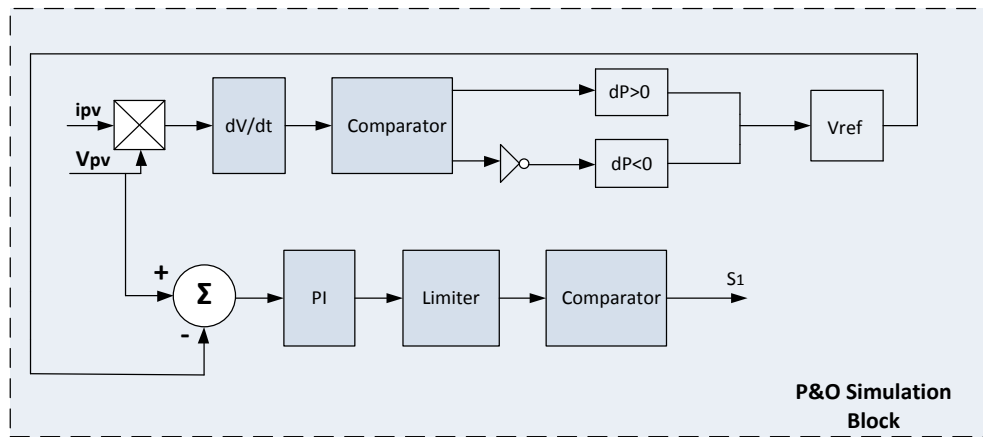
Figure 2. P&O simulation block

3.2. IC Method

Instantaneous voltage is adjusted according to MPP voltage in incremental conductance (IC) method. MPP voltage is dependent on incremental and instantaneous voltage of the PV panel. The principle of the method is that voltage-power characteristic curve of the PV panel is zero at MPP (dP/dV=0), greater than zero on the left of MPP (dP/dV>0), and smaller than zero on the right of MPP (dP/dV<0). Power-voltage characteristic showing the operating principle of IC method is given in Figure 3.
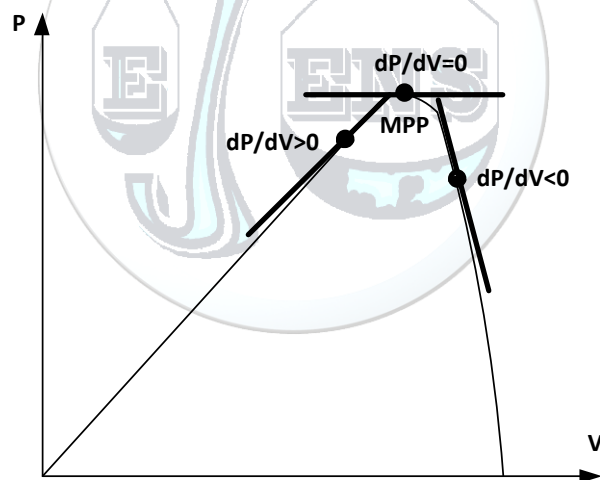
Figure 2. The operating curve of IC method

IC simulation block diagram is shown in Figure 4. The voltage and current values are used in IC block as input. The changes in voltage are converted into absolute value and the values are feedback to the positive input terminal of the comparator. If dV is not equal to zero, logic 1 will be the output. Otherwise, logic 0 will be the output. Therefore, it is determined whether dI is greater or lower than zero. In the third comparator it is determined whether dI/dV>-I/V or dI/dV<-I/V or not. Input logic combination activates Vn+K or Vn-K. So, the desired switching is provided by adding K to Vn or subtracting K from Vn [15, 16].
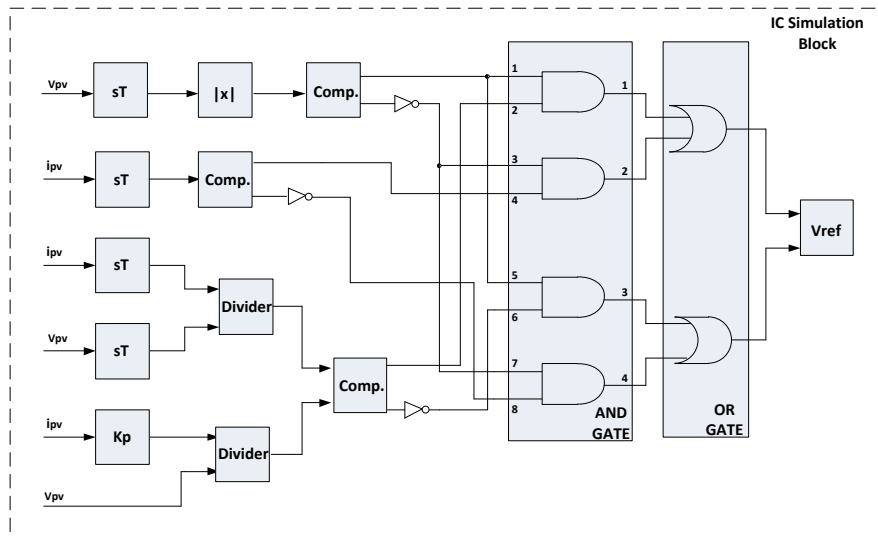
Figure 3. IC simulation block

4. SIMULATION RESULTS AND DISCUSSIONS

In the simulation, ramp and step inputs are applied to the input of solar radiation terminals to provide rapidly changing and slowly changing climate conditions. The simulation total time is 1 s. Solar radiation level is changed from 600 W/m^2 to 1000 W/m^2. The temperature terminal input remains constant at 25 °C in the simulation. Rapidly and slowly changing climate conditions are shown in Figure 5.

Figure 4. Rapidly and slowly changing radiation

The same standard environmental conditions are applied to compare the performance of P&O and IC MPPT algorithms. In Figure 6, P&O and IC MPPT algorithms tracking the maximum power point of PV panels are shown.

Figure 6. (a) P&O MPPT algorithm   (b) IC MPPT algorithm

Figure 7 and 8 show the rapidly changing radiation effect on P&O and IC MPPT performance, respectively.
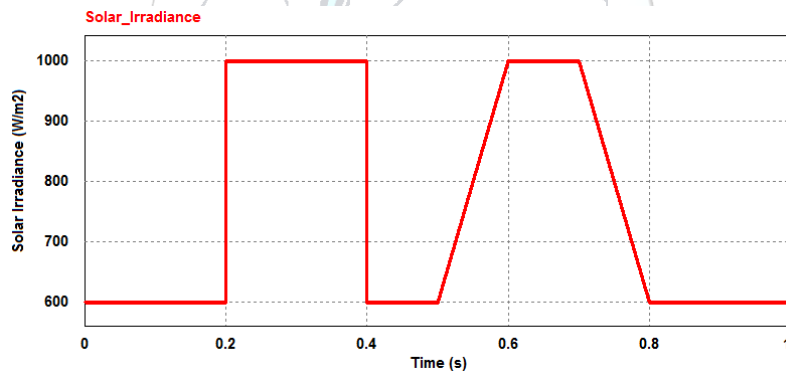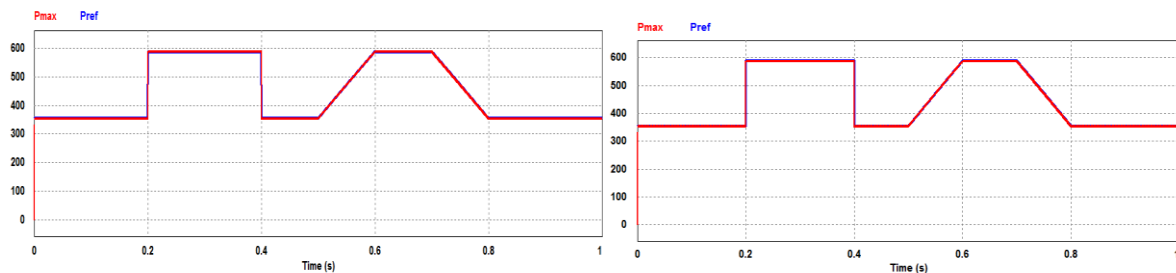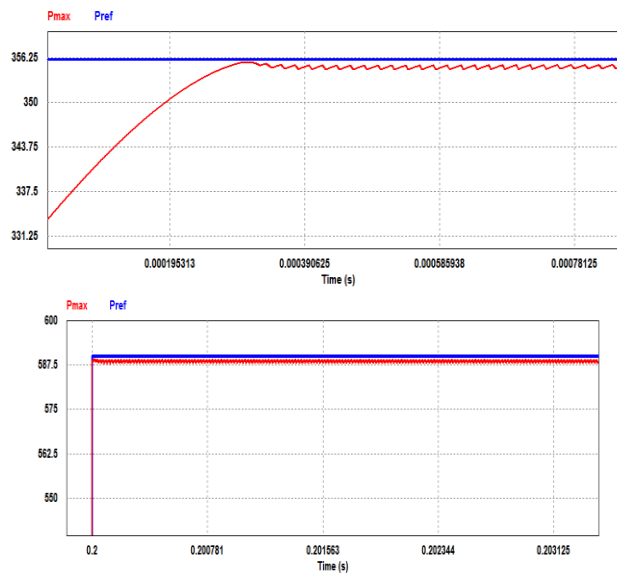

Figure 5. Zoomed window of P&O MPPT oscillations
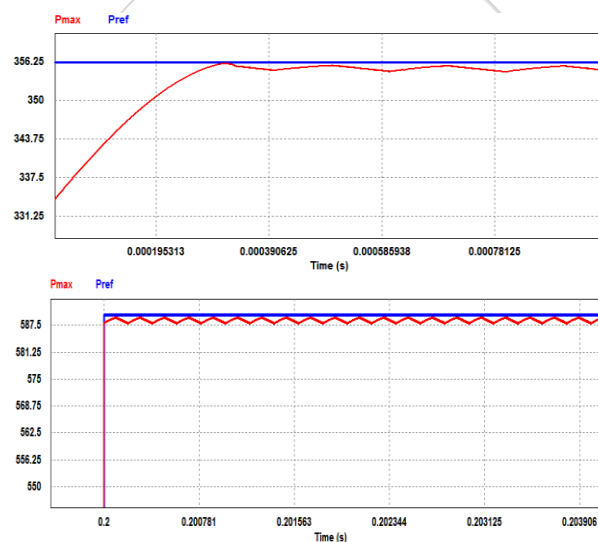
Figure 6. Zoomed window of IC MPPT oscillations

It can be concluded from the zoomed window Figure 7. showing the rapidly changing radiation that P&O oscillates around MPP resulting in some power losses. On the contrary, no such oscillations occur in IC algorithm. Moreover, P&O algorithm cannot find the new MPP quickly when radiation level changes rapidly. This is the main drawback of the P&O algorithm. IC algorithm finds the new MPP more accurately under rapidly changing radiation level. However, P&O MPPT is most commonly used due to its simplicity.

5. CONCLUSION

This paper presents the comparison of P&O and IC MPPT algorithms using PSIM simulation of the flyback converter under rapidly and slowly changing solar conditions by using PSIM. No significant differences are observed for P&O and IC MPPT algorithms when the climate changes slowly. However, IC algorithm finds the MPP quickly under rapidly changing climate conditions. Moreover, no additional oscillation occurs around MPP in IC algorithm. Therefore, it can be concluded that IC algorithm gives better results under rapidly changing climate conditions.

ACKNOWLEDGMENT

REFERENCES

[1]. M. Obi and R. Bass, "Trends and challenges of grid-connected photovoltaic systems–A review,"*Renewable and Sustainable Energy Reviews*, vol. 58, pp. 1082-109, 2016.
[2]. T. K. Soon and S. Mekhilef, "A fast-converging MPPT technique for photovoltaic system under fast-varying solar irradiation and load resistance,"*IEEE Transactions on Industrial Informatics,*vol. 11, no. 1, pp. 176-186, Feb. 2015.
[3]. H. T. Duru, "A maximum power tracking algorithm based on I mpp= f (P max) function for matching passive and active loads to a photovoltaic generator,"*Solar Energy*, vol. 80, no. 7, pp. 812-822, 2006.
[4]. H. Bounechba, A. Bouzid, H. Snani, and A. Lashab, "Real time simulation of MPPT algorithms for PV energy system,"*International Journal of Electrical Power & Energy Systems*, vol. 83, pp. 67-78, 2016.
[5]. Q. Zhang, C. Hu, L. Chen, A. Amirahmadi, N. Kutkut, Z. J. Shen, and I. Batarseh, "A center point iteration MPPT method with application on the frequency-modulated LLC microinverter,"*IEEE Transactions on Power Electronics*, vol. 29, no. 3, pp. 1262-1274, 2014.
[6]. Mohammad B. Shadmand, Robert S. Balog, and Haitham Abu Rub, "Maximum Power Point Tracking using Model Predictive Control of a flyback converter for photovoltaic applications," *Power and Energy Conference at Illinois (PECI)*,2014, pp. 1-5.
[7]. Y. H. Kim, J. G. Kim, Y. H.Ji, C. Y. Won, and T. W. Lee, "Flyback inverter using voltage sensorless MPPT for AC module systems,"in *Power Electronics Conference (IPEC), 2010 International IEEE*, 2010, pp. 948-953.
[8]. P. Konghuayrob and S. Kaitwanidvilai,"Maximum Power Point tracking using neural network in flyback MPPT inverter for PV systems,"in *Soft Computing and Intelligent Systems (SCIS) and 13th International Symposium on Advanced Intelligent Systems (ISIS), 2012 Joint 6th International Conference on IEEE*, 2012, pp. 1504-1507.
[9]. J. Beopjun, N. Hyunjun, C. Yeonok, M. Euna, and C. GeumBae, "IncCond MPPT control using flyback converter," in *Electrical Machines and Systems (ICEMS), 2013 International Conference on IEEE*, 2013, pp. 357-361.
[10]. Z. Housheng, "Research on MPPT for Solar Cells Based on Flyback Converter," in *Intelligent Computation Technology and Automation (ICICTA), 2010 International Conference on IEEE*, 2010, vol. 3, pp. 36-39.
[11]. H. Rezk and A. M. Eltamaly, "A comprehensive comparison of different MPPT techniques for photovoltaic systems,"*Solar Energy*, vol. 112, pp. 1-11, 2015.
[12]. D. Ouoba, A. Fakkar, Y. El Kouari, F. Dkhichi, and B. Oukarfi,"An improved maximum power point tracking method for a photovoltaic system,"*Optical Materials*, vol. 56, pp. 100-106, 2016.
[13]. T. Esram and P. L. Chapman, "Comparison of photovoltaic array maximum power point tracking techniques,"*IEEE Transactions on Energy Conversion EC*, vol. 22, no. 2, pp. 439, 2007.
[14]. B. Subudhi and R. Pradhan, "A comparative study on maximum power point tracking techniques for photovoltaic power systems,"*IEEE transactions on Sustainable Energy*, vol. 4, no. 1, pp. 89-98, 2013.
[15]. N. I. Natasha, W. T. Bhuiyan, and M. A. Razzak, "Implementation of Maximum Power Point Tracking in a photovoltaic inverter using Incremental Conductance technique,"in *Electrical and Computer Engineering (ICECE), 2014 International Conference on IEEE*, 2014, pp. 329-332.
[16]. H. Zheng, S. Li, K. Bao, and D. Zhang,"Comparative study of maximum power point tracking control strategies for solar PV systems,"in *Transmission and Distribution Conference and Exposition (T&D), 2012 IEEE PES IEEE*, 2012, pp. 1-8.

Isotherm and Kinetic Modelling of Azo Dyes Adsorption

Onur Isik[1], Ibrahim Demir[1], Ahmet Yuceer[2], Ozer Cinar[3*],

[1]Department of Environmental Engineering, Istanbul Technical University, 34469, Maslak/Istanbul, Turkey.

[2]Department of Environmental Engineering, Cukurova University, 01330, Saricam/Adana, Turkey.

[3*] Department of Environmental Engineering,Yildiz Technical University, 34220, Esenler/Istanbul, Turkey.
*Corresponding Author email: ocinar@yildiz.edu.tr

Publication Info

Abstract

Textile and dye industries' wastewaters are one of the major problem in the water pollution. This wastewater causes serious environmental pollution, because of non-biodegradable and toxic dye molecules. Azo dyes are widely used in the textile industry. In the anaerobic condition azo dyestuff decompose to toxic byproducts. The aim of this work is to understand the adsorption mechanisms of various azo dyestuff adsorbed by domestic wastewater treatment plant inactivated sludge. To determine the adsorption mechanisms, various isotherms and kinetics were used and constants of each isotherms and kinetics were calculated for each dyestuff. In this study, Reactive Black 5 (RB5), Reactive Blue 21 (RB21), Acid Brown 283 (AB283) and Basic Violete 3 (BV3) azo dyestuff adsorption data were used for isotherms and kinetics calculations. The results of this study showed that, the best isotherm which describe the adsorption process was Freundlich. This isotherm model assumes that heterogeneous sorption occurs on adsorbent surface, stated in other words adsorption power varies at every sorption point. For RB5 and AB283 dyes, the best kinetic model which describe the adsorption process was pseudo-second-order kinetic model. This kinetic model assumes that adsorption rate dependent to adsorbent material quantities and contact time.

Keywords

Azo Dyes, Dyestuff Adsorption, Equilibrium Isotherms and Kinetic Models

1. INTRODUCTION

Dye manufacturing is a large industry. There are more than 100,000 commercially available dyes in the world trade market [1].It is estimated that approximatively 1 million tones dyestuff produced annually, and 20-25% of these produced dyestuff is discharged to the receiving environment as waste [2]. Furthermore, Dyes are widely used in many industries, such as textile, packaging industry, automotive industry, food industry, etc. These industries colored wastewaters are caused serious aesthetic and environmental problems. The colored substances prevent the passes of the sun ray into the water. So that, photosynthetic reactions are reduced [3]. Dyes can cause mutagenic and carcinogenic effects on living organisms. At that, dyes can affect brain, central nervous, reproduction system, and organs such as kidney, lung, liver, etc. [4]. The majority of the synthetic dyes are resistant to biological degradation, because of its' complex structures, such as azo dyes [5]. Azo dyes have at least one double bounded nitrogen (N=N), and these dyes are named according to the number of double bounded nitrogen pairs. Azo dyes which have one double bound nitrogen molecules are called monoazo, and azo dyes which have 2 or 3 double bound nitrogen molecules are called diazo or triazo dyes [6].In the anaerobic conditions, azo dyes are degraded to colorless and toxic aromatic amines [7]. Many physical, chemical and biological techniques have been developed for dye removal. Adsorption is one of the most important techniques for dye removal. Many adsorbents have been as scientifically or commercially tested for dye removal. Peat, activated sludge, coir pith, waste organic peel, tree fern, red mud and minerals can bered given as examples for these adsorbents [8,9,10,11,12,13,14,15]. Biological activated sludge systems are one of the most common treatment method for colored wastewaters, particularly textile industries wastewater treatment [16].

One of the dye remove mechanisms that occur in activated sludge system is adsorption. Adsorbable substances can transferred into the cell, and take a part in metabolic / co-metabolic activities. In this reason, studies on adsorption of dyestuff with activated sludge, and understand of the adsorption mechanisms of dyestuff is important for colored wastewater treatment [9]. Isotherms and kinetic models are important to understand the adsorption mechanisms, identify optimum operation conditions, and design effective treatment systems.

The aim of this work is to understand the adsorption mechanisms of various azo dyestuff adsorbed by domestic wastewater treatment plant inactivated sludge.

2. MATERIAL AND METHOD

In this paper, some isotherms and kinetics used to understand Reactive Black 5 (RB5), Reactive Blue 21 (RB21), Acid Brown 283 (AB283) and Basic Violete 3 (BV3) azo dyestuff adsorption mechanisms by domestic wastewater plant inactivated sludge.

Table 1. RB5, RB21, AB283, and BV3 dyes properties

ColorIndex	RB5	RB21	AB283	BV3
Type	Anionic	Anionic	Anionic	Cationic
Chemical Property	Reactive	Reactive	Acidic	Basic
Chromophore Group	Azo	Azo	Azo	Azo
CAS	17095-24-8	12236-86-1	12219-66-8	42555
Molecular Weight	991.82	377.43	882.25	407.99
Molecule Formula	$C_{26}H_{21}N_5Na_4O_{19}S_6$	$C_{18}H_{15}N_7OS$	$C_{32}H_{19}CrN_8O_{11}S.H.Na$	$C_{25}H_{30}ClN_3$
λ_{maks}	579	626	328	590

The adsorption data used in the modeling was taken from a MS. Thesis of the year 2014 [17]. The material and method part can be stated in this MS. Thesis. To sum up, adsorption experiments were performed at room temperature, and the study was conducted at different concentrations of initial dye concentrations.

3. RESULT AND DISCUSSION

3.1. Adsorption Isotherms

Adsorption isotherms demonstrate adsorption phenomena during the adsorption process reaches an equilibrium state [18]. Design parameters can be determined fitting isotherm data to different isotherm models [19]. Adsorption isotherm is show the interaction between solutes and adsorbents. It is important for optimizing the use of adsorbents [18].

Langmuir, Freundlich, Temkin and Dubinin-Radushkevich isotherms were used in this study.

3.1.1. Langmuir Isotherm

Langmuir isotherm model assumes that adsorbent surface has adsorptive points and each point can adsorb one molecule. So that, mono layer occurred on the adsorbent and the layer disperse homogenous [18,20]. Langmuir isotherm equation linearized form is given as:

$$\frac{q_e}{C_e} = K_L q_{max} + K_L q_e \tag{1}$$

where; Ce is the equilibrium concentration of adsorbate in solution (mg/L), qe is the equilibrium solid phase concentration (mg/g), KLis the Langmuir constants. Ce/qe data is plotted against Ce to calculate KLand qmax[21,22].

3.1.2. Freundlich Isotherm

Freundlich isotherm model assumes that heterogeneous sorption occurs on adsorbent surface, stated in other words adsorption power varies at every sorption point [23]. Freundlich isotherm equation line arized form is given as:

$$\log(q_e) = \log K_f + \left(\frac{1}{n}\right) \log C_e \tag{2}$$

where; Ce is the equilibrium concentration of adsorbate in solution (mg/L), qe is the equilibrium solid phase concentration (mg/g), Kfand n are Freundlich constant. Kf (L/mg) represents the quantity of dye adsorbet onto adsorbent for a unit equilibrium concentration. n (unitless) shows that the degree of favourability of adsorption. 1/n value change between 0 and 1. Surface heterogeneity increase as 1/n value gets closer to zero. logqe data is plotted against log Ce to calculate Kf and 1/n [18,22,24].

3.1.3. Temkin Isotherm

Temkin isotherm model is evaluated interactions between adsorbed substances. This isotherm assumed that heat of adsorption decreases linearly with coverage due to adsorbate/adsorbent interactions [18,25].Temkin isotherm equation line arized form is give as:

$$q_e = \frac{RT}{b_T} \ln K_T + \frac{RT}{b_T} \ln C_e \tag{3}$$

where; Ce is the equilibrium concentration of adsorbate in solution (mg/L), qe is the equilibrium solid phase concentration (mg/g), 1/bT corresponds to the adsorption potential of the adsorbent (J/mol), KT is the Temkin isotherm constant (L/g), T is temperature (Kelvin) and R gas constant (8.314 J/mol.K). qe data is plotted against lnCe to calculate KT and bT [26].

3.1.4. Dubinin-Radushkevich Isotherm

Dubinin-Radushkevich isotherm model is based on the micro pore volume filling theory. This isotherm assumes that multilayer adsorption mechanisms [27].Dubinin-Radushkevich isotherm equation line arized form is given as:

$$\ln q_e = \ln q_{max} + B_D \varepsilon^2 \tag{4}$$

where; qe is the equilibrium solid phase concentration (mg/g), qmax is the maximum solid phase concentration (mg/g), BD is free energy adsorption constant. To calculate the equation (4) the initial value of Ɛ must be calculated with the below equation:

$$\varepsilon = RT \ln \left(1 + \frac{1}{C_e}\right) \tag{5}$$

where; Ce is the equilibrium concentration of adsorbate in solution (mg/L),T is temperature (Kelvin) and R gas constant (8.314 J/mol.K). lnqe data is plotted against Ɛ2 to calculate BD and qmax. Equation (6) is applied after the BD value find. In equation (6), E refers to free energy [27]:

$$E = \frac{1}{\sqrt{2B_D}} \tag{6}$$

If the free energy value range between 1-8 kj/mol, Van der Waals forces are effective and physical adsorption is happened. If free energy value greater than 8 kj/mol, chemical adsorption is happened [28].

3.1.5. Evaluation of Isotherms:

Calculated isotherm parameters summarized on the Table 2 for RB5, RB21, AB283 and BV3 dyes. The results on the Table 2 show that, the best isotherm which describe the adsorption process was Freundlich for all dyes, because of the higher regression coefficient (R2) values. This isotherm model assumes that heterogeneous sorption occurs on adsorbent surface, stated in other words adsorption power varies at every sorption point. Moreover, calculated "1/n" values were range between 0.378-0.957 (1/n<1). Its mean that chemical adsorption happened. Chemical adsorption is generally irreversible. For AB283 dye, calculated regression coefficient (R2=0.991) was very high for AB283 dye. It means that the heat of adsorption decreased linearly with coverage due to adsorbate/adsorbent interactions, so we assume that the adsorption process of AB283 by inactivated sludge is an endothermic reaction.

Table 2. Isotherms parameters of RB5, RB21, AB283 and BV3 dyes

Ishotherm	Parameters	RB5	RB21	AB283	BV3
Langmuir	q_{max}	2.956	-0.00295	0.0376	888
	K_L	0.0285	-0.0006	0.0237	0.0063
	R^2	0.715	0.0243	0.875	0.089

	$1/n$	0.378	0.957	0.625	0.930
Freundlich	K_F	3.01	0.247	3.128	6.045
	R^2	0.964	0.950	0.960	0.989
	b_t	3655	213	172	83
Tempkin	K_T	5.390	0.060	0.248	0.607
	R^2	0.915	0.836	0.991	0.865
	q_{max}	2.03	16.665	33.36	47.375
Dubinin-Raduskevich	B_D	$8*10^{-5}$	$9*10^{-5}$	$2*10^{-5}$	$1*10^{-5}$
	R^2	0.663	0.671	0.904	0.771

3.2. Adsorption Kinetics

Intraparticle diffusion model, Lagergren kinetic model, Pseudo second order kinetic model and Elovich kinetic model were used in this study. BV3 dye reached equilibrium point in 1 minute. So, BV3 dye data could not use in the kinetic models.

3.2.1. Intraparticle Diffusion Model

Intraparticle diffusion model assumes that adsorbate substances in solution enter the pores which are state at the adsorbate, and hold on the surface of the pores [29,30]. Intraparticle diffusion equation is given as:

$$q_t = k_p t^{0.5} \tag{7}$$

where; qt is theamount of material collected on the adsorbent during the t time (mg/g), t is the time (minute), kp is the intraparticle diffusion rate constant. qt data is plotted against t0.5 to calculate kp [31,22].

Intraparticle diffusion model parameters calculated and summarized on the Table 3 for RB5, RB21 and AB283 dyes. High regression coefficient values proved that the intraparticle diffusion theory is valid for all these dyes. It can be assumed, the adsorbent substances which come to the adsorbent pores were entered the pores and kept the pore surface.

Table 3. Intraparticle diffusion model parameters of RB5, RB21 and AB283 dyes

Initial Dye Concentration	Parameters	RB5	RB21	AB283
25 mg/L	R^2	0.994	0.974	0.961
	K_L (mg/g.min$^{0.5}$)	0.323	1.053	2.396
50 mg/L	R^2	0.973	0.968	0.979
	K_L (mg/g.min$^{0.5}$)	0.363	1.413	4.933
75 mg/L	R^2	0.978	0.994	0.958
	K_L (mg/g.min$^{0.5}$)	0.4513	1.834	6.002
100 mg/L	R^2	0.9821	0.995	0.964
	K_L (mg/g.min$^{0.5}$)	0.5327	3.013	7.893
150 mg/L	R^2	0.988	0.991	0.950
	K_L (mg/g.min$^{0.5}$)	0.6828	4.197	9.67

3.2.2. Lagergren (First Order) Kinetic Model

Lagergren equation is used to evaluate the relationship between adsorption rate and adsorption capacity [32]. This model generally in compliance with low adsorbent concentration process [33]. Lagergren kinetic model equation is given as:

$$\log \frac{q_e - q_t}{q_e} = -\frac{k_1 t}{2.303} \tag{8}$$

where; qe is the equilibrium solid phase concentration (mg/g), qt is the amount of material collected on the adsorbent during the t time (mg/g), k1 is the Lagergren rate constant adsorption (min-1), t is the time (min) [34, 18].

Table 4. Lagergren kinetic model parameters of RB5, RB21 and AB283 dyes

Initial Dye Concentration	Parameters	RB5	RB21	AB283
25 mg/L	R^2	0.996	0.934	0.962

Initial Dye Concentration	Parameters	RB5	RB21	AB283
	K_L (min^{-1})	0.171	0.149	0.150
50 mg/L	R^2	0.997	0.968	0.857
	K_L (min^{-1})	1.170	0.103	0.220
75 mg/L	R^2	0.981	0.981	0.922
	K_L (min^{-1})	0.210	0.0744	0.189
100 mg/L	R^2	0.976	0.996	0.897
	K_L (min^{-1})	0.216	0.076	0.171
150 mg/L	R^2	0.919	0.997	0.893
	K_L (min^{-1})	0.231	0.073	0.157

Lagergren kinetic model parameters calculated and summarized on the Table 4 for RB5, RB21 and AB283 dyes. Calculated regression coefficient values for RB21 were increased in direct proportion to initial dye concentration. However, RB5 and AB283 dyes regression coefficient values were decreased depending on the increase initial dye concentration. So, it can be said that Lagergren kinetic model is available for RB21 dye.

3.2.3. .Pseudo Second Order Kinetic Model

This kinetic model assumes that adsorption rate dependent to adsorbent material quantities and contact time [35]. This kinetic model equation linearized form is given as:

$$\frac{1}{q_t} = \frac{1}{q_e} + \left(\frac{1}{k_2 q_e^2}\right)\frac{1}{t} \tag{9}$$

where; qe is the equilibrium solid phase concentration (mg/g), qt is the amount of material collected on the adsorbent during the t time (mg/g), k2 is the pseudo second order rate constant (g/mg.min), t is the time (minute) [36,37].

Pseudo second order kinetic model parameters calculated and summarized on the Table 5 for RB5, RB21 and AB283 dyes. Calculated regression coefficient values for RB5 and AB283 were increased in direct proportion to initial dye concentration. However, RB21 dye regression coefficient values were decreased depending on the increase initial dye concentration. So, it can be said that adsorption rate of RB5 and AB283 dependent to adsorbent material quantities and contact time.

Table 5. Pseudo Second Order kinetic model parameters of RB5, RB21 and AB283 dyes

Initial Dye Concentration	Parameters	RB5	RB21	AB283
25 mg/L	R^2	0.990	0.958	0.922
	K_L (g/mg.min)	0.078	0.085	0.034
50 mg/L	R^2	0.998	0.990	0.909
	K_L (g/mg.min)	0.087	0.020	0.061
75 mg/L	R^2	0.996	0.976	0.964
	K_L (g/mg.min)	0.169	0.009	0.026
100 mg/L	R^2	0.994	0.978	0.964
	K_L (g/mg.min)	0.163	0.005	0.018
150 mg/L	R^2	0.898	0.991	0.971
	K_L (g/mg.min)	0.237	0.002	0.011

3.2.4. Elovich Kinetic Model

Elovich kinetic model has been determined the kinetics of the adsorption and desorption of inorganic substances on solid surface [38]. This kinetic model assumes that the solid (adsorbent) surface is heterogeneous, and adsorption kinetic not affected the low adsorption/desorption interaction [39]. This kinetic model equation linearized form is given as:

$$q_t = \frac{1}{\beta}\ln(\alpha\beta) + \frac{1}{\beta}\ln t \tag{10}$$

where; qt is the amount of material collected on the adsorbent during the t time (mg/g), t is the time (minute), α is the adsorption rate constant (mg/g.min). β is a constant related with to expand the activation energy for chemical sorption and the surface coverage (g/mg). qt data is plotted against lnt to calculate α and β [40,41].

Elovich kinetic model parameters calculated and summarized on the Table 5 for RB5, RB21 and AB283 dyes. High regression coefficient values proved that the Elovich kinetic model is valid for all these dyes. It can be assumed that desorption phenomena do not occur, and adsorption rate decrease with the coverage of adsorbent surface.

Table 6. Elovich kinetic model parameters of RB5, RB21 and AB283 dyes

Initial Dye Concentration	Parameters	RB5	RB21	AB283
25 mg/L	R^2	0.979	0.998	0.971
	α (mg/g.min)	0.486	17.121	22.623
	β (g/mg)	2.547	1.442	0.598
50 mg/L	R^2	0.994	0.992	0.992
	α (mg/g.min)	0.663	0.973	89182
	β (g/mg)	2.300	0.579	0.785
75 mg/L	R^2	0.996	0.967	0.988
	α (mg/g.min)	2.180	2.264	948
	β (g/mg)	2.809	0.319	0.397
100 mg/L	R^2	0.997	0.985	0.998
	α (mg/g.min)	3.237	3.460	604
	β (g/mg)	2.557	0.183	0.272
150 mg/L	R^2	0.967	0.989	0.985
	α (mg/g.min)	17.125	4.459	186
	β (g/mg)	2.796	0.119	0.176

4. CONCLUSION

The study was carried out to understand adsorption mechanisms of RB5, RB21, AB283 and BV3 dyes. Four different isotherms and four different kinetics were used and constants of each isotherms and kinetics were calculated for each dyestuff. The best isotherm which describe the adsorption process was Freundlich isotherm. The best kinetic model which has the highest regression coefficient values was Pseudo second order kinetic model for RB5 and AB283 dyes and Lagergren kinetic model for RB21 dye.

REFERENCE

[1]. J.W. Lee, S.P. Choi, R. Thiruvenkatachari, W.G. Shim, H. Moon, "*Evaluation of the performance of adsorption and coagulation processes for the maximum removal of reactive dyes,*" Dyes Pigments, 69 (2006) 196–203.

[2]. A.B. dos Santos, F.J. Cervantes, J.B. van Lier, "*Review Paper on Current Technologies for Decolourisation of Textile Wastewaters: Perspectives for Anaerobic Biotechnology,*" Bioresource Technology, 98 (2007) 2369-2385.

[3]. A.A. Attia, B.S. Girgis, N.A. Fathy, "*Removal Of Methylene Blue Bycarbons Derived From Peach Stones By H3PO4 Activation: Batch And Columnstudies,*" Dyes And Pigments, (2008) 282-289.

[4]. M.A.M. Salleh, D.K. Mahmoud, W.A. Karim, A. Idris, "*Cationic and anionic dye adsorption by agricultural solid wastes: A Comprehensive review,*" Desalination, 280 (2011) 1-13.

[5]. A. Stolz, "*Basic and applied aspects in the microbial degradation of azo dyes,*" Appl. Microbiol. Biotechnol. 56 (2001) 69–80.

[6]. H. Zollinger, Synthesis, *Properties and Applications of Organic Dyes and Pigments*, Weinheim, (1991) 367p.

[7]. O. Cinar, K. Demiroz, *Biodegradation of Azo Dyes in Anaerobic–Aerobic Sequencing Batch Reactors*, Handbook Environmental Chem., Biodegradation Azo Dyes, (2010) 215.

[8]. Y.S. Ho, G. McKay, Chemical Eng. J., 70 (1998) 115.

[9]. M. Basibuyuk, C.F. Forster, "*An Examination of Adsorption Characteristics of A Basic Dye (Maxilon Red BL-N) on to Live Activated Sludge System,*" Process Biochemistry, 38 (2013) 1311-1316.

[10]. C. Namasivayam, R. Radhika, S. Suba, Waste Manag., 1 (2001) 381.

[11]. C. Namasivayam, N. Muniasamy, K. Gayatri, M. Rani, Bioresour. Technol., 57(1996) 37.

[12]. Y.S. Ho, T.H. Chiang, Y.M. Hsueh, Process. Biochem., 40 (2005) 119.

[13]. C. Namasivayam, D. Arasi, Chemosphere, 34 (1997) 401.

[14]. A.S. Ozcan, A. J. Ozcan, Colloid. Interf. Sci., 276 (2004) 39.

[15]. B. Meroufel, O. Benali, M. Benyahia, Y. Benmoussa, M.A. Zenasni, "*Adsorptive removal of anionic dye from aqueous solutions by Algerian kaolin: Characteristics, isotherm, kinetic and thermodynamic studies,*" J. Mater. Environ. Sci. 4 (3) (2013) 482-491.

[16]. M. Basibuyuk, C.F. Forster, "*The Use of SequentualAnaerobic/Aerobic Process for the Biotreatment of A Simulated Dying Wastewater,*" Environmental Technology, 28 (1997) 843-845.

[17]. Isik, "Inaktif Camurla Cesitli Boyar Maddelerin Adsorpsiyonu," MS Thesis, Cukurova University, Institute of Natural and Applied Sciences, Adana, Turkey, Aug. 2014.

[18]. I.A.W. Tan, B.H. Hammed, A.L. Ahmad, "*Equilibrium and kinetic studies on basic dye adsorption by oil palm fibre activated carbon,*" Chemical Eng. J., 127 (2007) 111-119.

[19]. M. El-Guendi, "*Homogeneous surface diffusion model of basic dyestuffs onto natural clay in batch adsorbers,*" Adsorpt. Sci. Technol., 8 (2) (1991) 217–225.

[20]. Balci, "Atıksulardan Bisfenol-A Gideriminde Biyotik ve Abiyotik Süreçlerin Araştırılması," PhD Thesis, , Cukurova University, Institute of Natural and Applied Sciences, Adana, Turkey, 2014

[21]. I. Langmuir, J. Am. Chem. Soc., 40, 1361 (1918)

[22]. O. Keskinkan, B. Balci, "*Adsorptive Removal of Dyes Using Crude Tree Barks: Equilibrium Isotherm and Kinetics,*" Asian J. of Chem., 25 (8) (2013) 4693-4698.

[23]. M.S.Chiou, H.Y.Li, "*Equilibrium And Kinetic Modeling of Adsorption of Reactive Dye on Cross-Linked Chitosan Beads,*" Journal of Hazardous Materials, 93(2) (2002) 233-248

[24]. F. Haghseresht, G. Lu, "*Adsorption characteristics of phenolic compounds onto coal-reject-derived adsorbents, Energy Fuels,*" 12 (1998) 1100–1107.

[25]. J. Febrianto, A.N. Kosasih, J. Sunarso, Y.H. Ju, N. Indraswati, S. Ismadji, "*Equilibrium and kinetic studies in adsorption of heavy metals using biosorbent: a summary of recent studies,*" Journal of Hazardous Materials, 162 (2009) 616–645.

[26]. J.F. Farah, Nour Sh. El-Gendy, "*Performance, Kinetics and Equilibrium in Biosorption of Anionic Dye Acid Red 14 by the Waste Biomass of Saccharomyces cerevisiae as a Low-Cost Biosorbent,*" Turkish J Eng Env Sci., 37 (2013) 146-161.

[27]. A. Dabrowski, "*Adsorption-From Theory To Practice. Advances in Colloid and Interface Science,*" 93 (2001) 135-224.

[28]. A.H. Chen, S.M.Chen, "*Biosorption of Azo Dyes from Aqueous Solution Byglutaraldehyde-Cross Linked Chitosans,*" Journal Hazardous Material, 172 (2009) 1111-1121.

[29]. H.C. Chu, K.M. Chen, "*Reuse of Activated Sludge Biomass: I. Removal of Basic Dyes from Wastewater By Biomass,*" Process Biochemistry, 37 (2002) 595-600.

[30]. O. Keskinkan, A. Yuceer, M.Z.L. Goksu, M. Basibuyuk, C.F. Forster, "*Heavy metal adsorption characteristics of a submerged aquatic plant (Myriophyllum spicatum),*" Process Biochemistry, 39 (2003) 179-183.

[31]. W.J. Weber, J.C. Morris, J. Sanit. Eng. Div. Am. Soc. Siv. Eng., 89 (1963) 31.

[32]. Y. Song, Y. Du, D. Lu, G. Ye, J. Wang, "*Macrocyclic receptors immobilized to monodisperse porous polymer particles by chemical grafting and physical impregnation for strontium capture: A comparative study,*" Journal of Hazardous Materials, 274 (2014) 221-228.

[33]. W. Hassan, U. Farooq, M. Ahmad, M. Athar, M.A. Khan, "*Potential biosorbent, Haloxylon Recurvum plant systems, for the removal of methylene blue dye,*" Arabian Journal of Chemistry (2013).

[34]. S. Langergren, B.K. Svenska, "*Zur theorie der sogenannten adsorption geloester stoffe,*" Veternskapsakad Handlingar 24 (4) (1898) 1–39.

[35]. H. Ghodosi, J. Farhoudi,M.H. Omid, A. Mahdavi, Mazdeh, "*Comparison of different methods for linear regression of pseudo second order adsorption kinetics of cadmium,*" Journal of Civ. Eng. and Urb. 3, Issue 2 (2013) 73-76.

[36]. Y.S. Ho, G. McKay, Sorption of dye from aqueous solution by peat, Chem. Eng. J., 70 (1998) 115–124.

[37]. N. Ghasemi, P. Tamrı, A. Khademi, N.S. Nezhad, ALWI, "*Alwi, Linearized equations of pseudo second-order kinetic for the adsorption of Pd(II) on Pistacia Atlantica Shells,*" IERI Procedia, 5 (2013) 232-237.

[38]. D.L. Sparks, *Environmental Soil Chemistry*, Academic Press, Second Edition, 350 p., USA, 2002.

[39]. S.S. Gupta, K.G. Bhattacharyya, "*Kinetics of adsorption of metal ions on inorganic materials: A review. Advances in Colloid and Interface Science,*" 162 (1–2) (2011) 39–58.

[40]. Y.S. Ho, G. Mckay, "*Comparative Sorption Kinetic Studies of Dye and Aromatic Compounds onto Fly Ash,*" J. Environ. Sci. Health, A34 (35) (1999) 1179-1204.

[41]. F.E. Erkurt, B. Balci, "*Investigation of Adsorption of Reactive Black 5 Dye onto Activated Carbon by Using Kinetic and Adsorption Models,*" Cukurova Uni. J. of the Faculty of Engi. And Arch., 30(1) (2015) 257-269.